ENTROPY AND SUPERFLUID CRITICAL PARAMETERS OF A STRONGLY INTERACTING FERMI GAS

by

Le Luo

Department of Physics
Duke University

Date:____________________________
Approved:

____
Dr. John Thomas, Supervisor

____
Dr. Steffen Bass

____
Dr. Daniel Gauthier

____
Dr. Haiyan Gao

____
Dr. Stephen Teitsworth

Dissertation submitted in partial fulfillment of the
requirements for the degree of Doctor of Philosophy
in the Department of Physics
in the Graduate School of
Duke University

2008

ABSTRACT

(Physics)

ENTROPY AND SUPERFLUID CRITICAL PARAMETERS OF A STRONGLY INTERACTING FERMI GAS

by

Le Luo

Department of Physics
Duke University

Date:____________________________
Approved:

____
Dr. John Thomas, Supervisor

____
Dr. Steffen Bass

____
Dr. Daniel Gauthier

____
Dr. Haiyan Gao

____
Dr. Stephen Teitsworth

An abstract of a dissertation submitted in partial fulfillment of
the requirements for the degree of Doctor of Philosophy
in the Department of Physics
in the Graduate School of
Duke University

2008

Abstract

Strongly interacting Fermi gases provide a paradigm for studying strong interactions in nature. Strong interactions play a central role in the physics of a wide range of exotic systems, including high temperature superconductors, neutron stars, quark-gluon plasmas, and even a particular class of black holes. In an ultracold degenerate ^{6}Li Fermi gas, interactions between the atoms in the two lowest hyperfine states can be widely tuned by a magnetic-field-dependent collisional resonance. At the resonance, the strongly interacting Fermi gas has an infinite s-wave scattering length and a negligible potential range, which ensures that the behavior of the gas is independent of the microscopic details of the interparticle interactions. In this limit, a strongly interacting Fermi gas is known as the unitary Fermi gas. The unitary Fermi gas emerges as one of the most fascinating problems in current many-body physics. It not only exhibits universal thermodynamic properties in common with a variety of strongly interacting systems, but also shows ideal hydrodynamic behavior.

In this dissertation, I present the first model-independent thermodynamic study of a strongly interacting degenerate Fermi gas. The measurements determine the entropy and energy. The entropy versus energy data has been adopted by several theoretical groups as a benchmark to test current strong-coupling many-body theories, which reveals universal thermodynamics in unitary Fermi gases. My measurements show a transition in the energy-entropy behavior at

$S_c/k_B = 2.2 \pm 0.1$ corresponding to the energy $E_c/E_F = 0.83 \pm 0.02$, where S_c and E_c are the critical entropy and energy per particle respectively, k_B is Boltzmann constant, and E_F is the Fermi energy of a trapped gas. This behavior change of entropy is interpreted as a thermodynamic signature of a superfluid transition in a strongly interacting Fermi gas. By parametrization of energy-entropy data, the temperature is extracted by $T = \partial E/\partial S$, where E and S are the energy and entropy of a strongly interacting Fermi gas. I find that the critical temperature is about $T/T_F = 0.21 \pm 0.01$, which agrees extremely well with very recent theoretical predictions.

I also present an investigation of viscosity from the hydrodynamics of a strongly interacting Fermi gas. First, the study of the hydrodynamic expansion of a rotating strongly interacting Fermi gas reveals nearly prefect irrotational flow arising in both the superfluid and the normal fluid regime. Second, by modeling the damping data of the breathing mode, I present an estimation of the upper bound of viscosity in a strongly interacting Fermi gas. Using the entropy data, this study provides the first experimental estimate of the ratio of the viscosity η to the entropy density s in strongly interacting Fermi systems. Recently the lower bound of η/s is conjectured by using a string theory method, which shows $\eta/s \geq \hbar/(4\pi k_B)$. Our experimental estimate indicates that this quantity in strongly interacting Fermi gases approaches the lower bound limit.

Finally, I describe the technical details of building a new all-optical cooling and trapping apparatus in our lab for the purpose of the above research as well as our studies on optimizing the evaporative cooling of a unitary Fermi gas in an optical trap.

Acknowledgements

During my whole time as a graduate student, I feel truly blessed to have had all of these people in my life. Without the supports and encourages from them, this accomplishment will never come to be true. My heartfelt gratitude and love towards them will never be successfully expressed by the following words .

I must begin with my parents, Jilan Zhang and Zhenzhong Luo. They provided an endless source of care and love since I was born. I come to realize that what magnificent sacrifices they made in order to raise me and help me grow up so that I can freely choose what I like to do and become whom I want to be. Their wisdom and love give me constant courage to face any challenges in my life I had met, and will meet.

At Duke University, I am fortunate to have had the privilege of having Dr. John Thomas as my advisor. I am deeply indebted to John for his support and advice in my research as well as my career. John has the charm to attract any student who loves physics. He has the magic to express the physics in his insightful, jovial, and quick-witted way. As a world-class talent, he is a master in the professional field with rich knowledge as well as deep insights. More surprising from John, you can not find any self-importance that so often accompanies such prominence. Instead, you will enjoy the way he teases students and banters himself in the time of exploring the science. I tried to learn how to practice science from John as more as possible. One of the great things John taught me is “A good experimental physicist is always an excellent engineer,” which is one of many John’s quotations I love. John has been a fantastic mentor and a true friend during my years at Duke. I am sure that I will look back on this time in my life with fond memories with such a great mentor.

In our close research group at Duke, many members played significant roles in my development. Bason Clancy was the person I worked with most closely in the group. He is my classmate as well as my coworker to build a whole new cold atoms lab. We began with an empty room together, overcame the difficulties together, experienced suffering time as well as exciting moments together. Without his talent in making equipment, I would never accomplish the work of building a whole new apparatus. I will keep the heart-warming time we passed through in mind. I especially appreciate the patient training that Staci Hemmer supplied in my early days in the laboratory. I thank the senior student Joseph Kinast and the postdoctoral researcher Andrey Turlapov, who worked in the other Fermi atoms lab for the most of time I stayed in the group. They provided many help and suggestions for my projects in the new lab. Joe’s relentless perfectionism and Andrey’s constant optimism brought me lots of fun during my time of doing research. James Joseph is another peer graduate student working with me. While he put his main energy in the old lab, I really appreciate his important contributions on building the new lab. I thank Ingrid Kaldre and Eric Tang, two undergraduate researchers in our laboratory, for helping us building a Zeeman slower and logic gates. I also thank the visiting scholar Martine Oria for her helps on the diode laser project.

My last year in the lab was also made more enjoyable by the presence of inductees into the research group: Xu Du and Jessie Petricka, two postdoc researchers, Chenglin Cao a Yingyi Zhang, two graduate students. I believe our lab will have a bright future through their capable hands.

I thank the members of my advisory committee, including Dr.Steffen Bass, Dr.Daniel Gauthier, Dr.Haiyan Gao, and Dr.Stephen Teitsworth. They provide many advices which benefit my Ph.D. research, from quantum monte carlo calculation, nucleus shape deformation, to fiber optics. I particularly thank Dr. Teitsworth, who spent one semester to review quantum many-body theories with me, where I learned plenty of theoretical background of my experimental work. I also thank him for providing important suggestions and support for my career plan.

I am thankful for the assistance from department staffs, Donna Ruger for her continuous assistance for graduate student, Angela Garner for her careful work on equipment purchase, Gary Swift for his skills in high vacuum part welding, and Barry Wilson for his daily helps in computing. All of these were invaluable for my study and research.

I am thankful for the assistance from outside of Duke. Dr. Qijin Chen from Prof. Kathy Levin's Group at University of Chicago had a nice discussion with me on thermodynamic measurements, and provided pseudogap calculations on the thermodynamic paraments of trapped Fermi gases. Dr. Aurel Bulgac at University of Washington developed the quantum Monte Carlo calculation for trapped Fermi gases, and made a carefully caparison with our experimental data. Also, Dr. Hui Hu from Prof. Peter Drummond's group in University of Queensland provided their calculation based on a T-matrix theory.

Luckily, out of the group I have met a number of other friends at graduate school at Duke. They are my physics classmates Zheng Gao, Qiang Ye, Andy Dawes, and Jie Hu etc. and as well as students in other departments Hao Zhang, Jing Huang, Junan Zhang etc. They provided me many helps in my study and life as well as having some fun together.

Finally, I come to my wife Xiaofang Huang, to whom I owe everything during the past decade since we met and made it through. Without her love and caring, I surely would not have enough courage to pursue dreams in science half-the-earth away from our family. Without her love and support, I surely would not have enough perseverance to pass the long time throughout my graduate career. I cherish every moment that she is by my side, and look forward to the future time we will have together. Anywhere and anytime, Xiaofang, my love belongs to you.

For Xiaofang Huang

Contents

List of Tables

List of Figures

Chapter 1

Introduction

When my friends and family members asked me "What are you doing in the graduate school?" I always hesitated for a moment considering how to explain my research to my curious questioners. It is not easy to explain an atomic physics research to a general audience with simple words while still being interesting enough to satisfy their curiosity. Usually I will tend to give an easy answer like "Study a gas." "A gas?" people's face registered surprise, for whom modern physicists should study more "fancy" things such as semiconductors or quarks. "Yes, it is a gas, but it is one of the coldest materials in the universe." I began to show the "fancy" point. "Really, what it is used for?" people began to be interested. "By studying it, we can better understand the baby universe and even a black hole." "Cool, tell me the story!" finally I got the chance to describe the "cool" story about "laser frozen atoms" which occupied my life during the past several years.

The same story is described in this dissertation. I will try to tell my readers a "cool" story about the ultracold atoms in my lab. More specifically, they are strongly interacting ferminonic atoms of ^{6}Li.

In this introduction, first I will explain why strongly interacting Fermi gases have a prominent role in understanding some of the most fundamental physics in nature. Following that, I will give a brief review of the progress in the field of cold Fermi gases in recently years. Then I will talk about the significance of my Ph.D. research, which is focused on experimental studies of thermodynamics of strongly interacting Fermi gases as well as its nearly ideal fluidity. Finally an outline of this dissertation will be provided.

1.1 Strongly Interacting Fermions in Nature

As a law of nature, identical fundamental particles are indistinguishable. In quantum mechanics, this law causes the wavefunction of identical particles to fall into two classes of symmetry: symmetric or antisymmetric. If two identical particles have a symmetric wavefunction, they are named as bosons and obey Bose-Einstein statistics. In contrast, the particles with an antisymmetric wavefunction are called fermions and obey Fermi-Dirac statistics. For atoms, the intrinsic spin decides whether an atom is a boson or fermion: atoms with integer spin (0, 1, and so on) are bosons, while fermions have half-integer spin (1/2, 3/2, and so on).

At very low temperature, these two classes of atoms show quite different behavior: bosons "like each other," and occupy the same quantum state to form a condensate, whereas the Pauli-exclusion principle makes the fermions "avoid each other" by filling the energy levels from the lowest state up to the highest state labeled as Fermi energy. Such Fermi gases have a tower structure in the energy domain and are called as degenerate Fermi gases. From the perspective of modern physicists, Fermi gases are more important sources of new physics than Bose gases, because all the material elementary particles are fermions, such as quarks, electrons, muons, taus and neutrinos.

The intriguing properties of many-body quantum physics are usually related to complex interactions between fermionic particles. One of the most compelling problems is to study strong interacting fermions. In an interacting system, strong interaction is defined by the condition that the scattering length of the interacting particles is much larger than the average interparticle spacing. Strong interactions between fermions dominate behavior of a wide scale of matter in the universe, which appears in terms of all four fundamental forces. In condensed matter, high-temperature superconductor is a well-known example of strongly interacting system, where strong interactions arise through electromagnetic forces. In nuclear matter, neutron stars are examples of strongly interacting systems, where strong interactions are produced by gravity and strong forces. In high energy matter, an example of strongly interacting Fermi systems is a quark-gluon plasma (QGP), where fermionic quarks interact strongly by exchanging the gauge boson of gluons in a certain energy range. QGPs are believed to be the initial state of matter in the universe that existed only within ten of microseconds after the Big Bang [1]. Recently a QGP created at the Relativistic Heavy Ion Collider in Brookhaven National Laboratory exhibited amazing hydrodynamic properties, which is believed to be a signature of strong interactions in this system [2]. Very recently, string theory methods showed that a class of black holes in higher dimensional space have elegant connections with strongly interacting quantum fields, which adds another type of strongly interacting system [3].

Strongly interacting Fermi gases created by ultracold Fermi atoms provide a clean, controllable laboratory environment to study those novel strong interacting Fermi systems in nature. For our lab, this system is realized by laser cooling and trapping an ultracold degenerate ^{6}Li Fermi gas in the two lowest hyperfine states.

When a Fermi gas becomes degenerate, the Pauli exclusion principle prevents collisions between the identical atoms. So trapping a Fermi gas with atoms in different spin states is a precondition for creating an interacting Fermi gas. The tunability of interactions in our degenerate ^{6}Li gas relies on a magnetic field dependent collisional resonance known as Feshbach resonance. By tuning a bias magnetic field, the s-wave scattering length of the colliding atoms changes from an infinite positive value to a infinite negative value at the field below or above Feshabach resonance.

At resonance, a strongly interacting Fermi gas has an infinite s-wave scattering length and a negligible potential range, which ensures the behavior of such systems becomes totally independent of the microscopic details of their interparticle interactions. In this limit, a strongly interacting Fermi gas is usually known as a unitary Fermi gas. Unitary Fermi gases exhibit universal behavior in both thermodynamics and hydrodynamics, which can be used to study other strongly interacting Fermi systems mentioned in the above. For example, unitary Fermi gases are predicted to exhibit finite temperature thermodynamics that is universal in a variety of strongly interacting systems [4–6]. The other example is nearly ideal fluidity in a strongly interacting Fermi gas, which is believe to be a common phenomena in all strongly interacting Fermi systems [3, 7].

Even now, a complete understanding of the physics of strongly interacting systems from a theoretical viewpoint has been impossible due to the lack of small coupling parameters at the unitary limit [8]. There is a pressing need for independent experimental investigations in strongly interacting Fermi gases.

1.2 Overview of Current Progress in Ultracold Fermi Gases

After the breakthrough of Bose-Einstein condensations (BECs) created in dilute cold bose gases in 1995, the realization of degenerate strongly interacting Fermi gases with ultracold fermionic atoms immediately became the next milestone targeted by the whole field of cold atom physics [9–11].

The first degenerate strongly interacting Fermi gas was created in our lab at Duke in 2002 [12]. Before that, degenerate Fermi gases were created by several methods, such as double RF knife evaporative cooling [13], sympathetic cooling both bosons and fermions in a magnetic trap [14–16], and direct evaporative cooling in an optical dipole trap [17,18]. Six groups, including our group at Duke, Jin's group at JILA, Hulet's group at Rice, Ketterle's group at MIT, Grimm's group at Innsbruck, and Salomon's group at ENS, have made major contributions to the experimental investigations.

Several milestones have been realized by those groups, including studies of thermodynamics and superfluidity of unitary Fermi gases [19, 19–25], realization of molecular BEC [26–28], Fermi condensation [29, 30], and creation of novel quantum phases such as spin polarized Fermi superfluids [31, 32].

Below the Feshbach resonance, a degenerate Fermi gas has a positive scattering length, where a tightly bounded molecular state is formed [33, 34]. Molecular BECs were first observed in ^{40}K and ^{6}Li in 2003 [26, 28].

Far above the Feshbach resonance, the scattering length has a small negative value and the effective interaction is attractive. This permits the existence of the Cooper pair predicted by BCS theory, developed by Bardeen, Cooper, and

Schrieffer [35].

Near resonance, a high temperature Fermi superfluid in a strongly interacting Fermi gas was sought for a long time [9, 36]. Evidence of this new state of matter appeared in both microscopic and macroscopic measurements in recent years. Anisotropic expansion of a strongly interacting Fermi gas was firstly observed in 2002 [12], suggesting that the Fermi gas entered into the superfluid hydrodynamic regime. In 2004, Fermi condensates were observed by pair projection experiments using fast magnetic field sweep [29, 30]. The collective mode measurements in breathing mode [19–22], quadrupole mode [37] and scissors mode [23] showed superfluid transition behavior in the damping versus temperature data. Radio-frequency (RF) spectroscopy revealed a pairing gap near the transition point [38]. Vortex lattices in a rotating strongly interacting Fermi gas directly demonstrated a high temperature superfluidity in this system [24, 25]. Very recently, normal-superfluid phase separation in spin polarized Fermi gases [31, 32] provides a rich source for exploring novel quantum phases in strongly interacting Fermi gases.

1.3 Significance of My Doctoral Research

My Ph.D. research is divided into two stages: apparatus building and scientific research in the time period before and since 2006 respectively. I will present the scientific results first. In Section 1.3.1, I will discuss the significance of my research on model-independent thermodynamic measurements of both the energy and the entropy of a strongly interacting Fermi gas. Following that, in Section 1.3.2, I will present our studies of nearly ideal hydrodynamics in a strongly interacting Fermi gas, which shows extremely low viscosity behavior. I will put my emphasis on the topic of thermodynamics. A more detailed description about the hydrodynamics will be presented in the concurrent thesis of my colleague student Bason Clancy [39]. In Section 1.3.3, I will summarize my work on developing a new compact all-optical cooling and trapping system for ultracold ^{6}Li gas.

1.3.1 Thermodynamics of a Strongly Interacting Fermi Gas

Strong interactions play a central role in thermodynamics for a wide range of exotic strongly interacting systems, including high temperature superconductors, neutron stars, quark-gluon plasmas, and even a particular class of black holes. It is very surprising that, although the above systems are different by many orders in the energy scale, their thermodynamic properties are all independent of the details of the microscopic interactions. Theoretical studies in recent years predict that there exists a universality in the unitary Fermi gas. For the ground state of a uniform gas, the universality indicates that the difference between the energy of a strongly interacting Fermi gas E_{SI} and the energy of a noninteracting ideal Fermi gas E_{NI} can be characterized by $E_{SI} = (1+\beta)E_{NI}$, where β is a universal many-body parameter. At finite temperature, universality predicts universal thermodynamics for strongly interacting Fermi gases that is valid for different particles and different energy scales.

Among the most interesting thermodynamic properties are the critical parameters of the normal-superfluid transition in strongly interacting Fermi gases. This phase transition attracts intense interest from condensed matter physicists because it represents a novel superfluid phase with a very high transition temperature: up to 30% the Fermi temperature. The critical temperature is much "higher" than any superfluid or superconductor that exists in the liquid or solid phase, where "higher or lower critical temperature" refers to the ratio of their absolute transition temperature T_c to the Fermi temperature T_F. T_F is a characteristic temperature of the Fermi system corresponding to the Fermi energy by $E_F = k_B T_F$, where k_B is the Boltzmann constant. In cuprate high temperature superconductors, the absolute transition temperature is about 100 K and a typical Fermi temperature is on the order of 10^4 K, which gives the critical temperature is about $T_c/T_F \approx 10^{-2}$ [40]. Very surprisingly, in strongly interacting Fermi gases T_c/T_F is predicted up to 0.30 by a strongly pairing mechanism [41–44]. So studying high temperature superfluidity in ultracold Fermi gases will help to shed light on the mysterious mechanisms of high temperature superconductivity in solids.

The primary efforts presented in this dissertation are experimental investigations of thermodynamics of strongly interacting Fermi gases in the unitary limit. Previously our lab made the first thermodynamic study of strongly interacting Fermi gases by measuring heat capacity, where the heat capacity was extracted from the temperature dependence of the energy [45]. However, the temperature was determined in a model-dependent way. They first fit the profile of a strongly interacting Fermi gas to get an empirical temperature, then use a theoretical model based on pseudogap theories to extract the real temperature from the empirical temperature. Unfortunately, in the strongly interacting regime, no theoretical model including the pseudogap theory is well accepted. There is no strong-coupling theory that has been verified to give precise predictions in the unitary regime. For this reason, this previous measurement of the heat capacity only provides a self-consistent test of the pseudogap theory and is a model-dependent result.

Several other methods have been used previously to characterize the temperature of a strongly interacting Fermi gas. One method is based on connecting the temperature of a strongly interacting Fermi gas to the temperature of a molecular BEC or a noninteracting Fermi gas [30, 38]. A magnetic field is swept to change the scattering length, which converts a strongly interacting Fermi gas to a molecular BEC or a noninteracting Fermi gas. Then the temperature of the molecular BEC or the noninteracting Fermi gas is measured by well established theoretical models. The temperature of the strongly interacting gas is then estimated from the temperature of the molecular BEC or the noninteracting gas Fermi gas by strong-coupling theoretical models that relates the temperature in different regimes [46]. It is very obvious that those methods for thermodynamic measurements are still model-dependent. A model-independent method of determining the temperature of a spin-polarized strongly interacting Fermi gas was recently developed by the MIT group, which is based on the phase separation of superfluid-normal fluid in imbalanced spin mixtures of a two-component Fermi gas [47]. This method fits the noninteracting edge of the majority spin by a Thomas-Fermi distribution to extract the temperature. However, this method is only appropriate for spin-polarized systems with phase separation, and it is not applicable to a spin-balanced strongly interacting Fermi gas.

To provide experimental data for the comparison with many-body theories, model-independent measurements of the thermodynamic parameters are required for a strongly interacting Fermi gas. For this purpose, we measured both the entropy and the energy of a strongly-interacting Fermi gas in the unitary limit. The energy is determined by measuring the mean square size of the atom cloud in the strongly-interacting regime. Our laboratory have proven that the virial theorem is strictly valid for a scale-invariant strongly interacting system [48], which assures a simple relation between the cloud size and the total energy. The entropy measurement proceeds by adiabatically sweeping the magnetic field from the strongly interacting regime to the weakly interacting regime, during which the entropy of the gas is conserved. In the weakly interacting regime, the entropy of gas can be well determined: The entropy of the weakly interacting Fermi gas has a well defined relation with the mean square size of the cloud, which is readily measured.

This method gives a very precise model-independent measurement of both entropy and energy in a strongly-interacting Fermi gas. From the entropy-energy relation, I determine the ground state energy of a strongly interacting Fermi gas and find a transition behavior in the entropy versus energy curve. This transition is interpreted as a thermodynamic signature of a normal-superfluid phase transition in a strongly interacting Fermi gas [49]. Furthermore, the energy dependence of the entropy data provides the most important evidence for proving universal thermodynamics in strongly interacting Fermi gases [6]. The parametrization of the energy-entropy data provides a real thermometry for a strongly interacting Fermi gas, which can be used to classify the order of this novel phase transition for future research.

1.3.2 Nearly Ideal Fluidity in a Strongly Interacting Fermi Gas

The nearly ideal fluid behavior of strongly interacting Fermi gases is a very interesting topic. It is predicted that a strongly interacting Fermi gas shows fermionic superfluidity below the critical temperature, where superfluids exhibit collisionless hydrodynamics with zero shear viscosity η in frictionless flow [41–44]. Surprisingly, above the critical temperature, a strongly-interacting Fermi gas still shows nearly perfect hydrodynamics, which is confirmed by both the previous anisotropic expansion and breathing mode experiments in our laboratory [12, 19, 20]. This hydrodynamics originates from the unitary-limited elastic collisions between the fermionic atoms in the different spin states, and is believed to have very low viscosity behaviors [50].

One of the interesting behaviors for ideal fluids is irrotational flow, which is usually thought of as symbol of a superfluid instead of a normal fluid, unless the normal fluid has extremely low viscosity. In this dissertation, I will present our experiment of the expansion dynamics of a rotating strongly interacting Fermi gas [51], where nearly perfect irrotational flow in the normal fluid is observed and indicates the extremely low viscosity in this system.

The irrotaional hydrodynamics suggests a normal strongly interacting Fermi gas may reach a nearly "perfect fluidity" regime, which is a new concept appearing in studies of the strongly interacting quantum particles and fields. The "perfectness" of fluidity is determined by the temperature dependence of the viscosity. At a given temperature, the smaller the viscosity, the better the fluidity. Through a string theory calculation, Kovtun *et al* predicted that the ratio of shear viscosity η to entropy density s has a lower bound of $\eta/s \geq \hbar/(4\pi k_B)$ for strongly interacting fluids [3], which constitutes the quantum limit of viscosity in nature for a given entropy density. According to their theory, this extremely low quantum viscosity exists in strongly interacting quantum fields or particles that are in the unitary limit. In this dissertation, by using a simple hydrodynamic model based on viscous force, I reanalyze the previous damping data of the collective oscillations of the cloud in our laboratory, and find η/s for a strongly interacting Fermi gas at the unitarity approaches the lower bound limit conjectured by the strong theory method.

1.3.3 Building an Apparatus for Cooling and Trapping ^{6}Li Atoms

When I joined the group in 2003, our lab only had one all-optical cooling and trapping system, which was built in 2000. Due to the strong competition in this field, we decided to build a second apparatus for research on ultracold ^{6}Li atoms. One reason to build a new system is to update the technology for all-optical cooling and trapping. Our old system is the first apparatus in the world for all-optical cooling and trapping of fermions. The equipment was built according to the principle of "as long as it works." After several years of experiments, we found there is plenty of room to improve the whole capability and reliability of the all-optical cooling and trapping system by redesigning or simplifying some key components. Bason Clancy and I spent about two years building the new system.

To give a better description for what we built, it is worth summarizing the subsystems of the all-optical cooling and trapping apparatus used in our lab:

1. Vacuum and atom source: a main atomic oven, an atomic beam Zeeman slower, and an ultrahigh vacuum chamber.

2. Magnetic-optical trap (MOT): lasers and optics for ^{6}Li MOT, wavemeter and Fabry-Perot cavity for laser frequency measurement, an auxiliary atomic beam and optoelectronics for laser frequency locking.

3. Ultrastable CO_2 laser optical dipole trap: an ultrastable CO_2 laser system, optics and high vacuum viewport for the infrared beam, a high power acoustic-optic modulator, and ultralow noise electronics for beam controlling.

4. Magnets: MOT and high field magnets, magnet power supplies, and water cooling and self-protection electronics.

5. Imaging and probing system: a charge-coupled device (CCD) camera for absorption imaging, a photo-multiplier tube (PMT) for atom's fluorescence detection, and an antenna for radio-frequency (RF) spectroscopy,

6. Computer control and data acquisition: a high speed 32-bit digital pulse timing system, a multiplexer for digital to analog conversion, a GPIB control system for arbitrary wavefuntion generation, and a high precision optical and RF pulse generation system.

7. Software programs: a program package for timing and instrument control by combining Labview, Perl, C++ and SCPI languages, the Andor camera program, and image processing and data analysis programs written in Igor and Mathematica.

My main contribution to the new lab is designing and constructing the optics and electronics for the ultrastable CO_2 laser trap. There are several key techniques for applying a high power CO_2 laser in all-optical cooling and trapping experiments. In the new lab, we used a commercial stable CO_2 laser from Coherent. I designed and built a liquid-cooling system, which is not included in this commercial package and is crucial to the laser stability. I measured the intensity and pointing noise of the CO_2 laser beam to ensure the stability is appropriate for our application.

An important technique for the ultrastable CO_2 laser trap is controlling the high power CO_2 beam very quietly. We used a commercial acoustic-optic modulator (AO) from IntraAction Corp. But the noise level of the internal RF source in the modulator does not satisfy our requirements for forced evaporation of ^{6}Li in an optical trap. I modified the electronics of the modulator to applying the external RF source instead of the internal RF source.

The high power CO_2 laser beam was transported into the high vacuum chamber through homemade ultrahigh vacuum infrared viewports. For high power CO_2 laser beams, zinc selenide (ZnSe) crystals are the best choice for the vacuum viewports to get high transparency and high beam quality. However, ZnSe crystals are very soft and are not appropriate for the application of ultrahigh vacuum windows, since ultrahigh vacuum windows usually requires high torques for hard sealing that will break the soft crystal material. Soft sealing viewports for ultrahigh vacuum require very special vacuum techniques. The commercial products are sold by very few companies, whose products are extremely expensive and not always available. For these reasons, we decided to develop our own techniques for making infrared ZnSe viewports. By combining two vacuum sealing techniques "differential pumping" and "soft seals with a Pb-Ag-Sn alloy", I developed a novel high vacuum infrared viewport for our new cooling and trapping system. The home-made viewports support a 10^{-11} torr vacuum and at least 100 watt laser power. The total material cost of making this new window is only one third of the price of the commercial ones.

I also designed and built the whole electronics system for timing and data acquisition. There are two main functions for the electronic control system: precision timing and digital-to-analog conversion. A cycle for cooling and trapping cold atoms runs according to precise timing sequences. Most elements require time steps of 100 microseconds and some need sub-microsecond precision. In the new timing system, I used a National Instruments high speed 32-bit digital pulse card for the first application, while I used Stanford pulse generators for the higher precision applications. The digital pulse sequence is described in the "timing files," which guided the Labview program to control the activity of every element. For some applications, analog signals are needed instead of the digital one. For this purpose, a home-made multiplexer is used for digital-to-analog conversion.

We created our first CO_2 laser trap in the new apparatus in October 2005. Then we spent time investigating the unique characteristics of forced evaporation in the strongly interacting regime. By doing this, we optimized the forced evaporation of a strongly interacting Fermi gas, and enabled a run-away evaporation by lowering the optical trap according to a certain lowering curve. Finally we obtained the absorption images of strongly interacting Fermi gases near the ground state in the spring of 2006. This was the stepping-stone to experimentally exploring the physics of strongly interacting Fermi gases.

1.4 Organization of Dissertation

Chapter 2 summaries the physical system of ^{6}Li atoms in the hyperfine states that we used to create strongly interacting Fermi gases. I first present the hyperfine structures of ^{6}Li atoms in a magnetic field. After that, I give a brief introduction on quantum collision physics and the s-wave Feshbach resonance, which is the key method to make cold atoms strongly interacting.

In Chapter 3, I introduce the general experimental methods we use to generate and characterize a strongly interacting Fermi gas, which includes: absorption imaging in a magnetic field, evaporative cooling of the unitary Fermi gas, creating strongly interacting, weakly interacting and noninteracting Fermi gas, and calibrating the magnetic field.

In Chapter 4, I describe the theory for determining the total energy of a strongly interacting Fermi gas from the mean square size of the cloud. First, I give a proof of the virial theorem for the unitary Fermi gas, which enables me to make an elegant connection between the energy and the cloud size. Then, I explain how to measure the mean square size of the cloud by fitting the column density with the Thomas-Fermi profile. In the end, I apply the virial theorem for the trapped gas in both harmonic traps and Gaussian profile potentials.

In Chapter 5, I describe my method to measure the total entropy of a strongly interacting Fermi gas. Due to the lack of a reliable method to determine the entropy in the strongly interacting regime, I adiabatically sweep the gas from the unitary regime to the weakly interacting regime by smoothly varying the magnetic field, so that the total entropy is conserved. I summarize our calculation of the entropy versus the mean square size of the cloud for a trapped noninteracting gas. In the end, I will demonstrate that the entropy of weakly interacting Fermi gas can be well determined based on the entropy of a trapped noninteracting Fermi gas with a small mean field correction to the ground state energy.

In Chapter 6, the experimental measurements of both energy and entropy are presented. First, the method of preparing the atom clouds at different energies is introduced. After that, the technique of the adiabatical sweep is described. Then, I give the primary measurements for the energy and entropy. By parameterizing these data, I extract the ground state energy of a strongly interacting Fermi gas, the critical parameters of the superfluid phase transition, and the temperature of a strongly interacting Fermi gas. I also obtain the chemical potential and the heat capacity from basic thermodynamic relations. Finally, I compare my model-independent energy-entropy with the calculations from some strong-coupling theories. My measurement provides the first model-independent benchmark to test the theories as well as important evidence for universal thermodynamics in strongly interacting Fermi gases.

In Chapter 7, I describe the study on the hydrodynamic expansion of a rotating strongly interacting Fermi gas. I observed the quenching of the moment of inertia in the expansion, indicating that irrotational flow exists in this system. By conservation of angular momentum, I test a fundamental relation between the effective moment of inertia and the rigid body moment of inertia for this irrotational hydrodynamics. After that, I describe a theoretical model for extracting the shear viscosity from the previous data of the damping of the collective breathing mode in our laboratory. Combined with the entropy data, I make an estimate of the energy dependence of η/s in a strongly interacting Fermi gas.

In Chapter 8, I describe the technical details of how to build an all-optical cooling and trapping apparatus. While the basic cooling and trapping techniques are summarized briefly, I focus on the key techniques of the ultrastable CO_2 laser optical dipole trap. This chapter can provide a "technical manual" for building similar CO_2 laser traps.

Chapter 9 offers a conclusion to this dissertation, possible improvements to the apparatus, and an outlook for future studies of strongly interacting Fermi gases.

There are two appendices included in this dissertation.

Appendix A presents Mathematica programs for calculating a number of thermodynamic properties of a noninteracting trapped Fermi gases in both harmonic and Gaussian potentials. A program that calculates the thermodynamic properties of the ground state gases in the whole regime of BEC-BCS crossover is also included in this appendix. This appendix is intended for the future study of thermodynamics of a strongly interacting Fermi gas.

Appendix B includes the updated Igor procedure file I wrote for imaging processing. These new user-defined functions are very helpful for the ongoing and future projects in our lab that requires 2D image processing and double-spin imaging processing.

Chapter 2

^{6}Li Hyperfine States and Collisional Properties

In our experiments, a strongly interacting Fermi gas comprise a two-component mixture of ^{6}Li atoms in the lowest hyperfine states. At very low temperature, a magnetic field is applied to tune the s-wave scattering length of the atoms in different hyperfine states to diverge, due to the collisional effect known as a Feshbach Resonance. In this chapter, I will describe the hyperfine states of ^{6}Li atoms, and explain how the Feshbach resonance makes the interaction strength tunable in this system.

2.1 Hyperfine States of ^{6}Li

2.1.1 Hyperfine States in Zero Magnetic Field

To study an ultracold Fermi gas, we need to choose the proper species of Fermi atoms which can be laser cooled and trapped. The relatively simple atomic structures and spectra of the alkali metal atoms make them the most common ones for the experiments in cold atom physics. ^{6}Li atoms are one of the isotopes of the third element in the periodic table composed of 3 protons, 3 neutrons, and 3

Property	Symbol	Value	Reference
Electron Spin Angular Momentum	s	1/2	
Electron Orbit Angular Momentum	$l(2\,^2S)$	0	
	$l(2\,^2P)$	1	
Electron Total Angular Momentum	$J(2\,^2S_{1/2})$	1/2	
	$J(2\,^2P_{1/2})$	1/2	
	$J(2\,^2P_{3/2})$	3/2	
Total Electronic g-Factor	$g_J\ (2\,^2S_{1/2})$	-2.0023010	[52]
	$g_J\ (2\,^2P_{1/2})$	-0.6668	[52]
	$g_J\ (2\,^2P_{3/2})$	-1.335	[52]
Magnetic Dipole Constant	$A_{2\,^2S_{1/2}}$	152.136 840 7 MHz	[52]
	$A_{2\,^2P_{1/2}}$	17.375 MHz	[52]
	$A_{2\,^2P_{3/2}}$	-1.155 MHz	[52]
Electric Quadrupole Constant	$B_{2\,^2P_{3/2}}$	-0.10 MHz	[52]
Nuclear Spin Angular Momentum	I	1	
Nuclear Spin g-Factor	g_I	0.0004476540	[52]

Table 2.1: The fine energy levels of ^{6}Li and the corresponding g-factors.

electrons. The nuclear spin of ^{6}Li is one. The unpaired valence electron makes the total atom spin half integral so that neutral ^{6}Li atoms are fermions.

The fine structure of ^{6}Li atoms is induced by the spin-orbit interaction, which is the magnetic dipole interaction between the spin angular momentum $\hat{\mathbf{S}}$ and the orbit one $\hat{\mathbf{L}}$. The coupling of $\hat{\mathbf{S}}$ and $\hat{\mathbf{L}}$ gives the total electron angular momentum $\hat{\mathbf{J}} = \hat{\mathbf{L}} + \hat{\mathbf{S}}$. Because of this interaction, the transition from the ground state to the excited state splits into the D_1 and D_2 lines, corresponding to the fine structure transitions of $2\,^2S_{1/2} \leftrightarrow 2\,^2P_{1/2}$ and $2\,^2S_{1/2} \leftrightarrow 2\,^2P_{3/2}$ respectively. The quantum numbers and g-factors of the fine structure energy levels of ^{6}Li are listed in Table 2.1.

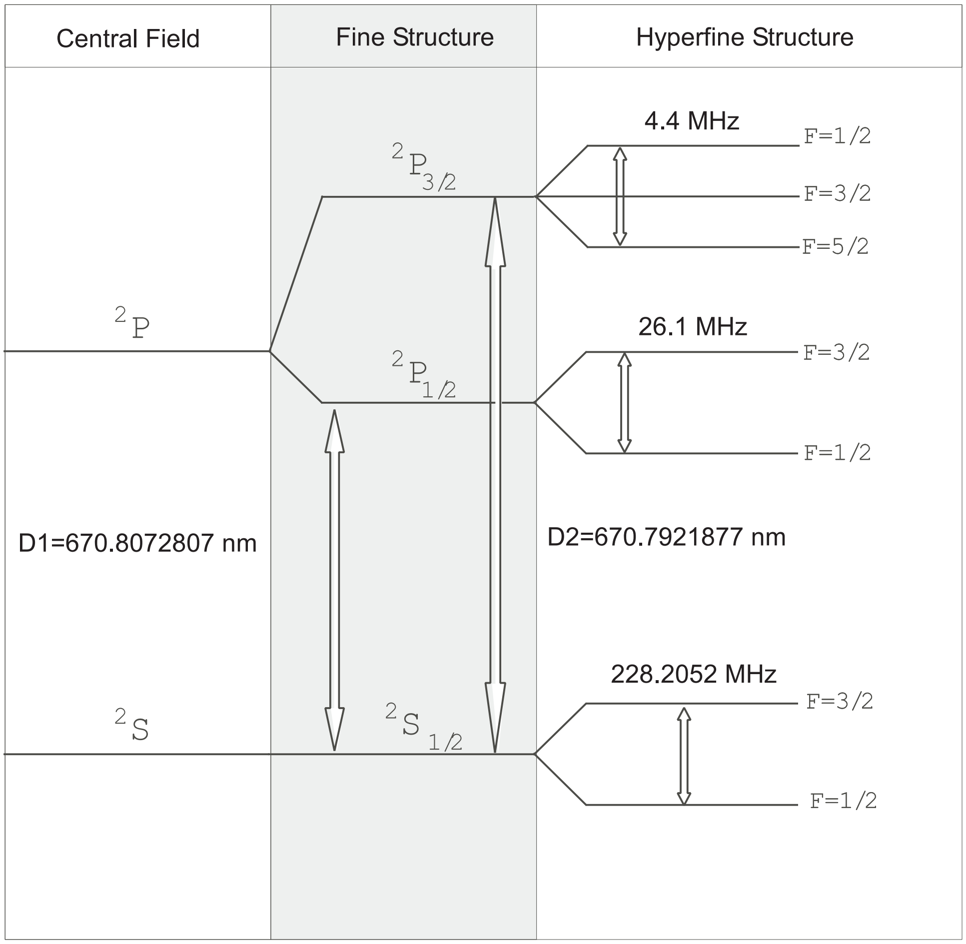

Figure 2.1: The hyperfine energy levels of ^{6}Li. The energy splitting is not to scale.

Hyperfine splitting appears within the D_1 and D_2 lines due to the interaction between the valence electron and the non-spherically-symmetric nucleus. The Hamiltonian of the hyperfine interaction includes both the nuclear magnetic dipole and nuclear electric quadrupole interactions. The eigenstates of the hyperfine interaction are represented by the total angular momentum quantum number $\hat{\mathbf{F}}$, which is given by the sum of the total electron angular momentum $\hat{\mathbf{J}}$ and the nucleus angular momentum $\hat{\mathbf{I}}$ according to the relation of $\hat{\mathbf{F}} = \hat{\mathbf{J}} + \hat{\mathbf{I}}$. The measured hyperfine splitting of ^{6}Li atoms [52] is shown in Fig. 2.1.

The hyperfine splitting of the excited states is about one or two orders of magnitude smaller than the the ground state hyperfine splitting. So the effects due to the hyperfine splitting of the excited states are not primary concerns for the resonance frequency shift we used in this thesis. The accurate calculation of the hyperfine structure splitting is shown in Appendix A in [53], which includes the interaction energies arising from both magnetic dipole and electric quadrupole moments.

2.1.2 Hyperfine States in a Magnetic Field

In the presence of a strong magnetic field, the magnetic interaction energy can not be treated as a perturbation on the electron-nucleus interaction in the most general cases. That means F and m_F are no longer good angular momentum quantum numbers. The strict way to find the eigenstates is to diagonalize the Hamiltonian of the total interaction energy in the $|S\, m_S\, L\, m_L\, I\, m_I\rangle$ basis. The total interaction combines both the hyperfine interaction and magnetic interactions is

$$\begin{aligned} H_{int} &= H_B + H_{hyperfine} \\ &= -\mu_B\left(g_S\,\mathbf{S} + g_I\,\mathbf{I} + g_J\,\mathbf{J}\right)\cdot\mathbf{B} - \hat{\boldsymbol{\mu}}\cdot\hat{\mathbf{B}}(0) + \frac{1}{6}\,e\sum_{\alpha\beta}\hat{Q}_{\alpha\beta}\frac{\partial^2\phi(0)}{\partial x_\alpha\partial x_\beta}, \end{aligned} \quad (2.1)$$

where $\mathbf{B}$ is the external magnetic field, and $\hat{\boldsymbol{\mu}}$ and $\hat{Q}$ are the nuclear magnetic dipole moment and nuclear electric quadrupole moment operators, respectively, $\hat{\mathbf{B}}$ is the operator of the magnetic field due to the electrons, and ϕ is the electric potential from the electrons. The last two terms represent the primary electron-nucleus interactions.

For the electron in the $2\,^2S_{1/2}$ ground state, the angular wavefunction is spherically symmetric so that it does not support the nuclear electric quadrupole interaction. Eq. (2.1) can be simplified as

$$H_{ground} = h\, A_{2\,^2S_{1/2}}\, \mathbf{S} \cdot \mathbf{I} - \mu_B \left[g_J(2\,^2S_{1/2})\, \mathbf{S} + g_I\, \mathbf{I} \right] \cdot \mathbf{B}, \tag{2.2}$$

where $A_{2\,^2S_{1/2}}$ and $g_J(2\,^2S_{1/2})$ are listed in Table 2.1. $\mathbf{S}$ and $\mathbf{I}$ are the dimensionless angular momenta.

The six eigenstates for the above interactions in the basis $|m_S\; m_I\rangle$ are shown below from the lowest to highest energy by

$$|1\rangle \;=\; \sin\,\Theta_+\; |1/2\; 0\rangle - \cos\,\Theta_+\; |-1/2\; 1\rangle \tag{2.3}$$

$$|2\rangle \;=\; \sin\,\Theta_-\; |1/2\; -1\rangle - \cos\,\Theta_-\; |-1/2\; 0\rangle \tag{2.4}$$

$$|3\rangle \;=\; |-1/2\; -1\rangle \tag{2.5}$$

$$|4\rangle \;=\; \cos\,\Theta_-\; |1/2\; -1\rangle + \sin\,\Theta_-\; |-1/2\; 0\rangle \tag{2.6}$$

$$|5\rangle \;=\; \cos\,\Theta_+\; |1/2\; 0\rangle + \sin\,\Theta_+\; |-1/2\; 1\rangle \tag{2.7}$$

$$|6\rangle \;=\; |1/2\; 1\rangle\,. \tag{2.8}$$

The coefficients are defined as

$$\begin{aligned}
\sin\,\Theta_{\pm} &= \frac{1}{\sqrt{1+\left(Z^{\pm}+R^{\pm}\right)^{2}/2}} && (2.9)\\
\cos\,\Theta_{\pm} &= \sqrt{1-\sin^{2}\Theta_{\pm}} && (2.10)\\
Z^{\pm} &= \frac{\mu_B\,B}{A_{gnd}}(-g_J^{gnd}+g_I)\pm\frac{1}{2} && (2.11)\\
R^{\pm} &= \sqrt{\left(Z^{\pm}\right)^{2}+2}, && (2.12)
\end{aligned}$$

where A_{gnd} and g_J^{gnd} are the magnetic dipole constant and electronic g-factors of the $2\,{}^2S_{1/2}$ ground state respectively.

The eigenvalues E_n of the above eigenstates $|n\rangle$ are plotted as a function of the magnetic field in Fig. 2.2 given by

$$\begin{aligned}
E_1 &= -\frac{1}{4}\left(A_{gnd}+2\,g_I\,\mu_B\,B+2\,A_{gnd}\,R^{+}\right) && (2.13)\\
E_2 &= -\frac{1}{4}\left(A_{gnd}-2\,g_I\,\mu_B\,B+2\,A_{gnd}\,R^{-}\right) && (2.14)\\
E_3 &= \frac{A_{gnd}}{2}+\mu_B\,B(g_I+g_J^{gnd}/2) && (2.15)\\
E_4 &= -\frac{1}{4}\left(A_{gnd}-2\,g_I\,\mu_B\,B-2\,A_{gnd}\,R^{-}\right) && (2.16)\\
E_5 &= -\frac{1}{4}\left(A_{gnd}+2\,g_I\,\mu_B\,B-2\,A_{gnd}\,R^{+}\right) && (2.17)\\
E_6 &= \frac{A_{gnd}}{2}-\mu_B\,B(g_I+g_J^{gnd}/2). && (2.18)
\end{aligned}$$

At the zero field position in Fig. 2.2, the total angular momentum quantum numbers $F = 1/2$ and $F = 3/2$ are good quantum numbers. When the magnetic field increases, the six energy levels evolve into two groups because the hyperfine interaction is much smaller than the magnetic interaction when the magnetic field is large enough. Under this condition, the eigenstates eventually are the states of

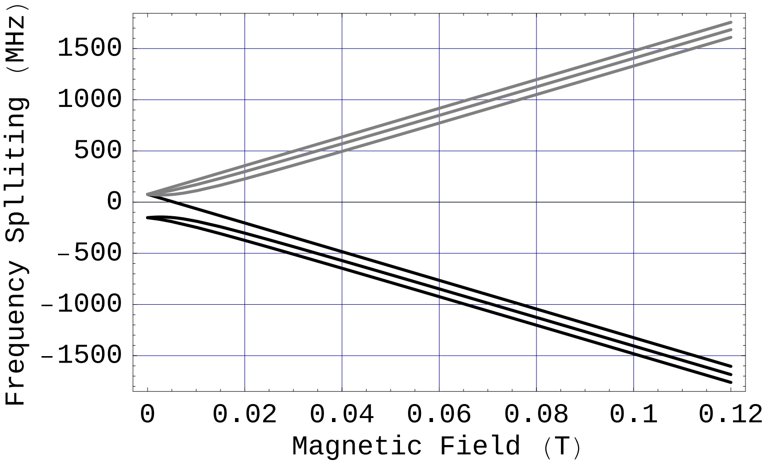

Figure 2.2: The Zeeman energy levels of the ^{6}Li hyperfine states are plotted in frequency units versus applied magnetic field in gauss. There are six energy levels at nonzero magnetic field, and are labeled $|1\rangle$, $|2\rangle$, and so on, in order of increasing energy.

$|m_S\ m_I\rangle$. Because g_S is much larger than g_I, the three $m_S = -1/2$ states remain in the bottom group in Fig. 2.2 and the three $m_S = 1/2$ states remain in the top one. Note that magnetic trapping only works for the states in the top group, which are attracted to a region of a local minimum of the magnetic field. In contrast, the states in the bottom group are attracted to a region of a local maximum of the magnetic field, which is forbidden in free space. For this reason, we use an optical dipole trap to trap the lowest two hyperfine state.

In the next section, I will describe a broad s-wave collision resonance between $|1\rangle$ and $|2\rangle$. This resonance constitutes the physical basis for creating a strongly interacting Fermi gas.

2.2 Collisional Resonance in an Ultracold ^{6}Li Gas

Strongly interacting Fermi gases in my experiments are two-component Fermi gases in the $|1\rangle$ and $|2\rangle$ states of ^{6}Li atoms near a collisional resonance, which is usually called a *Feshbach Resonance*. To understand the Feshbach resonance, I will give a brief introduction to low energy quantum scattering, then quantitatively explain why the ^{6}Li atoms in the lowest hyperfine levels have a broad collisional resonance when they are in a bias magnetic field. Finally, I will describe the s-wave scattering length dependence on a magnetic field in an ultracold ^{6}Li gas.

2.2.1 S-wave Quantum Scattering

The quantum scattering of two particles is a central topic in nearly every quantum mechanics textbook [54–57]. Here, I will provide a brief introduction to s-wave quantum scattering, which is necessary to understand the important physics and experimental methods presented in this thesis.

S-wave, or zero angular momentum quantum scattering, happens in quantum collisions at very low temperature. Assume a single incident particle of reduced mass μ that is scattered by a spherically symmetric potential $\mathrm{V}(\boldsymbol{r})$. The incident particle traveling in the $+\hat{\mathbf{z}}$ direction with momentum $\hbar k$ can be described by an incident plane wave e^{ikz}. After the scattering, the asymptotic scattered wavefunction at infinite distance equals the incoming plane wave plus an spherical wave $f(\theta)\, e^{ikr}/r$ [58]. The function f is known as the *scattering amplitude*, and θ is the angle between the incident direction $\hat{\mathbf{z}}$ and the scattered direction of the particle.

The differential cross section $d\sigma/d\Omega$ equals the square magnitude of the scattering amplitude by

$$\frac{d\sigma}{d\Omega} = |f(\theta)|^2. \tag{2.19}$$

If we assume the scattering potential is a central potential, it allows us to expand the scattered wave functions in an orbital angular momentum basis $|l\rangle$ with the Legendre polynomials $\mathrm{P}_l(x)$,

$$f(\theta) = \sum_{l=0}^{\infty}(2l+1)f_l(k)\mathrm{P}_l(\cos\theta). \tag{2.20}$$

The coefficients of this expansions are known as the *partial wave amplitudes*, which are related to the scattering phase shifts δ_l by [56],

$$f_l(k) = \frac{\exp(i\,\delta_l)\,\sin\delta_l}{k}. \tag{2.21}$$

In the case of an ultracold gas of neutral atoms, the dominant quantum scattering process is the s-wave ($l = 0$) due to the extremely low kinetic energy of the colliding atoms. Suppose the interatomic potential has some finite range r_0 and the relative linear momentum for the two atoms is $p = h/\lambda_{dB}$, where λ_{dB} is the de Broglie wavelength of the relative momentum. Then the maximum relative orbital angular momentum is given by the $L \simeq r_0 p$. We know the relative angular momentum between two atoms is quantized by $L = l\hbar$ where l is an integer. By using the typical interacting potential $r_0 \sim 10$ Å and the typical size of the de Broglie wavelength of 7000 Å for ^{6}Li atoms at $\simeq 1\,\mu$K, we readily get

$$l \simeq \frac{2\pi r_0}{\lambda_{dB}} \simeq 0.01 << 1, \tag{2.22}$$

This shows that the only relevant value for ℓ is zero for scattering processes of Fermi gases at such ultracold temperatures.

We rewrite all the above equations only with the lowest order scattering phase shift δ_0. Eq. (2.20) reduces to

$$f(\theta) = e^{i\delta_0}\frac{\sin(\delta_0)}{k}, \tag{2.23}$$

The total scattering cross section of s-wave scattering is obtained by integrating Eq. (2.19),

$$\sigma = \int d\Omega\,|f(\theta)|^2 = 4\pi\frac{\sin^2\delta_0}{k^2}. \tag{2.24}$$

The total scattering cross section also can be written in term of the s-wave scattering length by

$$a_s \equiv -\lim_{k\to 0}\frac{\tan\delta_0}{k}, \tag{2.25}$$

$$\sigma = \frac{4\,\pi\,a_s^2}{1+k^2\,a_s^2}. \tag{2.26}$$

The physical interpretation of the scattering length is given in [56]. We assume the center of the scattering potential is located at the origin of a spherical coordinate system. Without the scattering potential, the free particle asymptotic function will intersect the r axis at the origin. In the limit of $k \to 0$, the scattering length is defined as the distance between the origin and the crossing point of the asymptotic radial wavefunction on the r axis. So the value of a_s represents how much the particle wavefunction is modified by the scattering potential. Larger a_s represents stronger interactions between the particles. A positive a_s indicates that the scattering wavefunction is pushed away from the origin by the scattering potential, which indicates that the effective interaction is repulsive. On the contrary, a negative scattering length a_s means the scattering wavefunction is pulled closer to the origin, which represents an effective attractive interaction.

The strength of the interaction is represented by the value of the scattering length. For weak interactions $a_s \ll 1/k \simeq \lambda_{dB}/2\pi$, which means that the zero energy s-wave scattering length is much smaller than the de Broglie wavelength of the relative momentum of the colliding atoms, the scattering cross section is $\sigma \approx 4\,\pi\, a_s^2$. For strong interactions, the zero energy s-wave scattering length is much larger than the de Broglie wavelength, so that $a_s \gg 1/k \simeq \lambda_{dB}/2\pi$. When $a_s \to \pm\infty$, the s-wave atomic cross section is given by

$$\lim_{a_s \to \pm\infty} \sigma = \frac{4\,\pi}{k^2}. \tag{2.27}$$

This gives the unitary limit of the s-wave scattering for distinguishable particles that are in the different hyperfine states of a two-component gas (Note that for a single-component gas, this limit is $8\,\pi/k^2$ because the colliding particles are indistinguishable). Eq. (2.27) implies that the collisional behavior of the system is effectively completely independent of the scattering length. In the other words, the collisional behavior only depends on the wave vector of the thermal energy instead of any microscopic structure of the interparticle potentials.

Strongly interacting Fermi gases in this limit are known as unitary Fermi gases. In this dissertation, I will use both terms to refer to Fermi gases with a divergent s-wave scattering length. In the following, I will discuss how to tune $a_s \to \pm\infty$ in ultracold ^{6}Li atoms by applying a magnetic s-wave Feshbach resonance.

2.2.2 The Broad Feshbach Resonance of ^{6}Li Atoms

A much more thorough discussion of ^{6}Li atom collisions can be found in the previous thesis of Ken O'Hara [59]. I strongly suggest reading that dissertation to understand why the mixture of ^{6}Li atoms in the $|1\rangle$ and $|2\rangle$ hyperfine state are an ideal system for experimental studies of a strongly interacting Fermi gas.

The ^{6}Li atoms in the different spin states of $|1\rangle$ and $|2\rangle$ interact via either a singlet or triplet molecular potential for s-wave scattering. The singlet potential means that the valence electrons from two different atoms form a spin singlet state with the total spin $S = S_1 + S_2 = 0$. In contrast, the triplet potential is made by the electrons combining to a spin triplet state $S = S_1 + S_2 = 1$. For fermions, the total wavefuntion should be antisymmetric. In the singlet state, the spin wavefunction is antisymmetric, so the spatial wavefunction of electrons should be symmetric. A symmetric spacial wavefunction means that the density of electrons at the midpoint between two nuclei can be nonzero. On the contrary, in the triplet state, the space wavefunction is antisymmetric, which requires the space density of the electrons to be zero in the midpoint between the two nuclei. Because the nonzero electron density in the midpoint between two nuclei helps to shield the repulsive forces between the nuclei, the singlet potential is much deeper than the triplet potential. This causes the energy of colliding atoms that are unbounded in the triplet potential can be the same as that of a bound state in the singlet potential. Under this condition, the scattering length between the colliding atoms is enhanced dramatically, which results in the Feshbach resonance shown in Fig. 2.3. The triplet potential is usually called as the "open channel,"while the the singlet potential is named the "closed channel."

The energy difference between the energy of the unbound colliding atoms

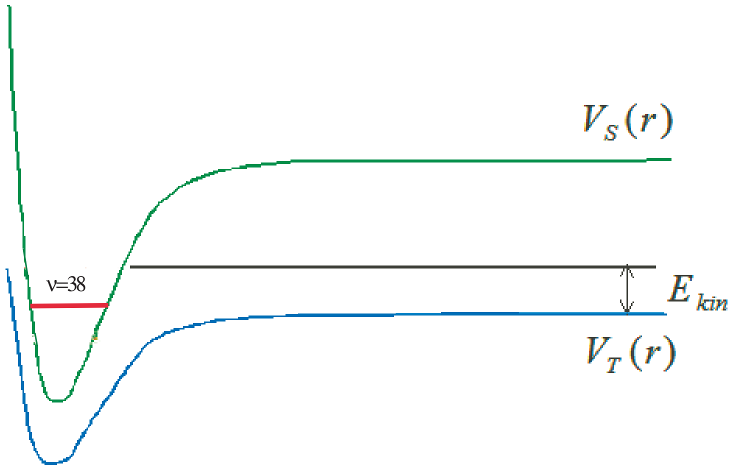

Figure 2.3: Phenomenological explanation of the origin of the Feshbach resonance. V_S is the singlet potential and V_T is the triplet potential. The relative energy gap between the singlet potential and the triplet potential is tunable by a magnetic field. When the total energy of the unbound colliding atoms in the triplet state equals to the energy of the $\nu = 38$ bound state in the singlet potential, a Feshbach resonance occurs due to the hyperfine mixing of the singlet and triplet states.

in the open triplet channel and the energy of the bound atoms in the closed singlet channel depends on the strength of magnetic field. This energy difference determines the s-wave scattering length between the atoms in $|1\rangle$ and $|2\rangle$, which can calculated. [1]

It is predicted in theory [60] and confirmed by the experimental measurement [61] that there is a strong enhancement of the scattering length occurring at the magnetic fields of approximately $B = 834$ gauss, due to the Feshbach resonance

---

[1] The collision channel for the $|1\rangle - |2\rangle$ has a total spin projection $m_F = 0$. m_F is conserved in s-wave scattering. In a magnetic field, the $|1\rangle - |2\rangle$ collision processes are coupled to four $m_F = 0$ channels:$|4\rangle - |5\rangle$,$|3\rangle - |6\rangle$,$|2\rangle - |5\rangle$,$|1\rangle - |4\rangle$. All those channels have higher energy than the $|1\rangle - |2\rangle$ with the minimum 10 mK energy difference. Thus, those channels are prohibited at very low temperatures so that the $|1\rangle - |2\rangle$ collision can be treated as an elastic process. However, in the exact calculation of the elastic scattering length [60], those prohibited channels have effects on the scattering process because virtual collisions, so all the coupled channels should be included in the calculation

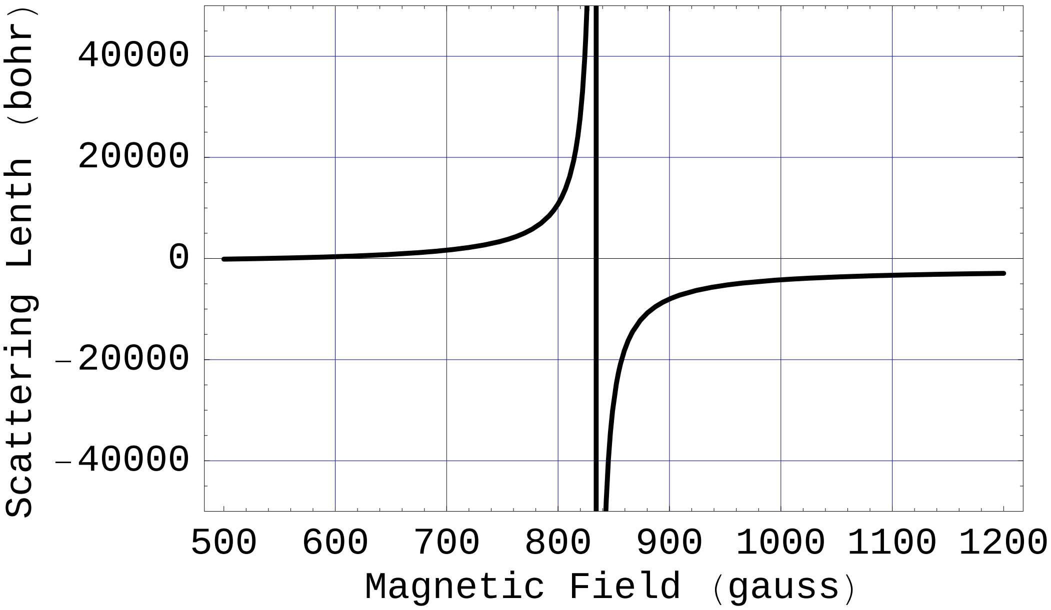

Figure 2.4: The s-wave scattering Length of the Feshbach resonance of ^{6}Li atoms versus the magnetic field. Note that a narrow Feshbach resonance located at 543 gauss with width less than 1 gauss is omitted in this figure.

for the $|1\rangle$-$|2\rangle$ mixture. This resonance occurs as the energy of colliding atoms in the triplet state is magnetically tuned to equal the energy of the $\nu = 38$ bounded molecular state in the singlet potential.

The broad Feshbach resonance can be calculated from the parameters of the singlet and triplet potentials, which are determined by radio-frequency spectroscopy of weakly bound ^{6}Li molecules [62]. The Feshbach resonance is parameterized as a function of the magnetic field B, and shown in Fig. 2.4 by

$$a_s(B) = a_b \left(1 + \frac{\Delta}{B - B_0}\right)(1 + \alpha(B - B_0)), \tag{2.28}$$

where the background scattering length $a_b = -1450\, a_0$, and a_0 is the Bohr radius. The resonance field $B_0 = 834.149G$, and the resonance width $\Delta = 300G$. The first-order correction parameter is $\alpha = 0.00040G^{-1}$. This parameterized curve fits the numerical calculation to better than 1% in the regime between 600 G to 1200 G.

This broad Feshbach resonance provides a controllable system to explore strongly interacting Fermi gases experimentally. In Chapter 3, I will show that Fermi gases are much easier to cool in the strongly interacting regime. The broad Feshbach resonance provides a unique system, the so called "BEC-BCS crossover". Below the Feshbach resonance at 834 G, with repulsive interactions, the scattering length can be continuously tuned from a very large positive scattering length to a zero scattering length at about 528 Gauss. In this regime, stable bound molecules form from atoms in the two different hyperfine states, producing molecular BECs below the critical temperature. Thus, this regime is referred to as the "BEC side". Above the Feshbach resonance, Fermi gases have an attractive interaction energy. The scattering length is tunable from a very large negative scattering length to a very small negative one. In the limit of a small negative scattering length, the system is described by BCS theory and referred as the "BCS side". Near the Feshbach resonance, the scattering length a_s is much larger than the average interparticle spacing between ^{6}Li atoms L_a. On the other hand, in a dilute ultracold atom gas, the potential range of ^{6}Li atoms R_p is much smaller than L_a. So the diverging scattering length and negligible potential range satisfy

$$a_s \to \infty \gg L_a \gg R_p \to 0. \tag{2.29}$$

This condition ensures that the local macroscopic behavior of such systems only depends on the local density and temperature. In this limit, a strongly interacting Fermi gas exhibit universal behavior, which is totally independent of the microscopic details of interparticle interactions.

For most experiments presented in this thesis on studying a strongly interacting Fermi gas, we use an ultracold degenerate Fermi gas at the Feshbach resonance of 834 gauss or a field a few gauss above the resonance. To study a noninteracting Fermi gas, we set the bias magnetic field at the zero crossing of the scattering length, near 528 gauss [17, 18].

Chapter 3

General Experimental Methods

In our lab, all-optical cooling and trapping techniques provide a simple and efficient method for creating a strongly interacting Fermi gas. In this chapter, I will introduce the general experimental methods we use to generate and characterize a strongly interacting Fermi gas. First, I will describe the optical transition we use to take absorption images of cold atoms in a magnetic field. Then I will talk how we calibrate the magnetic field by locating the zero crossing of the s-wave scattering length in a broad Feshbach resonance. After that, I will present our studies of evaporative cooling of strongly interacting ^{6}Li atoms in an optical trap [63]. In the end, I will overview the general experimental procedures of using cold ^{6}Li atoms to create strongly interacting, weakly interacting, and noninteracting Fermi gases.

3.1 Optical Transition for Absorption Imaging

Absorption imaging of ^{6}Li atoms in a high magnetic field (above 300 Gauss) can be treated as an optical dipole transition between a nearly perfect two-level system [53, 64], shown in Fig. 3.1. The two-level system for absorption imaging avoids optical pumping of the atoms into the other states, thereby increasing the

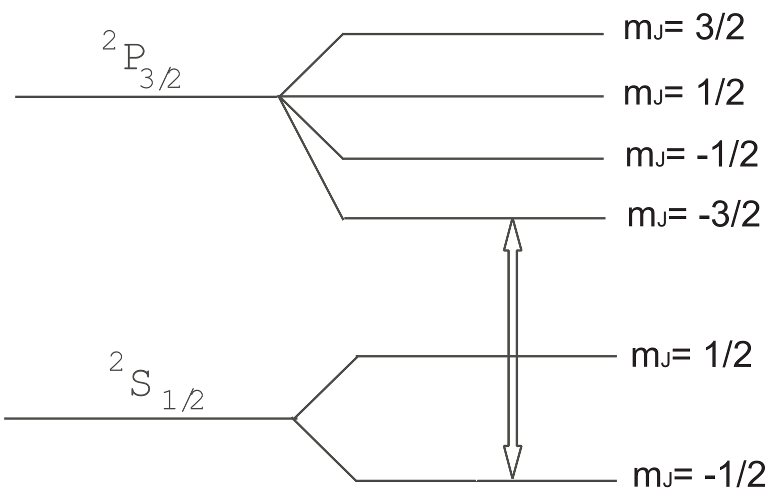

Figure 3.1: The two-level system used for absorptive imaging of ^{6}Li atoms at the ground states when a high magnetic field is present. In high magnetic fields, the energy levels can be treated as approximate eigenstates in the J, m_J basis.

signal-to-noise ratio of the absorption images.

In Section 2.1.2, I described the two lowest hyperfine ground states of the ^{6}Li atom: $|1\rangle$ and $|2\rangle$, which we used for a strongly interacting Fermi gas. In high magnetic fields, the hyperfine interaction between the electron and nuclear spin states becomes small compared with the magnetic field energy of the electron spin. The $|1\rangle$ and $|2\rangle$ states can be treated as approximate eigenstates in the $|J\, m_J\, I\, m_I\rangle$ basis,

$$\begin{aligned} |1\rangle &= |1/2, -1/2; 1, 1\rangle \\ |2\rangle &= |1/2, -1/2; 1, 0\rangle \,. \end{aligned} \tag{3.1}$$

According to the selection rule for electric dipole transitions [58], the electric dipole changes the total and orbital angular momentum by

$$\begin{aligned} \Delta J &= \pm 1, 0 \\ \Delta L &= \pm 1 \\ \Delta m_J &= \pm 1, 0. \end{aligned} \tag{3.2}$$

Now consider the $|1\rangle$ state as the initial state of an optical transition for absorption images. Because the nuclear spin is not changed by this optical dipole transition, according to Eq. (3.1) and Eq. (3.2), the possible final states for $|1\rangle$ through the D2 line transition where $\Delta J = 1$ are

$$\begin{aligned} |F1\rangle &= |3/2, -3/2; 1, 1\rangle \\ |F2\rangle &= |3/2, -1/2; 1, 1\rangle \\ |F3\rangle &= |3/2, 1/2; 1, 1\rangle . \end{aligned} \tag{3.3}$$

From the selection rule, we know that the $|F1\rangle, |F2\rangle, |F3\rangle$ states correspond to left-circularly, linear, and right-circularly polarized imaging beams, respectively. We note that at high magnetic field, m_J states are well separated by a couple of GHz, which is much larger the natural linewidth of the D2 line, which is 5.9 MHz for full width at half maximum (FWHM). For single-frequency absorption imaging, the $|F1\rangle, |F2\rangle, |F3\rangle$ states are not coupled. For the application of the absorption imaging, we need to choose a final state that can be used for the upper level in a two-level system. For the above state, only $|F1\rangle$ satisfies our requirement of a two level system while the atoms in $|F2\rangle$ and $|F3\rangle$ can decay to the dark state of $|1/2, 1/2; 1, 1\rangle$.

For the excited states of $|F1\rangle$, left-circularly polarized light is used when the imaging beam propagates coaxially along the quantization axial of the magnetic field $\hat{\mathbf{z}}$. This coaxial imaging setup is used in our old system. However, in the new system, our imaging beam propagates in a direction perpendicular to the axis of the magnetic field. For this setup, circularly-polarized light for the $|F1\rangle$ state is not a possible polarization for the light beam. Instead, laser light with linear polarization perpendicular to the quantization axis of the magnetic field is used for absorption imaging, and its frequency is adjusted to select the $m_J = -1$ transition.

We need to pay attention to the optical absorption cross-section: it is different for the linear polarized light in comparison to the left-circularly polarized light. The resonant optical cross-section for two-level system is given by

$$\sigma_{opt} = \frac{4\pi k(\hat{\mathbf{e}} \cdot \hat{\boldsymbol{\mu}})^2}{\hbar\gamma_s/2}, \tag{3.4}$$

where $\hat{\boldsymbol{\mu}}$ is the vector of the optical transition element pointing along the quantization direction of the magnetic field, and $\hat{\mathbf{e}}$ is the unit vector of the linear momentum of the photon, and k is the wavevector of the photon, and $\gamma_s = 4\mu^2k^3/(3\hbar)$ is the natural line width of the transition.

In the case of left-circularly polarized imaging light propagating coaxially with the quantization axis of the magnetic field, we define $\hat{\mathbf{e}} \cdot \hat{\boldsymbol{\mu}} = \mu$, and we obtain

$$\sigma^-_{opt} = \frac{3\lambda^2}{2\pi}. \tag{3.5}$$

In the case of imaging light with $\hat{\mathbf{x}}$ linear polarization perpendicular to the quantization axis of the magnetic field, we have $\hat{\mathbf{e}}_x = -\hat{\mathbf{e}}_+/\sqrt{2} + \hat{\mathbf{e}}_-/\sqrt{2}$, where $\hat{\mathbf{e}}_+$ and

$\mathbf{\hat{e}}_-$ correspond to right-circular and left-circular polarized light, respectively. As I pointed out above, right-circular right is for the $\Delta m_J = 1$ transition, which is well separated from with the $\Delta m_J = -1$ transition, so only one component of the light can be absorbed by the atoms. We readily get the optical cross-section for the imaging light whose linear polarization perpendicular to the magnetic field,

$$\sigma^*_{opt} = \frac{3\lambda^2}{4\pi}. \tag{3.6}$$

For ^{6}Li atoms, $\sigma^*_{opt} = 0.107\,\mu m^2$. This optical cross-section is a factor of 2 smaller than that of the absorption imaging using left-circularly polarized light, which propagates coaxially along the quantization axial of the magnetic field. This effect decreases the signal-to-noise ratio of absorption images in our imaging system compared with the old system. The compensation for this drawback is that we avoid imaging beams sharing the same viewports as vertical MOT beams. This ensures a large aperture for the imaging system, which can increase the resolution of the imaging system. In the future, this apparatus will be used for one-dimensional optical lattice experiments, where high imaging resolution is required for imaging the atoms in a single site of optical lattice.

3.2 Magnetic Field Calibration for Feshbach Resonance

In our system, the high field magnets are controlled by a DC command voltage, which determine the magnetic field we apply to the atoms. The precise command voltage for the zero crossing point of the s-wave scattering length is calibrated

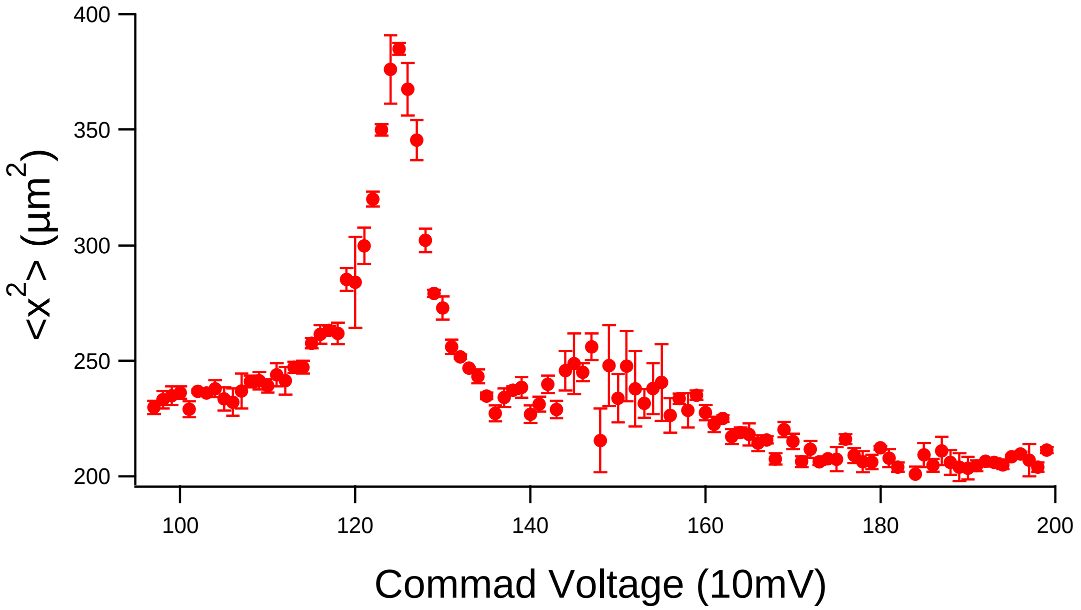

Figure 3.2: Mean square cloud size in the trap versus the commanding voltage for the magnetic field. The maximum mean square size is located at 1.249 ± 0.001 V.

experimentally. To locate the magnetic field for the zero crossing, we hold the atoms in a CO_2 trap with a fixed trap depth for a fixed time and measure the decrease of the atoms number and the cloud size as a function of the magnetic field. At the zero crossing, the cloud size will have a maximum value, indicating no evaporation. A similar method that probed the temperature and the atom number was used in [61]. For calibrating the new system, we hold the optical trap in a specific magnetic field for 10 seconds, then sweep the cloud to a fixed magnetic field of 400 G to take an image. In Fig. 3.2, I show the radial mean square size versus the command voltage for the required magnetic field.

The maximum cloud size locates at the 1.249 volt command voltage, which corresponds to the zero crossing of the s-wave scattering length at 528 G [61]. We have verified that the magnetic field has a very good linear dependence on the command voltage [39]. By extrapolation, we have the following relation for the command voltage V as function of the magnetic field,

$$B(V)(gauss) = 528 \times V(volt)/1.249. \tag{3.7}$$

3.3 Evaporative Cooling in the Unitary Limit

Prior to evaporative cooling, there are two methods to load the optical trap. The simplest is by directly loading the atoms from a MOT [12, 27], and the other is after initial evaporative cooling in a MOT-loaded magnetic trap [16,29,30,65]. We utilize the first method, where efficient evaporation in the optical trap is crucial for the whole experiment. The evaporation efficiency determines not only the cloud temperature but also the final cold atom number.

Efficient evaporation in the optical trap is realized by keeping the ratio H of the trap depth U to the thermal energy k_BT large. A large value of H for the elastic processes assures that the energy carried away by the evaporating atoms is much larger than the average thermal energy of the atoms. This condition also assures a large fraction of the initial atom number remains in the optical trap when the desired temperature is achieved. However, an arbitrary time dependent trap lowering curve $U(t)$ can not make H constant. In a previous theoretical study of evaporative cooling in optical trap [66], our laboratory derived the scaling law for the number of atoms as a function of the trap depth, which assures a constant H during the evaporation. Then, based on the energy conservation, our laboratory derived a scaling law for the trap lowering curve in the case of evaporative cooling of a weakly interacting Fermi gas.

Evaporative cooling a unitary Fermi gas exhibits new physics compared with cooling a weakly interacting Fermi gas. The weakly interacting Fermi gas has an energy-independent s-wave scattering cross section $\sigma = 4\,\pi\,a^2$, so the collision rate for evaporation always decreases as the trap is lowered [66]. In contrast, near the Feshbach resonance, the s-wave scattering cross-section for a two-component Fermi gas reaches the unitarity value of $\sigma = 4\pi/k^2$, where k is the relative wavevector of the colliding particles. This energy-dependent cross-section indicates that the cross-section of a unitary Fermi gas actually increases when the temperature of the gas drops during the evaporation. In that case, the resulting collision cross-section for evaporation $\sigma_{evap} \propto 1/U$, where U is the trap depth, which can compensate for the suppression of the evaporation rate due to the decrease of the temperature and density. This mechanism enables a high H of about 10 for the whole evaporation process, which enables runaway evaporation being possible for the unitary conditions.

Before the studies presented in [63], our lab used a lowering curve optimized for an energy-independent scattering cross section to operate the evaporative cooling in the strongly interacting regime. It is important to make a careful study of evaporative cooling in the unitary limit. In this section, I will review our studies. I first describe the scaling law for the number of atoms and the cloud size as a function of trap depth. After that, I will derive the optimal trap lowering curve which maintains a constant H for a unitary gas. Then, I will demonstrate the experimental results of applying this lowering cure. I found that, in the strongly interacting regime, the new evaporation curve generates a quantum degenerate Fermi gas in a fraction of a second from a classical gas with only a factor of 3 loss in atom number.

3.3.1 Scaling Laws for Evaporative Cooling in an Optical Trap

The scaling laws for evaporative cooling in optical traps were first derived in [66]. Here, I only give the major results from the theoretical model in [63, 66] instead of repeating the whole calculation.

The evaporation process can be described with a time-dependent optical trapping potential

$$U(\mathbf{x},t) = -U(t)\, g(\mathbf{x}), \tag{3.8}$$

where U is the trap depth and $g(\mathbf{x})$ describes the Gaussian-like trap shape with $g(0) = 1$, and $g(\pm\infty) \to 0$. I assume that evaporation is carried out at low temperatures where the average thermal energy $kT << U$.

For $kT << U$ and an approximate harmonic potential, we have

$$\dot{E} = \frac{\dot{U}}{U}\frac{E}{2} + \dot{N}(U + \alpha kT). \tag{3.9}$$

Here the first term arises from the change in the harmonic potential energy. The second term $U + \alpha\, k_B T$ is the total evaporation energy per particle. The net effect is that the trapped gas loses energy at a rate $\dot{E} < 0$ by both evaporation and lowering the trap potential. Note that $\alpha\, k_B T$ represents the excess evaporation energy per particle with the value of α between 0 and 1 [67]. In the case of a unitary Fermi gas, the value of α is nearly the same as that of a weakly interacting Fermi gas, which has the value $\alpha = (H-5)/(H-4)$. Both the energy loss and the number loss are related to the collision integral of the cross-section for evaporation σ_{evap}.

At unitarity, the cross-section for evaporative collisions σ_{evap} is only a function of the trap depth U. I give the following heuristic explanation. For a collision between two atoms of energies ϵ_1 and ϵ_2, energy conservation dictates that $\epsilon_1+\epsilon_2 = \epsilon_3+\epsilon_4$, where ϵ_3 and ϵ_4 are the energies of the outgoing atoms. For evaporation, we require that $\epsilon_4 > U$ while $\epsilon_3 \leq k_BT$. For atoms that collide at position x_c which is close to the bottom of the trap, we have $U(x_c) \leq k_BT << U$ for a trap with large H. Here we take $v_3 \simeq 0$, compared to the other speeds for 1,2, and 4. According to energy and momentum conservation, we readily have that $v_4^2 = v_1^2 + v_2^2$ and $\mathbf{v}_1 + \mathbf{v}_2 = \mathbf{v}_4$, which yields $\mathbf{v}_1 \cdot \mathbf{v}_2 \simeq 0$ and $v_{rel}^2 = (\mathbf{v}_1 - \mathbf{v}_2)^2 \simeq v_4^2 \simeq 2U/M$. The unitary cross-section of evaporation for a single component Bose gas is given by $\sigma = 8\pi/k^2$. Applying $k = Mv_{rel}/(2\hbar)$, we obtain the evaporative cross section

$$\sigma_{evap} = \frac{16\pi\hbar^2}{MU}. \tag{3.10}$$

For a 50-50 mixture Fermi gas of two spin states, the effective collision rate is reduced by a factor of 1/2 because s-wave scattering requires the antisymmetric spin state that has 1/2 possibility for the colliding atoms. Eq. (3.10) shows the evaporative collision cross section is determined only by the trap depth $U >> kT$. Hence, the cross section is nearly constant in both the collision integral for energy loss and in that for the number loss, and can be factored out in the ratio of $\dot{E}/\dot{N} = U + \alpha kT$. For this reason, the value of α is not a sensitive value whether the cross-section is energy-dependence or energy-independent for the case when the optical trap has $H >> 1$.

For evaporative cooling from the classical regime to degeneracy, we can take the total energy to be that of a classical gas in a harmonic potential by $E =$

$3Nk_BT$, and use it in Eq. (3.9) for a fixed H, which yields

$$\frac{N(t)}{N_0} = \left(\frac{U(t)}{U_0}\right)^{\frac{3}{2(\eta'-3)}}, \tag{3.11}$$

where the subscript 0 denotes the initial condition at $t = 0$, and $\eta' = H + \alpha = H + (H - 5)/(H - 4)$.

The phase-space density scaling also can be determined form Eq. (3.11). The phase space density ρ for a 50-50 mixture of two spin states in the classical regime is essentially $N/2$ divided by the total number of accessible harmonic oscillator states $\rho = (N/2)(H\bar{\nu}/k_BT)^3$, where $\bar{\nu} \equiv (\nu_x\nu_y\nu_z)^{1/3}$. Using $\bar{\nu} \propto \sqrt{U}$ and $k_BT \propto U/H$ in Eq. (3.11), we obtain

$$\frac{\rho}{\rho_0} = \left(\frac{U_0}{U}\right)^{\frac{3(\eta'-4)}{2(\eta'-3)}} = \left(\frac{N_0}{N}\right)^{\eta'-4}. \tag{3.12}$$

According to Eq. (3.12), the evaporation efficiency χ is

$$\chi = \frac{\ln(\rho/\rho_0)}{\ln(N_0/N)} = \eta' - 4. \tag{3.13}$$

While $\chi \leq 3$ is typical for BECs produced in magnetic traps [68], we find from Eq. (3.13) that an optical trap with a typical value of $H = 10$ in our experiments yields $\chi = 6.83$. This indicates that a quantum degenerate Fermi gas can be produced with much smaller reduction in atom number in an optical trap.

A dramatic consequence of keeping H constant during the evaporation process is that the mean square cloud size in the trap does not change. This follows from the scaling of the total energy as the function of the mean square size, $E = 3NM\omega_x^2\langle x^2\rangle_{trap}$. This relation holds generally for both a unitary gas and an ideal gas in a harmonic trap according to the virial theorem discussed in Chapter 4. In the classical region, since $E = 3Nk_BT = 3NU/H$, we have the following relation

$$\langle x^2 \rangle_{trap} = \frac{U}{HM\omega_x^2}. \tag{3.14}$$

By assuming a harmonic approximation to a gaussian trap $U[1-\exp(-2x^2/a_x^2)] \simeq M\omega_x^2 x^2/2$, where a_x is the trap field $1/e$ radius in the x-direction, we obtain the spring constant $M\omega_x^2 = 4U/a_x^2$. By applying this relation in Eq. (3.14), we get

$$\langle x^2 \rangle_{trap} = \frac{a_x^2}{4H}, \tag{3.15}$$

which shows the mean square size of the trapped cloud does not change as the trap is lowered with a constant value of H.

3.3.2 Trap Lowering Curve for a Unitary Gas

In this section, I will determine the trap depth lowering curve to maintain constant H in a unitary gas. I start by calculating the evaporation rate. From the s-wave Boltzmann equation [67], we obtain the evaporation rate to the lowest order in $\exp(-H)$. Neglecting background gas collisions for simplicity, we get

$$\dot{N} = -2(H-4)\exp(-H)\gamma\, N. \tag{3.16}$$

Since the cloud size does not change, the collision rate for evaporation $\gamma = nv_{rel}\sigma$. Because the relative speed scales as $U^{1/2}$ and the cross section as $1/U$, we obtain

$$\frac{\gamma}{\gamma_0} = \left(\frac{U}{U_0}\right)^{\frac{6-\eta'}{2(\eta'-3)}}. \tag{3.17}$$

The initial collision rate γ_0 for a single component Bose gas is obtained by using the results given in [66]

$$\gamma_0 = \frac{4\pi N_0 M\sigma\bar{\nu}^3}{kT_0}. \tag{3.18}$$

Now we insert the cross section from Eq. (3.10) into Eq. (3.18), and apply it to a unitary Fermi gas of a 50-50 mixture of two spin states. Note that the effective collision rate is reduced by a factor of 1/2 because s-wave scattering requires the antisymmetric spin state, and another factor of 1/4 arising from a 50:50 spin mixture, where only N/2 atoms in each spin state. But the evaporation rate includes both spin states which gives a factor of 2 to the collision rate. Totally, we find the evaporation is reduced by a factor of 1/4 for a two-component Fermi gas compared with a single component Bose gas. By using $kT_0 = U_0/H$, we obtain

$$\gamma_0 = \frac{16N_0\pi^2\hbar^2\bar{\nu}^3 H}{U_0^2}. \tag{3.19}$$

In contrast to the collision rate for a constant cross section, where the collision rate decreased as the trap depth is lowered, the unitary collision rate increases as the trap depth is lowered in case of $\eta' > 6$. This is a consequence of the faster increase of the cross section compared with the decrease of flux nv_{rel}.

Differentiating Eq. (3.11) with respect to t and using the results in Eq. (3.16) and Eq. (3.19), we obtain the lowering curve for a unitary Fermi gas

$$\frac{U(t)}{U_0} = \left(1 - \frac{t}{\tau_u}\right)^{2(\eta'-3)/(\eta'-6)}, \tag{3.20}$$

where $0 \leq t \leq \tau_u$. The time constant for the lowering curve is given by

$$\frac{1}{\tau_u} = \frac{2}{3}(H-4)(\eta'-6)\exp(-H)\,\gamma_0. \tag{3.21}$$

Note that, for $\eta' = 6$, one can show that the trap lowering curve is exponential.

In Fig. 3.3, I show trap lowering curves for a gas with an energy-independent collision cross section and for a unitary gas. The dashed lowering curve is for an energy-independent cross section with $H = 10$, $U/U_0 = 1/(1+t/\tau)^{1.45}$ [66], where $\tau = 0.08$ second is chosen to optimize the evaporation in our experiment. The solid line is for a unitary gas with $H = 10$, where $U(t)$ is determined by Eq. (3.20) with $U/U_0 = (1-t/\tau_u)^{3.24}$, and $\tau_u = 0.77$ second is calculated by Eq. (3.21). The unitary lowering process is much faster, as it achieves runaway evaporation, which does not occur for an energy-independent cross section.

We can estimate the ratio U/U_0 that is required to achieve degeneracy for a Fermi gas. Assuming a 50-50 mixture of spin-up and spin-down atoms, the initial phase space density is $\rho_0 = (N_0/2)(H\bar{\nu}_0/k_BT)^3$. For our full trap depth of $U_0 = 550\,\mu$K, we have $\bar{\nu}_0 = 1780$ Hz and $k_BT_0 \simeq U_0/H = 55\,\mu$K for $H \simeq 10$. With $N_0 = 8\times 10^5$, $\rho_0 = 1.5\times 10^{-3}$, from Eq. (3.12) with $H = 10$, we have $\rho = \rho_0\,(U_0/U)^{1.3}$. Lowering the trap by a factor of 150 yields $\rho \simeq 1$, which corresponds to 0.61 second in the unitary gas lowering curve, and 2.45 seconds for the constant cross section curve.

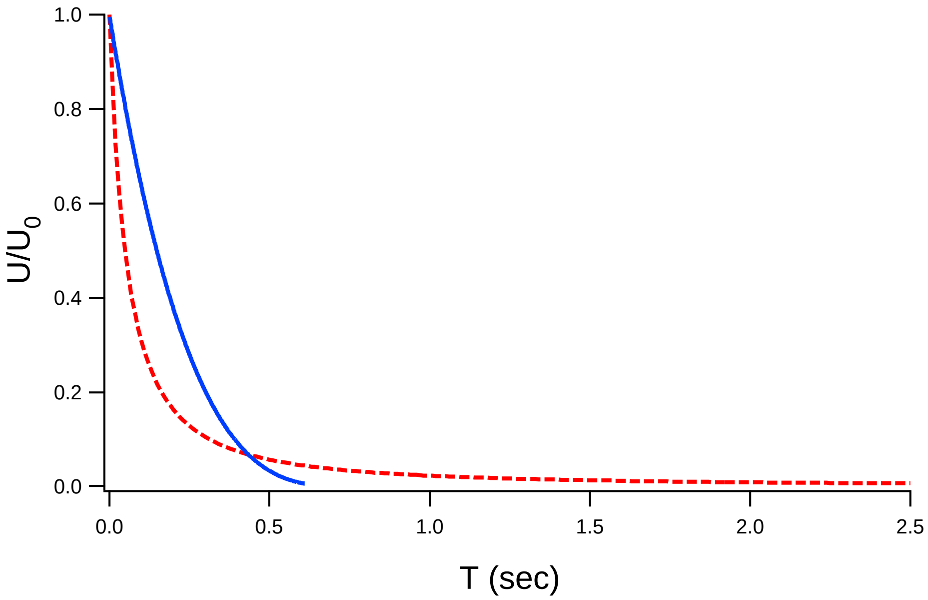

Figure 3.3: Trap depth U/U_0 versus time for evaporative cooling of a unitary Fermi gas. Dashed line: Lowering curve for a gas with an energy-independent collision cross section. Solid line: Lowering curve for a unitary gas. Each curve ends when $U/U_0 = 1/150$, where the gas becomes quantum degenerate.

3.3.3 Experiments on Evaporative Cooling of a Unitary Fermi Gas

Our experiments employ evaporative cooling of a 50-50 mixture of the two lowest hyperfine states of ^{6}Li fermions in a CO_2 laser trap at 834 G, for which the s-wave scattering length diverges to produce a unitary Fermi gas. The CO_2 laser trap is directly loaded from a ^{6}Li magneto-optical trap. Typically, the total number of loaded atoms is 2×10^6. The magnetic field is ramped to the Feshbach resonance and the atoms are allowed to evaporate at fixed trap depth first, which yields $N_0 = 8 \times 10^5$ at stagnation. The trap depth is then lowered according to the lowering curve $U(t)/U_0$ shown in Fig. 3.3.

The maximum laser power P_0 at the trap focus is between 50 and 60 W. Parametric resonance measurements in the weakly interacting regime at low magnetic field yield the typical harmonic oscillator frequencies at full trap depth U_0 as, $\omega_x = 2\pi\nu_x = 2\pi \times 5500$ Hz, $\omega_y = 2\pi\nu_y = 2\pi \times 5400$ Hz, and $\omega_z = 2\pi\nu_z = 2\pi \times 190$ Hz.

We estimate the maximum trap depth using the known power and $U_0 = 4\alpha_g\, P_0/(c\, a_x a_y)$, where α_g is the ground state static polarizability of ^{6}Li (24.3×10^{-24} cm^3 [69]), $c = 3 \times 10^{10}$ cm/s is the speed of light, and a_x, a_y are $1/e$ radii of the electric field for a Gaussian trap in the x- and y-direction, respectively. We can determine a_x for a given laser power according to $a_x^4 = 4(\nu_y/\nu_x^3)\alpha_g\, P_0/(\pi^2 Mc)$, where $M = 1.0 \times 10^{-23}$ g is the ^{6}Li atom mass and $a_y = a_x\nu_x/\nu_y$. We obtain $U_0/k_B = 550\,\mu$K with $a_x = 50.3\,\mu$m, $a_y = 51.2\,\mu$m for $P_0 = 60$ W, and $U_0/k_B = 500\,\mu$K for $P_0 = 50$ W.

Fig. 3.4 shows how the observed total number of atoms N/N_0 scales with trap depth U/U_0 for the two different trap lowering curves shown in Fig. 3.3. We use $N/N_0 = (U/U_0)^p$ to fit the data in Fig. 3.4 obtained by using the trap lowering curve for unitary gases, and find $p = 0.21(0.01)$. For $H = 10$, Eq. (3.11) predicts $p = 0.191$, which is shown as the solid line in Fig. 3.4. The scaling law is obeyed down to about 1% of the maximum trap depth, where the Fermi gas becomes degenerate and the scaling law based on a classical gas fails as discussed further below.

We also measured the transverse cloud size after release and subsequent expansion for a time t_{exp}, which is between 400 and 1200 μs. The measured expanded transverse cloud size is found to scale linearly with trap depth U and quadratically with expansion time t_{exp}, which indicates the cloud size in the trap is independent of trap depth U, as we will show in the following.

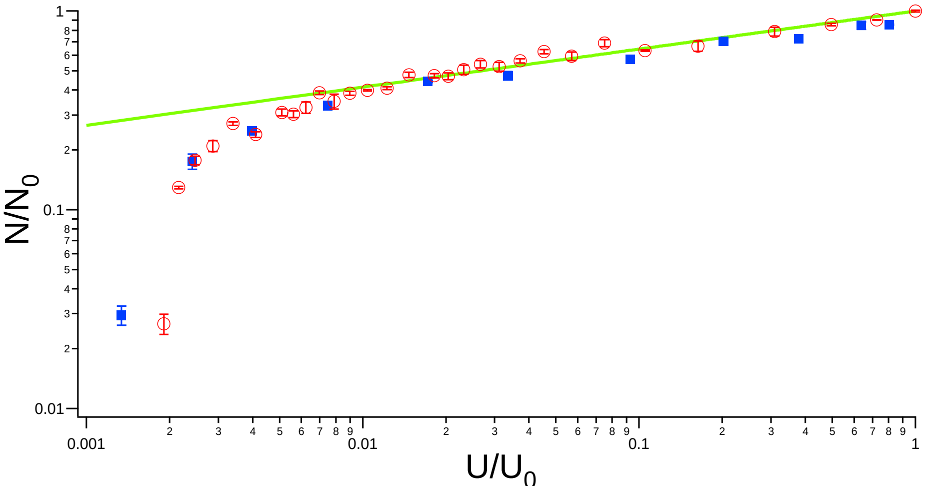

Figure 3.4: Remaining atom fraction versus trap depth for evaporative cooling of a unitary Fermi gas. Note that the trap lowering time increases from right to left. Open circles: Data obtained using a trap lowering curve for an energy-independent scattering cross section. Solid squares: Data obtained using the trap lowering curve for a unitary gas. The solid line shows the scaling law prediction for $H = U/k_BT = 10$. The data deviate from the scaling law prediction when the gas becomes degenerate near $U/U_0 = 0.007$.

The size of the observed expanded cloud is related to that of the trapped gas by $\langle x^2\rangle_{obs} = b_x^2(t_{exp})\,\langle x^2\rangle_{trap}$, where there is a known scale factor $b_x(t_{exp})$ for hydrodynamic expansion [12]. However, for $\omega_x t_{exp} >> 1$, the difference between the hydrodynamic and ballistic expansion factors is small. Hence, we take $b_x^2(t_{exp}) \simeq (\omega_x t)^2$, the ballistic value for large expansion time. Using $\omega_x^2 = 4U/Ma_x^2$ and Eq. (3.15), we see that

$$\frac{\langle x^2\rangle_{obs}}{(U/U_0)\,t_{exp}^2} = \frac{U_0}{HM} \tag{3.22}$$

should be nearly independent of U/U_0.

Fig. 3.5 shows the data corresponding to the left side of Eq. (3.22). As expected for a constant value of H, we find that the ratio $\langle x^2\rangle_{obs}/[(U/U_0)\,t_{exp}^2] \simeq 0.06\,\mathrm{m}^2/\mathrm{s}^2$

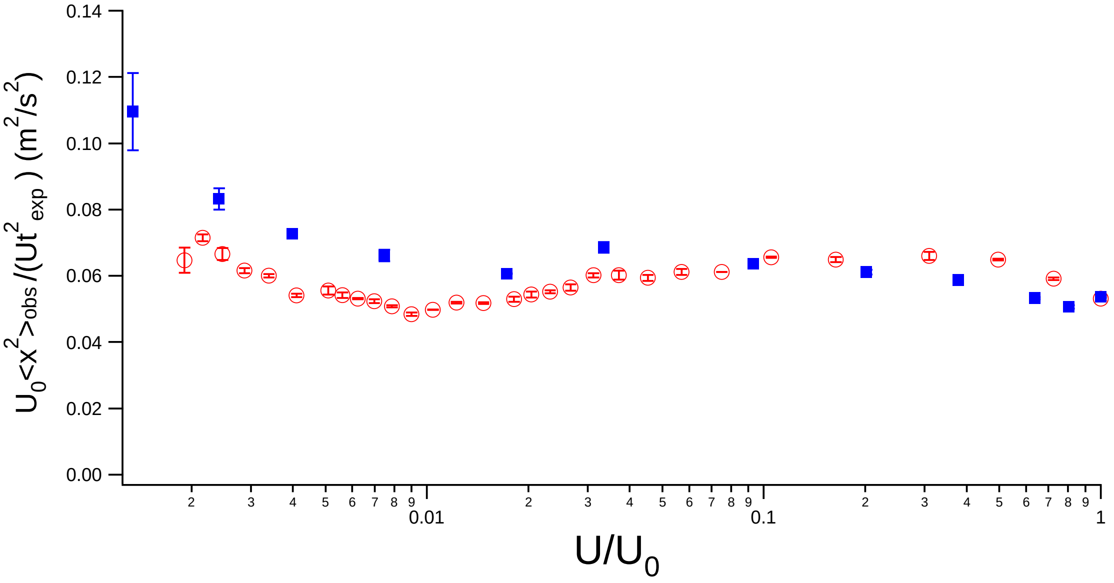

Figure 3.5: Mean square cloud size in the trap during evaporative cooling of a unitary Fermi gas. Open circles:Obtained using the trap lowering curve for an energy-independent scattering cross section. Solid squares: Obtained using the trap lowering curve for unitary gas. Note that the trap lowering time increases from right to left.

is nearly constant, which yields $U_0/k_B = 440\,\mu$K for a constant $H = 10$ from the number scaling. We find that this initial trap depth is comparable to the above estimates we made by the measured trap oscillation frequencies and power.

Our data shows that both of the two lowering curves yield similar results for the number and trap size, but the unitary lowering curve is much faster than that for the energy-independent cross section. From Fig. 3.4, the atom number data deviates from the scaling law predictions below $U/U_0 = 0.007 \simeq 1/150$, which is in good agreement with the predicted depth at which degeneracy occurs. In the degenerate regime, further lowering of the trap depth cuts into the Fermi surface and causes the scaling laws to fail. A different trap lowering curve is required to optimize the efficiency in this regime. However, in practice, one simply adjusts the final trap depth to slightly cut into the Fermi surface to achieve the minimum temperature in the degenerate regime.

3.3.4 Mean Free Path for Evaporating Atoms

The above modeling of evaporative cooling is based on the assumption that the evaporating atoms leave the trap experiencing only one binary collision. When the gas is unitary and the collision cross section is large, there exists a question: Do the evaporating atoms collide with other trapped atoms as they leave the trap? If this is true, the evaporative process must be modeled by much more complex multiple collisions. We now show that the chance for these collisions is small even when the gas is in the hydrodynamic region. This condition is achieved because the mean free path of the evaporative atoms is much larger than the transverse trap dimension.

Consider the ratio of the mean free path $l = 1/(\bar{n}\sigma)$ to the rms transverse trap size $d_x \equiv \sqrt{\langle x^2 \rangle_{trap}}$, where $\bar{n}$ is the average atoms density. Since the cloud size during the evaporation does not change, and the average density $\bar{n}$ scales as N and the σ scales as $1/U$, so that $1/\bar{n}\sigma$ scales as U/N. The ratio $l/d_x = (l_0/d_x)(l/l_0) = (\bar{n}_0\sigma_0/\bar{n}\sigma)/(\bar{n}_0\sigma_0 d_x)$ yields

$$\frac{l}{d_x} = \frac{N_0 U}{N U_0}\frac{1}{n_0\sigma_0 d_x}. \tag{3.23}$$

For $H = 10$, $N/N_0 = (U/U_0)^{0.19}$, l/d_x scales as $(U/U_0)^{0.81} \simeq U/U_0$. We find the mean free path decreases almost linearly with trap depth.

To achieve $l \geq d_x$, we require $(U/U_0)^{0.81} \geq n_0\sigma_0 d_x$. Using $\sigma_0 = \sigma_{evap}/4$ in Eq. (3.10) for a 50:50 spin mixture and $\lambda = \omega_z/\omega_x$, we obtain

$$(U/U_0)^{0.81} \geq \frac{2}{U_0\sqrt{\pi}}\frac{\lambda H\,\hbar^2 N_0}{M a_x a_y}. \tag{3.24}$$

For our trap, $\lambda = 0.035$ and $U_0 = 500\,\mu$K, we find $U/U_0 \geq (12.7/500)^{1.23} = 0.011$, which means that the evaporating atoms will not scatter with other atoms in the trap until the trap can be lowered by a factor of $\simeq 100$. After that limit, the evaporation process starts to become hydrodynamic. There is a very good agreement between the scaling law predictions and the data in Fig. 3.4, where the prediction of constant H is valid above $U/U_0 = 0.01$.

In conclusion, by reducing the trap depth with a lowering curve that maintains a fixed large ratio H, we find that atom loss is reduced and high efficiency is achieved in evaporative cooling of a unitary Fermi gas. The faster evaporation time is important for suppressing excess atom loss and excess heating, such as background gas collisions or intensity and pointing noises in the laser beam.

3.4 Creating Strongly Interacting, Weakly Interacting, and Noninteracting Fermi Gases

In this section, I will give a schematic introduction to the basic procedures we use to create ultracold Fermi gases with ^{6}Li atoms. The creation of a strongly interacting Fermi gas, a weakly interacting Fermi gas as well as a noninteracting one is shown in the block diagram of Fig. 3.6.

There are four kinds of ultracold Fermi gas samples that have been implemented in our apparatus: a 50:50 spin balanced strongly interacting Fermi gas; a 50:50 spin balanced noninteracting Fermi gas; a 50:50 spin balanced weakly interacting Fermi gas; and spin polarized noninteracting or strongly interacting Fermi gases. Spin polarized Fermi gases are beyond the scope of this dissertation, so I will not give details here. Instead, I will focus on how we generate spin balanced Fermi gases. Noted that all the Fermi gases presented in this thesis are spin balanced, except for specific mention.

The creation of Fermi gases with different interaction strength uses the same precooling methods. First, a collimated ^{6}Li atomic beam is generated from the hot vapor in an atomic oven. The beam propagates from the oven region to the trapped region through a Zeeman slower. Inside the slower, the atoms are slowed down by the counterpropagating slower laser beam due to Doppler cooling mechanism. After exiting the slower, the atoms enter a ultrahigh vacuum chamber where the atoms with speed less than 100 m/s can be captured by a MOT. The period of the slow atoms loading into the MOT is called "MOT loading phase", which lasts for about 10 seconds to load about 200 million atoms.

Throughout the MOT loading time, a CO_2 laser optical dipole trap is also

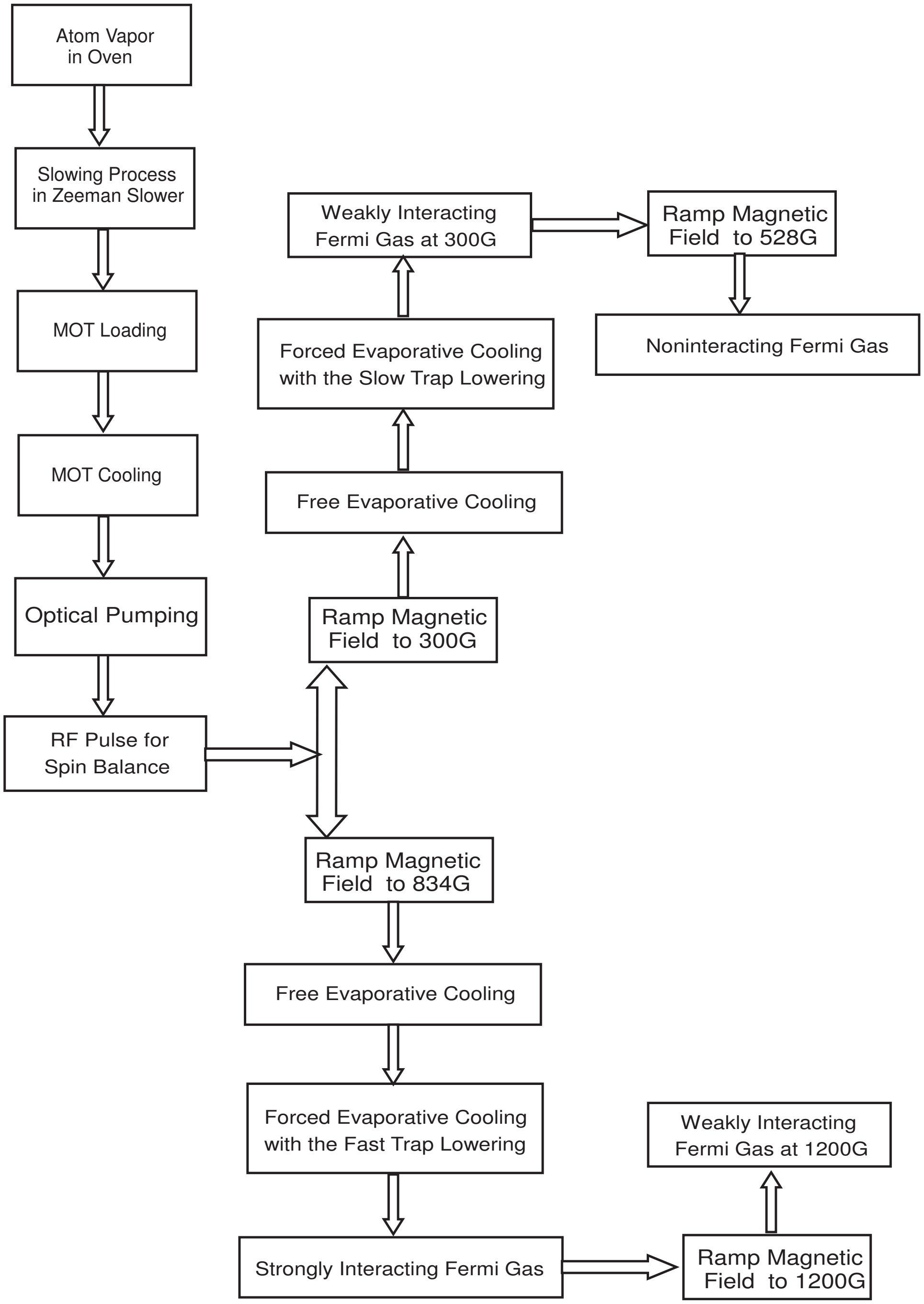

Figure 3.6: The schematic diagram for the procedure of producing ultracold Fermi gases with different strengths of interaction.

present in the region of the MOT. The positions of the MOT and that of the CO_2 laser trap are carefully overlapped by moving the MOT position slightly with several bias magnetic coils. To increase the trap depth of the CO_2 laser trap, the CO_2 laser trap is generated by both the forward propagating beam and the back-going beam. The back-going beam is retroreflected by a rooftop mirror, which rotates the linear polarized incoming beam by 90 degrees to avoid creating a standing wave trap. The back-going beam then retraces the path of the forward beam all the way to a thin-film polarizer, at which point the back-going beam is directed to a beam dump. The focus points of the forward beam and the back-going beam are aligned carefully to overlap with each other for providing the tightest spacial confinement. Approximately two million atoms at a temperature of 140 μK are loaded into the CO_2 laser trap.

After the laser beams and the spherical quadrupole magnetic field for the MOT are turned off, a bias magnetic field produced by a pair of high field magnets is turned on. First, the bias magnetic field is swept to 8 gauss to split the hyperfine states $|1\rangle$ and $|2\rangle$. A broadband white noise RF pulse is applied to equalize the spin population in those two states. After that, we use different procedures to create ultracold Fermi gases of different interacting strength. I will describe these procedures in the following paragraphs.

In the case of creating strongly interacting Fermi gases, the magnetic field is ramped to 834 G. Then the retroreflected CO_2 laser beam is adiabatically blocked to producing a forced evaporation, which only leaves a single forward propagating beam to form the optical trap. Then the optical potential is kept constant for about 5 seconds to allow thermalization and evaporation of the trapped atoms. I call this “free evaporation.” At the end of the free evaporation, about 1 million atoms at the temperature of $50\,\mu K$ are contained in a single beam optical trap with the trap depth of about $500\,\mu K$. The free evaporation is followed by the forced evaporation, which is achieved by lowering the optical trap by a factor of a thousand from the full trap depth according to the "unitary lowering curve" that I discussed in the previous section. This lowering curve generates atomic ensembles close to the ground state energy in a fraction of a second with about 1×10^5 atoms in each spin states. Once the forced evaporation is completed, the optical trap depth is held at its final value for a brief time of about a fraction of second to allow the atoms to thermalize. Then the depth of the CO_2 laser trap is adiabatically recompressed to a desired value in another fraction of second. Finally, the ultracold ^{6}Li atoms are prepared as a sample of a strongly interacting Fermi gas.

In the case of creating a noninteracting Fermi gas, there are two primary difference for the forced evaporative cooling shown in Fig. 3.6. First, the magnetic field is ramped to 300 gauss to operate the forced evaporation. Second, the forced evaporation process at 300 gauss is much longer than that at 834 gauss. At 300 gauss, the gas is weakly interacting with a small negative scattering length. Smaller interatomic collision rates make the thermalization process much slower at 300 gauss than that at the Feshbach resonance. Usually, the forced evaporative cooling at 300 gauss lasts about 10 seconds to cool the cloud to a temperature of $T/T_F \approx 0.20$ with the 2×10^5 atoms number in each spin state. Further cooling is very difficult in the weakly interacting regime since the collision rate decreases with the temperature decreases while the collision cross section is a constant. After evaporative cooling, we sweep the magnetic field from 300 gauss to the zero crossing of the scattering length at about 528 gauss, where $a_s \approx 0$ and a truly noninteracting gas is obtained. The sweep is done adiabatically over about 0.8 second to keep the temperature of the cloud almost constant. [1]

In Fig. 3.6, I also show how to use the evaporative cooling in the strongly interacting regime for producing a weakly interacting Fermi gas on the BCS side. We do the evaporative cooling at 834 gauss, then adiabatically sweep the magnetic field from the the unitary limit to the weakly interacting BCS region near 1200 gauss. This adiabatical sweep process is very stable. There is no heating or atom loss observed due to the ramping of the magnetic field. By doing adiabatic sweeping, the total entropy of the cloud is conserved, which provides a tool to connect thermodynamic properties of strongly interacting Fermi gases with those of weakly interacting Fermi gases, as described in Chapter 5.

After producing strongly interacting, noninteracting and weakly interacting Fermi gases, we mainly operate two kinds of experiments for ultracold atoms. One is to study dynamics, such as release of the atoms from the trap, excitation of collective oscillations, and rotation of the optical trap, etc. The other one is to study thermodynamics, such as heating the cloud and ramping the magnetic field, etc.

The final step of our experiment is to extract information from the cold atoms. In our lab, we use absorption imaging with resonant optical pulses as described before. We usually first release the atom cloud from the trap to let the cloud expand so that the transverse size of the cloud images are much larger than

---

[1] In zero magnetic field, $|1\rangle - |2\rangle$ mixture is also a nearly noninteracting Fermi gas. However, there are two reason preventing us to get a noninteracting gas in zero field [53, 64]. First, the signal-to-noise level for the absorption images of the atoms is reduced at zero magnetic field because the resonance imaging pulse optically pumps substantial atoms into the dark states. Second, there exists three p-wave Feshbach resonances for a $|1\rangle - |2\rangle$ mixture between 159 and 215 gauss [70, 71], which results in the significant heating and atom loss as the magnetic field is swept down.

the resolution of our imaging system. The expansion behavior depends on the collisional properties of the cloud and is explained in great detail in [64]. Based on the known expansion dynamics, we can trace back the cloud size to the trap before the release. The images of the cloud are recorded by a cooled ultralow noise CCD camera. Resonant imaging is a destructive imaging method. After the atoms disappear, a second optical pulse is sent into the imaging system and recorded by the CCD as the reference pulse.

In the end, the images of the atoms are acquired by a computer system and processed by Igor data analysis software. An image processing program was developed in our group to extract the atom information, such as the spatial density, atom number, cloud size etc. The updated part of this program for my experiments can be found in Appendix B.

Chapter 4

Method of Measuring the Energy of a Unitary Fermi Gas

From an experimental view, we take absorption images of the cold atoms to obtain the atom number and column density in the optical trap. When we say "measure" the energy and entropy, actually we "determine" the energy and the entropy from the atom number and column density. So there is a question about the measurement: Can we use a model-independent method to directly determine the energy and entropy from the atoms number and column density of a strongly interacting Fermi gas? The answers for the above question are quite different in the case of energy and entropy. For energy measurement, the answer is Yes. A strongly interacting Fermi gas obeys virial theorem at all temperatures [48], which enables a direct determination of the energy of a strongly interacting Fermi gas from the cloud size in the strongly interacting regime. However, we have no model-independent way to determined the entropy of a strongly interacting Fermi gas directly from their column density in the strongly interacting regime. Instead, we rely on adiabatically sweeping the magnetic field to the noninteracting or weakly interacting regime, where the entropy can be determined from the cloud size based only on the fundamental thermodynamic principles without invoking any specific theoretical models. In this chapter, I will focus on how to measure the energy of the cloud of a trapped strongly interacting Fermi gas. I will introduce the virial theorem for unitary Fermi gases first. The virial theorem provides a model-independent way to determine the total energy of a cloud from its mean square size. After that, I will describe our method to extract the axial mean square size of the cloud by fitting the cloud profile using a Thomas-Fermi distribution. In the end, I will show how to determine the total energy of a unitary Fermi gas in terms of the axial mean square size of a cloud.

4.1 Virial Theorem

In this section I will show that strongly interacting Fermi gases obey the virial theorem at all temperatures. According to the universal hypothesis for a strongly interacting Fermi gas, the thermodynamic functions of a homogeneous gas in the unitarity only depend on the local density n and temperature T [5].

First consider the local energy ΔE (kinetic and interaction energy) contained in a small volume ΔV of gas centered at position $\mathbf{x}$ in a harmonic trap. Assume that the volume ΔV contains a fixed number of atoms ΔN, so that $n = \Delta N/\Delta V$, where $\int d^3\mathbf{x}\, n(\mathbf{x}) = N$ is the total number of trapped atoms.

For such a unitary gas, the local energy ΔE and local entropy ΔS must be of the general form

$$\Delta E = \Delta N\, \epsilon_F(n)\, f_E\left[\frac{T}{T_F(n)}\right], \tag{4.1}$$

$$\Delta S = \Delta N\, k_B\, f_S\left[\frac{T}{T_F(n)}\right]. \tag{4.2}$$

Here, $\epsilon_F(n)\, f_E$ and $k_B\, f_S$ are the average energy and the average entropy per particle, respectively. The natural energy scale is taken to be the local Fermi energy $\epsilon_F(n) \equiv \hbar^2\,(3\pi^2\,n)^{2/3}/(2m) = k_B T_F(n)$, where n is the local particle density and $T_F(n)$ is the corresponding local Fermi temperature. Note that we have $f_E = 3/5$ for a zero-temperature ideal Fermi gas, while $f_E = 3(1+\beta)/5$ for a zero-temperature unitary gas, where β is a universal many-body parameter defined as the difference between the local energy of a strongly interacting gas and that of a noninteracting Fermi gas $\epsilon_{SI} = (1+\beta)\epsilon_{NI}$ [12, 72]. For a classical gas, the temperature dependent function $f_E = (3/2)T/T_F(n)$.

The local pressure of the gas is readily determined from the relation

$$P = -\left(\frac{\partial(\Delta E)}{\partial(\Delta V)}\right)_{\Delta N,\Delta S}. \tag{4.3}$$

From Eq. (4.2), we see that holding the local entropy constant requires f_S to be a constant, which means that we need to hold the local reduced temperature $T/T_F(n)$ constant in taking the derivative of ΔE with respect to volume ΔV. Hence, we only need to find the volume derivative to the local Fermi energy, which yields the local pressure

$$\begin{aligned} P(n,T) &= -\Delta N\,\frac{\partial(\epsilon_F(n))}{\partial(\Delta V)}\,f_E \\ &= \Delta N\,\frac{2}{3}\,\frac{\epsilon_F(n)}{n}\,\frac{\Delta N}{\Delta V^2}\,f_E \\ &= \frac{2}{3}\,n\,\epsilon_F(n)\,f_E \\ &= \frac{2}{3}\,\mathcal{E}(n,T). \end{aligned} \tag{4.4}$$

where the local energy density (total kinetic plus interaction energy per unit volume) $\mathcal{E}(n,T) = n\,\epsilon_F(n)\,f_E[T/T_F(n)]$. Eq. (4.4) relates the pressure and local energy density for the unitary gas in the same way as for an ideal, noninteracting homogeneous gas, although the energy densities are quite different. Since $\epsilon_F(n) \equiv \hbar^2\,(3\pi^2\,n)^{2/3}/(2m)$, the pressure of the unitary gas have the general form

$$P(n,T) = \frac{\hbar^2}{m} n^{5/3}\, f_P\left[\frac{T}{T_F(n)}\right], \tag{4.5}$$

where the f_P is a dimensionless function only depends on the the T/T_F.

In mechanical equilibrium, the balance of the forces arising from the pressure P and trapping potential U yields

$$\nabla P(\mathbf{x}) + n(\mathbf{x})\,\nabla U(\mathbf{x}) = 0. \tag{4.6}$$

Now we consider any arbitrary trap potential that satisfies the condition that the local atom density approaches zero at the surface of the cloud. Taking an inner product of $\mathbf{x}\cdot\nabla P(\mathbf{x})$ and integrating over the total volume of the trapped gas, we get

$$\int d^3\mathbf{x}\,\mathbf{x}\cdot\nabla P(\mathbf{x}) = \int d^3\mathbf{x}\,\nabla\cdot(\mathbf{x}\,P(\mathbf{x})) - \int d^3\mathbf{x}\,P(\mathbf{x})\,\nabla\cdot\mathbf{x} \tag{4.7}$$

Note that the first term on the right side of Eq. (4.7) equals zero because the integration of $\mathbf{x}\,P(\mathbf{x})$ is in the surface of the trap, where both the atoms density and the local pressure is zero. In the second term on the right side, $\nabla\cdot\mathbf{x} = 3$. Inserting Eq. (4.6) into Eq. (4.7), we get

$$3\int d^3\mathbf{x}\,P(\mathbf{x}) = \int d^3\mathbf{x}\,n(\mathbf{x})\,\mathbf{x}\cdot\nabla U(\mathbf{x}). \tag{4.8}$$

Applying the relation of $P(\mathbf{x}) = \frac{2}{3}\,\mathcal{E}(\mathbf{x})$ and $\int d^3\mathbf{x}\,n(\mathbf{x})\,\mathcal{E}(\mathbf{x}) = NE - N\langle U\rangle$, where E and $\langle U \rangle$ are the total energy and the potential energy per particle, we then obtain

$$E = \langle U \rangle + \frac{1}{2}\langle \mathbf{x} \cdot \nabla U(\mathbf{x}) \rangle, \tag{4.9}$$

where $\langle \mathbf{x} \cdot \nabla U(\mathbf{x}) \rangle$ is defined as

$$\langle \mathbf{x} \cdot \nabla U(\mathbf{x}) \rangle = \frac{\int d^3\mathbf{x}\, n(\mathbf{x})\, \mathbf{x} \cdot \nabla U(\mathbf{x})}{N}. \tag{4.10}$$

Eq. (4.9) is the general form of the virial theorem for any trapping potential. In the following, we will consider the virial theorem for a specific trapping potential. First, we consider a harmonic potential $U(\mathbf{x}) = m(\omega_x^2\, x^2 + \omega_y^2\, y^2 + \omega_z^2\, z^2)/2$. For the harmonic trap, applying $\mathbf{x} \cdot \nabla U(\mathbf{x}) = 2\, U(\mathbf{x})$ in Eq. (4.9), we readily get

$$E = 2\langle U \rangle. \tag{4.11}$$

In the local density approximation, the pressure of the cloud is equal in all three direction, we have $\langle x\frac{\partial U}{\partial x}\rangle = \langle y\frac{\partial U}{\partial y}\rangle = \langle z\frac{\partial U}{\partial z}\rangle$ from Eq. (4.8). So the potential energies are equal in three dictions since by $\langle U_x \rangle = \langle U_y \rangle = \langle U_z \rangle = m\omega_z^2\langle z^2\rangle/2$, then we have the total energy for a harmonic potential as

$$E = 3\, m\, \omega_z^2 \langle z^2 \rangle. \tag{4.12}$$

A more realistic potential of the optical dipole trap is a Gaussian profile. The anharmonicity arising from the Gaussian trap will add a small correction for the total energy in Eq. (4.11) and Eq. (4.12). The Gaussian potential is given by

$$U(x, y, z) = U_0 - U_0\, \exp\left[-\frac{m}{2U_0}\left(\omega_x^2\, x^2 + \omega_y^2\, y^2 + \omega_z^2\, z^2\right)\right]. \tag{4.13}$$

Using the geometric mean trap frequency $\bar{\omega} = (\omega_x \, \omega_y \, \omega_z)^{1/3}$, we can rewrite Eq. (4.13) as a symmetric effective potential

$$U(\mathbf{x}) = U_0 - U_0 \, \exp\left(-\frac{m\bar{\omega}^2\mathbf{x}^2}{2U_0}\right), \tag{4.14}$$

where $\mathbf{x}$ is the reduced space vector with $\mathbf{x}^2 = x_i^2 + x_j^2 + x_k^2$ and $x_i = \omega_x x/\bar{\omega}, x_j = \omega_y y/\bar{\omega}, x_k = \omega_z z/\bar{\omega}$.

To obtain the anhamonicity effects of the Gaussian trap, we use the Taylor expansion of Eq. (4.14) up through quadratic terms, which is given by

$$U(\mathbf{x}) = \frac{m\bar{\omega}^2\mathbf{x}^2}{2} - \frac{m^2\bar{\omega}^4\mathbf{x}^4}{8U_0}. \tag{4.15}$$

The square term in Eq. (4.15) is the harmonic potential and the quartic term provides the anharmonicity correction for the harmonic trap. Now we can calculate the anharmonicity correction for the virial theorem by applying Eq. (4.15) into Eq. (4.9) which yields

$$E = m\bar{\omega}^2\langle\mathbf{x}^2\rangle - \frac{3m^2\bar{\omega}^4\langle\mathbf{x}^4\rangle}{8U_0}. \tag{4.16}$$

Note that a symmetric potential gives $\langle x^2\rangle = \langle y^2\rangle = \langle z^2\rangle = \langle\mathbf{x}^2\rangle/3$, and $\langle\mathbf{x}^4\rangle = 5\langle x^4\rangle = 5\langle y^4\rangle = 5\langle z^4\rangle$. Eq. (4.16) can be written in terms of the mean square size in the z direction by

$$\begin{aligned} E &= 3m\omega_z^2\langle z^2\rangle - \frac{15m^2\omega_z^4\langle z^4\rangle}{8U_0} && (4.17) \\ &= 3m\omega_z^2\langle z^2\rangle\left(1 - \frac{5m\omega_z^2\langle z^4\rangle}{8U_0\langle z^2\rangle}\right). && (4.18) \end{aligned}$$

Now we can make an estimate for the value of $\langle z^4\rangle/\langle z^2\rangle$ by assuming the density distribution of the atoms in a Gaussian shape, which is valid at the higher temperature $T > 0.5T_F$. We should admit that the density profile is precisely a Gaussian shape only at high temperatures $T \geq T_F$. However, at low T/T_F, the correction is so small that the error in the Gaussian approximation is negligible. So here, for the purpose of estimating the anharmonic correction, the Gaussian approximation should be good enough. By assuming $n(z) = exp(-\frac{z^2}{a^2})/(a\sqrt{\pi})$, we get

$$\langle z^4\rangle = \int_{-\infty}^{\infty} dx \frac{exp(-\frac{z^2}{a^2})x^4}{a\sqrt{\pi}} = \frac{3}{4}a^4 = 3\langle z^2\rangle^2. \tag{4.19}$$

By inserting Eq. (4.19) into Eq. (4.18), we finally obtain

$$E = 3m\omega_z^2\langle z^2\rangle\left(1 - \frac{15m\omega_z^2\langle z^2\rangle}{8U_0}\right). \tag{4.20}$$

It is worth noting that the anharmonicity correction only depends the ratio between the mean square size and the depth of the Gaussian trap, while is independent of the interactions. This provides us with a unified method to calculate the anharmonic corrections for both noninteracting and strong interacting gases.

Hence, universality requires a strongly interacting Fermi gas to obey the virial theorem just as a noninteracting ideal Fermi gas, where the total energy of the cloud can be determined by measuring the mean square size of the cloud in the trap. The mean square size of the cloud can be readily measured in a model-independent way from the atom column density. In the next section, I will describe how to calculate the mean square size from the column density by fitting the density profile.

4.2 Mean Square Size of a Unitary Fermi Gas

To calculate the mean square size of the cloud, one can either directly use the column density to calculate it by the definition of the mean square size, or use a density profile to fit the cloud shape, then determine the mean square size from the fitting curve. For the first method, it is always a problem to deal with the background noise of absorption images. Instead, we use the curve fitting method, which provides a consistent way to extract the mean square size from the could images.

For the application of fitting the cloud profile, the optical dipole trap can be well approximated by a harmonic trap. In a harmonic trap, a noninteracting ideal Fermi gas has a Thomas-Fermi profile. Even though we are trying to fit the density profile of a unitary Fermi gas, we will show that the density profile of a unitary Fermi gas in the ground state is exactly the Thomas-Fermi shape by using an effective particle mass in the equation of state for a unitary Fermi gas. For the finite temperature states, the Thomas-Fermi profile can be treated as a very good approximation for the profile of a unitary Fermi gas [45].

4.2.1 Equation of State for a Ground State Unitary Gas

Let us study a noninteracting ideal Fermi gas in a harmonic trap first. Suppose the harmonic potential is given by

$$U_{HO}(x,y,z) = \frac{m}{2}\left(\omega_x^2\, x^2 + \omega_y^2\, y^2 + \omega_z^2\, z^2\right). \tag{4.21}$$

A noninteracting Fermi gas at the zero temperature with $N/2$ atoms per spin state has a Fermi energy given by

$$E_F = \hbar\,\bar{\omega}(3N)^{1/3}, \tag{4.22}$$

where the geometric mean of the trap oscillation frequencies is given by $\bar{\omega} = (\omega_x\,\omega_y\,\omega_z)^{1/3}$. The Fermi energy sets a characteristic energy scale, below which the Fermi occupation number becomes unity for all energy levels and above which it is zero for any energy levels. The corresponding temperature scale is the Fermi temperature T_F, which is given by

$$T_F = \frac{E_F}{k_B} = \frac{\hbar\,\bar{\omega}(3N)^{1/3}}{k_B}. \tag{4.23}$$

The Fermi radii for an noninteracting ideal Fermi gas are defined as

$$\sigma_i = \left(\frac{2\,E_F}{m}\right)^{1/2} \frac{1}{\omega_i}\,,\; i = x, y, z. \tag{4.24}$$

Accordingly, the harmonic potential can be rewritten as

$$U_{HO}(\mathbf{r}) = E_F\,\left(\frac{x^2}{\sigma_x^2} + \frac{y^2}{\sigma_y^2} + \frac{z^2}{\sigma_z^2}\right). \tag{4.25}$$

The equation of state of a ground state noninteracting Fermi gas trapped in a potential $U_{HO}(\mathbf{r})$ is given by [73]

$$\frac{\hbar^2\,k_F(\mathbf{r})^2}{2\,m} + U(\mathbf{r}) = \mu, \tag{4.26}$$

where $k_F(\mathbf{r})$ represents the position dependent local Fermi wave vector, and μ is the global chemical potential of the trap which is defined as the chemical potential at the center of the trap. For the ground state, μ is equal to the Fermi energy

$$\mu = E_F = \hbar\,\bar{\omega}(3\,N)^{1/3}. \tag{4.27}$$

Now we look at the equation of state for a unitary Fermi gas at zero temperature $T = 0$. As I discussed in Section 2.2.1, when $a_s \to \pm\infty$, the ground state unitary gas has a cross section given by $\sigma = 4\,\pi/k^2$. The equation indicates that the collisional behavior of the ground state unitary Fermi gas only depends effectively on the the Fermi wavevector k_F while being completely independent of the sign and strength of the interparticle interactions.

Following this argument, the interaction energy also depends only on the Fermi energy. Let us look back at the weakly interacting case, where the mean field interaction energy is approximately to the scattering length and particle density $U_{int}(r) \propto a_s n(r)$ [74, 75], where $n(r)$ is local atoms density related to the local Fermi wavevector via $n(r) = k_F^3(r)/(3\pi^2)$. When the strength of the interparticle interactions approaches the unitarity, the s-wave scattering length should be replaced by an effective scattering length a_{eff}. Because the only remaining length scale related to the system is the local Fermi wave vector $k_F(r)$, we require that $a_{eff} \propto 1/k_F(r)$ from dimensional analysis, which yields $U_{int} \propto k_F(r)^2$. From the local density approximation, the local Fermi energy is determined by the local density $n(r)$ by

$$\epsilon_F(r) = \frac{\hbar^2\,k_F(r)^2}{2\,m} = \frac{\hbar^2(3\pi^2\,n(r))^{\frac{2}{3}}}{2\,m}. \tag{4.28}$$

So we can rewrite the interaction energy as [4, 12]

$$U_{int} = \beta\, \epsilon_F(r), \tag{4.29}$$

where β is a universal many-body constant for a strongly interacting Fermi system with the unitary scattering length.

The additional term of the interaction energy should be added into the equation of state by

$$(1+\beta)\frac{\hbar^2\, k_F(r)^2}{2\, m} + U(r) = \mu^*, \tag{4.30}$$

where the asterisk on the global chemical potential in Eq. (4.30) represents the case of a strongly interacting gas in the unitary limit.

Our goal is to determine what is the value of the μ^*. The method we use is to define an effective mass $m^* = m/(1+\beta)$. By doing that, Eq. (4.30) is rewritten as

$$\frac{\hbar^2\, k_F(r)^2}{2\, m^*} + U(r) = \mu^*. \tag{4.31}$$

Comparing Eq. (4.26) and Eq. (4.31), we find the equation of state for a unitary gas is the same as the equation of state for a noninteracting gas with a scaled mass. Since $\bar{\omega}^2 \propto 1/m$, the scaled geometric mean of the trap oscillation frequencies is given by $\bar{\omega}^* = \sqrt{1+\beta}\,\bar{\omega}$. As a result, the chemical potential for the ground state unitary Fermi gas is given by

$$\mu^* = \sqrt{1+\beta}\,\mu = \sqrt{1+\beta}\, E_F. \tag{4.32}$$

From the result of the chemical potential, we find the thermodynamic parameters of the ground state unitary Fermi gas only depends on the Fermi energy and a universal many-body constant β. At finite temperature, the thermodynamics of a strongly interacting Fermi gas is known as "universal thermodynamics" since thermodynamic properties have the same dependence on the temperature and density while are completely independent of microscopic interparticle interactions in all strongly interacting systems. From Eq. (4.30), we can see that the ground state unitary gas behaves similarly to a noninteracting gas composed of particles with an effective mass $m^* = m/(1+\beta)$. For attractive interactions $\beta < 0$, the effective mass exceeds the bare mass, $m^* > m$. So the shape of a noninteracting Fermi gas in a harmonic trap should be exactly the shape for a unitary Fermi gas in the same trap only differing with a constant. In the next section, I will describe this difference.

4.2.2 Mean Square Size of a Ground State Unitary Fermi Gas

The three-dimensional distribution of atomic density of a noninteracting Fermi gas in the harmonic trap is given by the zero temperature Thomas-Fermi profile [53],

$$n_g(x,y,z) = \frac{4\,N}{\sigma_x\,\sigma_y\,\sigma_z\,\pi^2}\left(1-\frac{x^2}{\sigma_x^2}-\frac{y^2}{\sigma_y^2}-\frac{z^2}{\sigma_z^2}\right)^{3/2}\Theta\left[1-\frac{x^2}{\sigma_x^2}-\frac{y^2}{\sigma_y^2}-\frac{z^2}{\sigma_z^2}\right], \quad (4.33)$$

where the Heaviside step function Θ restricts the integration to the regime of space of $\frac{x^2}{\sigma_x^2}+\frac{y^2}{\sigma_y^2}+\frac{z^2}{\sigma_z^2} < 1$, and σ_i is the Fermi radius defined in Eq. (4.24). Integrating in the x and y direction, the normalized one-dimensional ground state distribution in the z direction is found to be

$$n_g(z) = \frac{8\,N}{5\,\pi\,\sigma_z}\left(1-\frac{z^2}{\sigma_z^2}\right)^{5/2}\Theta\left[1-\frac{z^2}{\sigma_z^2}\right]. \quad (4.34)$$

Note that integration of Eq. (4.34) over x is confined from $-\sigma_x$ to $+\sigma_x$. By definition, the ground state mean square size $\langle z_g^2\rangle$ is given by

$$\begin{aligned} \langle z_g^2\rangle &= \int_{-z_{max}}^{z_{max}} z^2\, n_g(z)\, dz & (4.35) \\ &= \frac{\sigma_z^2}{8}. & (4.36) \end{aligned}$$

For a unitary Fermi gas with $\mu^* = \sqrt{1+\beta}\, E_F$, we find that the Fermi radius in the unitary case σ_i^* is related to the noninteracting Fermi radius σ_i via

$$\sigma_i^* = (1+\beta)^{1/4}\,\sigma_i. \tag{4.37}$$

Accordingly, the mean square size of the unitary Fermi gas $\langle z_g^2\rangle^*$ is given by

$$\langle z_g^2\rangle^* = (1+\beta)^{1/2}\frac{\sigma_z^2}{8} \tag{4.38}$$

In the experiment, we always have a finite temperature gas, so we need to use a finite temperature Thomas-Fermi profile to calculate the mean square size of the cloud. In the following, I will describe this method.

4.2.3 Mean Square Size of a Unitary Fermi Gas at Finite Temperature

Now we look at the finite temperature case for a noninteracting Fermi gas. The three- and one-dimensional density distributions are given by the 3D and 1D finite temperature Thomas-Fermi profiles [53] as

$$n(x,y,z;T) = -\frac{3\,N}{\pi^{3/2}\,\sigma_x\,\sigma_y\,\sigma_z}\left(\frac{T}{T_F}\right)^{3/2} Li_{3/2}\left[\exp\left(\frac{\frac{\mu}{E_F}-\frac{x^2}{\sigma_x^2}-\frac{y^2}{\sigma_y^2}-\frac{z^2}{\sigma_z^2}}{T/T_F}\right)\right], \tag{4.39}$$

$$n(z;T) = -\frac{3\,N}{\sqrt{\pi}\,\sigma_z}\left(\frac{T}{T_F}\right)^{5/2} Li_{5/2}\left[\exp\left(\frac{\frac{\mu}{E_F}-\frac{z^2}{\sigma_z^2}}{T/T_F}\right)\right], \tag{4.40}$$

where $Li_n(x)$ is the nth-order polylog function given by

$$Li_n(x) = \sum_{k=1}^{\infty}\frac{x^k}{k^n},\, |x| < 1. \tag{4.41}$$

Here μ is the chemical potential at the finite temperature, which depends on the E_F and T by an integral equation [64]

$$\frac{E_F^3}{3} = \int_0^{\infty}\frac{\epsilon^2 d\epsilon}{\exp\left(\frac{\epsilon-\mu}{k_B T}\right)+1}. \tag{4.42}$$

By fitting the one-dimensional density distribution with Eq. (4.40), we obtain the fitting parameters σ_z and T/T_F from the absorption images. Since the virial theorem ensures the mean square size $\langle z^2(T)\rangle \propto E(T)$ in a harmonic trap, we can write the mean square size $\langle z^2(T)\rangle$ at the finite temperature by

$$\langle z^2(T)\rangle = \langle z_g^2\rangle\frac{E(T)}{E_0} = \frac{\sigma_z^2}{8}\frac{E}{E_0}\left[\frac{T}{T_F}\right]. \tag{4.43}$$

Here $\frac{E}{E_0}\left[\frac{T}{T_F}\right]$ is a numerical function that only depends on the scaled temperature $\frac{T}{T_F}$ of the noninteracting Fermi gas in the harmonic trap, which is shown in Fig. 4.1. This function is calculated by counting the energy levels and the Fermi occupation number, then integrating the energy from the lowest energy state up to

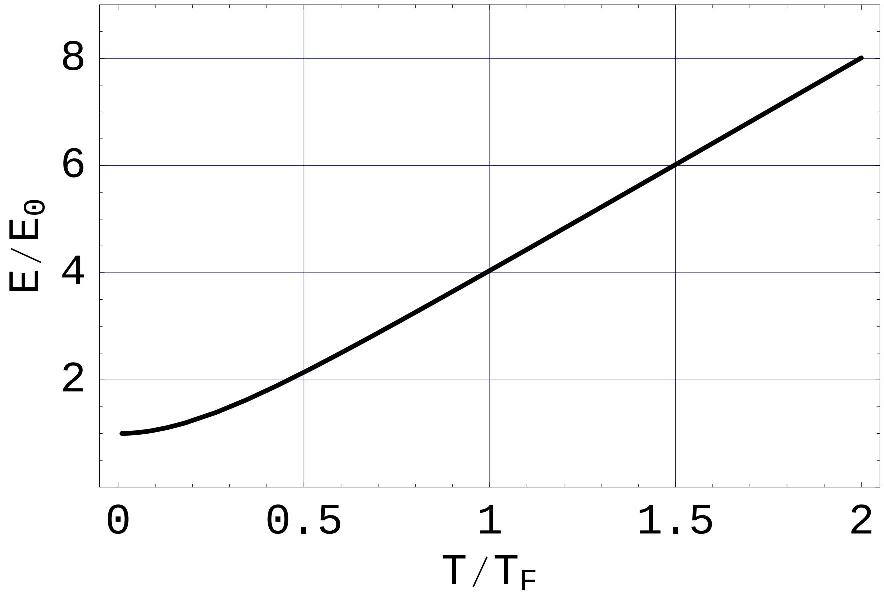

Figure 4.1: The numerical function of E/E_0 versus T/T_F for a noninteracting Fermi gas in a harmonic trap.

the highest state, which is determined by the finite temperature chemical potential. The detailed calculation and Mathematica program are given in Appendix A.

Now we look at the case for the unitary Fermi gas. We have found that a modified 1D noninteracting Fermi gas Thomas-Fermi profile can be used to fit the strongly interacting gas very well in the whole temperature range we studied from previous studies [45]. The only modification for fitting the unitary Fermi gas is to use σ_i^* instead of σ_i in Eq. (4.40), and to replace T/T_F by an empirical reduced temperature $\tilde{T}$

$$n(z;\tilde{T}) = -\frac{3\,N}{\sqrt{\pi}\,\sigma_z^*}\tilde{T}^{5/2}\ Li_{5/2}\left[\exp\left(\frac{\frac{\mu}{\mu^*}-\frac{x^2}{(\sigma_z^*)^2}}{\tilde{T}}\right)\right], \tag{4.44}$$

where μ^* is the chemical potential for the ground state unitary Fermi gas defined in Eq. (4.32).

It is worth noting that the formalism described above does not mean we can determine the real temperature T/T_F in the strongly interacting regime. To extract the temperature information from $\tilde{T}$, we need rely on a specific theoretical model, such as pseudogap theory our lab used in the previous study of the heat capacity [45].

For very high temperatures in the classical limit, the reduced temperature $\tilde{T}$ is related to the real temperature using the following argument. In the very high temperature limit, such as $T/T_F > 0.8$, the cloud profile is actually a Gaussian shape following $e^{\frac{-m\,\omega_z^2\,z^2}{2\,k_B\,T}} = e^{\frac{-z^2}{\sigma_z^2\,T/T_F}}$ [45], where the Fermi radius and temperature enter into the expression of the Gaussian profile as a product. In this high T/T_F limit, the product should be invariable by $(\sigma_z^*)^2\tilde{T} = \sigma_z^2 T/T_F$, which requires

$$\tilde{T} = \frac{T}{T_F\,\sqrt{1+\beta}}. \tag{4.45}$$

In the real experiment, we fit the coldest temperature cloud with a zero temperature Thomas-Fermi profile to get σ_z^*, then hold σ_z^* constant in a finite temperature Thomas-Fermi profile to obtain $\tilde{T}$. Although the fit value of $\tilde{T}$ can not tell us the real temperature of a unitary Fermi gas in a model-independent way, $\tilde{T}$ and σ_z^* can give an accurate determination of the mean square size of the cloud in the unitary limit. We replace σ_z with σ_z^* and T/T_F with $\tilde{T}$ in Eq. (4.43), then obtain

$$\langle z^2(\tilde{T})\rangle = \frac{(\sigma_z^*)^2}{8}\frac{E}{E_0}\left[\tilde{T}\right]. \tag{4.46}$$

In this section, I showed that I can measure the mean square size of the unitary Fermi gas by fitting the profile with a finite temperature Thomas-Fermi profile of the noninteracting Fermi gas. This procedure does not invoke any specific model, and is valid for the temperature range I studied, since it is has been proved that the finite temperature Thomas-Fermi profile describes the profile of a strongly interacting profile very well for both below and above the superfluid transition in a strongly interacting Fermi gas [45]. In the next section, I will show that the total energy of a strongly interacting Fermi gas can be readily obtained from the mean square cloud size by applying the virial theorem.

4.3 Energy of a Unitary Fermi Gas

4.3.1 Energy for a Unitary Gas in a Harmonic Trap

From the virial theorem given by Eq. (4.12) and Eq. (4.35), the total energy of a noninteracting ideal Fermi gas is given by

$$E_{NI0} = 3m\omega_z^2\langle z_g^2\rangle = \frac{3m\omega_z^2\sigma_z^2}{8} = \frac{3}{4}E_F. \tag{4.47}$$

Similarly, from Eq. (4.12) and Eq. (4.38), we get the total energy of a strongly interacting Fermi gas in the ground state

$$E_{SI0} = \frac{3m^*(\omega_z^*)^2(\sigma_z^*)^2}{8} = \frac{3}{4}\sqrt{1+\beta}E_F. \tag{4.48}$$

Now we look at the finite temperature case. From Eq. (4.12) and Eq. (4.43), the total energy for a noninteracting Fermi gas is given by

$$E_{NI}(T) = 3m\omega_z^2\langle z^2(T)\rangle = \frac{3}{4}\,E_F\,\frac{E}{E_0}\left[\frac{T}{T_F}\right]. \tag{4.49}$$

From the mean square size of a unitary gas at finite temperature given by Eq. (4.46), we obtain the total energy of the unitary Fermi gas as

$$E_{SI}(\tilde{T}) = 3m^*(\omega_z^*)^2\langle z^2(\tilde{T})\rangle = \frac{3}{4}\sqrt{1+\beta}\,E_F\,\frac{E}{E_0}[\tilde{T}]. \tag{4.50}$$

In summary, my method to determine the total energy of a strongly interacting Fermi gas in the unitary limit has the following steps: First, by fitting the 1D column density with a finite temperature Thomas-Fermi profile, I get the empirical reduced temperature $\tilde{T}$ and the effective cloud width σ_z^* for a strongly interacting Fermi gas. Second, I obtain the function $\frac{E}{E_0}[\tilde{T}]$ from our numerical calculation. In the end, by applying Eq. (4.50), we obtain the total energy of the cloud.

4.3.2 Anhamonicity Correction for the Energy of a Unitary Gas in a Gaussian Potential

For precision measurements, we need to consider the correction to the total energy dependence on the mean square size of the cloud due to the anhamonicity arising form the Gaussian potential.

According to Eq. (4.20), the anharmonicity correction only depends the ratio between the mean square size and the depth of the Gaussian trap and is irrelevant to the interactions. This provides us a method to estimate the anharmonic corrections for both the noninteracting and strong interacting gas.

As noted above, the nature energy scale in our system is the Fermi energy E_F. Now we define the mean square size of the cloud with the total energy E_F as z_F^2, where we call z_F^2 the mean square size of the Fermi energy. Note that z_F^2 is not equal to the square of the Fermi radius σ_z since $m\omega_z^2\sigma_z^2/2 = E_F = 3m\omega_z^2 z_F^2$

giving $z_F^2 = \sigma_z^2/6$. Inserting z_F^2 into Eq. (4.20), we get the scaled total energy of the cloud with anharmonicity correction

$$\begin{aligned} \frac{E}{E_F} &= \frac{\langle z^2 \rangle}{z_F^2}\left(1 - \frac{15}{24}\frac{E_F}{U_0}\frac{\langle z^2 \rangle}{z_F^2}\right) && (4.51) \\ &= \frac{\langle z^2 \rangle}{z_F^2}\left(1 - \kappa\right), && (4.52) \end{aligned}$$

where κ is the anharmonic correction factor, which is less than 10% for most of our experiments as determined from the measured mean square cloud size and our knowledge for the trap depth and the Fermi energy. The Fermi energy is determined by the atom number and the axial trap frequency measured by parametric oscillation [64]. For the trap depth, we can either estimate it using the parameters of our CO_2 laser trap as described in Chapter 8 or extract it by modeling the evaporation cooling data shown in Chapter 3.

Chapter 5

Method of Measuring the Entropy of a Unitary Fermi Gas

For a strongly interacting gas in the unitary limit, the entropy dependence on the macrovariable of a unitary Fermi gas can be simplified by the argument of the universality. For a homogeneous unitary Fermi gas, the only length scale of the system is the Fermi wavevector k_F. Correspondingly, the only energy scale of the system is the Fermi energy E_F. So the entropy S per particle can be written as a universal function of the total energy

$$S = S\left[\frac{E}{E_F}\right]. \tag{5.1}$$

For a unitary Fermi gas, ideally Eq. (5.1) includes all the information about the thermodynamics. For this reason, the primary goal in this chapter is to develop methods to measure the entropy of a unitary Fermi gas. To make a model-independent measurement on the entropy, I rely on adiabatically sweeping the magnetic field to the noninteracting interacting regime, where the entropy is conserved by the adiabatic sweep

$$S_I = S_{SI}. \tag{5.2}$$

In the noninteracting regime, the entropy S_I can be calculated in terms of the mean square cloud size of a ideal gas from the first principle without invoking any specific models, which ensures a model independent method of measuring the entropy of a strongly interacting Fermi gas by the adiabatic sweep. Note that I will normally use the S and E to refer the entropy per particle and the energy per particle, respectively, in the following chapters.

In real experiments, an adiabatic sweep from the strongly interacting regime at 834 gauss to the noninteracting regime at 528 gauss is not applicable in ^{6}Li atoms. During such sweeping, atoms would be nearly totally lost from the optical trap at the magnetic fields of about 680 and 540 gauss due to the seriously heating mechanism discussed in the following [15, 61]. A possible reason for the heating mechanism at 680 gauss is that ^{6}Li-^{6}Li molecules are created by the magnetic field ramping to the BEC side, then those molecules collide with a third atom. The three-body collisions would make the molecules decay to the deep bound molecular states while releasing a huge kinetic energy to the third atom. Near 540 gauss, the heating is due to a narrow Feshbach resonance that is less than 1 gauss wide [65, 71]. This is an additional reason that, in Section 3.4, we do not utilize evaporative cooling in the strongly interacting regime to produce a noninteracting Fermi gas by a downward magnetic sweep.

Instead, we sweep a strongly interacting Fermi gas to the weakly interacting regime at 1200 gauss as an alternative method, where we measure the mean square axial cloud size $\langle z^2\rangle_{1200}$ at 1200 gauss. The entropy of a weakly interacting gas $S_{WI}(\langle z^2\rangle_{1200} - \langle z^2\rangle_0)$ has been calculated by several theoretical groups [6, 76, 77], where $\langle z^2\rangle_0$ is the ground state size of a weakly-interacting Fermi gas at 1200 gauss that automatically includes the mean field energy shift due to the weak interactions. $\langle z^2\rangle_0$ is also determined by measuring the coldest cloud size in our experiments. Then we calculate $S_I(\langle z^2\rangle_{1200} - \langle z^2\rangle_{I0})$ in the simplest approximation, by assuming a noninteracting Fermi gas in a Gaussian trapping potential. Here, we apply a first principle calculation based on the occupation number $f(\epsilon)$ of a finite temperature ideal Fermi gas to find $S_I(\langle z^2\rangle_{1200} - \langle z^2\rangle_{I0})$, where $\langle z^2\rangle_{I0}$ is the ground state size of an ideal gas. By comparing $S_{WI}(\langle z^2\rangle_{1200} - \langle z^2\rangle_0)$ and $S_I(\langle z^2\rangle_{1200} - \langle z^2\rangle_{I0})$, we find the entropy in the weakly interacting regime is very close to the noninteracting gas entropy over most of the energy range

$$S_{SI} = S_{WI} \approx S_I. \tag{5.3}$$

This result shows that the entropy in the weakly interacting regime can be determined by calculating the noninteracting gas entropy plus a mean field shift of the cloud size.

Curious readers may ask why we do not determine the entropy of a strongly interacting Fermi gas directly from the column density in the strongly interacting regime. In contrast with measuring the energy in the strongly interacting regime, where the virial theorem provides a model-independent method to determine the energy from the mean square size of the cloud, the entropy can not be determined in an model-independent way in the strongly interacting regime. The reason can be simply understood as following: To determine the energy of a strongly interacting Fermi gas, we only need to know the relation between the internal energy (the interaction energy plus the kinetic energy) and the potential energy. The virial theorem provides an elegant relation between the potential energy and the internal energy in the unitary system, which makes the energy readily determined. However, to find the entropy, we need know more information about how the kinetic and the interaction energy distribute in the quantum states, which determines the amount of randomness of the microvariables in a macroscopic ensemble. For this reason, the determination of entropy in the strongly interacting regime involves the calculation of many-body quantum states in the unitary limit, thus unavoidably requires strong coupling many-body theories.

In summary, our method to measure the entropy follows this scenario: Generate a unitary Fermi gas in the strongly interacting regime; Measure the mean square size of the cloud in the strongly interacting regime to determine the total energy of the gas; Generate the identical cloud in the strongly interacting regime and adiabatically sweep the magnetic field to the weakly interacting regime; Measure the mean square size of the weakly interacting cloud to determine the entropy; Repeat the above steps for strongly interacting gases at different energies; Finally, we obtain both the entropy and energy for a strongly interacting Fermi gas.

In the following, I will first review the calculation of the entropy of the noninteracting ideal Fermi gas in an optical trap. Then, the determination of the entropy of a weakly interacting Fermi gas will be discussed in the second section.

5.1 Entropy for a Noninteracting Fermi Gas

I will first introduce the calculation of the entropy of a noninteracting ideal Fermi gas in a harmonic trap. Following this simple example, I will discuss the more complex situation for the entropy of a noninteracting Fermi gas in a Gaussian potential.

5.1.1 Entropy of a Noninteracting Fermi gas in a Harmonic Trap

Let us consider a 50:50 spin mixture of a noninteracting Fermi gas in a harmonic trap. The entropy per orbital is given by

$$s(\epsilon) = -k_B[f(\epsilon)\, lnf(\epsilon) + (1 - f(\epsilon))\, ln(1 - f(\epsilon))], \tag{5.4}$$

where $f(\epsilon, T)$ is the occupation number for a Fermi gas

$$f(\epsilon) = \frac{1}{\exp\left(\frac{\epsilon - \mu}{k_B\, T}\right) + 1}. \tag{5.5}$$

To calculate the dependence of the entropy on the cloud size, we need to go through five steps, which are listed below. The numerical calculation for each step is achieved by a Mathematica file listed in Appendix A

1. From the general theory of the Fermi statistics [75], the particle number distribution in energy basis $n(\epsilon, T)$ is determined by $n(\epsilon, T) = f(\epsilon, T) * g(\epsilon)$, where the density of states $g(\epsilon)$ for a harmonic trap is

$$g(\epsilon) = \frac{\epsilon^2}{2\, (\hbar\, \bar{\omega})^3}. \tag{5.6}$$

2. Integration of $n(\epsilon, T)$ is normalized to the atom number by

$$\frac{N}{2} = \int_0^\infty g(\epsilon) f(\epsilon)\, d\epsilon = \frac{1}{2(\hbar\bar{\omega})^3} \int_0^\infty \frac{\epsilon^2 d\epsilon}{\exp\left(\frac{\epsilon - \mu}{k_B\, T}\right) + 1}. \tag{5.7}$$

With the scaled energy and chemical potential $\epsilon' = \epsilon/E_F$ and $\mu' = \mu/E_F$,

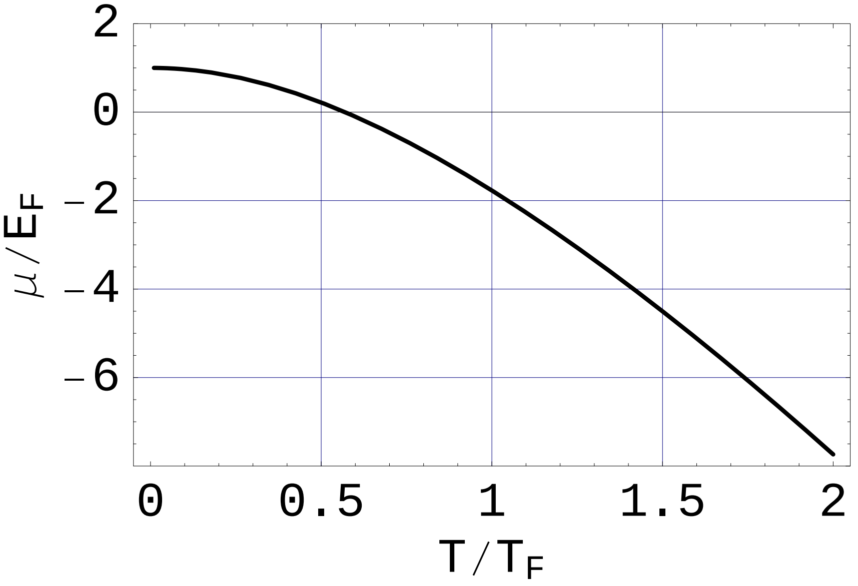

Figure 5.1: The chemical potential of the noninteracting gas in the harmonic trap versus the temperature.

and $T' = T/T_F$, Eq. (5.7) can be rewritten as

$$1 = 3\int_0^\infty \frac{\epsilon'^2 d\epsilon'}{\exp\left(\frac{\epsilon'-\mu'}{T'}\right)+1}, \tag{5.8}$$

which yields the chemical potential $\mu(T)$, shown in Fig. 5.1.

3. We obtain the entropy per particle $S_I(T)$ by integrating the entropy per orbital $s(\epsilon)$, and obtain

$$\begin{aligned} S_I(T) &= \frac{2}{N}\int_0^\infty g(\epsilon)\, s(\epsilon)\, d\epsilon \\ &= -3\, k_B \int_0^\infty d\epsilon'\, \epsilon'^2 \, \{f(\epsilon')\, ln\, f(\epsilon') \\ &\quad +(1-f(\epsilon'))\, ln(1-f(\epsilon')\}. \end{aligned} \tag{5.9}$$

The temperature dependence of the entropy per particle is shown in Fig. 5.2.

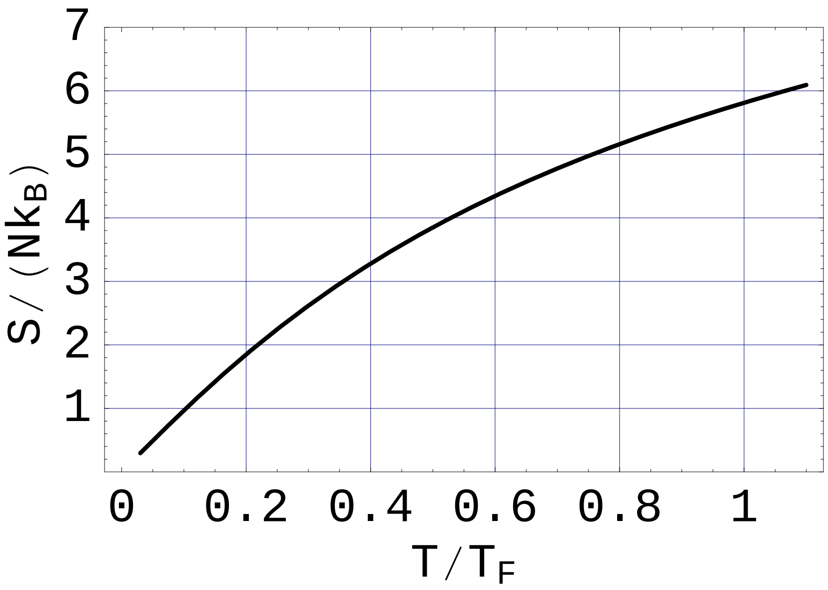

Figure 5.2: The entropy per particle of a noninteracting Fermi gas in a harmonic trap versus the temperature.

4. The energy $E_I(T)$ per particle is obtained by integrating $\epsilon f(\epsilon)$ with the density of states by

$$E_I(T) = \frac{2}{N}\int_0^\infty \epsilon\, g(\epsilon)\, f(\epsilon)\, d\epsilon = 3\, E_F \int_0^\infty \frac{\epsilon'^3 d\epsilon'}{\exp\left(\frac{\epsilon'-\mu'}{T'}\right)+1}. \tag{5.10}$$

   From the virial theorem, we know that the scale mean square size $\langle z^2(T)\rangle/z_F^2$ is equal to $E_I(T)/E_F$. The temperature dependence of $\langle z^2(T)\rangle/z_F^2$ is shown in Fig. 5.3.

5. Finally, the results of $S_I(T)$ and $\langle z^2(T)\rangle/z_F^2$ yield $S_I(\langle z^2(T)\rangle/z_F^2)$, which is shown in Fig. 5.4.

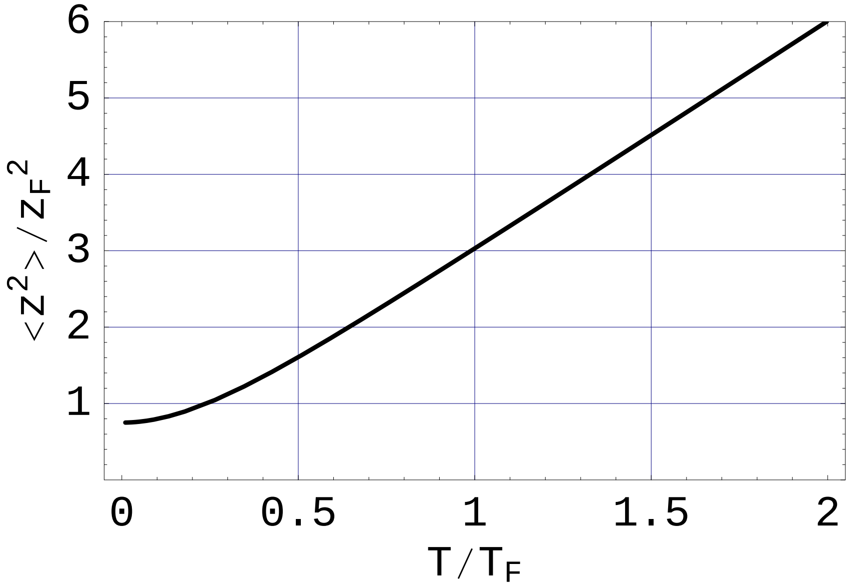

Figure 5.3: The mean square size of a noninteracting gas in a harmonic trap versus the temperature.

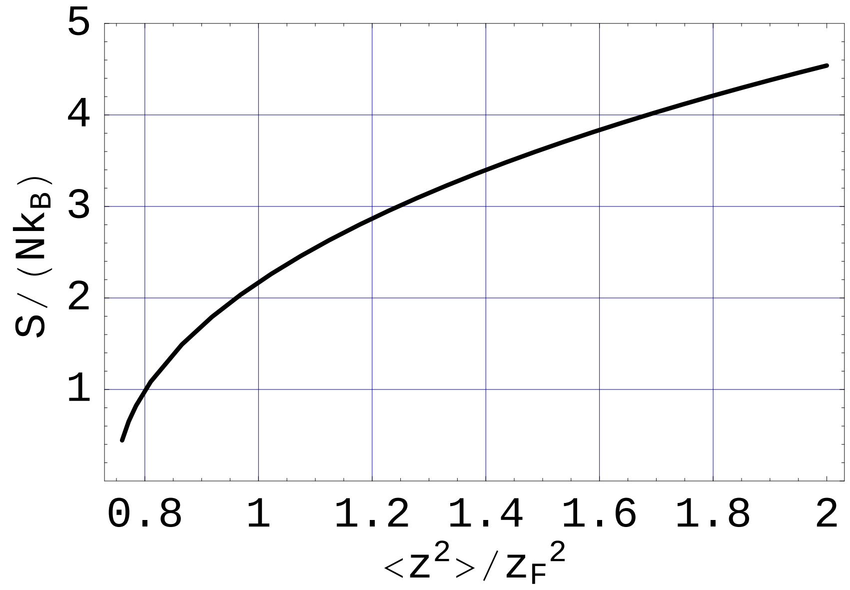

Figure 5.4: The entropy per particle of the noninteracting gas in the harmonic trap versus the mean square size.

5.1.2 Entropy of a Noninteracting Fermi gas in a Gaussian Trap

Now we will present the method of calculating the entropy of a noninteracting Fermi gas in a Gaussian trap. The main difference between the calculation for a harmonic trap and that for a Gaussian trap is the density of energy state $g(\epsilon)$. While the density of energy state in a harmonic trap is obtained directly from the well-known energy eigenstates in a harmonic potential, the function $G(E_1)$ in a Gaussian trap needs to be calculated based on the phase-space density $W(\mathbf{x},\mathbf{p})$ in the position-momentum space. Note that we use $G(E_1)$ for the density of state in a Gaussian trap to make it discrepant from that $g(\epsilon)$ for a harmonic trap.

Assuming the Gaussian potential is given by

$$U(x,y,z) = -U_0\,\exp\left(-\frac{x^2}{a^2}-\frac{y^2}{b^2}-\frac{z^2}{c^2}\right) = -U_0\,\exp\left(-{r'}^2\right), \tag{5.11}$$

where the r' is the effective raius with ${r'}^2 = {x'}^2+{y'}^2+{z'}^2$ and $x = x'a, y = y'b, z = z'c$.

The phase space density is given by

$$\begin{aligned} W(\mathbf{x},\mathbf{p}) &= \frac{1}{(2\pi\hbar)^3}\Theta[-H(\mathbf{x},\mathbf{p})]f[H(\mathbf{x},\mathbf{p})] \\ &= \frac{1}{(2\pi\hbar)^3}\int_{-U_0}^{0} dE_1\,\delta[E_1-H(\mathbf{x},\mathbf{p})]\,f(E_1), \end{aligned} \tag{5.12}$$

where $H(\mathbf{x},\mathbf{p})$ is the hamiltonian of the noninteracting gas in the Gaussian trap. Here we use the integration form of the definition of the Θ function.

The normalization of the particle density gives the total number of atoms by

$$\begin{aligned}\frac{N}{2} &= \int d^3\mathbf{x}\, d^3\mathbf{p}\, W(\mathbf{x}, \mathbf{p}) \\ &= \int_{-U_0}^{0} dE_1\, f(E_1) \int d^3\mathbf{x}\, d^3\mathbf{p}\, \frac{1}{(2\pi\hbar)^3}\delta[E_1 - H(\mathbf{x}, \mathbf{p})] \\ &= \int_{-U_0}^{0} dE_1\, f(E_1)\, G(E_1), \qquad (5.13)\end{aligned}$$

where the density of state in the Gaussian trap $G(E_1)$ is defined as

$$G(E_1) = \int d^3\mathbf{x} d^3\mathbf{p} \frac{1}{(2\pi\hbar)^3}\delta[E_1 - H(\mathbf{x}, \mathbf{p})]. \qquad (5.14)$$

From the particle density in the phase space, we also can obtain the mean square size of the cloud $\langle z^2 \rangle$ given by

$$\begin{aligned}\frac{N}{2}\langle z^2 \rangle &= \int d^3\mathbf{x}\, d^3\mathbf{p}\, W(\mathbf{x}, \mathbf{p})\, z^2 \\ &= \int_{-U_0}^{0} dE_1\, f(E_1) \int d^3\mathbf{x} d^3\mathbf{p} \frac{z^2}{(2\pi\hbar)^3}\delta[E_1 - H(\mathbf{x}, \mathbf{p})] \\ &= \int_{-U_0}^{0} dE_1\, f(E_1)\, I(E_1), \qquad (5.15)\end{aligned}$$

where the integral for the mean square size $I(E_1)$ is defined as

$$I(E_1) = \int d^3\mathbf{x}\, d^3\mathbf{p}\, \frac{z^2}{(2\pi\hbar)^3}\delta[E_1 - H(\mathbf{x}, \mathbf{p})]. \qquad (5.16)$$

Using $H(\mathbf{x}, \mathbf{p}) = \frac{\mathbf{p}^2}{2m} + U(\mathbf{x})$ in Eq. (5.14) and Eq. (5.16), we have the following result for the integration in momentum space

$$\int d^3\mathbf{p}\, \delta[E_1 - \frac{\mathbf{p}^2}{2m} - U(\mathbf{x})] = 2\pi(2m)^{3/2} \sqrt{E_1 - U(\mathbf{x})}\, \Theta[E_1 - U(\mathbf{x})]. \qquad (5.17)$$

Then by using the above relation in $G(E_1)$ and $I(E_1)$, we get

$$G(E_1) = \frac{2\pi(2m)^{3/2}}{(2\pi\hbar)^3} \int_{U\leq E} d^3\mathbf{x}\sqrt{E_1 - U(\mathbf{x})}, \tag{5.18}$$

$$I(E_1) = \frac{2\pi(2m)^{3/2}}{(2\pi\hbar)^3} \int_{U\leq E} d^3\mathbf{x} z^2 \sqrt{E_1 - U(\mathbf{x})}. \tag{5.19}$$

We note that the symmetric effective potential shown in Eq. (5.11) is redefined by the energy scale $\varepsilon = \frac{E_1+U_0}{U_0}$, which gives the energy relative to the trap bottom. After some algebra, we evaluate Eq. (5.18) and show that the density state $G(E_1)$ in the Gaussian trap differs with the density state in the harmonic trap $g(\epsilon)$ (see Eq. (5.6)) by a factor $g_0(\varepsilon)$, which is given by

$$g_0(\varepsilon) = \frac{16}{\pi} \int_0^1 du\, u^2 \sqrt{(1-\varepsilon)^{u^2} - (1-\varepsilon)}\, \frac{[-ln(1-\varepsilon)]^{3/2}}{\varepsilon^2}. \tag{5.20}$$

I plot $g_0(\varepsilon)$ as a function of $\varepsilon = \frac{E_1+U_0}{U_0}$ in Fig. 5.5.

Now we can do the next steps of the calculation, which are similar with step 2 and step 3 for calculating the entropy in the harmonic trap (see Section 5.1.1). We only need to modify the formula for the harmonic trap by replacing the density of state $g(\epsilon/E_F)$ in a harmonic trap with that for a Gaussian trap $g_0(\varepsilon)g(\epsilon') = g_0(\frac{E_F}{U_0}\epsilon')g(\epsilon')$, where $\epsilon' = \frac{E_1+U_0}{E_F}$ is the energy related to the trap bottom scaled by the Fermi energy.

Similar with Eq. (5.8), we have the normalization for generating the chemical potential $\mu'(T')$

$$1 = 3\int_0^{\frac{U_0}{E_F}} \frac{g_0(\frac{E_F}{U_0}\epsilon')\, \epsilon'^2\, d\epsilon'}{\exp\left(\frac{\epsilon'-\mu'}{T'}\right)+1}, \tag{5.21}$$

where $T' = T/T_F$, and $\mu' = \frac{\mu+U_0}{E_F}$ is the chemical potential relative to the trap

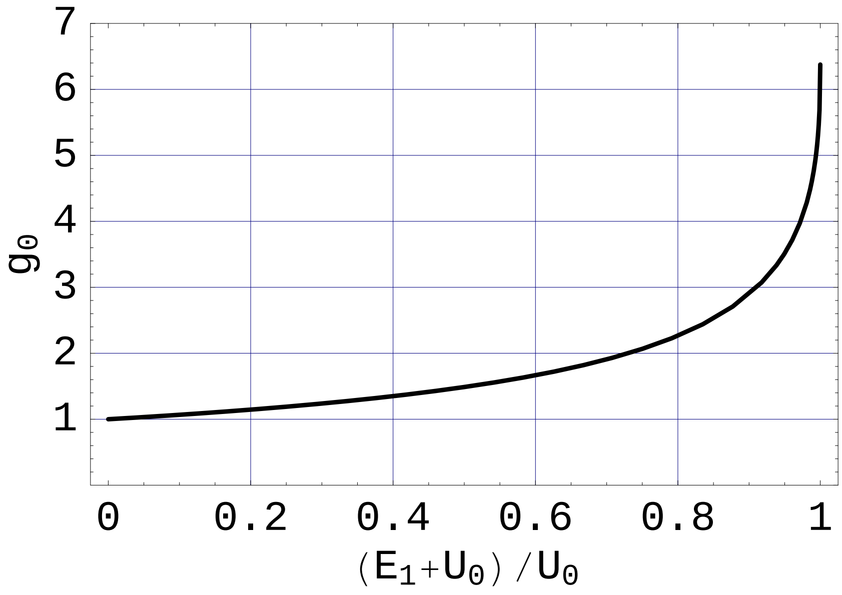

Figure 5.5: The ratio of the density state in a Gaussian trap to that in a harmonic trap g_0 versus the energy relative to the bottom of a Gaussian trap.

bottom. As an example, I plot the chemical potential $\mu'(T/T_F)$ in a Gaussian trap for $\frac{U_0}{E_F} = 10$ in Fig. 5.6.

The entropy per particle of a noninteracting Fermi gas $S_{GI}(T)$ in a Gaussian trap is obtained by adding the factor $g_0(\frac{E_F}{U_0}\epsilon')$ into Eq. (5.9), which generates

$$S_{GI}(T) = -3\,k_B \int_0^{\frac{U_0}{E_F}} d\epsilon'\, g_0(\frac{E_F}{U_0}\epsilon')\,\epsilon'^2\,\{f(\epsilon')\,lnf(\epsilon') + (1-f(\epsilon'))\,ln(1-f(\epsilon')\}. \tag{5.22}$$

The numerical result of the entropy per particle for a $\frac{U_0}{E_F} = 10$ is shown in Fig. 5.7, where $\frac{U_0}{E_F} = 10$ is close to the value of Gaussian traps used in our experiments.

The following step is to calculate the temperature dependence of the mean square size in a Gaussian trap. Here we calculate the integration of Eq. (5.15) and Eq. (5.19). Here we will use the scaled potential $\epsilon' = \frac{E_1+U_0}{E_F}$. After some

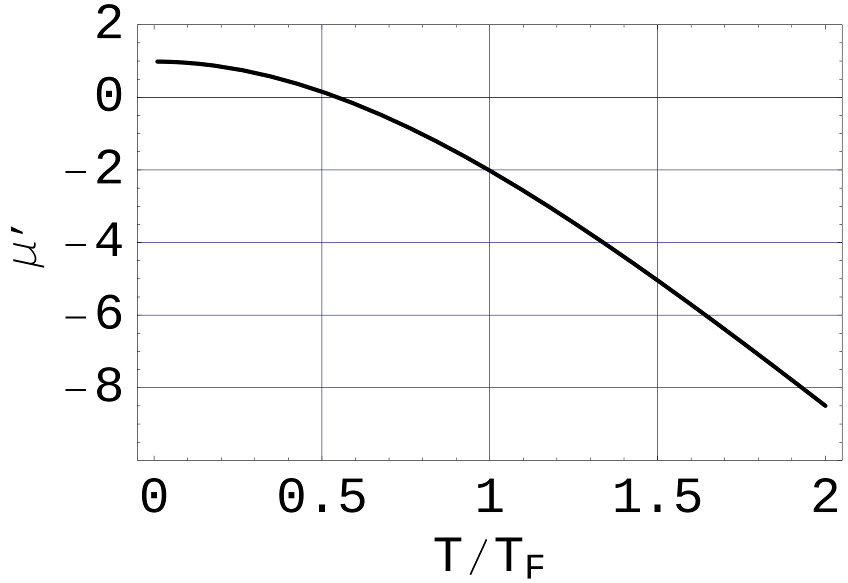

Figure 5.6: The chemical potential of a noninteracting gas in the Gaussian trap of $\frac{U_0}{E_F} = 10$ versus temperature. $\mu' = \frac{\mu + U_0}{E_F}$ is the chemical potential relative to the trap bottom.

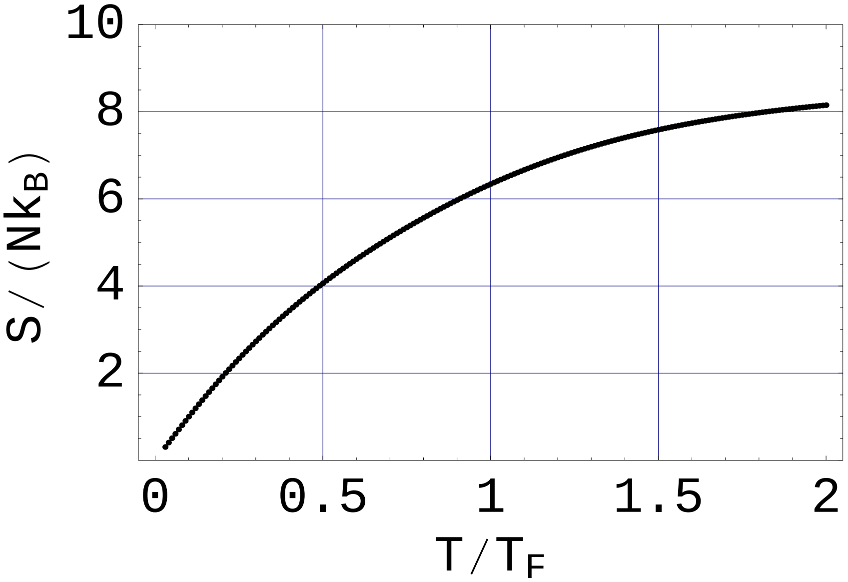

Figure 5.7: The entropy per particle of the noninteracting gas in the Gaussian trap for $\frac{U_0}{E_F} = 10$.

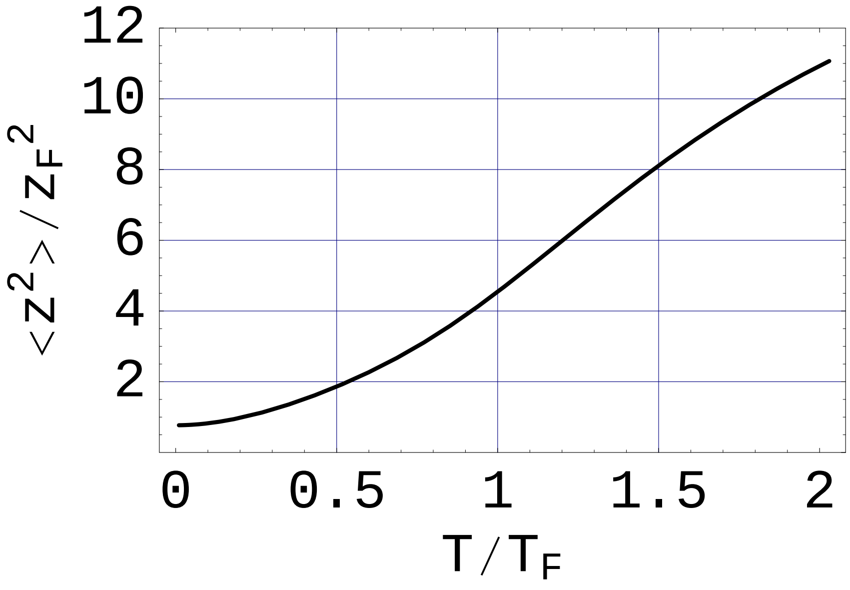

Figure 5.8: The mean square size of a noninteracting gas versus temperature in a Gaussian trap of $\frac{U_0}{E_F} = 10$. Note that $z_F^2 = \sigma_z^2/6$ is the mean square size of the Fermi energy as we defined in Eq. (4.52).

algebra, the means square size is given by

$$\langle z^2 \rangle = \frac{\sigma_z^2}{2} \int_0^{\frac{U_0}{E_F}} \frac{g_2(\frac{E_F}{U_0}\epsilon')\,\epsilon'^3\,d\epsilon'}{\exp\left(\frac{\epsilon'-\mu'}{T'}\right)+1}, \tag{5.23}$$

where $\sigma_z^2 = E_F\,c^2/U_0$ is the Fermi radius in the ẑ direction for a Gaussian trap. The function of $g_2(\varepsilon)$ is given by

$$g_2(\varepsilon) = \frac{32}{\pi} \int_0^1 du\, u^4\, \sqrt{(1-\varepsilon)^{u^2} - (1-\varepsilon)}\, \frac{[-ln(1-\varepsilon)]^{5/2}}{\varepsilon^3}. \tag{5.24}$$

The numerical result for the mean square size for a $\frac{U_0}{E_F} = 10$ Gaussian trap is shown in Fig. 5.8.

In the end, the results of $S_{GI}(T)$ and $\langle z^2(T)\rangle/z_F^2$ yield $S_{GI}(\langle z^2\rangle/z_F^2)$ for a Gaussian trap, which is shown in Fig. 5.9. The numerical calculations of the

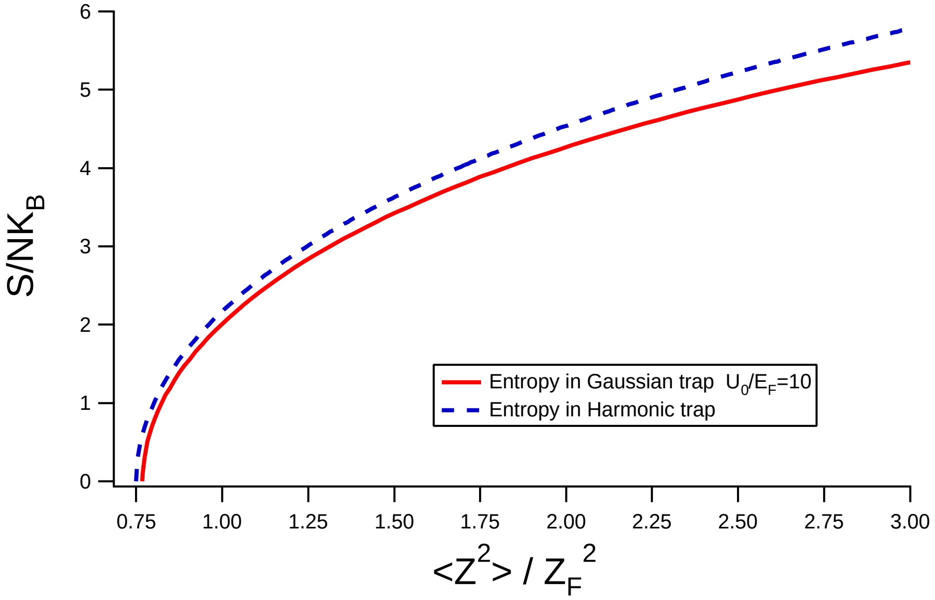

Figure 5.9: The entropy per particle of the noninteracting gas in the Gaussian trap versus the mean square size. The Gaussian trap depth have $\frac{U_0}{E_F} = 10$.

thermodynamic properties of a noninteracting Fermi gas in a Gaussian trap are operated by a Mathematica file included in Appendix A.

This entropy-size relation will be used to extract the entropy of a weakly interacting Fermi gas from its measurable mean square size in a Gaussian trap. There is only one more step we need to complete this calculation. That is a shift of the origin of the entropy-size curve due to the finite mean field interactions in a weakly interacting Fermi gas in 1200 G. The mean field correction of the ground state cloud size will be discussed in details in the next section.

5.2 Entropy Calculation for a Weakly Interacting Fermi Gas

Our method to obtain the entropy from the mean square cloud size $\langle z^2\rangle_{1200}$ at 1200 gauss depends on a precise calculation of the dependence of the entropy on $\langle z^2\rangle_{1200}$ in a Gaussian trapping potential. The gas at 1200 G is a weakly interacting Fermi gas with $k_F a_S = -0.75$. We obtain the entropy of a weakly interacting gas $S_{WI}(\langle z^2\rangle_{1200} - \langle z^2\rangle_0)$ from a many-body prediction [76] and a quantum Monte Carlo simulation [77] at $k_F a_S = -0.75$, where $\langle z^2\rangle_0$ is the ground state size of a weakly-interacting Fermi gas at 1200 gauss that automatically includes the mean field energy shift due to the weak interactions. We also calculate $S_I(\langle z^2\rangle_{1200} - \langle z^2\rangle_{I0})$ by assuming a noninteracting Fermi gas in a Gaussian trapping potential, where $\langle z^2\rangle_{I0}$ is the ground state size of an ideal gas. We find that the ideal Fermi gas $S_I(\langle z^2\rangle_{1200} - \langle z^2\rangle_{I0})$ differs from $S_{WI}(\langle z^2\rangle_{1200} - \langle z^2\rangle_0)$ by less than 1% over the range of energies we studied, except the region near the lowest measured energy, where they differ by 10%. From the above comparison, we conclude that the *shape* of the entropy versus cloud size curve at 1200 G is nearly identical to that for an ideal gas. Measurements of $\langle z^2\rangle_{1200}$ therefore provide an essentially model-independent estimate of the entropy of the strongly interacting gas. The only required correction is to determine the ground state size $\langle z^2\rangle_0$ at 1200 G, which is shifted from the ideal gas value to the weakly interacting gas value due to the mean field interaction. So we can use $S_I(\langle z^2\rangle_{1200} - \langle z^2\rangle_0)$ to extract entropy of a weakly interacting Fermi gas.

In this section, I will show the comparison between the entropy curve of a weakly interacting Fermi gas and that of a noninteracting Fermi gas first. Then

I will describe how to determine the ground state mean square size shift.

5.2.1 Comparison of the Entropy between a Weakly Interacting Gas and a Noninteracting Gas

Now we will consider the entropy at 1200 G, where $a_S = -2900$ bohr [62] and $k_F a_S = -0.75$ in our case. At this field, we observed ballistic expansion of the cloud even at our lowest temperatures, which indicates that the gas is still in the normal state. For this weakly interacting normal Fermi gas, a many-body calculation or a quantum Monte Carlo simulation can provide a entropy-mean square size curve, which is precise enough to judge the validity of using the entropy-mean square size curve of a noninteracting Fermi gas to determine the entropy of a weakly interacting gas at $k_F a_S = -0.75$.

The group in Chicago University, Qijin Chen and Kathy Levin, provided us with a pseudogap calculation of the entropy versus the mean square size for a weakly interacting Fermi gas in a Gaussian trap. Also the group in University of Washington, Aurel Bulgac and Joaquín Drut, provided us their quantum Monte Carlo simulation. We make a comparison between these theoretical results with our calculated entropy $S_{GI}(\langle z^2\rangle/z_F^2)$ of a noninteracting Fermi gas in a Gaussian trap in Fig. 5.10.

From Fig. 5.10, we find that the ideal gas entropy-size curve almost has the same shape as the weakly interacting Fermi gas curve except that its origin is different with that of the weakly interacting gas. This origin shift is expected because the interaction energy induces a small reduction of the ground state cloud size. At 1200 G, the mean field interaction energy is attractive so the mean square size decreases.

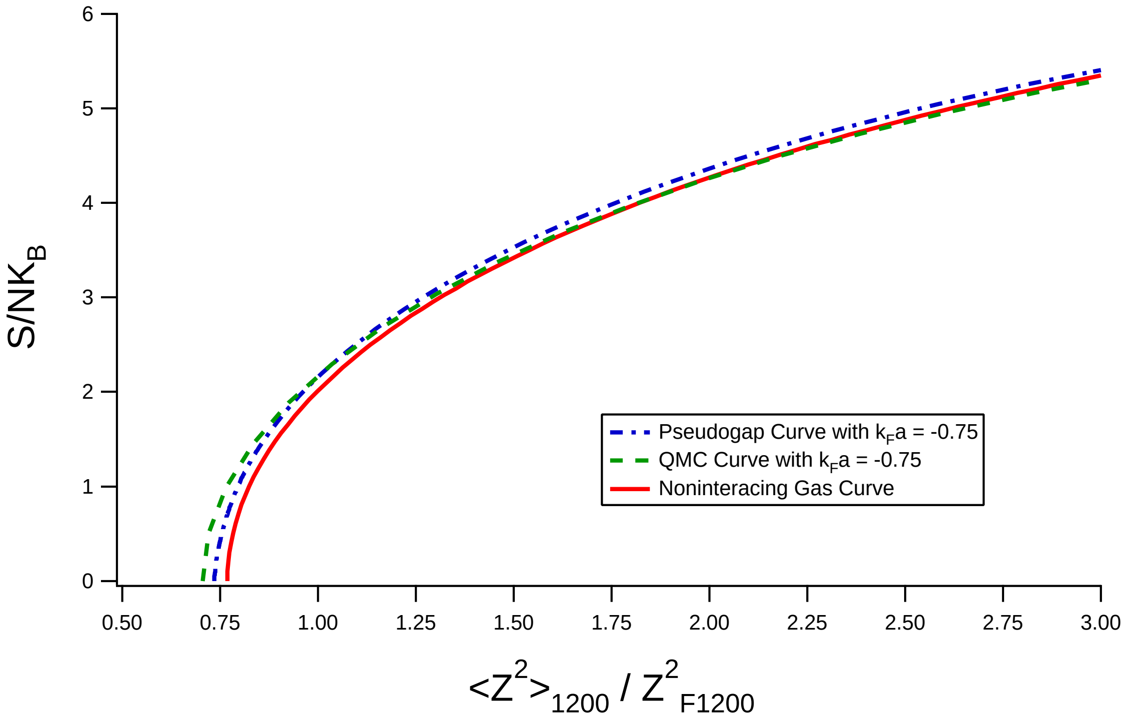

Figure 5.10: The weakly interacting case and noninteracting case of the entropy versus the mean square size. The Gaussian trap depth for all the calculation is $\frac{U_0}{E_F} = 10$.

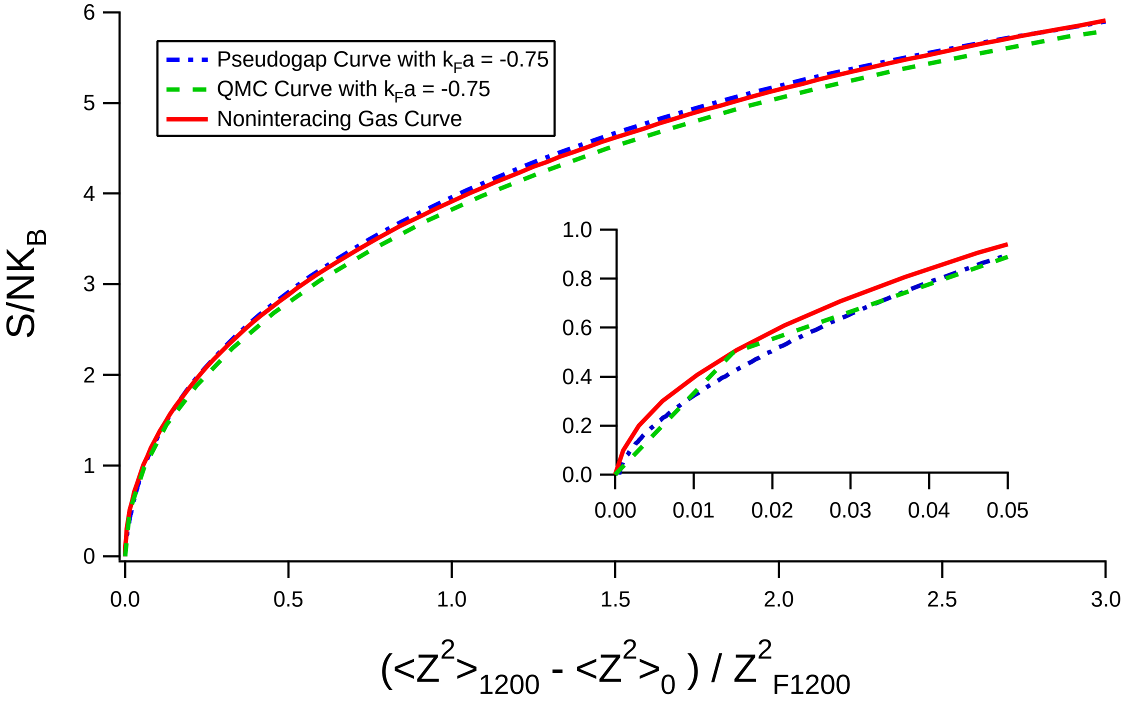

Figure 5.11: Entropy curve comparison between a weakly interacting gas and a noninteracting gas by overlapping at the origin. The Gaussian trap depth for all the calculation is $\frac{U_0}{E_F} = 10$. Note that for a weakly interacting gas, $\langle z^2 \rangle_0$ is the calculated ground cloud size for each theory which includes the mean field energy, while for noninteracting case $\langle z^2 \rangle_0$ is the unshifted value for a ideal Fermi gas.

To show this comparison more clearly, we shift the origins of all the three calculation to let them overlap, which is shown in Fig. 5.11. From this figure, we find $S_{GI}(\langle z^2\rangle)$ curve differers from the many-body prediction and the quantum Monte Carlo simulation by less than 1% over almost all the range we studied $(\langle z^2\rangle - \langle z^2\rangle_0)/z_F^2 < 3$. The only exception happens in the range of $(\langle z^2\rangle - \langle z^2\rangle_0)/z_F^2 < 0.05$, where the weakly interacting calculation and the noninteracting calculation have about 10% difference in the entropy. For such low energy, we only have one data point in our measurement of the entropy, so this effect has almost negligible effects on the measurement and data analysis. Hence, we could draw a conclusion that measurements of $\langle z^2\rangle_{1200}$ therefore provide an essentially model-independent determination of the entropy of a strongly interacting gas by using an adiabatically magnetic sweep.

5.2.2 The Ground State Mean Square Size Shift

From the discussion of the entropy curves in the last subsection, we know that the entropy curve of a weakly interacting Fermi gas almost has the same shape as that of a noninteracting Fermi gas. However, at the zero entropy point, which is the origin of the entropy curve, the ground state mean square sizes have different values for the weakly interacting case and the noninteracting case. In this subsection, I will describe how we determine the ground state mean square size at 1200 G, which is a necessary step to convert our mean square size data at 1200 G to the entropy data.

The determination of the ground state mean square size of a weakly interacting Fermi gas in a Gaussian trap requires three steps: First, we need to know the $k_F\,a$ dependence of the local chemical potential $\mu(n, k_F\,a)$, where k_F is defined as the Fermi wave number of a noninteracting Fermi gas. The interaction strength presented by $k_F\, a$ modifies the value of the local chemical potential. Second, inverting the function of $\mu(n, k_F\, a)$, we can determine the local density $n(\mu, k_F\, a)$ from μ and $k_F\, a$. Finally, using $\mu = \mu_g - U_G$, we obtain the density in a Gaussian potential U_G, where μ_g represents the global chemical potential.

After these three steps, we obtain the mean square size of a weakly interacting Fermi gas by using the same methods to obtain the mean square size of a noninteracting gas in Gaussian trap (see Section 5.1.2). We integrate $n(\mu, k_F\, a)$ over the whole trap for the normalization to the total atom number, which yields the global chemical potential μ_g. Then the mean square size $\langle r^2 \rangle$ is calculated by evaluating the quantity $r^2 n(\mu, k_F\, a)$ throughout the trap. Here r^2 is the square of radius for an effective Gaussian potential $U_G(\mathbf{r}) = U_0 - U_0\, exp(-\frac{m\bar{\omega}^2 r^2}{2U_0})$.

The first step, determining $k_F\, a$ dependence of the local chemical potential μ, is done by applying a mean field model of a weakly interacting Fermi gas in the BEC-BCS crossover. The model was conceived by Chin in [78]. Readers should review this paper to get the details of the model. In this thesis, I employ this model and write a Mathematica program to operate the calculation of the ground state size of a weakly interacting Fermi gas. The program is shown in Appendix A. From this model, we obtain the ground state chemical potential of an atom pair $\mu_p = 2\mu$ in a uniform Fermi gas versus the interacting parameter $k_F\, a$. The result is shown in Fig. 5.12.

For the second step, we invert the curve shown in Fig. 5.12 to obtain $n(\mu, k_F\, a)$. The local chemical potential for a weakly interacting gas in a 50-50 mix of $|1\rangle$

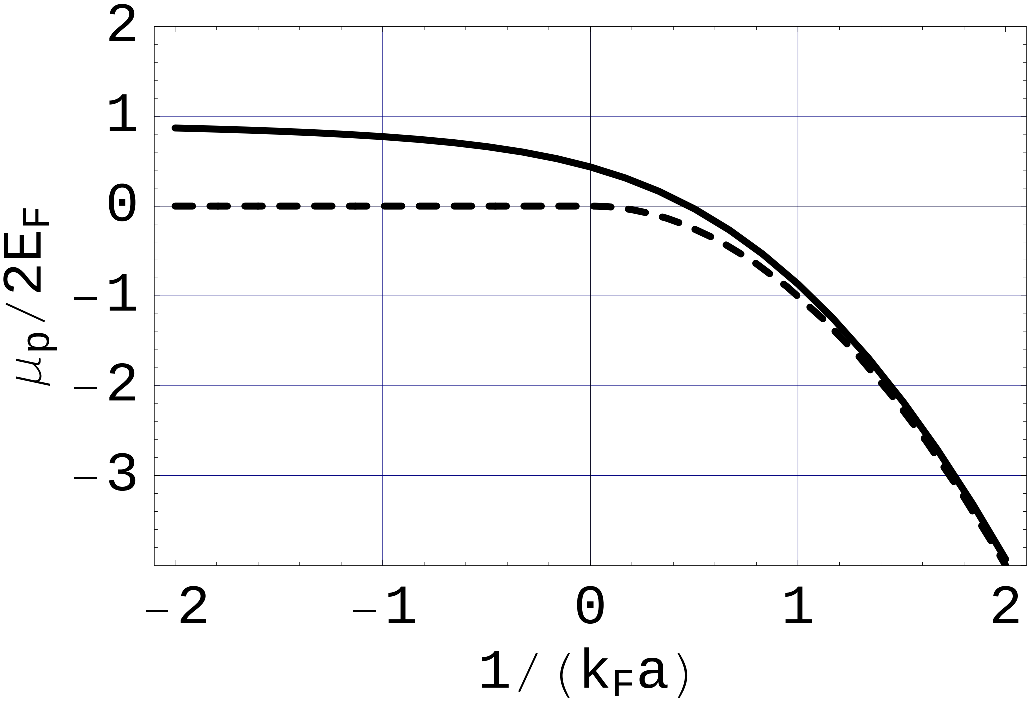

Figure 5.12: The solid line is the chemical potential of an atom pair in a uniform Fermi gas versus the interacting parameter $k_F\, a$. The dash line is the binding energy of the molecules. We can see the chemical potential approach $2E_F$ in the BCS limit, where $1/(k_F\, a) \ll 0$. This result is expected since the chemical potential μ_p here refers to a pair of atoms. In the BEC limit where $1/(k_F\, a) \gg 0$, the chemical potential approaches the binding energy of the real molecules because there are only tightly bind molecules existing in this region.

and $|2\rangle$ is given by

$$\mu(n) = \epsilon_{FW}(n)\, F[\frac{1}{k_{FW}\, a}] = \frac{\hbar^2 (6\pi^2 n)^{2/3}}{2m}\, F[\frac{1}{k_{FW}\, a}] = \frac{\hbar^2 k_{FW}^2}{2m}\, F[\frac{1}{k_{FW}\, a}], \quad (5.25)$$

where k_{FW} and ϵ_{FW} represents the local Fermi wavevector and local Fermi energy of a weakly interacting Fermi gas. Note that we use $k_F = (6\pi^2 n_{0I})^{2/3}$ and $E_F = \frac{\hbar^2 k_F^2}{2m}$ for the Fermi wavevector and the Fermi energy of a noninteracting Fermi gas in the center of the trap, where n_{0I} is the single spin density of an ideal Fermi gas in the center of a trap. $F[\frac{1}{k_{FW}\, a}]$ is the correction function of the chemical potential due to finite interactions. There is very subtle point here. In principle, the function of $F[\frac{1}{k_{FW}\, a}] = \mu(n)/\epsilon_{FW}(n)$ is not exactly μ/E_F that we obtain in Fig. 5.12, because the density n changes from a noninteracting value to a weakly interacting value. However, for a weakly interacting Fermi gas such as $k_F\, a = -0.75$, the cloud density is just slightly perturbed by the interaction so that we can treat μ/ϵ_{FW} and μ/E_F equal.

For the third step, we use the scaled chemical potential μ/E_F to rewrite Eq. (5.25), and obtain the scaled chemical potential by

$$\begin{aligned} \frac{\mu}{E_F} &= \frac{k_{FW}^2}{k_F^2}\, F\left[\frac{1}{k_F\, a}\,\frac{k_F}{k_{FW}}\right] && (5.26) \\ &= \left(\frac{n}{n_{0I}}\right)^{2/3} F\left[\frac{1}{k_F\, a}\,\left(\frac{n_{0I}}{n}\right)^{1/3}\right]. && (5.27) \end{aligned}$$

By inverting Eq. (5.26) using the numerical $\mu \sim 1/(k_F\, a)$ curve shown in Fig. 5.12, we show n/n_{0I} versus μ/E_F for a weakly interacting Fermi gas with $k_F\, a = -0.75$ in Fig. 5.13.

By using the global chemical potential μ_g, we get $\mu = \mu_g - U(r)$, where

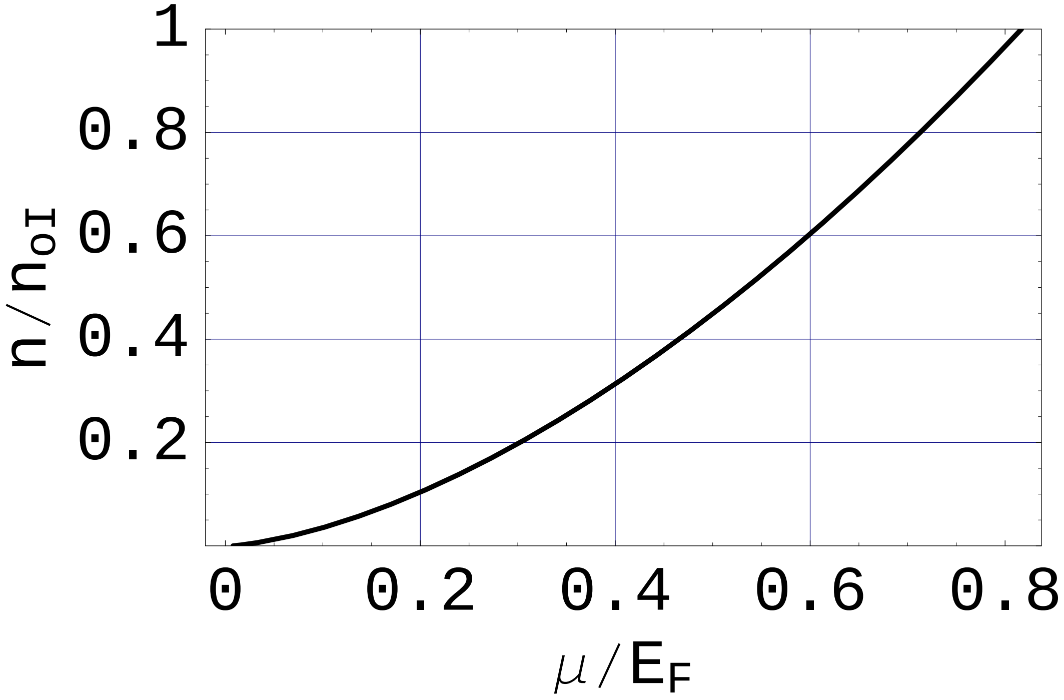

Figure 5.13: The atom density ratio between a weakly interacting Fermi gas and a noninteracting Fermi gas versus the local chemical potential, where $k_F\,a = -0.75$ for the weakly interacting Fermi gas.

$U(r) = U_0(1 - e^{-\frac{E_F}{U_0}\frac{r^2}{\sigma^2}})$ is a Gaussian trap potential and σ is the effective Fermi radius defined before. The global chemical potential is determined by the the normalization of the total atom number

$$\frac{1}{n_{0I}}\frac{N}{2} = \int d^3\mathbf{r}\frac{n}{n_{0I}}\left[\frac{\mu_g - U(r)}{E_F}\right]\Theta\left[\frac{\mu_g - U(r)}{E_F}\right], \tag{5.28}$$

where $\mu_g - U(r) > 0$ for a weakly interacting Fermi gas in the BCS side with $k_F\, a < 0$, which restricts the maximum integration range $\mathbf{r}$. After some algebra, Eq. (5.28) is rewritten as

$$\begin{aligned} 1 &= \frac{32}{\pi}\int_0^{q_{max}} dq\, q^2\,\frac{n}{n_{0I}}\,[\mu_s]\,\Theta\,[\mu_s]\,, \\ \mu_s &= \frac{\mu_g}{E_F} - \frac{U_0}{E_F}\left(1 - e^{-\frac{E_F}{U_0}q^2}\right), \end{aligned} \tag{5.29}$$

where $q = r/\sigma$, and q_{max} is determined by $\mu_s = 0$.

By using Eq. (5.29) to find the global chemical potential, we calculate the mean square size in the $\hat{\mathbf{z}}$ direction, which is given by

$$\frac{\langle z^2\rangle_0}{\langle z_F^2\rangle} = 2\langle q^2\rangle = \frac{64}{\pi}\int_0^{q_{max}} dq\, q^4\;[\mu_s]\,\Theta\,[\mu_s]\,. \tag{5.30}$$

Finally, I show the result of the dependence of the mean square size $\langle z^2\rangle_0$ on $1/(k_F\, a)$ in the BCS region of $k_F\, a < 0$ for both a harmonic trap and a Gaussian trap in Fig. 5.14.

For the case of our experiment $k_F\, a = -0.75$ at 1200 G, we find this mean field calculation gives $\langle z^2\rangle_0/z_F^2 = 0.69$. In experiment, we determine σ_z and T/T_F by fitting the spatial profiles at the lowest temperatures with a Sommerfeld approximation for the density [79]. We obtain $\langle z^2\rangle_0/z_F^2 = 0.71(0.02)$. The theoretical

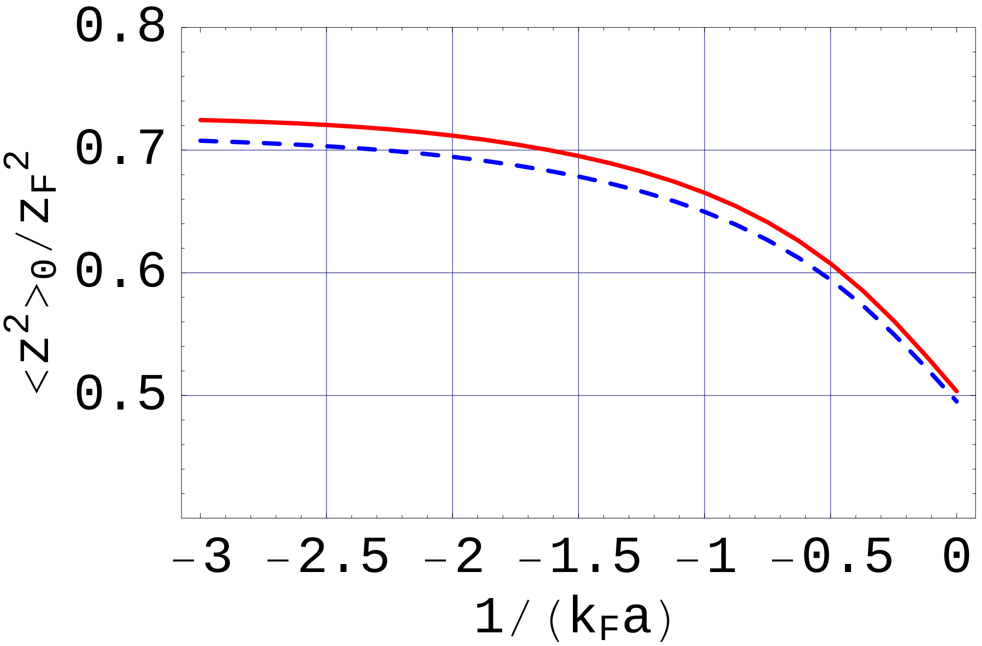

Figure 5.14: The ground state mean square size $\langle z^2 \rangle_0$ in the BCS region $1/(k_F\, a) < 0$ versus the interaction parameter $1/(k_F\, a)$. The dash line is calculated by an effective symmetric harmonic trap $U_{HO}(\mathbf{r}) = m\bar{\omega}^2 r^2/2$ and the sold line is calculated by an effective symmetric Gaussian trap $U_G(\mathbf{r}) = U_0 - U_0\, Exp(-\frac{m\bar{\omega}^2 r^2}{2U_0})$ with $U_0/E_F = 10$.

and experimental results are in very good agreement. This gives us confidence in using the measured lowest value $\langle z^2 \rangle_0 / z_F^2 = 0.71$ as the mean square size of the ground state cloud at 1200 G. This point works as the origin (the zero entropy point) for the shifted entropy curves shown in Fig. 5.11.

Chapter 6

Model-independent Thermodynamic Measurements in a Strongly Interacting Fermi Gas

Thermodynamic measurements play an important role to understand the physics of a macroscopic system. Here I follow the formalism developed by Callen [80] to explain the importance. In the case of a macroscopic system with large number of particles, the reproducible properties of the equilibrium state of this system is only characterized by a specification of variables that could have determined values. Such variables are called macrovariables $(X_0, X_1, ..., X_t)$. Usually the primary macrovariable is the total energy E with the convention that $X_0 = E$. Other variables for the particles are called microvariables, which are not directly measurable. In an equilibrium state, all the microvariables are random. To quantify the randomness of microvariables, the entropy S represents the amount of missing information. All possible thermodynamic information about a system is contained in the fundamental equation of entropy as

$$S = S(E, X_1, ..., X_t). \tag{6.1}$$

From the above statement, we can see that the primary thermodynamics is determined by the dependence of entropy on the macrovariables. In the research presented in this dissertation, we focused on the dependence of the entropy on the energy in a strongly interacting Fermi gas at the unitary limit. This ensures that we can implement model-independent thermodynamic measurements, which can be used to determine most of the important thermodynamic properties of a unitary strongly interacting Fermi system.

In the last two chapters, I already introduced the methods of measuring both the energy and entropy in a strongly interacting Fermi gas. Here I will summarize the procedure: Create a unitary Fermi gas in the strongly interacting regime; Measure the mean square size of the cloud in the strongly interacting regime to determine the total energy of the cloud; Create an identical cloud in the strongly interacting regime and adiabatically sweep the magnetic field to the weakly interacting regime; Measure the mean square size of the weakly interacting cloud to determine the entropy; Repeat the above steps for the clouds with different energies; Finally we obtain the energy-entropy curve for a strongly interacting Fermi gas.

The entropy is postulated to be a continuous and differentiable function, which can be inverted uniquely to give

$$E \equiv X_0 = E(S, X_1, ..., X_t). \tag{6.2}$$

From the fundamental relations between the entropy and energy, the temperature of the system can be readily determined by

$$T = \frac{\partial E}{\partial S}. \tag{6.3}$$

Other parameters like the chemical potential μ, the free energy F and the heat capacity C in a uniform system also can be determined from the fundamental thermodynamic relations given by

$$E = T\,S + \mu\,n - P, \tag{6.4}$$

$$F = E - TS, \tag{6.5}$$

$$C = \frac{dE}{dT}, \tag{6.6}$$

where n is the particle density, P is the pressure, μ is the chemical potential, E and S are the total energy and entropy.

In the following section, I will first describe our experimental measurement. Then I will show our measured data of energy-entropy curve. The behavior of the measured energy-entropy curve shows a clear thermodynamic signature of a superfluid-normal fluid transition in a strongly interacting Fermi gas. I will discuss how to parameterize the data to extract the critical parameters for this phase transition. After that, I will describe how to use the energy-entropy data to extract other thermodynamic properties. In the end, I will use our measurement as a benchmark to test the current strong coupling many-body quantum theories and simulations.

6.1 Preparing Strongly Interacting Fermi Gases at Different Energies

A strongly interacting Fermi gas is prepared using a 50:50 mixture of the two lowest hyperfine states of ^{6}Li atoms in an ultrastable CO_2 laser trap with a bias magnetic field of 840 G, just above a broad Feshbach resonance at $B = 834$ G [62]. At 840 G, the gas is cooled to quantum degeneracy by lowering the trap depth U [12]. Then U is recompressed to $U_0/k_B = 10\,\mu$K, which is large compared to the energy per particle of the gas.

At the final trap depth U_0, the measured trap oscillation frequencies in the transverse directions are $\omega_x = 2\pi \times 665(2)$ Hz and $\omega_y = 2\pi \times 764(2)$ Hz, while the axial frequency is $\omega_z = 2\pi \times 30.1(0.1)$ Hz at 840 G and $\omega_z = 2\pi \times 33.2(0.1)$ Hz at 1200 G. Note that axial frequencies differ due to the small change in the trapping potential arising from the bias magnetic field curvature. The total number of atoms $N \simeq 1.3(0.2) \times 10^5$ is obtained from absorption images of the cloud using a two-level optical transition at 840 G. The corresponding Fermi energy E_F and Fermi temperature T_F for an ideal (noninteracting) harmonically trapped gas at the trap center are $E_F = k_B T_F \equiv \hbar\bar{\omega}(3N)^{1/3}$, where $\bar{\omega} = (\omega_x\omega_y\omega_z)^{1/3}$. For our trap conditions, we obtain $T_F \simeq 1.0\,\mu$K.

To measure the entropy as a function of the energy, we start with an energy near the ground state and controllably increase the energy of the gas by releasing the cloud for an adjustable time and then recapturing it. This method is described in our previous study of the heat capacity [45]. We abruptly release the cloud and then recapture it after a short expansion time t_{heat}. During the expansion time, the total kinetic and interaction energy is conserved. When the trapping potential

$U(\mathbf{x})$ is reinstated, the potential energy of the expanded gas is larger than that of the initially trapped gas, which increases the total energy of the cloud. By choosing different heating kick times, we add different energies into the cloud in a controllable way. The amount of added energy can be precisely calculated. The calculation method is based on the hydrodynamic expansion of the cloud and can be found in [64]. In my dissertation, we use the virial theorem to determine the energy, so we don't need to rely on the theoretical calculation. After recapture, the gas is allowed to reach equilibrium for 0.7 s. This thermalization time is omitted for the measurement of the ground state size, where no energy is added.

After equilibrium is established, the magnetic field is either ramped to 1200 G over a period of 1 s, or the gas is held at 840 G for 1 s. In either case, after 1 s, the gas is released from the optical trap for a short time to increase the transverse dimension of the cloud for imaging, without significantly changing (less than 0.5%) the measured axial ($\hat{\text{z}}$ direction)cloud sizes. Those axial cloud sizes are used to determine S at 1200 G and E at 840 G respectively.

For our shallow trap, we find that there is a magnetic field and energy independent heating rate, which causes the mean square size to slowly increase at a rate of $\dot{\langle z^2\rangle} = 0.024\, z_F^2/s$, corresponding to 24 nK/s in energy units. Since we desire the energy and entropy just after equilibration, we subtract $\dot{\langle z^2\rangle} \times \Delta t$ from the measured mean square axial sizes for both the 840 G and 1200 G data by

$$\frac{\langle z^2(0)\rangle}{z_F^2} = \frac{\langle z^2(\Delta t)\rangle}{z_F^2} - \Delta t \frac{\dot{\langle z^2\rangle}}{z_F^2}, \tag{6.7}$$

where Δt= 1 second. The maximum correction is 5% for the smallest could size at the lowest energy.

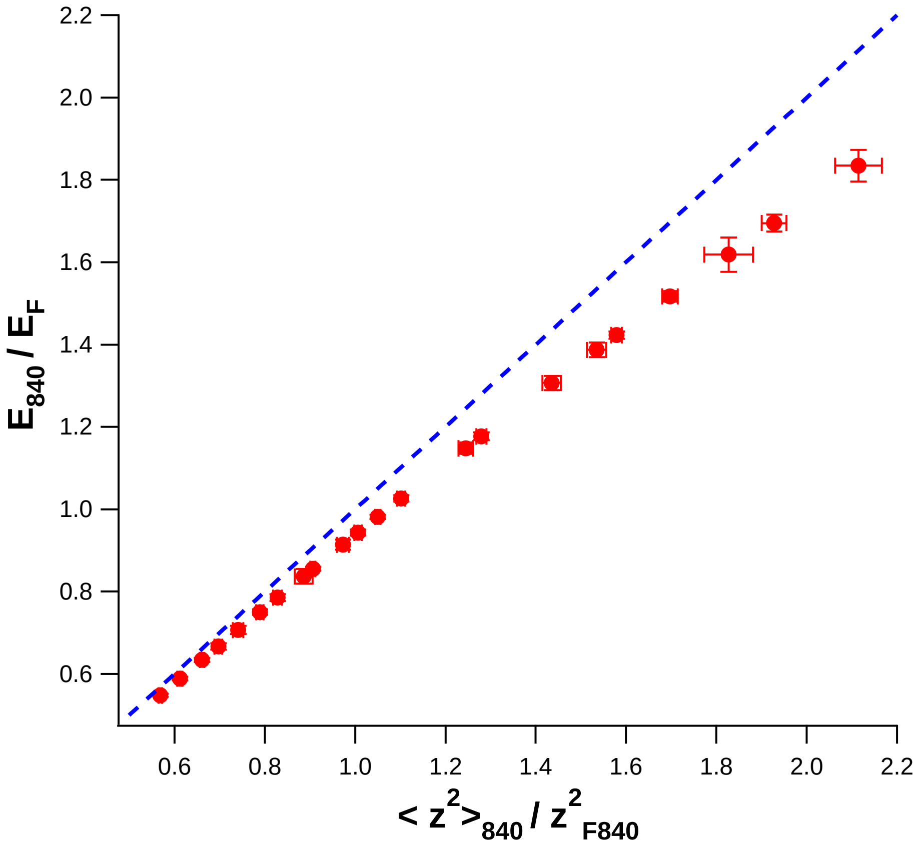

Figure 6.1: The energy determined from the virial theorem versus the measured mean square size at 840 G. The data points are the energies of the gas in the real Gaussian traps used in our experiments, which is determined from the virial theorem and includes anharmonic corrections. The dash line is the expectation value for a harmonic trap.

The energy determined from the virial theorem versus the measured mean square size at 840 G is shown in Fig. 6.1. The total data comprise about 900 measurements which have been averaged in energy bins of width $\Delta E = 0.04\, E_F$. For the shallow trapping potential $U_0 \simeq 10\, E_F$ used in our experiments, we find that the anharmonicity correction κ defined in Eq. (4.52) varies from 3% at our lowest energies to 13% at the highest.

For simplicity, we neglect an approximately 1% correction for the cloud energy arising from the finite scattering length at 840 G [6], where is about 6 G away from the exact unitary value.

6.2 Adiabatic Magnetic Field Sweep

First let us look at the mean square size of the cloud at 1200 G. As we explained in Chapter 5, we sweep the magnetic field towards the BCS regime at 1200 G. The magnetic field ramp is nearly linear and the whole sweep process lasts about 0.8 second. We permit 1 second to ensure that the gas reaches the equilibrium state at 1200 G. At 1200 G, we expect that the gas is weakly interacting in our shallow trap, since $k_F a_S = -0.75$ with $a_S = -2900$ bohr [62] and $k_F = (2mE_F/\hbar^2)^{1/2}$ with $E_F/k_B = 1\mu K$. We observe ballistic expansion of the cloud at this field at our lowest energy, which shows the gas is normal and weakly interacting.

We find that the magnetic field sweep is nearly adiabatic by the round-trip-sweep. The mean square size of the cloud at 840 G after a round-trip-sweep lasting 2 seconds is found to be within 3% difference of the cloud that remains at 840 G after a hold time of 2 second. Fig. 6.2 shows the atom number and the atom-number-independent mean square radial size of the cloud with and without the round-trip-sweep. The clouds at the different energies are produced by different heating kick times. From Fig. 6.2, we can see that the sweep does not cause any significant atom loss or heating, which ensures entropy conservation for the sweep.

To display the results of the measured mean square size at 1200 G, we show the ratio between the mean square size at 1200 G and that at 840 G. To make the comparison to be meaningful, the displayed ratio and energy scale should be independent of the atom number and trap parameters. This is accomplished

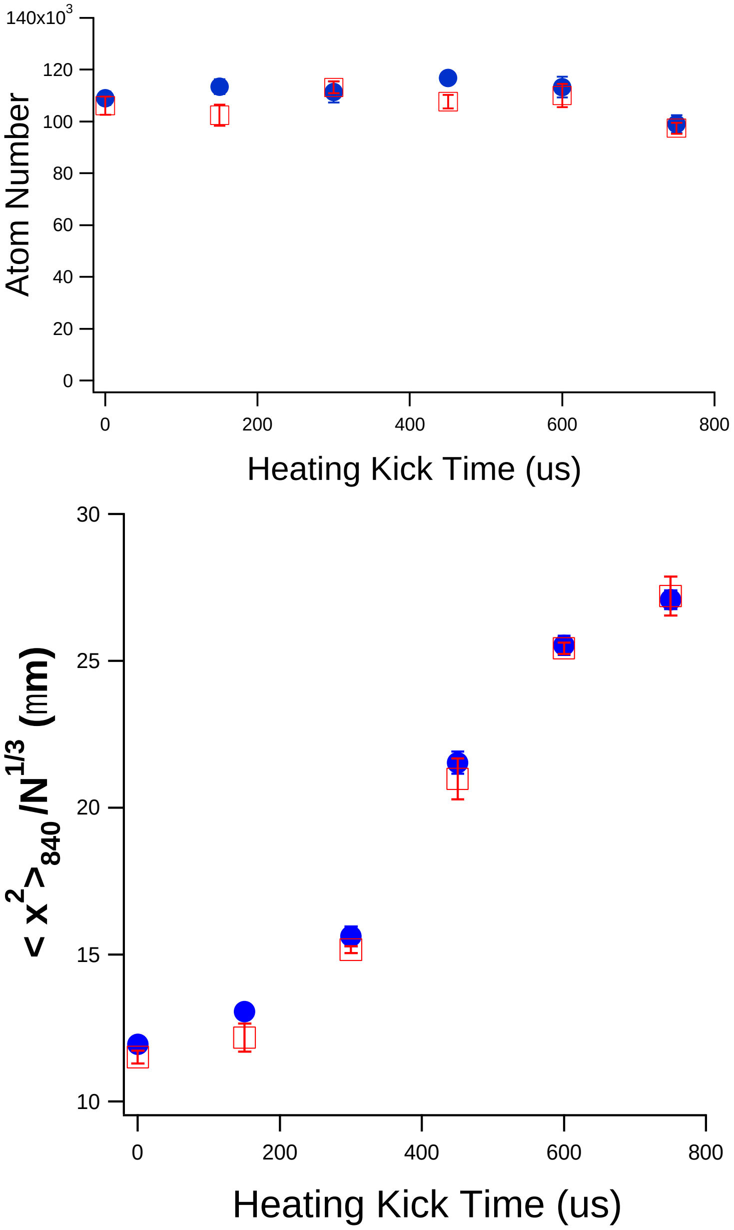

Figure 6.2: The atom number and the cloud size with and without the round-trip-sweep at 840 G. The solid dot is without the sweep, and the open square is with the sweep.

by scaling the mean square sizes at each field in units of z_F^2, where z_F^2 is given by the specific magnetic field and atom number. For example, at 1200 G this quantity is represented by $\langle z^2 \rangle_{1200}/z_{F1200}^2$. Note that, even for the same atom number, the mean square sizes of the Fermi energy z_F^2 are different at 840 G and 1200 G because of the small change of the axial trapping frequencies, which gives $z_F^2 \propto 1/\omega_z^{5/3}$. The axial frequencies ω_z at different magnetic fields differ with each other, due to the different magnetic potential provided by the magnetic field curvature. The total axial frequency depends on its optical potential contribution ω_{oz} and magnetic potential contribution ω_{mz} by $\omega_z^2 = \omega_{oz}^2 + \omega_{mz}^2$.

Fig. 6.3 shows the ratio of the mean square axial cloud size at 1200 G (measured after the sweep) to that at 840 G (measured prior to the sweep), as a function of the energy of a strongly interacting gas at 840 G. The energy at 840 G is directly measured from the axial cloud size at 840 G in Fig. 6.1. The total data comprise about 900 individual measurements of the cloud size at 840 G as well as the same number of measurements of the cloud size at 1200 G. We split the energy scale into the energy bins with width of $\Delta E = 0.04\, E_F$. For each energy bin, all the measured points within the width of the bin are used to calculate the average measured value and the corresponding standard deviation.

6.3 Entropy versus Energy in a Strongly Interacting Fermi Gas

Now we obtain the entropy from the data of the mean square sizes in Fig. 6.3. First, we extract the value of $(\langle z^2 \rangle_{1200} - \langle z^2 \rangle_0)/z_F^2$ using the measured $\langle z^2 \rangle_0 = 0.71\, z_F^2$ for the lowest energy state that we obtained at 1200 G. Then, we apply

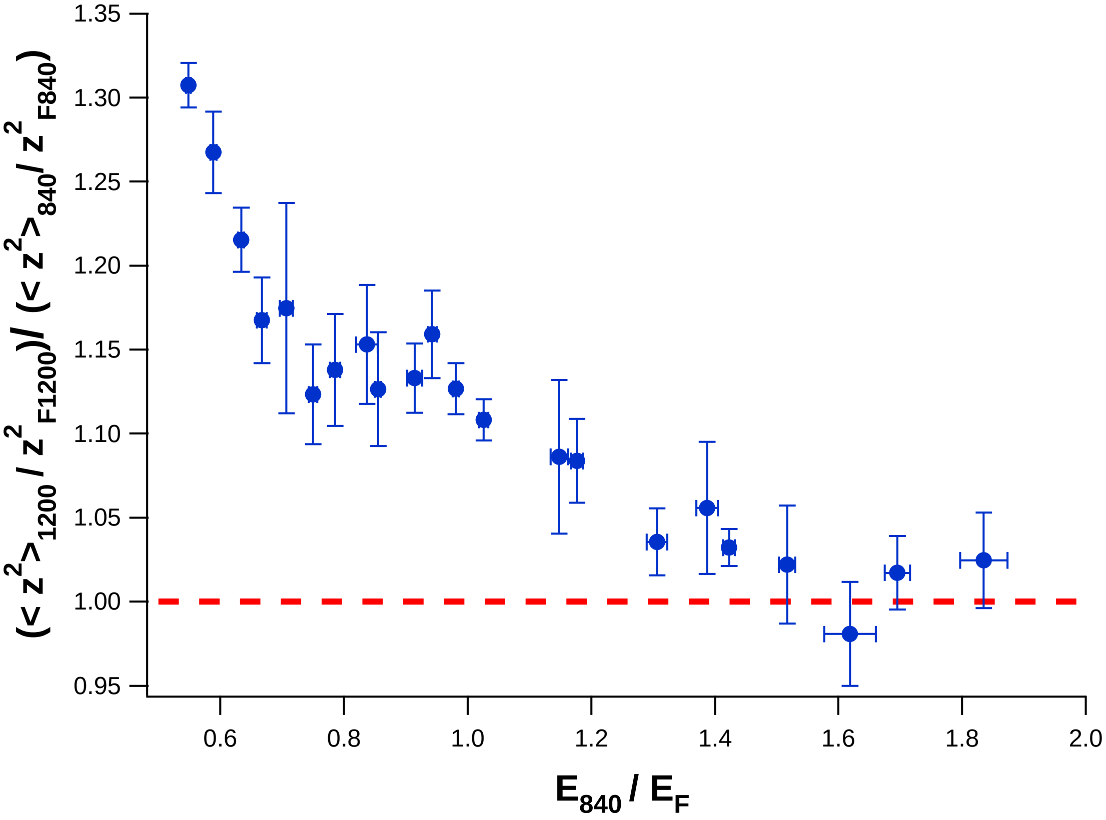

Figure 6.3: The ratio of the mean square cloud size at 1200 G, $\langle z^2 \rangle_{1200}$, to that at 840 G, $\langle z^2 \rangle_{840}$, for an isentropic magnetic field sweep. E_{840} is the total energy per particle of the strongly interacting gas at 840 G and E_F is the ideal gas Fermi energy at 840 G. The ratio converges to unity at high energy as expected (the dashed line).

the entropy curve for a ideal Fermi gas $S_I(\langle z^2\rangle_I - \langle z^2\rangle_{I0})/z_F^2$ shown in Fig. 5.11 to determine the entropy from the measured values of $(\langle z^2\rangle_{1200} - \langle z^2\rangle_0)/z_F^2$. This method automatically assures that $S = 0$ corresponds to the measured ground state $\langle z^2\rangle_0$ at 1200 G, and compensates for the mean field shift between the measured $\langle z^2\rangle_0$ for a weakly interacting Fermi gas and that calculated one $\langle z^2\rangle_{I0} = 0.77\, z_F^2$ for an ideal Fermi gas in our Gaussian trapping potential. For each point, the standard deviation of the entropy S is determined by the corresponding standard deviation of the measured mean square size $\langle z^2\rangle_{1200}$ using the same entropy curve. The result of the conversion of the entropy from the cloud size is shown in Fig. 6.4

Finally, we combine the entropy data measured at 1200 G after an adiabatically magnetic sweep and the energy data directly measured at 840 G. We obtain the energy-entropy curve for a strongly interacting Fermi gas in the unitary limit shown in Fig. 6.5.

6.4 Critical Parameters of Superfluid Phase Transition

One of the applications of the energy-entropy curve is to estimate the critical parameters for the phase transition. It has been theoretically predicted [41–44] and experimentally proved [12,20,24,30] that strongly interacting Fermi gases experience a superfluid-normal fluid phase transition near the ground state energy. However, the critical parameters, such as the critical temperature and entropy, were not determined yet. The studies of superfluid dynamics [47] and the model-dependent thermodynamic measurements [20] do not provide consistent results.

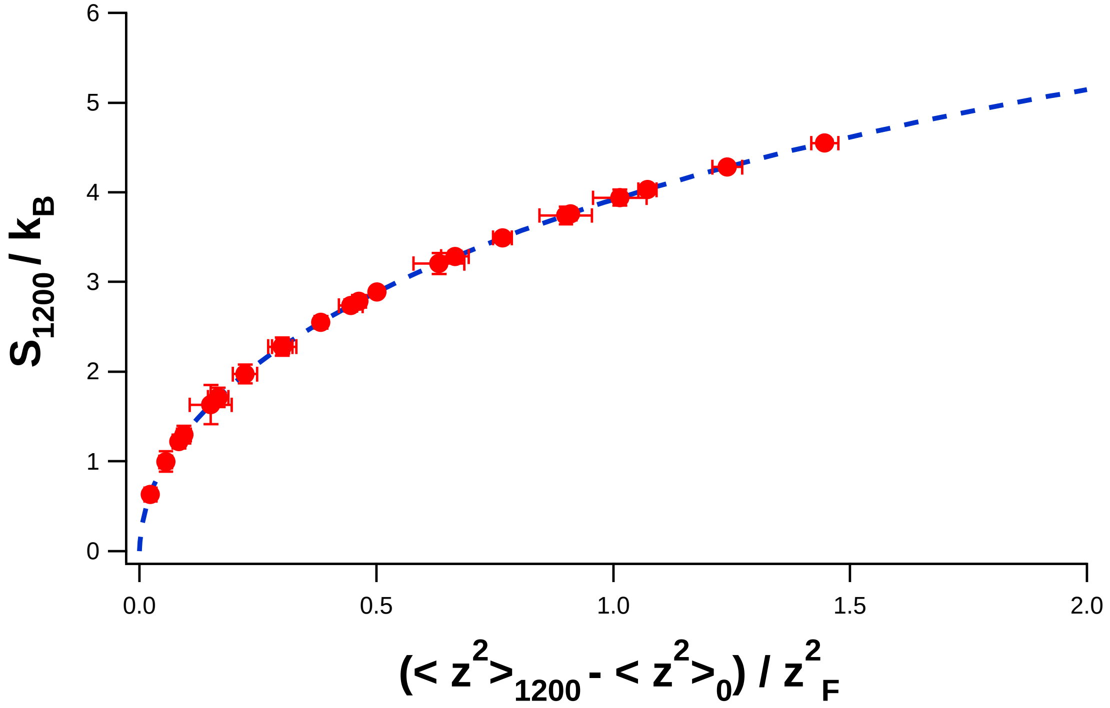

Figure 6.4: The conversion of the mean square size at 1200 G to the entropy. The dashed line is the calculated entropy for a noninteracting Fermi gas in the Gaussian trap with $U_0/E_F = 10$. $\langle z^2\rangle_0 = 0.71\, z_F^2$ is the measured ground state size for a weakly interacting Fermi gas. The calculated error bars of the entropy are determined from the measured error bars of the cloud size at 1200 G by the energy-entropy curve shown in Fig. 5.11.

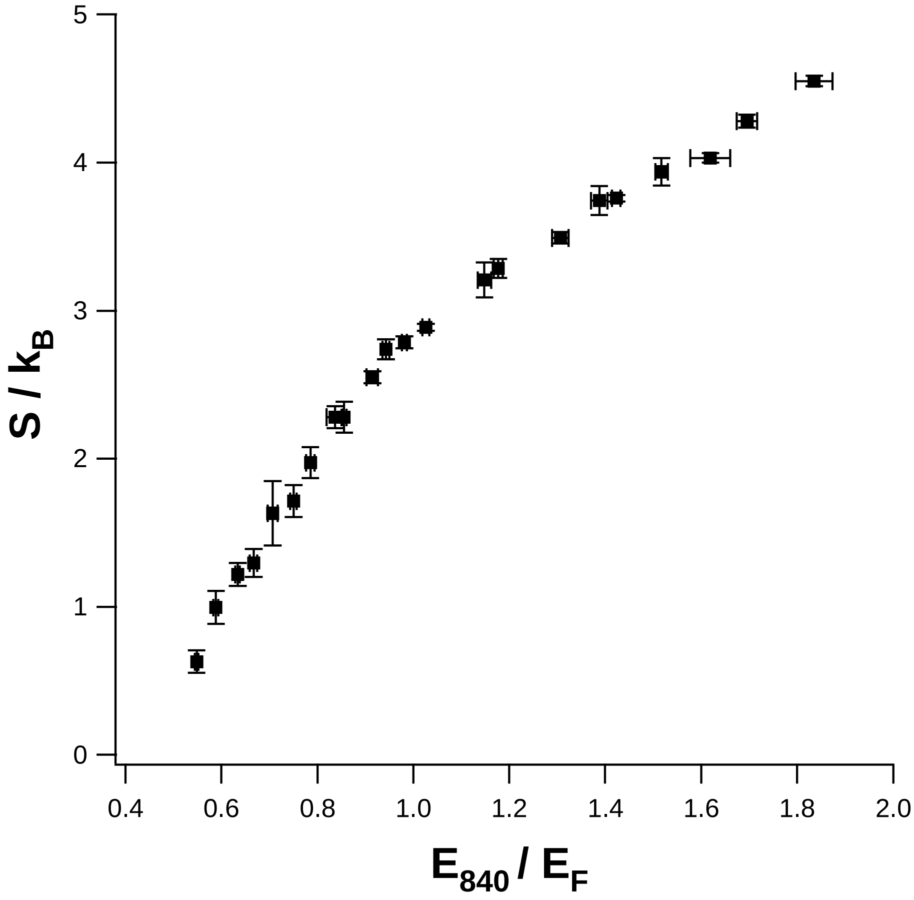

Figure 6.5: Measured entropy per particle of a strongly interacting Fermi gas at 840 G versus its total energy per particle in the range $0.4 \le E_{840}/E_F \le 2.0$. the slope of the entropy curve shows a behavior change near the region of $E_c = 0.90\,E_F$.

Meanwhile, different theoretical calculations and simulations produce quite different values for those critical parameters. So a model-independent measurement is required to provide a precise determination of such critical parameters for testing current predictions based on many-body theories.

From Fig. 6.5, it is obvious that the entropy of a strongly interacting Fermi gas as a function of its energy has a change in behavior near $E_c = 0.90\,E_F$, where a kink appears in the profile of the curve. This suggests that the entropy may have a different scaling law versus the energy below and above that behavior transition point. It is well known that the different scaling law of the entropy dependence on the energy or the temperature is usually a thermodynamic indication of phase transitions.

6.4.1 Power Law Fit without Continuous Temperature at the Critical Point

To find the critical energy and temperature, we need to parameterize the entropy data of a strongly interacting Fermi gas by a curve fitting. The fit curve of the entropy of a strongly interacting Fermi gas is shown in the Fig. 6.6 as well as the entropy of an ideal gas, which differs significantly with the entropy of a strongly interacting one with a larger ground state energy $E_{I0} = 0.75\,E_F$.

The simplest assumption consistent with $S(E = E_0) = 0$ is to approximate the data by a power law in $E - E_0$, where E_0 is the ground state energy. First, we try to fit the data by applying a single power law curve. The fit formula and results are given by

$$\begin{aligned}
S(E) &= k_B\, a \left(\frac{E-E_0}{E_F}\right)^b, \\
a = 3.97 \pm 0.02,\ E_0 &= 0.53 \pm 0.01,\ b = 0.47 \pm 0.01.
\end{aligned} \tag{6.8}$$

Then we use a simple model with two different power laws, one above and one below the critical energy E_c [49]. The fit formula and parameters a, b, d and E_C are given by

$$\begin{aligned}
S_<(E) &= k_B\, a \left(\frac{E-E_0}{E_F}\right)^b;\ E_0 \le E \le E_c \\
S_>(E) &= S_<(E_c) \left(\frac{E-E_0}{E_c-E_0}\right)^d;\ E \ge E_c \\
a &= 4.5 \pm 0.2,\ b = 0.59 \pm 0.03, \\
E_c &= 0.94 \pm 0.05,\ d = 0.45 \pm 0.01.
\end{aligned} \tag{6.9}$$

In this model, we assume S is continuous and ignore the requirement for the continuous $T = \partial E/\partial S$. For this fit, we hold $E_0 = E_{min} = 0.53(0.02)\, E_F$ as the minimum measured energy in our measurements, which is very close to the predicated ground state energy $0.50\, E_F$ for a unitary gas in a harmonic trap [45,81,82]. The standard deviation for each of the fit parameters is automatically calculated by Igor program.

We use the fitting error χ^2/N to judge the goodness of the fit, where $\chi^2 = \sum(\frac{y-y_i}{\sigma_i})^2$ is determined by the fitted value y for a given point, the original data value y_i and corresponding the standard error σ_i for a given point, and the total number of data N. Igor program uses the Levenberg-Marquardt algorithm to search for the coefficient values that minimize chi-square. This is a form of non-

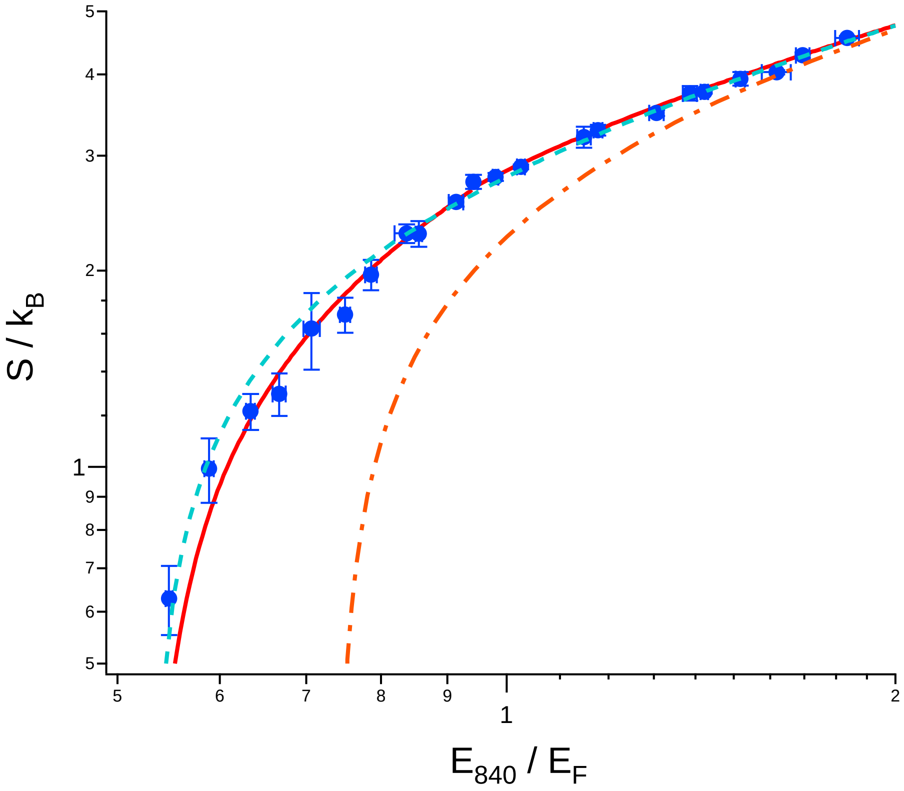

Figure 6.6: Parametrization of the energy-entropy curve by power laws. The dash line is the single power law fit using Eq. (6.8). The solid line is the two power law fit without the continuous slope using Eq. (6.9). The dash-dot line is the entropy of the noninteracting Fermi gas.

linear, least-squares fitting. We found the two power law fit yields a χ^2 per degree of freedom is about 1, almost a factor of two smaller than that obtained by fitting a single power law. This indicates that a two power law fit is required.

By implementing the two power law fit, the critical energy is found to be $E_c/E_F = 0.94 \pm 0.05$ with a corresponding critical entropy per particle $S_c = 2.7(\pm 0.2)\, k_B$. We find that the variances of a and b have a positive correlation, so that $S(E)$ is determined more precisely than the independent variation of a and b would imply. In comparison, by trying to fit the energy-entropycurve of a noninteracting gas with the two power laws, the fit fails to find the critical point, which indicates that such behavior change does not appear in the entropy curve of a noninteracting gas.

However, the drawback of this fit is that Eq. (6.9) ignores the smooth transition in slope near E_c, as required for the temperature to be continuous. The temperature is determined in a model-independent manner from $1/T = \partial S(E)/\partial E$. From the derivative of the fit function $S(E)$, we obtain the energy versus temperature $E(T)$. For $E \le E_c$,

$$\frac{E - E_0}{E_F} = \left(\frac{abT}{T_F}\right)^{\frac{1}{1-b}}. \tag{6.10}$$

We estimate the critical temperature T_c using the measured value of $E_c = (0.94 \pm 0.05)\, E_F$. Here, we interpret E_c as the critical energy for the superfluid transition, which is observed based on the collective mode damping and the heat capacity [20,45], and proved by the vortex lattice [24]. Ideally, to obtain T_c, the fit $S(E)$ should have a continuous slope near E_c. Since our fit function has different slopes above and below E_c, we use the average of the two slopes to approximate the slope of the tangent to a smooth curve through the data at E_c. Inverting Eq. (6.10) yields $T/T_F = 0.38\,[(E - E_0)/E_F]^{0.41}$ and $T_{c<}/T_F = 0.26$. Similarly, for $E(T) > E_c$, we find $T/T_F = 0.56\,[(E - E_0)/E_F]^{0.55}$ and $T_{c>}/T_F = 0.34$. Taking the average slope, $2/T_c \simeq 1/T_{c<} + 1/T_{c>}$, we find $T_c/T_F = 0.29(+0.03/-0.02)$. Here, the error estimate includes the cross correlations in the variances of a, b, E_c, and d.

6.4.2 Power Law Fit with Continuous Temperature at the Critical Point

More recently we found a fit formula that ensures a continuous slope for the energy-entropy curve. To make the Igor program do the fitting easier, we fit $E(S)$ instead of $S(E)$, which helps the program to find the ground state energy automatically by $E_0(S=0)$. The $E(S)$ fit formula (here the energy scaled by E_F and the entropy scaled by k_B) is defined as

$$\begin{aligned} E_<(S) &= E_0 + aS^b; \quad 0 \leq S \leq S_c \\ E_>(S) &= E_1 + cS^d; \quad S \geq S_c \\ E_<(S_c) &= E_>(S_c); \\ \frac{\partial E_<}{\partial S} &= \frac{\partial E_>}{\partial S} \quad at\ S_c. \end{aligned} \tag{6.11}$$

The continuation condition requires E_1 and c not independent. Further we have $E(S)$ fit formula with independent fit parameters E_0, S_c, a, b, d. The fit formula and result are given by

$$\begin{aligned} E_<(S) &= E_0 + aS^b;\ 0 \leq S \leq S_c \\ E_>(S) &= E_0 + aS_c^b \left[1 - \frac{b}{d} + \frac{b}{d}\left(\frac{S}{S_c}\right)^d\right];\ S \geq S_c \\ a = 0.12 \pm 0.01,\ b &= 1.35 \pm 0.11,\ d = 2.76 \pm 0.12 \\ E_0 &= 0.48 \pm 0.01,\ S_c = 2.2 \pm 0.1. \end{aligned} \tag{6.12}$$

The fit curve is shown in Fig. 6.7, where $E_<(S) = E_>(S)$ and $\frac{\partial E_<}{\partial S} = \frac{\partial E_>}{\partial S}$ at the joint point S_c. The standard deviation for each of the fit parameters is automat-

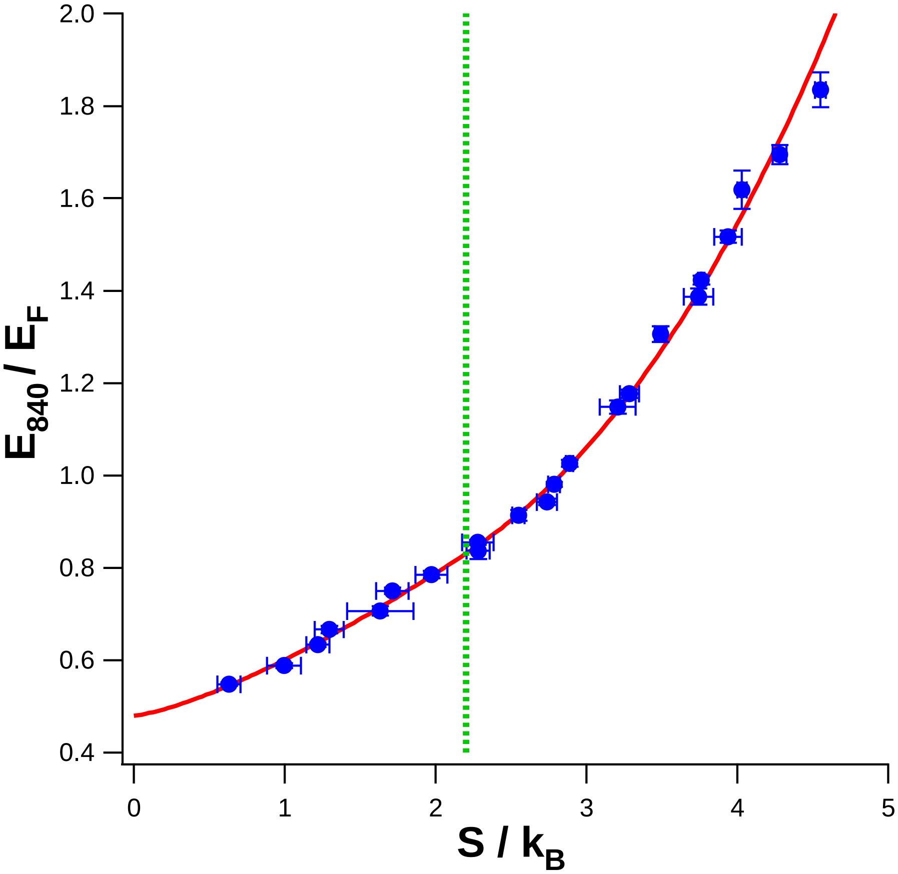

Figure 6.7: Parametrization of the energy-entropy curve by the continuous temperature fit. The solid line is the power law fit with the continuous slop at the joint point. The joint point is shown by the dashed line.

ically calculated by Igor program.

From Eq. (6.12), we can check the first derivative at the critical point S_c. The formula below and above the joint point give a consistent value of $\frac{\partial E}{\partial S} = abS_c^{b-1}$, which ensures that we can determine the temperature directly from this fit formula with continuous first derivative. From the fit, we find the critical entropy $S_c/k_B = 2.2 \pm 0.1$, and get the corresponding $E_c/E_F = 0.83 \pm 0.02$. The critical temperature is determined as $T/T_F = \partial E(S_c)/\partial S = 0.21 \pm 0.01$.

As a conclusion, I list the best estimates of the critical parameters of the superfluid transition in a strongly interacting Fermi gas from the parametrization of our model-independent measurements on both entropy and energy: The critical entropy $S_c/k_B = 2.2 \pm 0.1$, the critical energy $E_c/E_F = 0.83 \pm 0.02$, and the corresponding critical temperature $T/T_F = 0.21 \pm 0.01$.

6.5 Other Thermodynamic Properties

6.5.1 Many-body Constant β

In Section 4.3, I introduced β, the universal many-body constant for a strongly interacting system in the unitary limit, and showed that the ground state energy of a unitary Fermi gas in a harmonic trap is given by

$$E_{SI0} = \sqrt{1+\beta}\, E_{IG} = \sqrt{1+\beta}\, \frac{3}{4}\, E_F, \tag{6.13}$$

Form our measurement, we find $E_{SI0}/E_F = 0.48 \pm 0.01$, which gives the corresponding $\beta = -0.59 \pm 0.02$. This β value agrees fairly well with the most accurate quantum Monte Carlo simulation $\beta = -0.58 \pm 0.01$ [83], and predictions from strong coupling theories $\beta = -0.599$ [84] and $\beta = -0.55$ [81, 82, 85]. This measured β value can also be compared with other experimental investigations, such as $\beta = -0.49 \pm 0.04$ from the heat capacity measurement [45], $\beta = -0.565 \pm 0.015$ from the sound velocity measurement [86], and $\beta = -0.54 \pm 0.05$ from the spin separation experiment [32].

6.5.2 Chemical Potential

According to Ehrenfest's classification scheme for phase transitions [80], a phase transition is classified by the following scheme. If the n^{th} derivative of chemical potential μ with a thermodynamic variable exhibits discontinuity, but no discontinuity appears in any lower order derivatives, then the transition is an n^{th} order phase transition. For example, for a first order transition, the chemical potential is continuous while its first derivative is discontinuous at the critical point.

As we discussed at the beginning of the chapter, the chemical potential μ can be determined from the energy-entropy data based on the basic thermodynamic relations. So the energy-entropy curve should provide enough information to derive the chemical potential, from which we can classify the order of the phase transition in a strongly interacting Fermi gas.

According to Eq. (6.4), the local chemical potential μ is given by

$$\varepsilon = T\,s + \mu\,n - P, \tag{6.14}$$

where ε is the local internal energy (kinetic energy and interaction energy), and s is the total entropy in a local volume. From the virial theorem for a unitary Fermi gas, we have the pressure $P = 2\,\varepsilon/3$. Using $\mu = \mu_g - U$, where U is the local trap potential, we get

$$\mu_g = \frac{5}{3}\varepsilon + U - T\,s. \tag{6.15}$$

By integrating the formula for the whole trap, we have

$$\mu_g\, N = \frac{5}{3}\,(E - \langle U\rangle)\; N + \langle U\rangle\, N - T\, S\, N, \tag{6.16}$$

where $\langle U\rangle$ is the average trap potential per particle, and E and S are the total energy and total entropy per particle respectively. For a harmonic trap approximation, $E = 2\langle U\rangle$. Finally, the global chemical potential of the unitary Fermi gas in a harmonic trap is given by the total energy and entropy per particle

$$\mu_g = \frac{4}{3}\,E - T\,S = \frac{4}{3}\,E - \frac{\partial E}{\partial S}\,S. \tag{6.17}$$

By using the measured entropy and energy data and $T = \partial E/\partial S$ from the fit of Eq. (6.12), the global chemical potential of a trapped strongly interacting Fermi gas can be calculated from Eq. (6.17). We plot the chemical potential data in Fig. 6.8.

In Fig. 6.8, we can see that the chemical potential might show a discontinuity in its first derivative with the energy. I also should point out that the accurate behavior of chemical potential near the critical point is still not clear in our experiment, since I use the fit result of $T = \partial E/\partial S$ to obtain the chemical potential. The discontinuity in the first derivative of the chemical potential can only be treated as a possible scenario. If the discontinuity is true, according to the classification of phase transition by Ehrenfest, the superfluid transition in a strongly interacting Fermi gas might be the first order transition. For comparison, the ordinary superfluid phase transitions in weakly interacting systems are second order transitions, such as the superfluid transition in ^{4}He and the superconductor transition in Pb and Ag metals. Considering there is a possibility that the superfluid

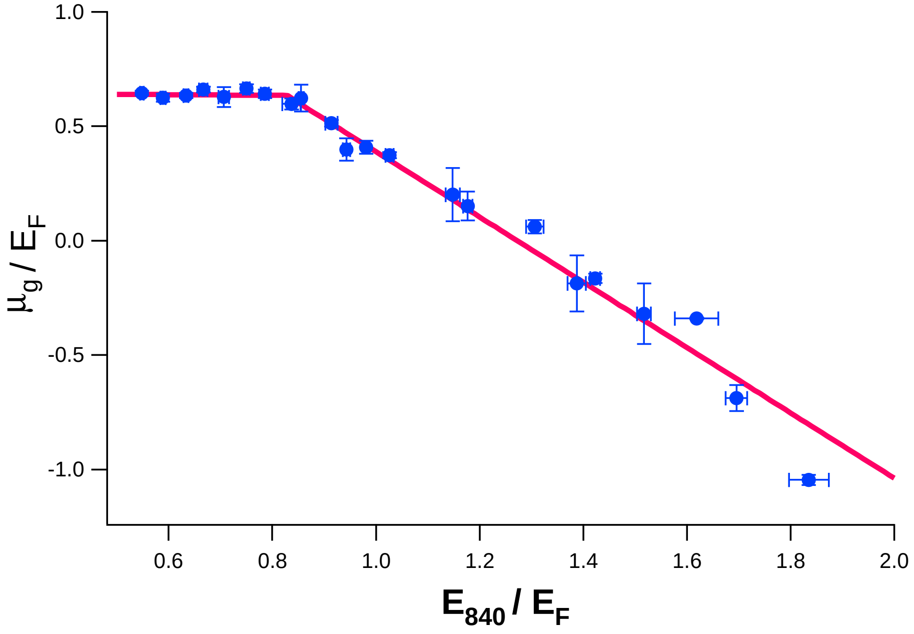

Figure 6.8: The global chemical potential versus the total energy of a strongly interacting Fermi gas. The data points are calculated from the measured S and E data and the parameterized T according to Eq. (6.17), where the parameterized T is given by the fit parameters in Eq. (6.12). The standard deviation for each point of the chemical potential is determined by the standard deviation of the energy and the entropy data. The solid line is completely determined by the fit parameters in Eq. (6.12), which gives $\mu_G = 4E/3 - 1.35(E - 0.48)$ when $E \leq 0.83$, and $\mu_g = 4E/3 - 2.76(E - 0.48) + 0.49$ when $E > 0.83$.

transition in a strongly interacting Fermi gas is the first order, the behavior of the chemical potential near the critical point needs to be more carefully investigated in further researches.

The free energy can be estimated according to the general thermodynamic relations. In a harmonic trap, we have $F = E - \frac{\partial E}{\partial S}\,S$, where F is the free energy per particle in a trap. Since the free energy includes equivalent information to the chemical potential, I will not repeat the calculation here. Readers who are interested in this thermodynamic quantity can extract it very easily from our energy and entropy data.

6.5.3 Temperature

As we discussed in Section 1.3.1, it is a difficult task to develop a precise thermometry for a strongly interacting Fermi gas. So it is important to extract the general temperature form the energy and entropy data for a strongly interacting Fermi gas.

Here we present a model-independent method to determine the temperature from the fundamental thermodynamic relation $T = \partial E/\partial S$. Our method is applicable for a strongly interacting Fermi gas in both superfluid and normal fluid regime. The only drawback is it requires a parametrization of data. However, with good curve fitting, the temperature is trustable.

Our best fit for the energy and entropy date in Eq. (6.12) generates the temperature T (in units of T_F) versus E (in units of E_F),

$$\begin{aligned}
For\ \ E_0 &= 0.48 \leq E \leq E_c = 0.83 \\
T_<(E) &= a^{\frac{1}{b}} b (E - E_0)^{\frac{b-1}{b}}; \\
&= 0.28(E - 0.48)^{0.26}; \\
For\ \ E &\geq E_c \\
T_>(E) &= a^{\frac{1}{b}} b (E_c - E_0)^{\frac{b-1}{b}} \left(\frac{d}{b} \frac{E - E_c}{E_c - E_0} + 1 \right)^{\frac{d-1}{d}}; \\
&= 0.21[5.84(E - 0.83) + 1]^{0.64}. \qquad (6.18)
\end{aligned}$$

In the previous investigation of heat capacity, we got a model-dependent temperature given in [64] by

$$\begin{aligned}
T_<(E) &= (\frac{1}{97.3} \frac{E - 0.48}{0.48})^{\frac{1}{3.73}};\ E_0 \leq E \leq E_c = 0.85 \\
T_>(E) &= (\frac{1}{4.98} \frac{E - 0.48}{0.48})^{\frac{1}{1.43}};\ E \geq E_c. \qquad (6.19)
\end{aligned}$$

It is quite interesting to compare these two temperatures. The scaling of temperature with the energy is shown in Fig. 6.9.

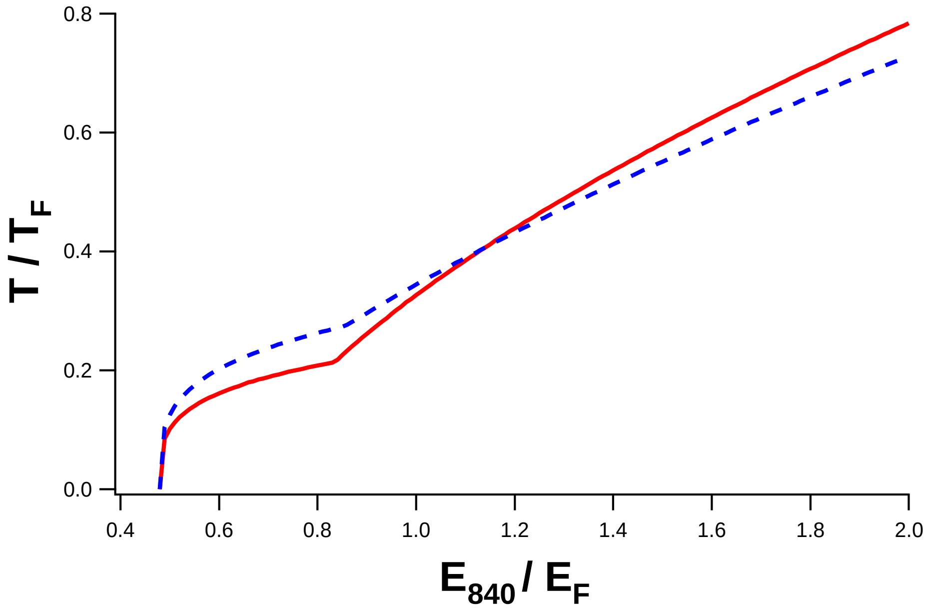

Figure 6.9: The temperature of a strongly interacting Fermi gas from the entropy measurement versus the energy is shown in the solid line given by Eq. (6.18). The dashed line is the temperature given by Eq. (6.19), which is extracted from the heat capacity measurement by a pseudogap theory.

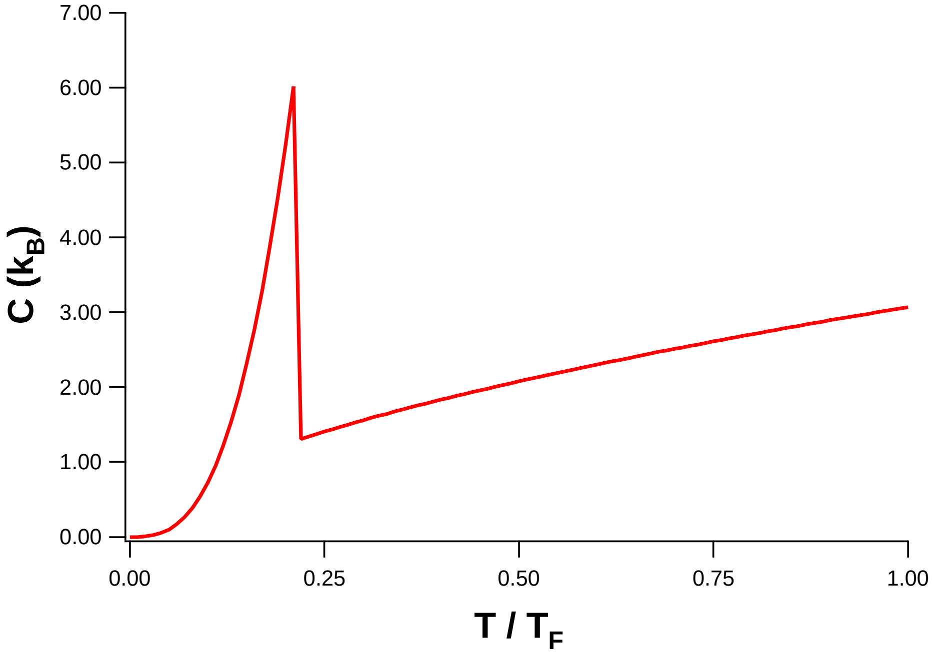

Figure 6.10: The heat capacity versus the temperature given by Eq. (6.20) for a strongly interacting Fermi gas. A heat capacity jump appears at about $T/T_F = 0.21$.

6.5.4 Heat Capacity

The next thing we can determine is the heat capacity by $C = \frac{dE}{dT}$. From Eq. (6.18), we obtain C in the unit of k_B

$$\begin{aligned} For T &\leq T_c = 0.21\, T_F \\ C_<(T) &= 514\, T^{2.85}; \\ For T &\geq T_c \\ C_>(T) &= 3.07\, T^{0.563}. \end{aligned} \tag{6.20}$$

The heat capacity curve is shown in Fig. 6.10, which exhibits a heat capacity jump at the critical temperature for the superfluid transition.

6.6 Comparison between Experimental Result and Strong-coupling Theories

In this section, I will give a short review of using our data as a benchmark to test several strong coupling many-body theories and simulations. I will compare our energy-entropy data with the prediction of a trapped strongly interacting Fermi gas made by those theories. It is noted that currently many groups are trying to improve their theoretical methods to give a more precise calculation for our system. Most of the work is still going on at the time I wrote this thesis. So I will only compare our data with the theoretical calculations that appeared shortly after our experiment in [49]. They are a pseudogap theory [76, 87], a T-matrix calculation by Nozières and Schmitt-Rink (NSR) approximation [6, 8], and a quantum Monte Carlo simulation [77, 88]. The experimental data and theoretical curves are shown in Fig. 6.11.

It is mentioning that the power law exponent of $S \propto T^q$ below T_c, which represent the characteristic low temperature excitation of the superfluid phase. From Eq. (6.18), we obtain $q = 2.85$. For comparison, the pseudogap theory gives $S \propto T^{3/2}$, while the NSR theory gives $S \propto T^3$ due to the low-lying Bogoliubov-Anderson phonon modes [8].

Our measured critical temperature $T_c/T_F = 0.21 \pm 0.1$ can be compared with our previous estimate of $T_c/T_F = 0.27$ from a model-dependent heat capacity mearement [45]. Moreover, the recent calculations of T_c/T_F for a trapped strongly interacting Fermi gas are 0.21 [6, 8, 89] and 0.25 [77], while previous rough estimations had given 0.29 [45], 0.30 [90], 0.31 [44], and 0.30 [50].

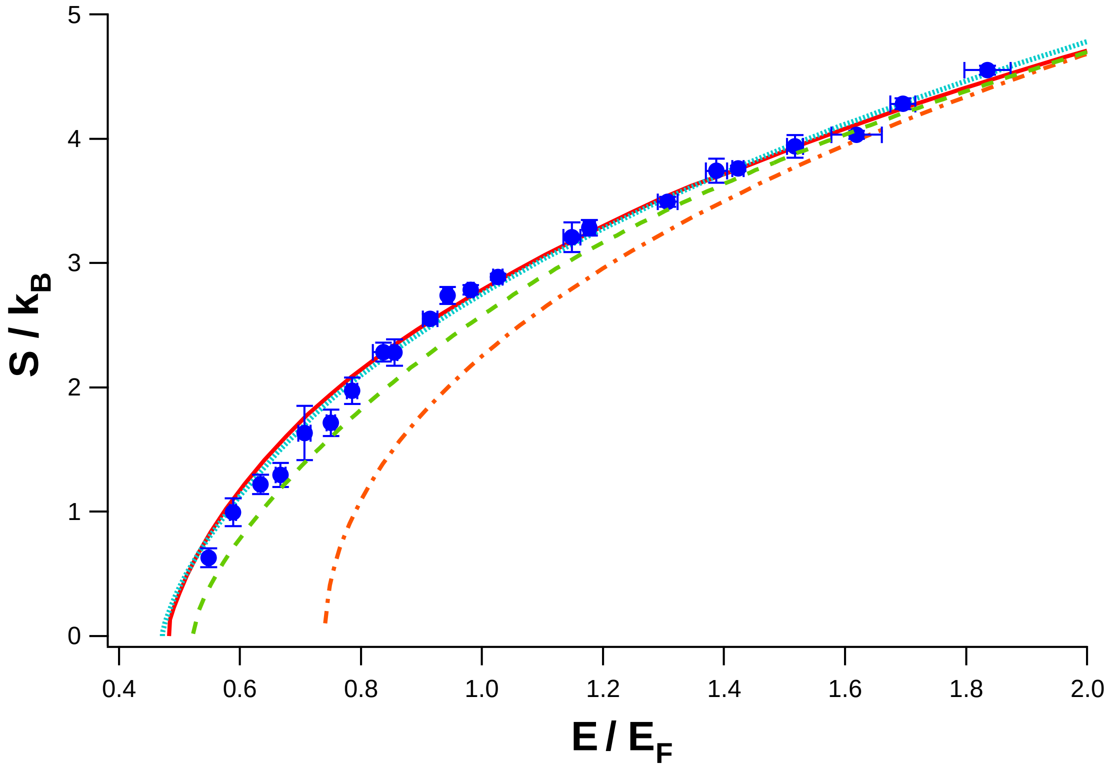

Figure 6.11: Comparison of the experimental entropy curve with the calculation from strong coupling many-body theories. The dashed line is a pseudogap theory [76, 87]. The dotted line is a NSR calculation [6, 8]. The solid line is a quantum Monte Carlo simulation [77, 88]. The dot-dashed line is the ideal Fermi gas result for comparison.

Chapter 7

Studies of Perfect Fluidity in a Strongly Interacting Fermi Gas

One intriguing feature of a strongly interacting Fermi gas is its nearly perfect fluidity. It is predicted and proven that a high temperature superfluid phase exists in a strongly interacting Fermi gas when the temperature of the gas is below the critical temperature. In Chapter 6, I have discussed the thermodynamic signature of the superfluid transition. In this chapter, I will investigate the nearly perfect fluidity of a strongly interacting Fermi gas, which exhibits hydrodynamic behavior with a very low viscosity.

The goodness of the fluidity is characterized by the viscosity. The viscosity is defined to describe the relation between the shear stress tensor $[P_{ij}]$ and the symmetric part of velocity tensor $[e_{ij}]$ of the fluid, where $e_{ij} \equiv (\partial v_i/\partial x_j + \partial v_j/\partial x_i)/2$, and $\mathbf{v}$ and $\mathbf{x}$ is the velocity and space coordinate of the flow. The detailed relations between stress tensor and velocity tenser can be referred to [91]. Here we assume a linear isotropic dependence of the shear stress tensor on the symmetric velocity tensor and obtain

$$P_{ij} = \eta(2e_{ij} - \frac{2}{3}\delta_{ij}e_{ij}) + \zeta\delta_{ij}e_{ij}, \tag{7.1}$$

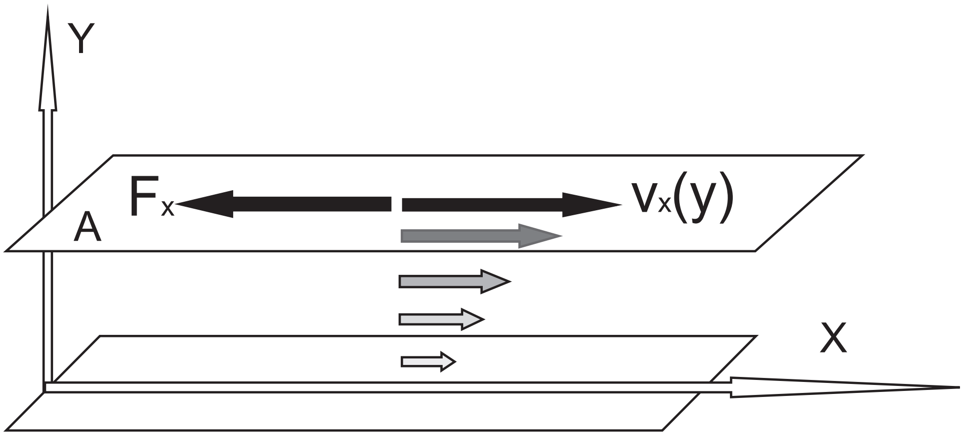

Figure 7.1: The definition of the shear viscosity. The proportionality between the friction force of per surface area and the velocity gradient from one layer to the other gives the definition of the shear viscosity by $\frac{F_x}{A} = -\eta \frac{\partial v_x}{\partial y}$.

where i, j represent the space coordinates, and $\delta_{ij} = 1$ when $i = j$, else δ_{ij} is zero. η is the shear viscosity and ζ is the bulk viscosity. The bulk viscosity is related to the change of the volume of the fluid, and vanishes for an incompressible fluid. For a unitary gas it is has been suggested that the bulk viscosity vanishes [92]. In this chapter, we will ignore the bulk viscosity and refer the term "viscosity" only to the shear viscosity. The shear viscosity originates from the tangential stresses, which is caused by the relative motions between the layers of the fluid close to each other, as shown in Fig. 7.1.

When viscous effects are absent, the fluid flows without any friction. Such flow is defined as ideal hydrodynamic flow. In recent years, hydrodynamic flow in strongly interacting quantum systems has attracted strong interest from different fields in physics, which includes ultrahot quark-gluon plasmas as well as ultracold fermionic atoms. One of the most compelling properties of strongly interacting Fermi gases is that ideal hydrodynamic flow not only exists in the superfluid regime, but also in the normal fluid regime as well. For superfluids, ideal hydrodynamic flow is a well known result as a consequence of zero viscosity in the superfluid component. However, ideal hydrodynamic flow in the normal fluids of strongly interacting system is still a novel phenomenon. Even though we know that hydrodynamic behavior can be induced by strong interparticle collisions, the extremely low viscosity in a strongly interacting Fermi gas still can not be well explained by current theories of strong collisions [50].

The extremely low viscosity also exists in other strongly interacting systems, such as a quark-gluon plasma [93, 94] and a type of strongly interacting quantum fields [3]. By string theory methods, Son's group predicted that the ratio of shear viscosity η to entropy density s has a lower bound given by

$$\frac{\eta}{s} \geq \frac{1}{4\pi}\frac{\hbar}{k_B}. \tag{7.2}$$

It is believed that the lower bound is approached only in a unitary strongly interacting system, which provides the quantum limit of the ratio between viscosity and entropy density.

In this chapter, I will first describe our studies of hydrodynamic expansion of a rotating strongly interacting Fermi gas. In this experiment, we observe nearly perfect irrotational flow appearing not only in the superfluid regime but also in the normal fluid regime. As I will show later, perfect irrotational flow actually is a primary signature of a very low viscosity. The experiment of expansion of a rotating cloud provides a very important tool to study the viscosity in a strongly interacting Fermi gas. The main results of this experiment will be reviewed in Section 7.1. More details for this experiment are presented in my colleague Bason Clancy's thesis [39].

In Section 7.2, I estimate the upper bound of the viscosity using our collective breathing mode data [19]. The viscosity is extracted from the damping of the breathing mode by applying a hydrodynamic model of the collective mode with finite viscous effects. Following that, I use our measured entropy of the gas to estimate the ratio of the shear viscosity to the entropy density [95]. Finally I will compare this results with the predicted lower bound that is conjectured by string theory methods.

7.1 Observation of Irrotational Flow in a Rotating Strongly Interacting Fermi Gas

Previously, the hydrodynamic expansion of a strongly interacting Fermi gas has been studied in the case of zero angular momentum [12, 96, 97]. The only investigation of finite angular momentum expansion for a strongly interacting Fermi gas is with the formation of vortex lattices, which has been used to demonstrate superfluidity in a strongly interacting Fermi gas [24, 25]. However, in the normal regime, finite angular momentum expansion has never been studied before.

In this section, I will study the hydrodynamic expansion of a rotating strongly interacting Fermi gas of ^{6}Li atoms. We release a cigar-shaped cloud with a known angular momentum L from an optical trap, and measure the angular velocity Ω about the y-axis and the aspect ratio of the principal axes (z, x) from the time-of-flight images. The data are in excellent agreement with irrotational hydrodynamics [98–100] in the superfluid regime, and surprisingly in the normal fluid regime as well.

In this experiment, conservation of angular momentum for an expanding cloud enables a model-independent measurement of the effective moment of inertia I by

$$I \equiv L/\Omega. \tag{7.3}$$

On the other hand, if the cloud is a rigid body, the rigid body value of the moment of inertia I_{rig} can be measured from the cloud images by

$$I_{rig} = Nm\langle x^2 + z^2 \rangle, \tag{7.4}$$

where the $\langle x^2 + z^2 \rangle$ is the mean square size in the $x - z$ plane, which is our imaging plane. By comparing the measured effective momentum of inertia I with the measured rigid body value I_{rig}, we find that the effective momentum of inertia of a rotating strongly interacting Fermi gas is suppressed with respect to the rigid body value in the process of the expansion. Our measured ratios show very good agreement with the fundamental prediction of ideal irrotational flow [98] as

$$\frac{I}{I_{rig}} = \delta^2 \equiv \frac{\langle z^2 - x^2 \rangle^2}{\langle z^2 + x^2 \rangle^2}, \tag{7.5}$$

where the deformation parameter δ is directly obtained from the cloud images. This measurement actually provides a clear proof of irrotaiotional flow in both the superfluid and normal fluid regimes of a strongly interacting Fermi gas.

7.1.1 Irrotational Flow in Superfluid and Normal Fluid

Let us first introduce irrotational flow. The well known requirement for a superfluid with the zero viscosity is irrotational hydrodynamics, which means the vorticity is zero $\varpi = \nabla \times \mathbf{v} = 0$, since $\mathbf{v} \propto \nabla\phi$ and ϕ is the phase of a macroscopic wavefunction of superfluid.

Now I will use 2D flow as an example to explain the difference between the rotational flow and irrotational flow. Assume the stream line of incompressible 2D flow can be described by a scalar function $\Psi = ax^2 + by^2$ in a 2D plane (x, y) [91]. The scalar function for the streamline can be divided into a pure rotation part and a pure shear(irrotational) part by

$$\Psi = ax^2 + by^2 = \frac{b+a}{2}(y^2 + x^2) + \frac{b-a}{2}(y^2 - x^2) = \Psi_{rot} + \Psi_{irrot}. \tag{7.6}$$

For the pure rotational part Ψ_{rot}, the velocity is given by

$$\begin{aligned} v_x &= \frac{\partial \Psi_{rot}}{\partial y} = (b+a)y \\ v_y &= -\frac{\partial \Psi_{rot}}{\partial x} = -(b+a)x \\ \nabla \times \mathbf{v} &= \left(\frac{\partial v_y}{\partial x} - \frac{\partial v_x}{\partial y}\right)\hat{\mathbf{z}} = -2(b+a)\hat{\mathbf{z}}. \end{aligned} \tag{7.7}$$

For the pure irrotational part Ψ_{irrot}, the velocity is given by

$$\begin{aligned} v_x &= (b-a)y \\ v_y &= (b-a)x \\ \nabla \times \mathbf{v} &= 0. \end{aligned} \tag{7.8}$$

The contour plots of the streamlines of pure rotation flow and pure shear flow are shown in Fig. 7.2.

In a superfluid, irrotational flow is a consequence of the macroscopic wavefunction, and usually evolves into the quantized vortex. The vorticity of a vortex

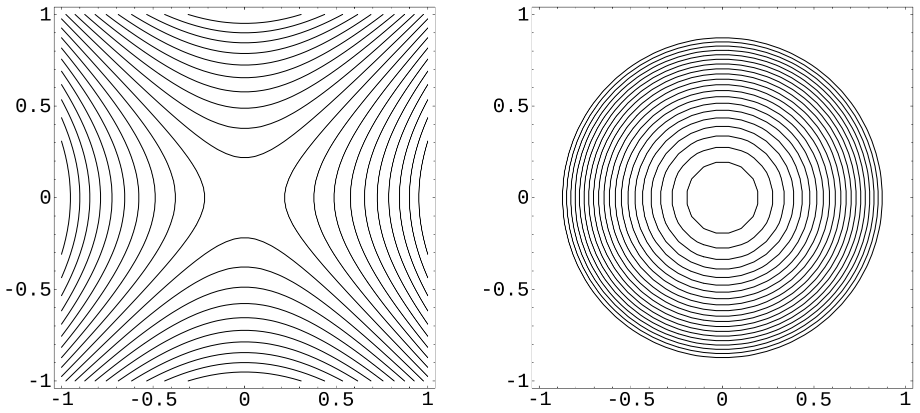

Figure 7.2: The definition of the streamline for irrotational and rotational flow. Here we plot $b - a = 2$ in Eq. (7.8) for a pure irrotational flow and $b + a = 2$ in Eq. (7.7) for a pure rotational flow.

is zero everywhere except of the singularity of vortex core in cylindrical polar coordinates (r, θ), where the voticity is localized and given by quantized values

$$\varpi = \frac{nh}{2m}\delta^{(2)}(r)\hat{\mathbf{z}}. \tag{7.9}$$

Here $\delta^{(2)}(r)$ is a two-dimensional δ function. h is Planck's constant and n is a positive integer. By comparison, for a rotational fluid with $\mathbf{v} = \omega \times \mathbf{r}$, the vorticity $\varpi = 2\omega$ is constant everywhere.

In the next section I will describe the experiment that we observe irrotational flow in both the superfluid regime and in the normal fluid regime in a strongly interacting Fermi gas by studying the hydrodynamic expansion of a rotating cloud.

7.1.2 Preparation of a Rotating Strongly Interacting Fermi Gas

In our experiments, a degenerate strongly interacting Fermi gas is prepared by the same procedures described in Chapter 3. For the rotating experiment, we use a trap depth about ten times deeper than we used in the entropy experiment. We employ a 50:50 mixture of the two lowest hyperfine states of ^{6}Li atoms in a bias magnetic field near a broad Feshbach resonance at 834G [62]. After evaporation, the trap depth is recompressed to $U_0/k_B = 100\,\mu$K, which is much larger than the energy per particle of the gas.

At the final trap depth U_0, the measured oscillation frequencies in the transverse directions are $\omega_x = 2\pi \times 2354(4)$ Hz and $\omega_y = 2\pi \times 1992(2)$ Hz while the axial frequency is $\omega_z = 2\pi \times 71.1(.3)$ Hz, which produce a cigar-shaped trap with $\omega_z/\omega_x = 0.032$. The total number of atoms N typically is 1.3×10^5. The corresponding Fermi energy E_F at the trap center is $E_F/k_B = \hbar(3N\omega_x\omega_y\omega_z)^{1/3} = 2.4\,\mu$K.

Samples with energies well above the ground state are prepared either by reducing the forced evaporation time, or starting from near the ground state and adding energy using release and recapture scheme. Then the cloud is held for 0.5 s to assure equilibrium. The total energy E of the cloud is determined in the strongly interacting regime from the axial (z) mean square cloud size, using $E = 3m\omega_z^2\,\langle z^2\rangle$, where m is the atom mass [48, 49].

Once the trapped gas has been prepared in a desired energy state, the trap is suddenly rotated as shown in Fig. 7.3. Rotation of the CO_2 laser beam is accomplished by changing the frequency of the acousto-optic modulator (AOM) that

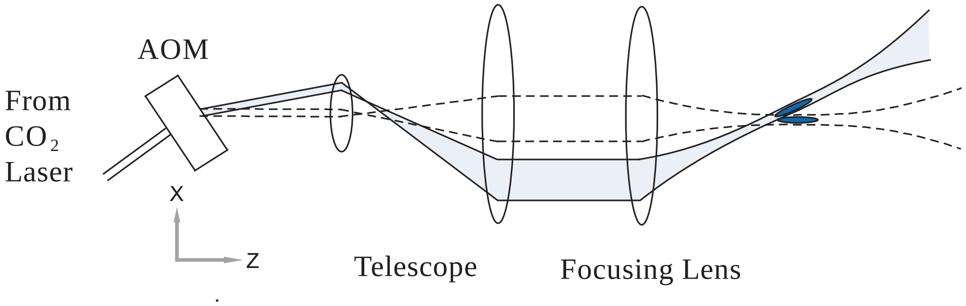

Figure 7.3: Scheme to rotate the optical trap by changing the frequency of an acoustooptic modulator(AOM).

controls the trap laser intensity. When the frequency is changed from the initial state 40.0 MHz to the final state between 40.1 and 40.2 MHz by a radio frequency (RF) switch, the position of the beam on the final focusing lens translates. This translation causes primarily a rotation of the cigar-shaped trap at the focal point about an axis (y) perpendicular to the plane of the cigar-shaped trap.

A scissors mode in the $x - z$ plane [101] is excited by this rotation. We note that there is also a slosh mode in the transverse direction (x) accompanying the scissors mode. In Fig. 7.4, we show the rotation angle in the $x-z$ plane and radial position in x direction of the cloud versus the evolution time, which is excited by the RF frequency switching from 40.0 MHz to 40.1 MHz. The cloud is permitted to oscillate in the trap for a chosen period. The oscillation time can be used to choose the initial angular velocity of the cloud before release.

7.1.3 Observation and Characterization of Expansion Dynamics

Fig. 7.5 shows cloud images as a function of expansion time for the coldest samples, with a typical energy $E = 0.56E_F$ near the ground state [49]. When the gas is

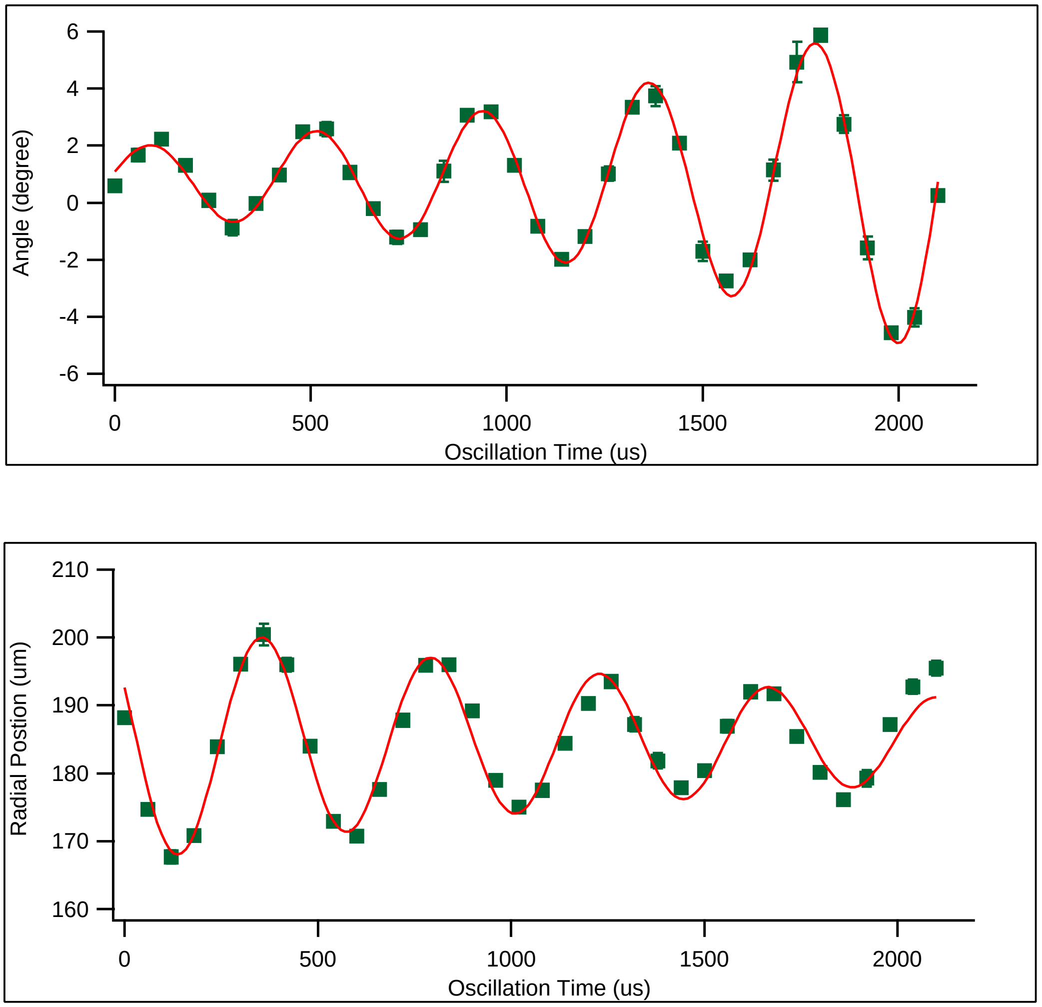

Figure 7.4: Scissors mode excited by a trap rotation. The angle is fitted by $A(t) = a + b \times Exp(t/\tau) \times Sin(ft + c)$, where $f = 2360 \pm 6$ Hz and $\tau = 1239 \pm 67 \mu$s. The radial position is fitted by $A(t) = a + b \times Exp(-t/\tau) \times Sin(ft + c)$, where $f = 2292 \pm 10$ Hz and $\tau = 1975 \pm 356 \mu$s. Note that the rotation angle slowly damps out after the initial increase, which is not shown here.

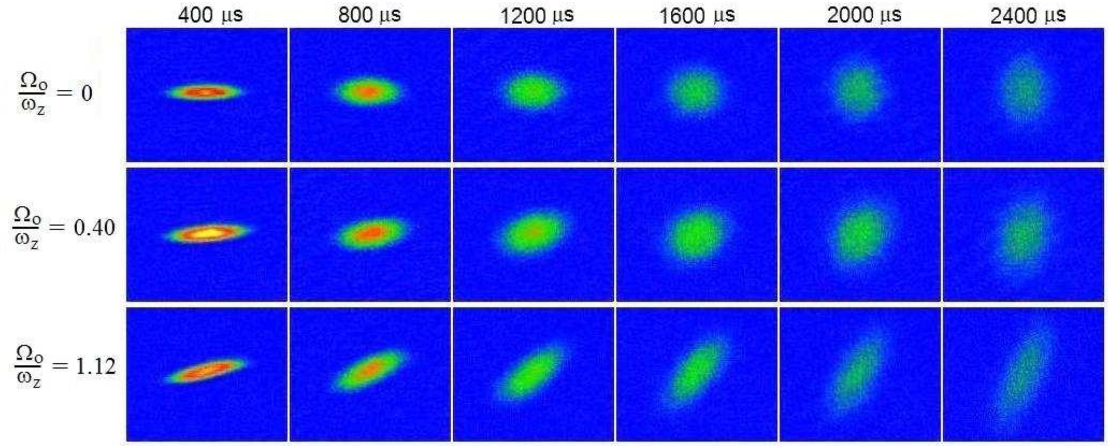

Figure 7.5: Expansion of a rotating, strongly interacting Fermi gas with different expanding time and different initial angular velocity. Ω_0, initial angular velocity; ω_z, trap axial frequency.

released without rotation of the trap, Fig. 7.5 (top), a strongly interacting Fermi gas expands anisotropically, as previously predicted [102] and observed [12]. In that case, the gas expands rapidly in the narrow (x, y) directions of the cigar while remaining nearly stationary in the long (z) direction. In the end the aspect ratio σ_x/σ_z is inverted as the cloud becomes elliptical in shape.

Quite different expansion dynamics occurs when the cloud is rotating prior to release shown in Fig. 7.5 (middle) and (bottom). In this case, the aspect ratio σ_x/σ_z initially increases toward unity. However, as the aspect ratio approaches unity, the moment of inertia decreases and the angular velocity of the principal axes increases to conserve angular momentum as previously predicted [98] and observed [99,100] in a superfluid BEC. After the aspect ratio reaches a maximum less than unity [98], it, as well as the angular velocity, begins to decrease when the angle of the cigar shaped cloud approaches a maximum value less than 90°.

Different from the case of a strongly interacting Fermi gas, at 528 G where the scattering length vanishes, we observe ballistic expansion of a rotating non-interacting Fermi gas. In that case, the aspect ratio asymptotically approaches unity, and there is no increase in angular velocity.

To determine the angle and aspect ratio, the measured density profiles are fit with a two-dimensional Gaussian distribution, which takes the form

$$f(\tilde{x},\tilde{z}) = A\exp[-a\tilde{z}^2 - b\tilde{z}\tilde{x} - c\tilde{x}^2], \tag{7.10}$$

where $\tilde{z},\tilde{x}$ are laboratory coordinates.

Accordingly, the two-dimensional Gaussian function in the coordinates of the principle axis of the rotating frame of the cloud is given by

$$f(x,z) = A\exp[-(\frac{x}{\sigma_x})^2 - (\frac{z}{\sigma_z})^2], \tag{7.11}$$

where $\sigma_{x,z}$ are defined as the Gaussian widths in the x and z direction.

From the values of a, b, c, the Gaussian widths $\sigma_{x,z}$, and the angle θ between the long z-axis of the cloud and the laboratory $\tilde{z}$-axis (anticlockwise is defined as the positive angle) are determined by

$$\begin{aligned}
\theta &= Arctan\left(\frac{b}{2(a-c)}\right) \\
\sigma_x^2 &= \begin{cases} \frac{2}{a+c+(a-c)\sqrt{1+\frac{b^2}{(a-c)^2}}} & \theta \leq \pi/4 \\ \frac{2}{a+c-(a-c)\sqrt{1+\frac{b^2}{(a-c)^2}}} & \theta > \pi/4 \end{cases} \\
\sigma_y^2 &= \begin{cases} \frac{2}{a+c-(a-c)\sqrt{1+\frac{b^2}{(a-c)^2}}} & \theta \leq \pi/4 \\ \frac{2}{a+c+(a-c)\sqrt{1+\frac{b^2}{(a-c)^2}}} & \theta > \pi/4. \end{cases}
\end{aligned} \tag{7.12}$$

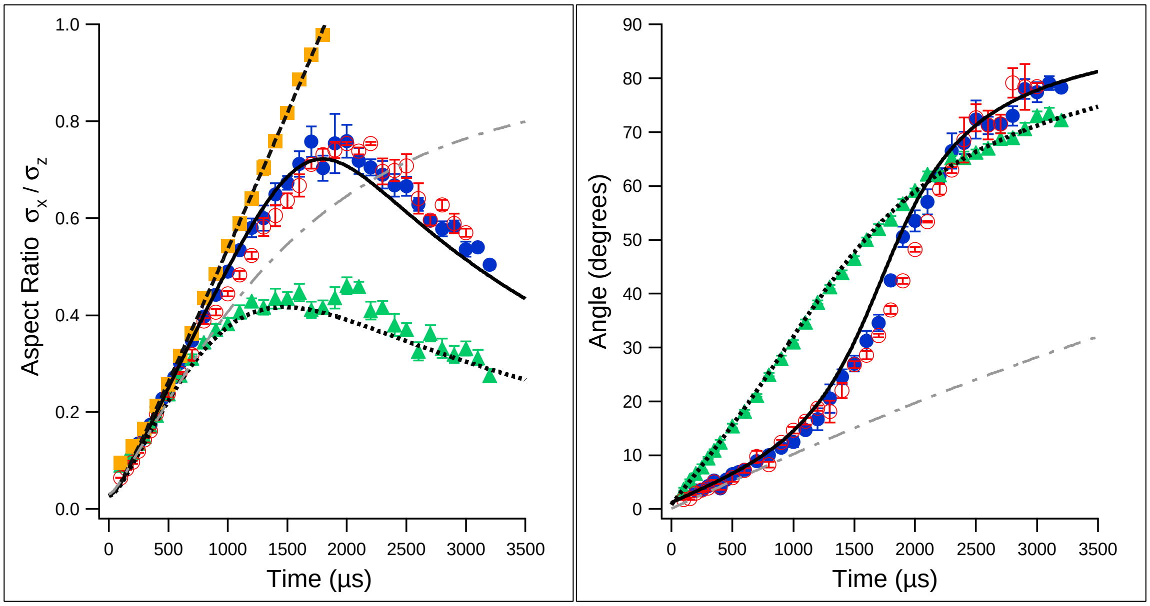

Figure 7.6: Aspect ratio and angle of the principal axis versus expansion time. Squares (aspect ratio for $\Omega_0 = 0$); Solid circles ($\Omega_0/\omega_z = 0.40$, $E/E_F = 0.56$); Open circles ($\Omega_0/\omega_z = 0.40$, $E/E_F = 2.1$); Triangles ($\Omega_0/\omega_z = 1.12$, $E/E_F = 0.56$). The dashed, solid, and dotted lines are theoretical calculations corresponding to the measured initial conditions. The gray dot-dashed line shows the energy-independent prediction for a ballistic gas with $\Omega_0/\omega_z = 0.40$.

Fig. 7.6 shows the measured aspect ratio and the angle of the principal axes versus expansion time, which are determined from the cloud images.

7.1.4 Modeling the Expansion Dynamics of a Rotating Cloud

We attempt to model the angle and aspect ratio data for a rotating cloud near the ground state (solid circles and triangles in Fig. 7.6). The model is based on a zero temperature hydrodynamic theory for the expansion of a rotating strongly interacting superfluid Fermi gas. The details of modeling the expansion dynamics are discussed in the dissertation of my colleague student Bason Clancy [39]. Here

I only give a brief introduction of the basic equations that we used to model the dynamics.

The similar hydrodynamic model was first used to describe the expansion dynamics of a rotating, weakly interacting BEC [98,103]. For perfect irrotational flow with $\nabla \times \mathbf{v} = 0$ and $\eta = 0$, the model of hydrodynamic expansion in free space consists of the continuity and Euler equations in the lab frame, which are given by

$$\frac{\partial n(\mathbf{r},t)}{\partial t} + \nabla \cdot (n\mathbf{v}) = 0, \tag{7.13}$$

$$\frac{\partial \mathbf{v}(\mathbf{r},t)}{\partial t} + \nabla \left(\frac{v^2}{2} + \mu(n) \right) = 0. \tag{7.14}$$

Here $n(\mathbf{r},t)$ and $\mathbf{v}$ are the cloud density and the velocity field respectively. The driving force for the expansion arises from the gradient of the chemical potential $\mu(n)$, which we take to be the zero temperature value for a strongly interacting Fermi gas [12,104] by

$$\mu(n) = (1+\beta)\frac{\hbar^2 (3\pi^2)^{\frac{2}{3}}}{2\,m}\, n^{\frac{2}{3}}. \tag{7.15}$$

We find that the hydrodynamic equations with the zero temperature chemical potential turn out to be a good approximation for modeling our data up to $E_0/E_F = 2$. We also include the force arising from the magnetic field curvature. The magnetic potential changes the angular momentum by 10% for the release time corresponding to the maximum aspect ratio, while changes the angle and aspect ratio by a few percent for the longest release times.

To determine the initial conditions for our model, we determine the initial angular velocity Ω_0 from the measured rotation angle versus time data during a short time just after release. The initial axial cloud radius σ_{z0} is obtained directly from the cloud images at the beginning of release, while assuming the initial transverse radius σ_{x0} is given by the zero temperature values according to the trap frequencies. The results yield excellent agreements with all the angle and aspect ratio data, with no free parameters, as shown in Fig. 7.6.

7.1.5 Measurement of Moment of Inertia

Eq. (7.3) enables a model-independent measurement of the effective moment of inertia $I \equiv L/\Omega$, where Ω is the angular velocity of the principal axes of the cloud after release. $L = \Omega_0 \, I_0$ is the initial angular momentum, which is conserved during the expansion. Note that we neglect the small change arising from the magnetic potential. The angular velocity Ω is calculated from the time derivative of a polynomial fit to the angle versus time data. The initial moment of inertia I_0 is for a cigar-shaped cloud with a large aspect ratio $\sigma_z/\sigma_x \approx 30$. In that case, the moment of inertia for the irrotational fluid is nearly equal to the rigid body value according to Eq. (7.5) for $\langle z^2\rangle_0 \ll \langle x^2\rangle_0$. For the clouds released from our cigar shape trap, $I_0 \simeq Nm\langle z^2\rangle_0$ within 0.3% accuracy, where $\langle z^2\rangle_0$ is measured from the cloud images. The measured effective moment of inertia after release is then $I(t) = I_0 \, \Omega_0/\Omega$.

The corresponding rigid body moment of inertia is determined from the fit to the cloud profile, $I_{rig}(t) = Nm\langle x^2 + z^2\rangle$. Hence, we obtain the ratio between the effective moment of inertia in the expansion and that of the rigid body value by

$$\frac{I(\Omega(t))}{I_{rig}} = \frac{\Omega_0}{\Omega(t)} \, \frac{I_0}{I_{rig}(t)}, \tag{7.16}$$

where all the quantities on the right side of the equation are measurable.

We note that the measured $I(\Omega)$ in our experiment generally is not the equilibrium moment of inertia of the cloud with a constant rotation frequency Ω. The equilibrium moment of inertia of the cloud requires that the velocity field of the normal and superfluid components reaches steady state after the cloud rotates enough time with a constant frequency [104]. However, in our highly cigar-shaped trap, whether the system is in equilibrium or not, the initial angular momentum is essentially equal to the rigid body value, independent of the superfluid and normal fluid composition. To see this physically, note that for rotation about the y-axis, the initial stream velocity for irrotatinal flow is $\mathbf{v} = \Omega_0 z\mathbf{i} + \Omega_0 x\mathbf{k}$, while for rotational flow, $\mathbf{v} = \Omega_0 z\mathbf{i} - \Omega_0 x\mathbf{k}$. These differ only for the z-components, which is negligible as the aspect ratio σ_x/σ_z tends to zero.

Fig. 7.7 shows the measured minimum value of $I_{min}(\Omega_{max})/I_{rig}$ as a function of initial angular velocity Ω_0. Fig. 7.7 indicates that the moment of inertia is quenched to well below the rigid body value for energies both above and below the superfluid transition.

For the coldest clouds (solid circles in Fig. 7.7), where the energy of the gas is close to that of the ground state, the gas is believed to be in the superfluid regime [24,45,49]. In this case, we observe values of I_{min}/I_{rig} as small as 0.05 in Fig. 7.7, smaller than those obtained from the scissors mode of a BEC of atoms [105,106]. The solid line shows I_{min}/I_{rig} predicted by the superfluid hydrodynamic theory, which is in very good agreement with our measurements. Such nearly perfect irrotational flow usually arises only in the superfluid regime. For example, normal weakly interacting Bose gases can not support irrotational flow above the critical temperature.

In contrast, for a normal strongly interacting Fermi gas (open circles in Fig. 7.7), we also observe significant quenching of the moment of inertia. To investigate the

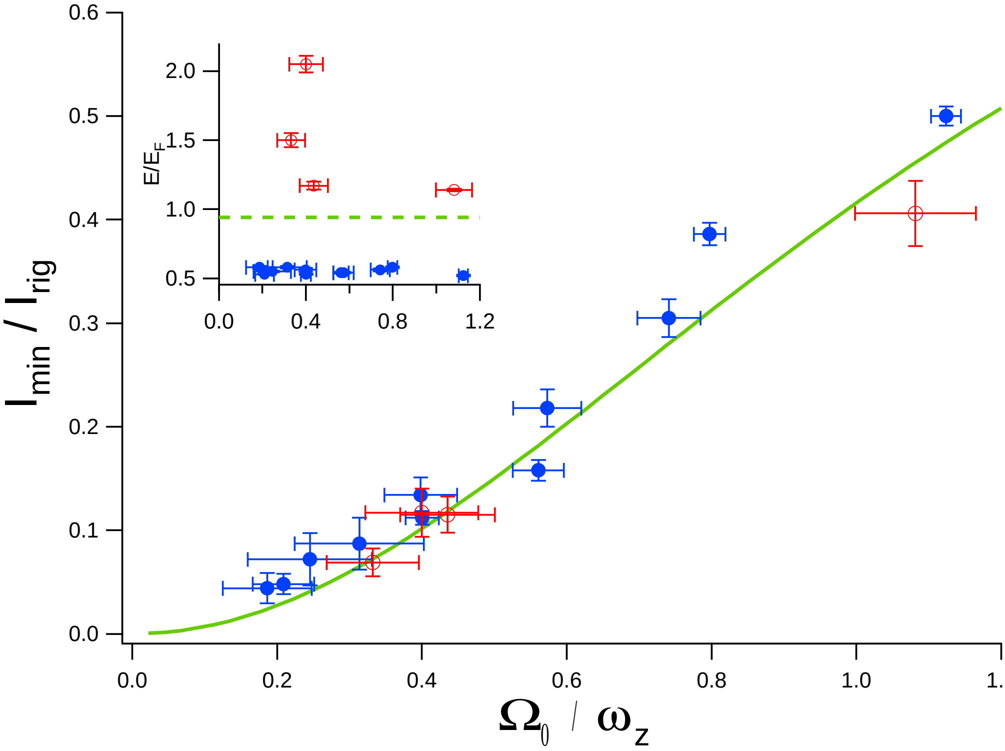

Figure 7.7: Quenching of the moment of inertia versus initial angular velocity Ω_0. I_{min}/I_{rig} is the minimum moment of inertia measured during expansion in units of rigid body value. Solid circles: initial energy before rotation below the superfluid transition energy $E_c = 0.94\,E_F$. Open circles: initial energy above E_c. Solid line: prediction for irrotational flow using a zero viscosity hydrodynamic model. Insert shows the energy for each data point with the dashed line at E_c.

normal fluid regime, we increase E up to $2.1\,E_F$, which is well above the transition energy of $E_c = 0.83\,E_F$ as estimated from the entropy experiment in Chapter 6. At $E = 2.1\,E_F$, the gas is in the normal phase and the measured entropy nearly coincides with that of an ideal gas [49]. The open circles in Fig. 7.6 show the aspect ratio and angle versus time for a cloud with $\Omega_0/\omega_z = 0.4$ and $E = 2.1\,E_F$. The results for the normal fluid are nearly identical to those obtained for $\Omega_0/\omega_z = 0.4$ in the superfluid regime (solid circles in Fig. 7.6).

The minimum value of I/I_{rig} occurs when the angular velocity Ω reaches its maximum value in the expansion. We find that the smaller Ω_0 is, the smaller the value of I_{min}/I_{rig}. This effect is a consequence of the conservation of both the energy and the angular momentum in the expansion. I will show this in the following: The initial energy of the gas has two parts $E_0 = E_{rot} + E_{exp}$, where $E_{rot} = \Omega_0^2\,I_0/2$ is the kinetic energy for the pure rotation and E_{exp} is the release energy for pure expansion. When the gas expands, the aspect ratio approaches unity. For a perfect irrotational fluid, Eq. (7.5) shows that the effective moment of inertia decreases dramatically, which results in an increase of Ω to conserve the angular momentum. This causes a transfer most of the energy into the rotational energy when Ω reaches the maximum. From the conservation of the energy and the angular momentum, we have

$$E_0 = \frac{\Omega_0^2\,I_0}{2} + E_{exp} = \frac{\Omega_{max}^2\,I_{min}}{2}, \tag{7.17}$$

$$L_0 = \Omega_0\,I_0 = \Omega_{max}\,I_{min}. \tag{7.18}$$

By solving the above equations for Ω_{max}, we get

$$\Omega_{max} = \Omega_0 + \frac{2\,E_{exp}}{\Omega_0\,I_0}, \tag{7.19}$$

$$I_{min} = \frac{I_0}{1 + \frac{2\,E_{exp}}{\Omega_0^2\,I_0}}. \tag{7.20}$$

Eq. (7.20) shows clearly that the smaller Ω_0 is, the smaller the value of I_{min} will be in the expansion.

We test Eq. (7.5) in a model-independent way, where the deformation parameter δ is measured with respect to the principal axes. Fig. 7.8 compares the measured minimum values of I_{min}/I_{rigid} with the values of δ^2. From the measured cloud radius $\sigma_{z,x}$ of a Gaussian shape in Eq. (7.11), δ^2 is directly obtained by

$$\delta^2 \equiv \frac{\langle z^2 - x^2\rangle^2}{\langle z^2 + x^2\rangle^2} = \frac{(\sigma_z^2 - \sigma_x^2)^2}{(\sigma_z^2 + \sigma_x^2)^2}. \tag{7.21}$$

The measurement directly verifies that the fundamental relation between the effective moment of inertia and the deformation parameter for ideal irrotational flow is valid in both the normal and superfluid regimes of a strongly interacting Fermi gas.

We attribute the observed irrotational flow in the normal strongly interacting fluid to low viscosity collisional hydrodynamics. After release from a harmonic trap, the stream velocity $\mathbf{v}$ is linear in the laboratory coordinates $\tilde{\mathbf{x}}$. For the rotation and expansion about the y-axis in free space, we have

$$\begin{aligned} v_{\tilde{x}} &= \alpha_x \tilde{x} + (\alpha + \hat{\Omega})\tilde{z}, \\ v_{\tilde{y}} &= \alpha_y \tilde{y}, \\ v_{\tilde{z}} &= \alpha_z \tilde{z} + (\alpha - \hat{\Omega})\tilde{x}. \end{aligned} \tag{7.22}$$

Here, $\alpha_i(t)$ and $\alpha(t)$ describe the irrotational velocity field and $\hat{\Omega(t)}$ is the rotational part. With zero viscosity, the hydrodynamic equations of motion yield the result [39]

$$\frac{\partial \hat{\Omega}}{\partial t} + (\alpha_x + \alpha_z)\hat{\Omega} = 0. \tag{7.23}$$

After release, when the stream velocity increases, α_x becomes the order of ω_x. Hence, $\hat{\Omega}$ decays rapidly on the time scale $1/\omega_x << 1/\hat{\Omega}$. That means for negligible viscosity, the gas cannot maintain the rigid body rotation during expansion.

7.2 Measuring Quantum Viscosity by Collective Oscillations

Our lab had measured the frequency and damping of a radial collective breathing mode in a strongly interacting Fermi gas over a wide range of temperatures. At temperatures both below and well above the superfluid transition, the frequency of the mode is nearly constant and very close to the hydrodynamic value. Below the transition temperature, this hydrodynamic behavior is explained by superfluidity [19, 20]. However, at temperatures well above the superfluid transition, the observed hydrodynamic frequency and the damping rate are not consistent

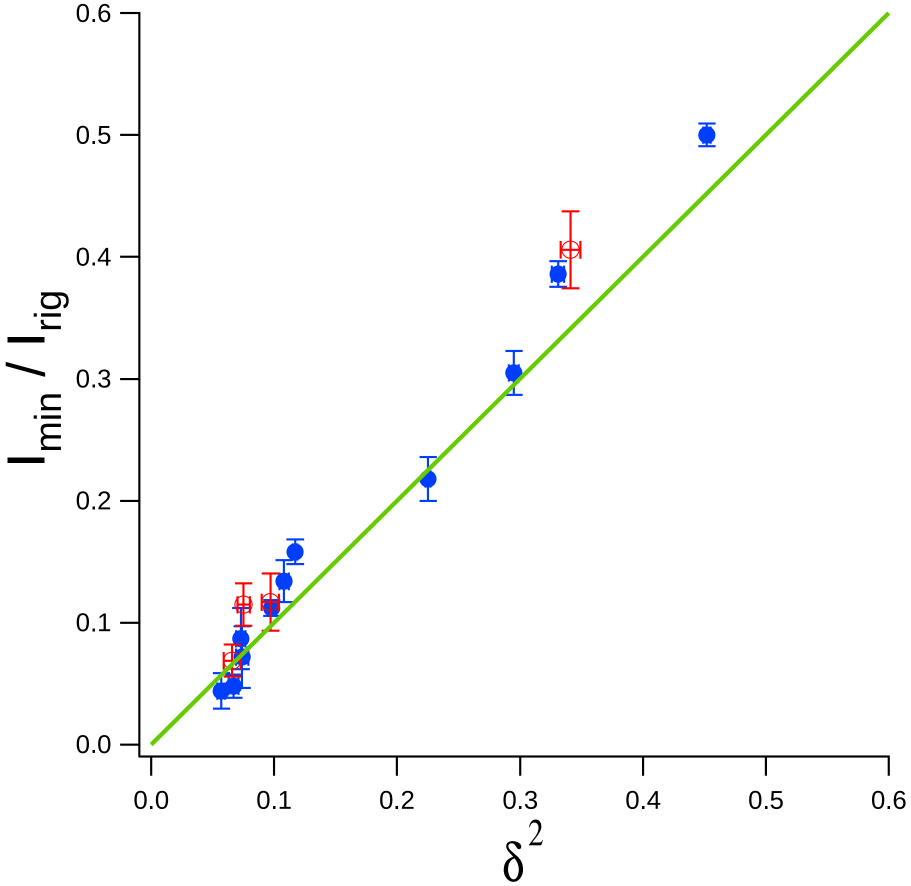

Figure 7.8: Quenching of the moment of inertia versus the square of the measured cloud deformation factor δ. Solid circles: initial energy below the superfluid transition energy $E_c = 0.94\, E_F$. Open circles: initial energy above E_c. Solid line: the prediction for ideal irrotational flow.

with a model of a collisional normal gas [50, 107]. The microscopic mechanism for hydrodynamic properties at high temperatures still remains as an open question.

In this chapter, I will present the damping rate as a function of the energy of the gas instead of the empirical temperature used in our previous study. Then a hydrodynamic equation with the quantum viscosity term is applied to estimate an upper bound on the viscosity. Furthermore, using our measured entropy of the gas, we estimate the ratio of the shear viscosity to the entropy density in strongly interacting Fermi gases, and compare the result with the prediction from string theory methods [3], which gives the lower bound of this ratio

$$\frac{\eta}{s} \geq \frac{1}{4\pi}\frac{\hbar}{k_B}. \tag{7.24}$$

7.2.1 Hydrodynamic Breathing Mode

The breathing mode data we used to estimate the viscosity was obtained in our previous measurements and described in Joseph Kinast's dissertation [64]. Here I only review it for the purpose of extracting the viscosity. Our breathing mode experiments start by preparing a strongly interacting Fermi gas of ^{6}Li. At the final trap depth, the trap aspect ratio $\lambda = \omega_z/\omega_\perp = 0.045$ ($\omega_\perp = \sqrt{\omega_x\omega_y}$) and the mean oscillation frequency $\bar{\omega} = (\omega_x\omega_y\omega_z)^{1/3} = 2\pi \times 589(5)$ Hz including anharmonicity corrections. The shape of the trap slightly departs from cylindrical symmetry by $\omega_x/\omega_y = 1.107(0.004)$. Typically, the total number of atoms after evaporative cooling is $N = 2.0(0.2)\times 10^5$. The corresponding Fermi temperature $T_F \simeq 2.4\,\mu K$ at the trap center. After the preparation of the gas at nearly the ground state, the energy of the gas is increased from the ground state value by abruptly releasing the cloud and then recapturing it after a short expansion time t_{heat}, which is same

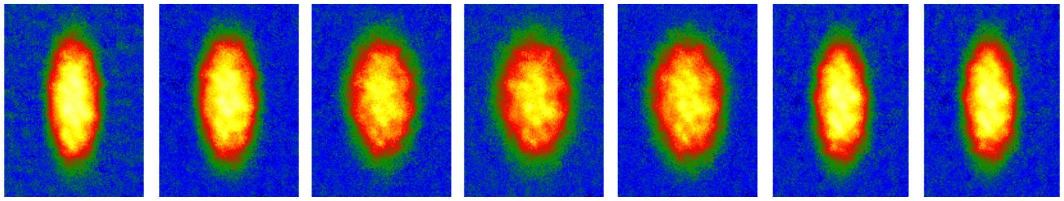

Figure 7.9: The gas after oscillating for a variable time t_{hold}, followed by release and expansion for 1 ms. t_{hold} is increasing from left to right for a complete oscillation period.

as the method we used in the entropy experiments. After waiting for the cloud to reach equilibrium, the sample is ready for subsequent measurements.

In the experiments, the radial breathing mode is excited by releasing the cloud and recapturing the atoms after 25 μs. After the excitation, we let the cloud oscillate for a variable time t_{hold}. Then the gas is released and imaged after $\simeq$ 1 ms of expansion [20]. The oscillating clouds are shown in Fig. 7.9.

The breathing mode of the gas has been investigated in our group [19,20,108]. The frequency and the damping rate is measured as functions of an empirical temperature. However,equilibrium thermodynamic properties of the trapped gas, as well as dynamical properties, can be measured as functions of either the temperature or the total energy per particle. In the strongly interacting regime, the temperature is difficult to obtain. In contrast, as described in Chapter 4, the cloud energy can be directly measured in a model-independent way from the mean square axial cloud size by

$$E = 3m\omega_z^2\langle z^2\rangle, \tag{7.25}$$

where z is the axial direction of the cigar-shaped cloud.

In this thesis, I represent the previous measurement on the frequency and

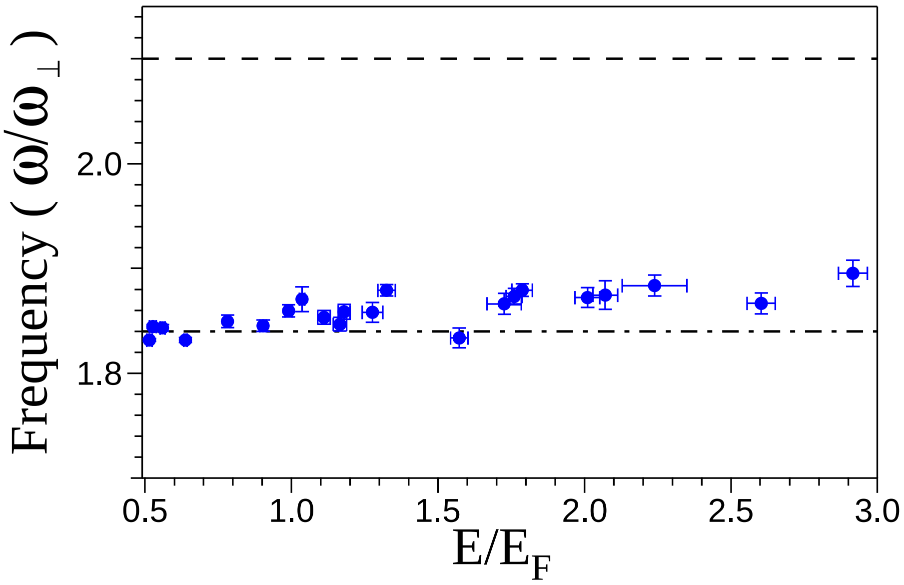

Figure 7.10: The frequency of a breathing mode versus the energy in a strongly-interacting gas. Normalized frequency versus the normalized energy per particle. The superfluid phase transition is located at $E_c \simeq E_F$. The upper dotted line shows the frequency for a noninteracting gas $\omega = 2.10\,\omega_\perp$. The bottom dot-dash line shows the frequency for a hydrodynamic fluid in the strongly interacting regime $\omega = 1.84\,\omega_\perp$.

damping rate in term of the total energy per particle in the trap. The frequency and damping are obtained by fitting the oscillating cloud sizes by $a+e^{-t/\tau}Cos(\omega t+\phi)$, where τ is the damping time and ω is the angular frequency of the oscillation. Corresponding to the temperature range of $T = 0.12 - 1.1\,T_F$ we measured before [19], the converted energy range is from nearly the ground state value $\simeq 0.5\,E_F$ to about $3.0\,E_F$.

The frequency of a breathing mode versus the energy is shown in Fig. 7.10 while the damping rate versus the energy is shown in Fig. 7.11.

In Fig. 7.10, the frequency stays far below the frequency of a noninteracting gas. No signatures of the superfluid transition are seen in the frequency de-

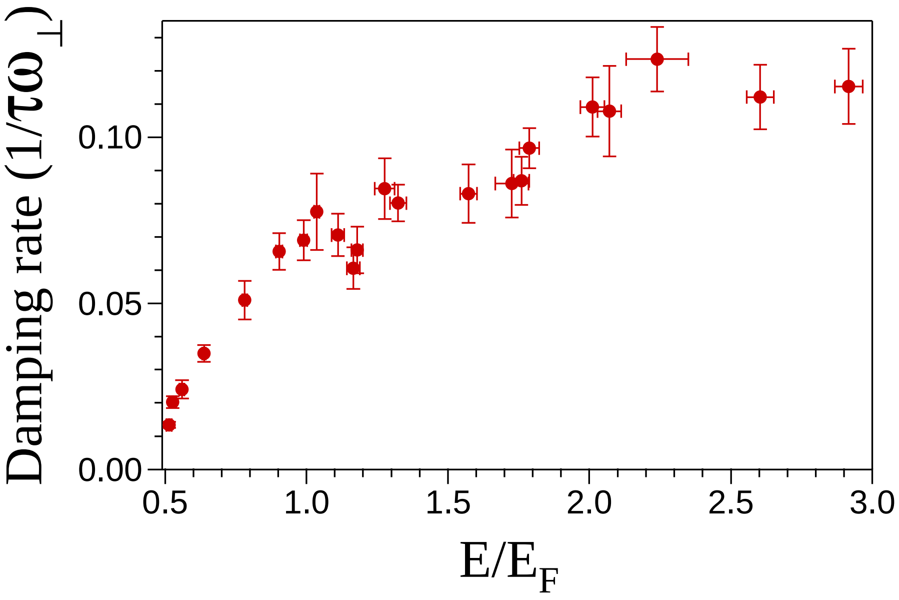

Figure 7.11: The normalized damping rate $1/\omega_\perp \tau$ versus the normalized energy per particle of a breathing mode in a strongly interacting Fermi gas.

pendence. Instead, in Fig. 7.11, the damping rate exhibits interesting features. At $E_c = 1.01\, E_F$ we observes a clear change in the damping versus energy dependance. The monotonic rise switches to flat dependance, which might be a signature of a phase transition.

In the next section, I will provide a hydrodynamic model to exact the viscosity from the above breathing mode data.

7.2.2 Determining the Quantum Viscosity from the Breathing Mode Damping

In this section, I will extract the the viscosity from the damping data based on a hydrodynamic equation with the viscous relaxation. Then I will compare this viscosity with that estimated by a kinetic model that uses a Boltzmann equation approach. This model takes into account strong coupling effects in thermodynamics and gives rise to a pseudogap in the spectral density for single-particle excitation [107].

In a strongly interacting Fermi gas, where the interparticle separation $l \propto 1/k_F$ sets the length scale, there is a natural unit of shear viscosity η that has dimension of the momentum divided by the area. The relevant momentum is the Fermi momentum, $\hbar k_F = \hbar/l$. The relevant area is determined by the unitarity-limited collision cross section $4\pi/k_F^2 \propto l^2$. Hence, $\eta \propto \hbar/l^3 = \hbar n$ [94], where n is the local total density. We can write

$$\eta = \alpha\,[T/T_F(n)]\;\hbar n, \tag{7.26}$$

where α is generally a dimensionless function of the local reduced temperature $T/T_F(n)$, where $T_F(n) \equiv \hbar^2(3\pi^2 n)^{2/3}/(2mk_B)$ is the local Fermi temperature. Eq. (7.26) shows that viscosity has a natural quantum scale, $\hbar n$. If the coefficient α is of order unity or smaller, the system is in the quantum viscosity regime [94]. For comparison, the normal fluid, such as water in room temperature has α of about 300, and air in room temperature has α of about 6000.

This viscosity can be used to determine the damping rate of collective modes of a trapped unitary Fermi gas. We begin with the equation for viscous flow [109]. We assume a small viscosity, and also assume approximately isentropic conditions for the gas oscillation. Then, the stream velocities of the normal and superfluid components must be equal, since the entropy per particle is different in the superfluid and normal components. We also assume that the local total density n and the stream velocity $\mathbf{u}$ obey a simple hydrodynamic equation of motion.

The convective derivative of the stream velocity $\mathbf{u}$ is the local acceleration which depends on the forces arising from the local pressure P and the trap potential U. For irrotational flow, $\nabla \times \mathbf{u} = 0$, we insert $\mathbf{u} \cdot \nabla \mathbf{u} = \nabla(\mathbf{u}^2/2)$ into the Navier-Stokes equations [91] and obtain

$$m\frac{\partial \mathbf{u}}{\partial t} = -\nabla\left(\frac{m}{2}\mathbf{u}^2 + U\right) - \frac{\nabla P}{n} + \frac{\nabla \overset{\leftrightarrow}{P'}}{n}, \tag{7.27}$$

where m is the bare atom mass since the interaction is generally included in the pressure term. P is the scalar pressure. For a unitary gas, according to Eq. (4.5), the scalar pressure takes the form

$$P(\mathbf{x}) = \frac{\hbar^2}{m} n^{5/3}\, f_P[T/T_F(n)], \tag{7.28}$$

where f_P is a dimensionless function and $\mathbf{x}$ is the position in the the cloud contained in a harmonic trap.

The viscosity arises in the pressure tensor $\overset{\leftrightarrow}{P'}$, which takes the form [110]

$$P'_{ij} = \eta\left(\frac{\partial u_i}{\partial x_j} + \frac{\partial u_j}{\partial x_i} - \frac{2}{3}\,\delta_{ij}\,\nabla\cdot\mathbf{u}\right) + \delta_{ij}\,\zeta\,\nabla\cdot\mathbf{u}, \tag{7.29}$$

where $\eta = \eta(\mathbf{x})$ is the shear viscosity, and ζ is the bulk viscosity that we neglect here for simplicity.

Initially, the gas is in a harmonic trap at a uniform temperature T_0 and has a density $n_0 \equiv n_0(\tilde{\mathbf{x}})$, where $\tilde{\mathbf{x}}$ is the position in the initial distribution. Force balance in the equilibrium state requires

$$\frac{\nabla_{\tilde{\mathbf{x}}} P_0(\tilde{\mathbf{x}})}{n_0(\tilde{\mathbf{x}})} = -\nabla_{\tilde{\mathbf{x}}} U(\tilde{\mathbf{x}}), \tag{7.30}$$

where $P_0(\tilde{\mathbf{x}})$ is the equilibrium pressure.

For small viscosity, we can solve Eq. (7.27) assuming a scaling ansatz [102,111], where each dimension changes by a scale factor $b_i(t)$, $i = x, y, z$, and $b_i(0) = 1$. The position is given by $\mathbf{x} \equiv (\tilde{x} b_x, \tilde{y} b_y, \tilde{z} b_z)$. The density and stream velocity then take the forms

$$\begin{aligned} n(\mathbf{x}, t) &= \frac{n_0(\tilde{\mathbf{x}})}{\Gamma}, \\ u_x = x\,\frac{\dot{b}_x(t)}{b_x(t)},\ u_y &= y\,\frac{\dot{b}_y(t)}{b_y(t)},\ u_z = z\,\frac{\dot{b}_z(t)}{b_z(t)}. \end{aligned} \tag{7.31}$$

Here an atoms is at the position $\tilde{\mathbf{x}}$ at time $t = 0$ while at position $\mathbf{x}$ at time t. $\Gamma \equiv b_x b_y b_z$ is the volume scale factor. The scaling ansatz is exact for $\eta = 0$ if the gas is contained in a harmonic trap and the pressure takes the form $P = c\, n^{\gamma}$, where c and γ are constants [102, 111].

For the breathing mode with small viscous relaxation, the gas flows under locally isentropic conditions [48], then the local reduced temperature does not change as the gas expands, which ensures $f_P[T/T_F[n(\mathbf{x})]] = f_P[T_0/T_F[n_0(\tilde{\mathbf{x}})]]$. Here T_0 is the initial temperature. In this case that local equilibrium is maintained, the pressure P is simply related to P_0 by

$$P(\mathbf{x}) = \frac{P_0(\tilde{\mathbf{x}})}{\Gamma^{5/3}}. \tag{7.32}$$

From Eq. (7.32), we have

$$\frac{\nabla_{\mathbf{x}} P(\mathbf{x})}{n(\mathbf{x})} = \frac{\nabla_{\mathbf{x}} P_0(\tilde{\mathbf{x}})}{n(\mathbf{x})\,\Gamma^{5/3}}. \tag{7.33}$$

Using $n_0(\tilde{\mathbf{x}}) = n(\mathbf{x})\Gamma$ in the above equation and applying the force balance relation by replacing $\nabla_{\tilde{\mathbf{x}}} \to \nabla_{\mathbf{x}}$ in Eq. (7.30), we obtain

$$\frac{\nabla_{\mathbf{x}} P(\mathbf{x})}{n(\mathbf{x})} = \frac{-\nabla_{\mathbf{x}} U(\tilde{\mathbf{x}})}{\Gamma^{2/3}}. \tag{7.34}$$

Note that the spatial derivatives of the velocity field are diagonal and position independent due to the scaling ansatz. Hence, the derivative of the pressure tensor is simplified to a vector, whose effects arises only through the spatial variation of the viscosity by

$$(\nabla \overset{\leftrightarrow}{P'})_i = \frac{\partial \eta}{\partial x_i}\left(2\frac{\dot{b}_i}{b_i} - \frac{2}{3}\Sigma_j \frac{\dot{b}_j}{b_j}\right). \tag{7.35}$$

By using Eq. (7.34) and Eq. (7.35) in Eq. (7.27), we obtain

$$m\frac{\partial u_i}{\partial t} = -\frac{\partial}{\partial x_i}\left(\frac{m}{2}\mathbf{u}^2 + U(\mathbf{x}) - \frac{U(\tilde{\mathbf{x}})}{\Gamma^{2/3}}\right) + \frac{1}{n}\frac{\partial \eta}{\partial x_i}\left(2\frac{\dot{b}_i}{b_i} - \frac{2}{3}\Sigma_j \frac{\dot{b}_j}{b_j}\right). \tag{7.36}$$

Note that the damping term vanishes for an isotropic trap, where all of the $\dot{b}_i/b_i$ are the same.

Now let us consider the radial breathing mode in a cylindrical trap $U(\mathbf{x}) = m\omega_\perp^2(x^2+y^2)/2 + m\omega_z^2 z^2/2$ with $\lambda = \omega_z/\omega_\perp << 1$. In that case, we can take $b_x = b_y = b_\perp$ and $b_z \simeq 1$, with $\dot{b}_z \simeq 0$. Eq. (7.36) then yields the result for the cylindrical trap

$$m\tilde{x}\ddot{b}_\perp = -m\omega_\perp^2 \tilde{x}\left(b_\perp - \frac{1}{b_\perp^{7/3}}\right) + \frac{2}{3}\frac{\partial \eta}{\partial \tilde{x}}\frac{1}{n}\frac{\dot{b}_\perp}{b_\perp^2}. \tag{7.37}$$

To calculate the average viscous effects for a trapped gas, we multiply Eq. (7.37) by $\int d^3\tilde{\mathbf{x}}\,\tilde{\mathbf{x}}\,n_0(\tilde{\mathbf{x}})/N$ and use the definition of $\langle \tilde{x}^2 \rangle \simeq \int d^3\tilde{\mathbf{x}}\,\tilde{\mathbf{x}}^2\,n_0(\tilde{\mathbf{x}})/N$. Finally we obtain

$$\ddot{b}_\perp + \omega_\perp^2\left(b_\perp - \frac{1}{b_\perp^{7/3}}\right) + \frac{2}{3}\frac{\int d^3\mathbf{x}\,\eta(\mathbf{x})}{m\langle \tilde{x}^2\rangle N}\frac{\dot{b}_\perp}{b_\perp^2} = 0. \tag{7.38}$$

It is noting that to get the above equation I use the following result of the integration

$$\int d^3\mathbf{x}\,\frac{\partial(\eta\mathbf{x})}{\partial x} = 0, \tag{7.39}$$

which is due to the viscosity disappearing at the boundary of the cloud.

For small vibrations, we take $b_\perp = 1 + \epsilon_\perp$ and $b_z = 1 = \epsilon_z$. Eq. (7.38) yields the equation for radial breathing oscillation

$$\ddot{\epsilon}_\perp + \frac{10\omega_\perp^2}{3}\epsilon_\perp + \frac{2}{3}\frac{\langle\alpha\rangle\hbar}{m\langle\tilde{x}^2\rangle}\dot{\epsilon}_\perp = 0, \tag{7.40}$$

where the oscillation frequency $\omega = \sqrt{10/3}\,\omega_\perp$, and the corresponding damping rate $1/(\omega_\perp\tau_\perp)$ is given by

$$\frac{1}{\omega_\perp\tau_\perp} = \frac{1}{3}\frac{\langle\alpha\rangle\hbar}{m\omega_\perp\langle\tilde{x}^2\rangle}. \tag{7.41}$$

Here we have used the trap average value of α by $\langle\alpha\rangle\hbar = \int d^3\mathbf{x}\,\eta(\mathbf{x})/N$.

We determine the energy per particle according to the virial theorem by $E = 3m\omega_\perp^2\langle\tilde{x}^2\rangle$. Using this equation in Eq. (7.41), we easily obtain the damping ratio

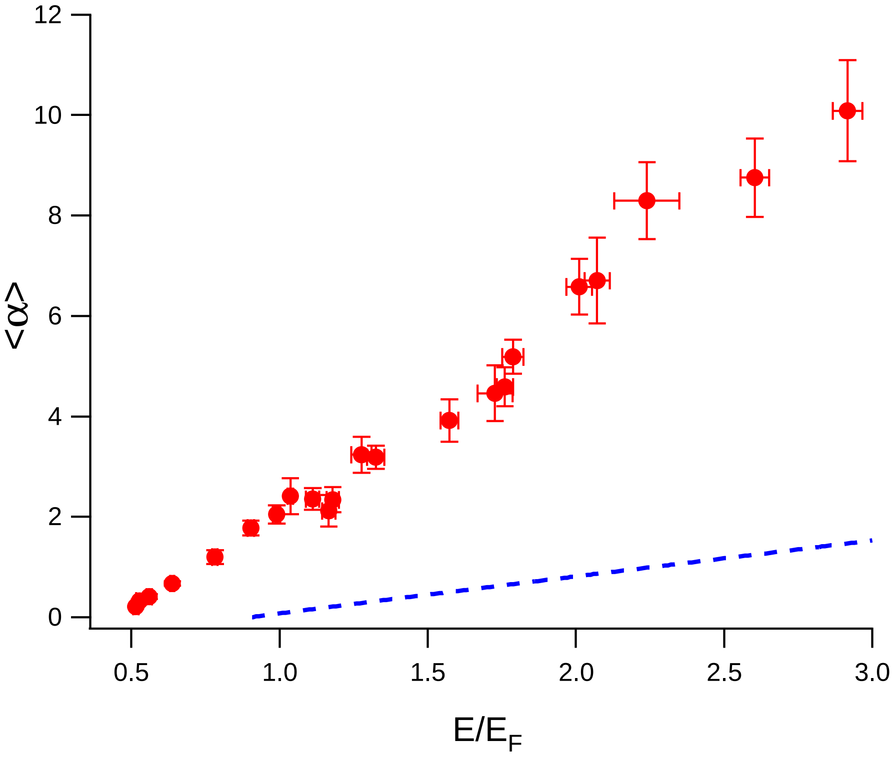

Figure 7.12: Quantum viscosity in a strongly-interacting Fermi gas. The local shear viscosity takes the form $\eta = \alpha\,\hbar\,n$. In the figure, $\langle\alpha\rangle$ is a trap-averaged value of the dimensionless parameter α. The dashed line is the theoretical prediction from Eq. (7.45).

$1/(\omega_\perp\tau_\perp)$ as a function of energy and $\langle\alpha\rangle$

$$\frac{1}{\omega_\perp\tau_\perp} = \frac{\hbar\omega_\perp}{E}\langle\alpha\rangle. \tag{7.42}$$

Using this relation and the damping rate of the radial breathing mode shown Fig. 7.11, we determine $\langle\alpha\rangle$ as a function of the energy as shown in Fig. 7.12.

It is quite interesting to compare our result with the theoretical calculation of α by Bruun and Smith [107]. In their prediction, α for the normal gas $T > T_c$ is given by the temperature dependence by

$$\alpha = -0.2 + 2.77(T/T_F^*)^{3/2}. \tag{7.43}$$

Note that Eq. (7.43) is for a uniform gas, where T_F^* is the Fermi temperature corresponding to a noninteracting gas with a uniform density. By contrast, for a trapped gas, we used T_F, the Fermi temperature for a noninteracting gas at the center of a harmonic trap. Now I use an approximate method to relate T_F^* with T_F. I assume T_F^* is the local Fermi temperature corresponding to the local density of a strongly interacting Fermi gas in the center of our harmonic trap. As we know from Chapter 4, the width of a strongly interacting Fermi gas gas decrease a factor of $(1 + \beta)^{1/4}$ comparing with a noninteracting Fermi gas. Accordingly the volume decreases by $(1 + \beta)^{3/4}$, and the density n increases by $1/(1 + \beta)^{3/4}$. Because the local Fermi temperature $T_F^* \propto n^{2/3}$, T_F^* increases by $1/(1+\beta)^{1/2}$ compared to T_F. Using $\beta = -0.59$ from our entropy measurement, I have $T_F^* = T_F/(1 + \beta)^{1/2} = 1.56\,T_F$, so I rewrite Eq. (7.43) as

$$\alpha = -0.2 + 2.77(0.64T/T_F)^{3/2}, \tag{7.44}$$

where T_F is the Fermi temperature for a harmonically trapped gas.

Using the relation of the reduced temperature T/T_F versus the reduced energy E/E_F above the critical energy in Eq. (6.18) from the entropy measurement, the energy dependence of α is given by

$$\alpha = -0.2 + 0.14[5.84(E - 0.83) + 1]^{0.96};\ E \geq E_c = 0.83E_F. \tag{7.45}$$

Our measured trap average α is significant larger than the prediction from the kinetic model with strong coupling effects. One possible reason for the higher measured viscosity is that other sources of relaxation may contribute the damping, such as anharmonicity of the trap potential and other effects due to the low density of the gas at the cloud edge, where the cloud is not hydrodynamic. Thus, our data from the breathing mode experiments only indicate the upper bound of the viscosity in a strongly interacting Fermi gas. Recently, we have found that viscosity can also be extracted from the expansion dynamics of a rotating strongly interacting Fermi gas which provides much lower values of α [39] and is very close to the prediction of the theoretical model.

7.2.3 η/s of a Strongly Interacting Fermi Gas

A string theory method has shown that for a wide class of strongly interacting quantum fields, the ratio of the shear viscosity to the entropy density has a universal minimum value [3], which gives $\eta/s \geq \hbar/(4\pi k_B) = 6.08 \times 10^{-13} K \cdot s$.

Based on the measurements on the shear viscosity and the entropy in this dissertation, we should be able to answer the important question: How close does η/s in a strongly interacting Fermi gas comes the quantum limit?

I separately integrate the numerator and denominator over the trap volume. Note that I use $\int d^3\mathbf{x}\, n = N$, where N is the total number of atoms. Also I have $\int d^3\mathbf{x}\, n\, \alpha(\mathbf{x}) \equiv N\langle\alpha\rangle$, where $\langle\alpha\rangle$ is the trap average of the dimensionless universal function α, and $\int d^3\mathbf{x}\, s = NS$, where S is the entropy per particle. Finally I get

$$\frac{\eta}{s} \simeq \frac{\int d^3\mathbf{x}\, \eta}{\int d^3\mathbf{x}\, s} = \frac{\hbar}{k_B}\frac{\langle\alpha\rangle}{S/k_B}. \tag{7.46}$$

Using the values of $\langle\alpha\rangle(E)$ in Fig. 7.12 and the measured entropy $S(E)$ in Fig. 6.5, we estimate the ratio of the viscosity to entropy density shown in Fig. 7.13. Note that the superfluid transition occurs near $E = 0.83E_F$, above which the gas is normal. We can make a comparison between the cold Fermi gases with other quantum systems with very low viscosity. For example, ^{3}He and ^{4}He near the λ-point have $\eta/s \simeq 0.7\hbar/k_B$, while for a quark-gluon plasma, a current theoretical estimate [112] shows $\eta/s = 0.16 - 0.24\hbar/k_B$.

In conclusion, in this chapter we have explored the perfect fluidity of a strongly interacting Fermi gas. We found that nearly perfect irrotational flow arising in both the superfluid and normal fluid regimes of a strongly interacting Fermi gas. This observation not only demonstrates the zero viscosity behavior of the superfluidity, but also indicates the nearly perfect fluidity of a normal system with the extremely low viscosity close to the quantum limit. We extract the viscosity from the measurements of the radial breathing mode. The measured viscosity reveals an upper bound of the viscosity in a strongly interacting Fermi gas. By combining the viscosity and entropy data, we estimate the viscosity over entropy density ratio (η/s), which shows that strongly interacting Fermi gases enter into the quantum viscosity regime.

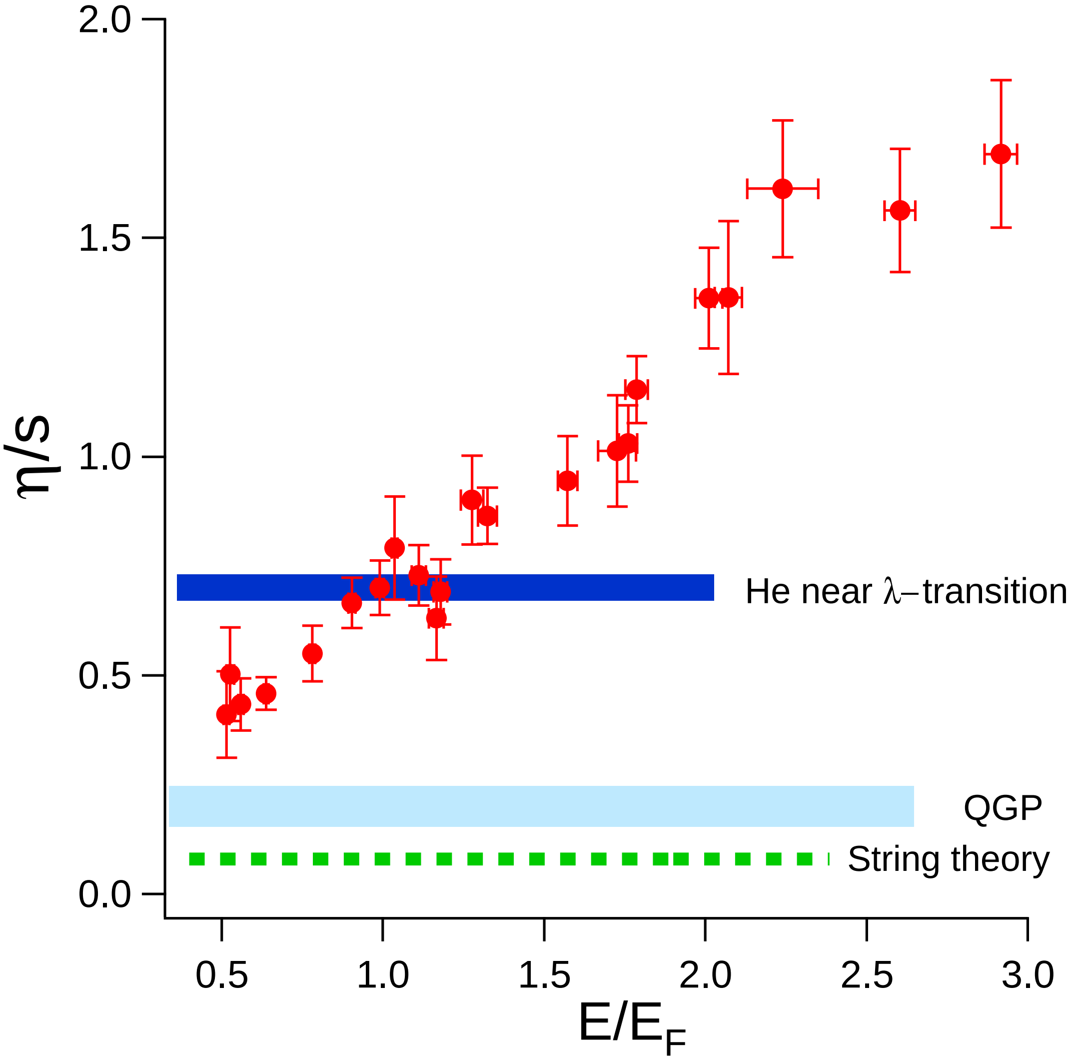

Figure 7.13: The ratio of the shear viscosity η to the entropy density s (in units of $\hbar/k_B$) for a strongly interacting Fermi gas as a function of energy E, red solid circles. The lower dotted line shows the string theory prediction $1/(4\pi)$. The light grey bar shows the estimate for a quark-gluon plasma (QGP) [112], while the solid black bar shows the estimate for ^{3}He and ^{4}He, near the λ- point.

Chapter 8

Building an All-Optical Cooling and Trapping Apparatus

In this chapter, I will describe the techniques of building a new all optical cooling and trapping apparatus for ^{6}Li atoms. Our apparatus uses a Zeeman slower to load a magneto-optical trap (MOT), then directly loads the atoms from the MOT to a stable CO_2 laser optical dipole trap for evaporative cooling. I will divide the apparatus into several subsystems, and describe the design, building and function of core components in each subsystem. My main effort is to explain how to build a stable CO_2 laser optical dipole trap, and describe the electronics, optics and vacuum viewports required for this high power infrared optical trap.

8.1 Ultrahigh Vacuum Chamber

To create an ultracold degenerate Fermi gas, the vacuum for trapping atoms is required to be 10^{-11} torr to reduce atoms heating and loss due to collisions with background gases. There are two major difficulties for creating such ultrahigh vacuum for the application of CO_2 laser trapping of ^{6}Li. First, ^{6}Li is a solid at room temperature with a melting point of 181 °C. To provide adequate atom flux, we need to use an oven to heat ^{6}Li up to 430 °C. So the vacuum for "experimental region" should be isolated with "oven region" to get the extremely high vacuum. Second, CO_2 laser beam needs viewports made of infrared optical materials, such as crystalline zinc selenide (ZnSe), which is very soft material inappropriate for standard sealing techniques used for ultrahigh vacuum.

Here we discuss the isolation problem first and describe making ZnSe viewports in Section 8.6. The isolation between the "experimental region" and "oven region" is achieved by the vacuum system design. The schematic diagram for the vacuum system is shown in Fig. 8.1, where a Zeeman slower is inserted between an oven and a main chamber. The zeeman slower also provides a differential pumping, which makes the vacuum pressure in the main chamber much smaller than that in the oven region. The main chamber is designed with a pancake geometry, which allows us to reduce the vertical distance between a pair of high field magnets above and below the chamber. This enables us to obtain high magnetic field with smaller currents and lower power. The main chamber is designed by our group and made by MDC Vacuum Products with a polish of the inside surface to reduce outgassing. The actual dimension of the vacuum chamber is listed in Fig. 8.2

8.2 ^{6}Li Cold Atom Source

The ^{6}Li cold atom source, which consists of an oven and a zeeman slower, provides a slow atom beam with substantial amount of atoms at a speed of about 100 m/s.

8.2.1 Lithium Oven

The design of lithium oven is shown in Fig. 8.3. The lithium oven is operated at the temperature of $300 \sim 500$ °C. The hottest part is the chamber and its

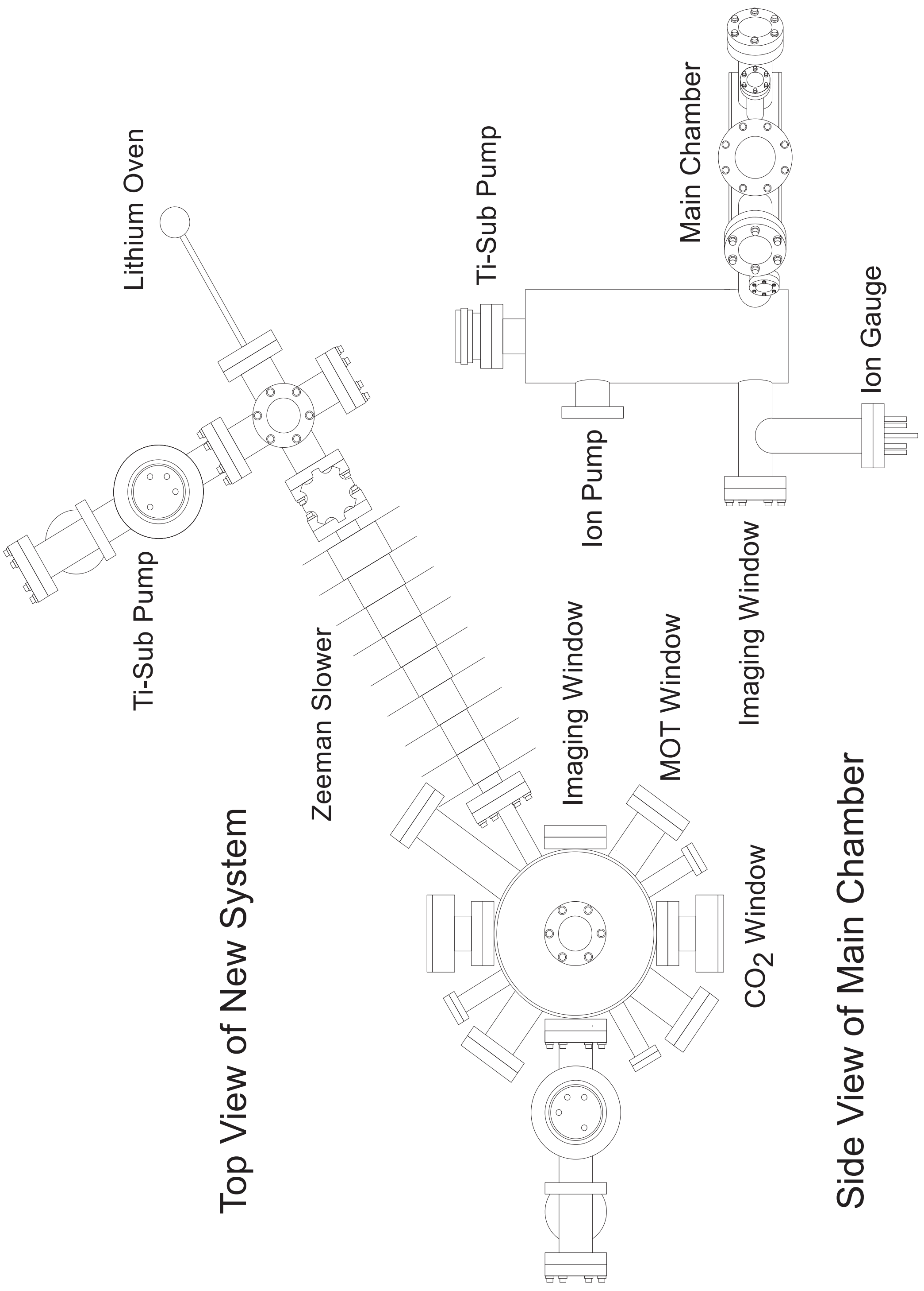

Figure 8.1: The ultrahigh vacuum system (not to scale). The port labels will be used throughout the thesis to describe the experimental setup.

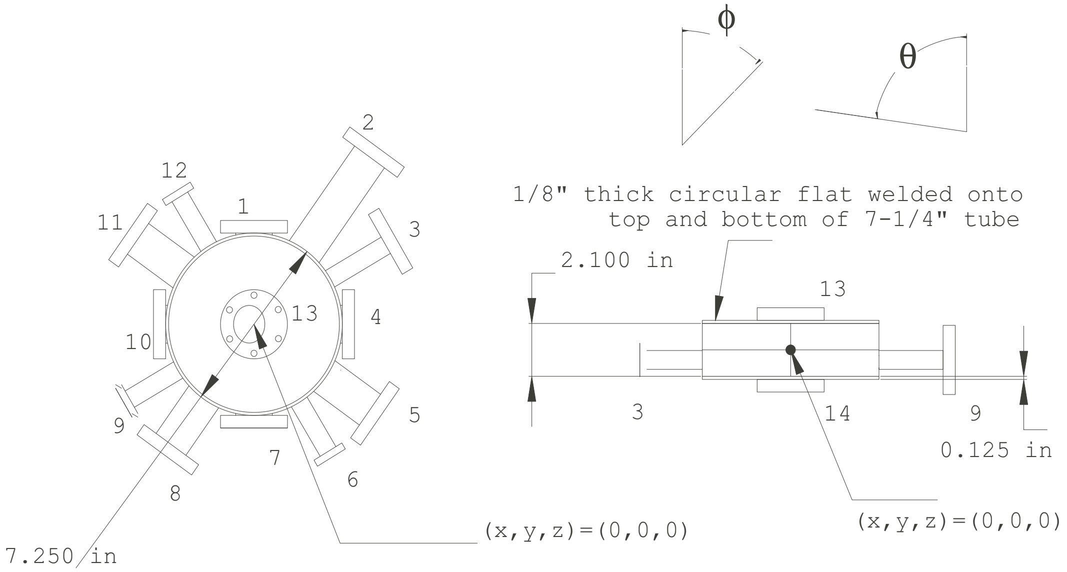

Port#	Focal Length (in)	θ	ϕ	Focal Point X	Focal Point Y	Focal Point Z	Conflat Size	Tube O.D.	Port Application
1	4.125	90	0	0	0	0	2-3/4 in	1.5 in	CO2 window
2	8.675	90	35.5	0	0	0	2-3/4 in	1.5 in	MOT window
3	6.75	90	59.8	0	0	-.4	2-3/4 in	0.75 in	Slow beam out
4	4.125	90	90	0	0	0	2-3/4 in	1.5 in	Imaging beam out
5	6.35	90	125.5	0	0	0	2-3/4 in	1.5 in	MOT window
6	6.18	90	149	0	0	0	1-1/3 in	.75 in	Probe window
7	4.125	90	180	0	0	0	2-3/4 in	1.5 in	CO2 window
8	6.36	90	215.5	0	0	0	2-3/4 in	1.5 in	MOT window
9	6.18	90	239.8	0	0	-.4	1-1/3 in	0.75 in	Slow beam in
10	4.125	90	270	0	0	0	2-3/4 in	1.5 in	Imaging beam in
11	6.35	90	305.5	0	0	0	2-3/4 in	1.5 in	MOT window
12	6.18	90	329	0	0	0	1-1/3 in	0.75 in	RF antenna port
13	1.675	0	--	0	0	0	2-3/4 in	flush mount	MOT window
14	1.675	180	--	0	0	0	2-3/4 in	flush mount	MOT window

Figure 8.2: The design of the main vacuum chamber, which was sent to MDC for manufacturing.

vicinity. The 2.75 inch diameter flange is at room temperature. The required vacuum sealing is for 10^{-10} torr when the oven is turned off. With cycling from the room temperature to the operating temperature at least once a day, the vacuum seals should be maintained at least for six months. For this requirement, 304 stainless steel is used as the building material.

To maintain adequate atom flux into the main trapping chamber, Lithium oven is usually heated to about 400 °C. The heating system includes a DC power supply (20V,20A), a current controller, and heater wires windings. The current controller uses five parallel units of N-channel Power MOSFETs (Harris Semiconductor, IRF243). The heater winding is made of five independent nichrome wires (Omega PN NI80-020-50). Each wire carries about 2-3 A current provided by one of the five units in the current controller.

The oven is enclosed by five layers placed from the inner to the outer side: an isolation layer made from thermal cement (Omega CC High Temperature Cement), thermocouplers for monitoring the temperature, the second isolation layer, nichrome heater wires, and the third isolation layer.

An appropriate temperature profile of the oven is the key to maximize the oven life time and reduce the divergence angle of the atom beam. The most important thing is to be sure that the vapor source is close to the joint place of the oven chamber and the nozzle, which helps for both the recirculation the lithium liquids and the reduction of the divergence angle. In Table 8.1, I list a temperature profile that works in a typical oven. In the real experiments, the optimal profile for each oven can be found by trial-and-error tests. When an oven gets older, the temperature tends to be higher than the initial profile.

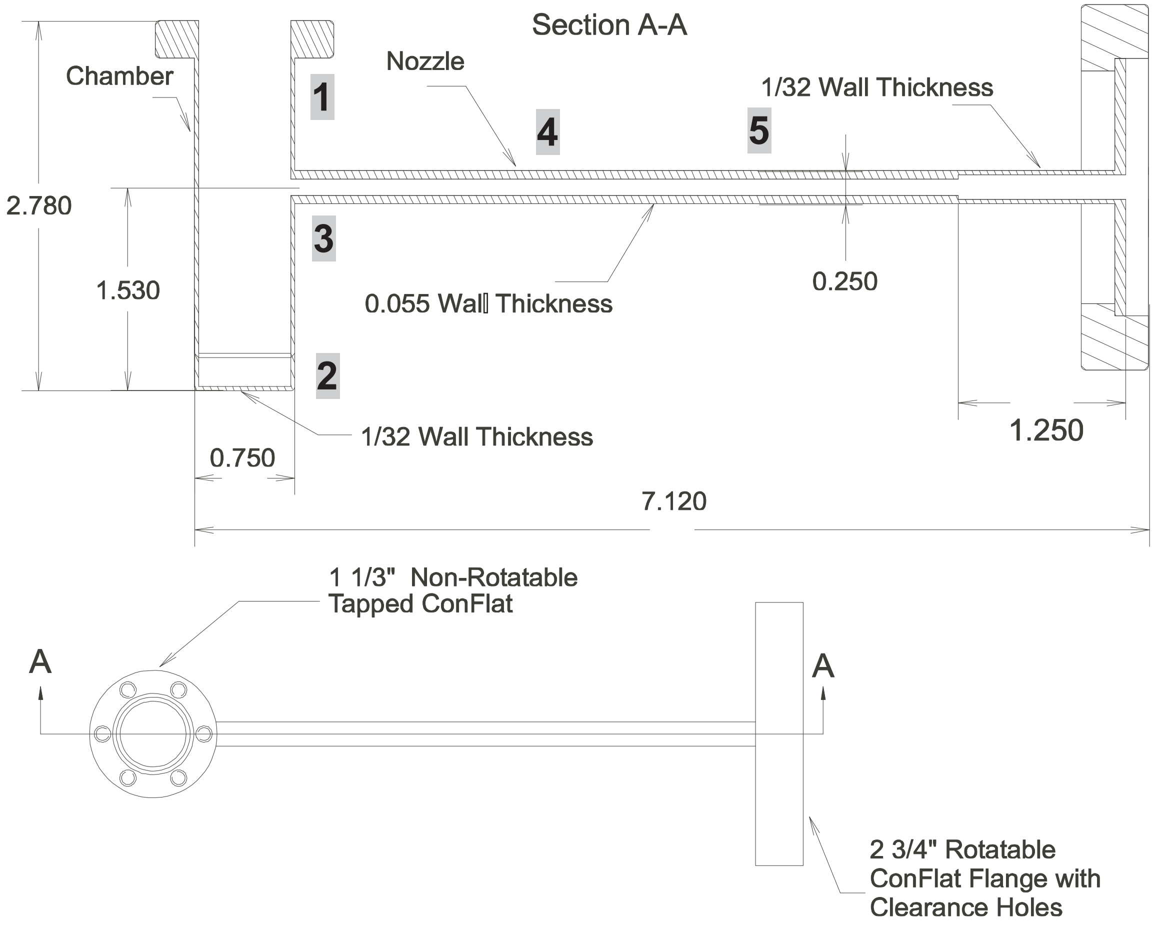

Figure 8.3: The design of ^{6}Li atoms oven (not to scale). There are two critical dimensions in the oven: the inner diameters of the nozzle should be 0.141”±0.005” and 0.188”±0.005” for the best efficiency of the oven. All other dimensions can be slightly altered for the ease of manufacturing. The interior of the oven is lined with 316 stainless steel mesh with the fineness of 300 cell per inch, which recirculates the liquid lithium from the exit of the nozzle back to the oven chamber.

Region No.	1	2	3	4	5
Temperature	370	380	410	370	260
Variation	10	10	20	20	20

Table 8.1: Temperature profiles for a typical atomic source oven. The region numbers correspond to the numbers shown in Fig. 8.3. Temperatures are given in °C.

8.2.2 Zeeman Slower

When an atomic beam is hit by a counterpropagating resonant laser beam, atoms absorb photons whose momentum has the opposite direction with that of the atoms. The atoms spontaneously emit photons in random directions. The net effect is that the atomic velocity along the slowing beam decreases.

To make a laser beam resonant with moving atoms, the Doppler shift of resonance frequency must be included. The shift frequency $\delta\omega = \omega\, v/c$, where ω is the laser frequency, v is the atom speed, and c is the light speed, depends the velocity of the atoms. To make the final velocity small enough, we need to maintain this slowing process as the atom speed decrease. There are two ways to do this: either vary the laser frequency to cope with the change of atom speed, or tune the atom energy level to compensate for the variation of the Doppler shift.

By applying the Zeeman shift of the atomic energy level in a magnetic field, we can make the atoms continuously absorb the photons. For this application, a Zeeman slower employs several wire coils coaxial with the slowing beam direction to apply a spatially varying bias magnetic field to the atoms [113]. The bias magnetic field provides larger Zeeman shifts of the resonance frequency near the oven, which compensates for the larger Doppler shift of “faster atoms”. The Zeeman shifts of the atoms decrease along the axis of the slower corresponding to the smaller Doppler shift of the ”slower atoms”.

The Zeeman slower used for ^{6}Li atoms in our lab is a compact air-cooled slower including eight coils with different numbers of windings. The sketch diagram of the slower is shown in Fig. 8.4. The first seven coils are connected in series with the same current going through each coil. The current of the last coil is controlled by a separate power supply for reversing the current direction, which

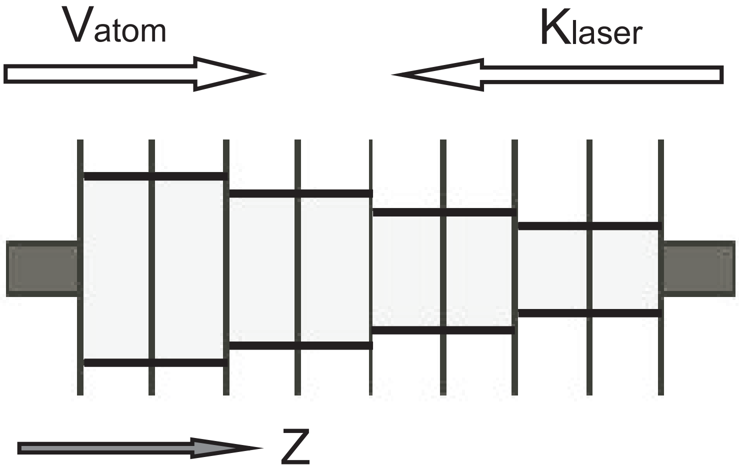

Figure 8.4: The sketch diagram of the slower.

can be used to abruptly detune the zeeman shift of atomic beam. The number of winding for each coils is chosen to produce the desired field. The total length of the slower is about 30 cm, which was predicted to provide a loading rate 3×10^7 atoms/second [114]. The slower was made by an undergraduate researcher Ingrid Kaldre in our group [115].

For a given initial velocity v_i of the atom, the desired B-field is given by [114]

$$B(z) = \frac{\hbar k}{\mu_B}\sqrt{v_i^2 - \frac{\hbar k \Gamma}{m} z}, \tag{8.1}$$

where k is the laser light wavevector, and Γ is the spontaneous emission and absorption rate for the transition used for the slowing beam. For the oven temperature between $600 \sim 700$ K, v_i is about 1300 m/s. The designed and measured magnetic field is shown in Fig. 8.5.

The transition we used for slowing the atoms is the Zeeman energy level from $|2\,^2S_{1/2}, F = 3/2, m_F = 3/2\rangle$ to $|2\,^2P_{3/2}, F = 5/2, m_F = 5/2\rangle$, which can be treated as a nearly ideal cycling transition. This transition requires a right circu-

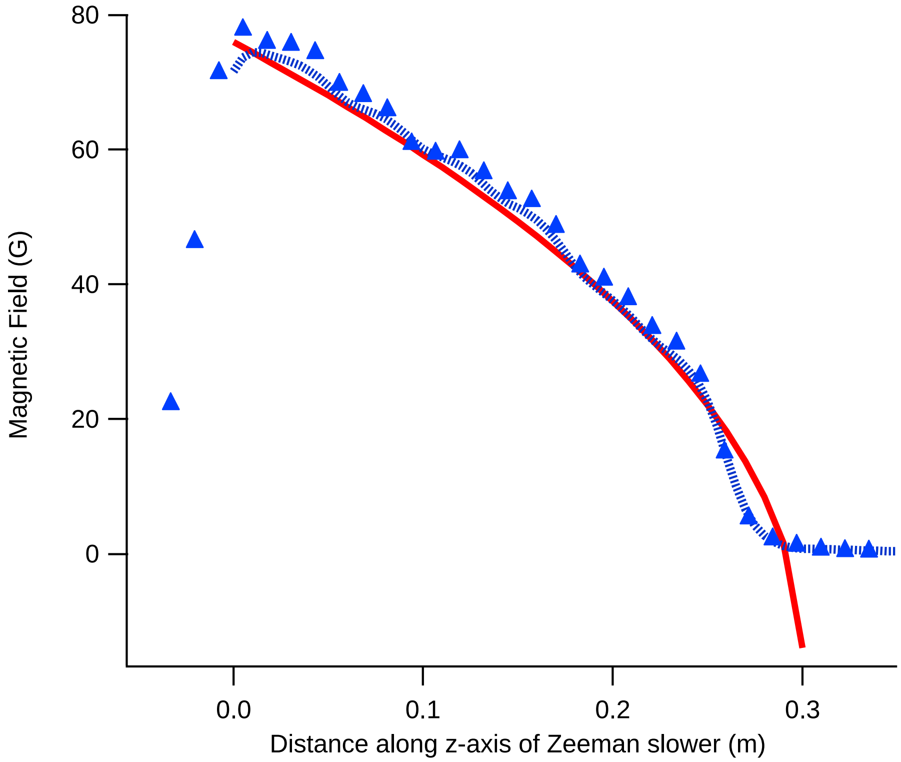

Figure 8.5: The measured magnetic field of the Zeeman slower was obtained by a DC power supply outputting 10 Amps and 17 Volts. The solid line is the curve predicted by Eq. (8.1). The dot line is the designed value with the last reverse coil from [115]. The triangle is the measurement value.

lar polarization light. We tested the Zeeman slower using the a "slowing-probing" scheme [115]. By setting the current of the first seven coils of the Zeeman slower at 9.5 A and the last coil at 0.65 A, we find a slow atom peak about 100 m/s arising from the broad peak of the fast atoms above 1000 m/s with a slowing beam of about 120 mW and 350 MHz red detuning from the resonance of the zero magnetic field.

8.3 Magneto-Optical Trap

8.3.1 Physics of ^{6}Li MOT

The basic precooling method used in our apparatus is a ^{6}Li MOT. MOT is a three dimensional Doppler cooling plus the spacial confinements.

The interpretation of the forces and spacial confinements in a MOT is shown in Fig. 8.6. For simplicity, we consider atoms that have a ground state with the total angular momentum $F = 0$, and the excited state with the total angular momentum $F' = 1$. We apply a spherical quadrupole magnetic field to the atoms, where zero magnetic field exists. Away from the zero point in any direction, the magnetic field increases nearly linearly. The excited state splits into three states with $m_F = -1, 0, 1$, which have the spacial dependence as shown in Fig. 8.6.

We apply two counterpropagating optical beams red detuned from the resonance frequency at zero magnetic field. The moving atoms absorb more photons from the beam propagating in the opposite direction to the atoms than that propagating in the same direction as the atoms. The net effect is that the atoms momentum decreases, which is Doppler cooling.

The spacial confinement is provided by the space varying Zeeman splitting

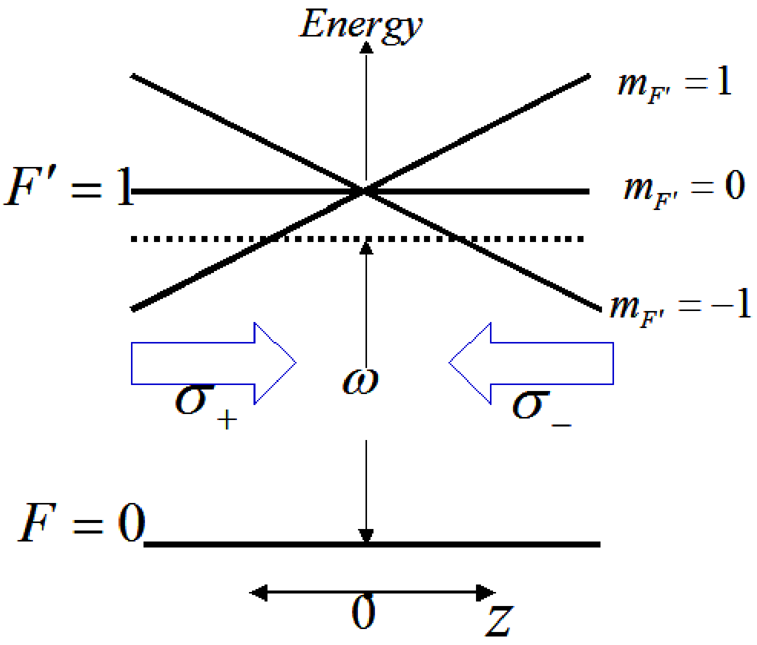

Figure 8.6: The schematic diagram to interpret the physics of a MOT

as shown in Fig. 8.6. The optical beam travelling from right to left has σ^- circular polarization, while the beam travelling from left to right has σ^+ circular polarization. The atoms moving to the $z > 0$ region, where the laser frequency is close to the $m_{F'} = -1$ state, will absorb more photons form σ^- beam and transfer to the $m_{F'} = -1$ state. For the same reason, the atoms moving to $z < 0$ region will absorb more photons from σ^+ beam and transfer to the $m_{F'} = +1$ state. So the resonance frequency detuning in the center of the trap are larger than that at the edge, which provides a larger attracting force at the trap edge than that in the trap center.

In Fig. 8.7, I show a schematic plot for a three dimension configuration of a MOT.

The D2 line is used for a ^{6}Li MOT. The excited state $2\,^2P_{3/2}$ in the D2 line has three hyperfine levels with $F' = 1/2, 3/2, 5/2$ which have a maximum splitting

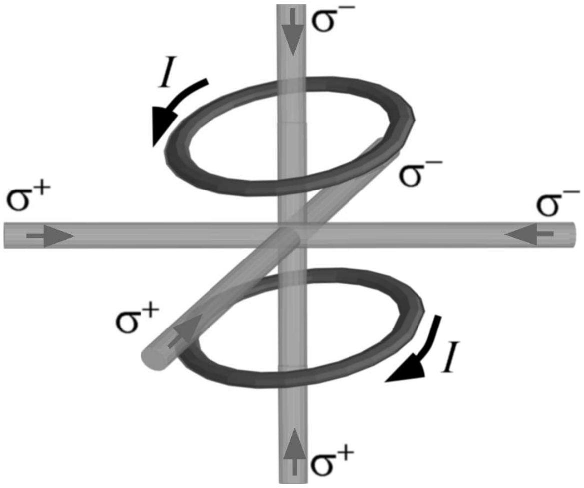

Figure 8.7: The schematic diagram for a three dimension configuration of a MOT from [59]. A pair of magnets coils has anti-Helmholtz configuration (the coils are coaxial and the direction of current in the upper coil and the lower coil is opposite.). The resulting zero magnetic field is at the midpoint of the axis of the coils.

about 4.4 MHz. Since the splitting is smaller the natural linewidth of the D2 line (about 5.9 MHz), we can ignore this splitting. For the ground state $2\,^2S_{1/2}$, where the hyperfine splitting of $F = 1/2, 3/2$ is about 228.2 MHz much larger than the linewidth of the D2 line. So we must use bichromatic beams for the ^{6}Li MOT. One of the frequencies is for $F = 3/2$ state and called as “MOT beam”, and the other one is for $F = 1/2$ state and refereed as “repumper beam”.

Now I want to make an estimate of the trap depth of the ^{6}Li MOT. For atoms near the trap center with a small velocity, it is a good approximation that the net force F reversely proportional to the the frequency detuning, which has a space dependence of $F = -Kz$. The optimal K is given by [59]

$$K = \frac{\hbar k}{2} \frac{\Delta\mu}{\hbar} \frac{\partial B}{\partial z}, \tag{8.2}$$

where k is the wavevector of laser photon, $\Delta\mu$ is the change of the magnetic moment from the lower level to the upper level, and $\frac{\partial B}{\partial z}$ is the gradient of the magnetic field. Suppose the MOT size z_{max} is determined by the maximum Zeeman tuning, which is about the same scale of the natural linewidth $\gamma_s = 5.9$ MHz. Then we have

$$\frac{\Delta\mu}{\hbar}\frac{\partial B}{\partial z}z_{max} \approx 2\pi\gamma_s. \tag{8.3}$$

From Eq. (8.2), the well depth of the MOT is given by

$$U_{max} \approx \frac{1}{2}K_{opt}z_{max}^2 = \frac{h\gamma_s}{4}kz_{max} = k_B T_{Doppler}\frac{kz_{max}}{2}, \tag{8.4}$$

where the $k_B T_{Doppler} = \hbar\gamma_s/2$ is the limit temperature of Doppler cooling due to the heating from the finite spontaneous emission. For ^{6}Li atoms, $T_{Doppler} \approx 140\,\mu$K. For a typical $\frac{\partial B}{\partial z} = 25$G/cm, the MOT size z_{max} is about 1.6 mm corresponding to a trap depth of $1.1K$. This trap depth is suitable for catching the slow atoms after passing through the Zeeman slower.

8.3.2 Apparatus for ^{6}Li MOT

Lasers for ^{6}Li MOT

The wavelength of ^{6}Li D2 line is approximately 671 nm. The total experimental setup needs about 500 mW power to generate the slowing beam, the MOT beam, the repumper beam, and the imaging beam. To produce this power, we use a Coherent 899-21 ring-cavity dye laser. The Coherent 899-21 has an autolock active-stabilization system for stable operation at a single frequency with linewidths less than 500 KHz rms. The dye used for 671 nm wavelength is 1.17

grams Coherent LD-688 dissolved in 1.1 liters of 2-phenoxyethanol solvent, which can cover the wavelength 640-710 nm. The pump laser for the Coherent 899 is a Coherent Verdi V-10 diode-pumped solid state laser. The Verdi usually runs at the wavelength of 532 nm with 5.5 W output power to avoid the saturation of the dye. With a good alignment and cleaning of the optics inside the dye laser, the dye laser output is more than 1.1 W for the broadband mode and about 800 mW for a single-frequency mode near 671 nm. Usually the dye is changed in every 4-6 months.

Laser Frequency Locking

Our experiments require many cycles of operating MOTs. It is necessary to lock the laser frequency within one MHz for several hours. The 899-21 dye laser has an internal locking system to lock the laser frequency to the laser reference cavity. However, the noise and thermal fluctuation in the environment may shift the frequency of the laser reference cavity. So we need to employ a locking system to keep the dye laser reference cavity locked to the optical transition line of ^{6}Li.

This is done by an electronic servo system, which locks the dye laser to the transition line of an atomic beam in a separate vacuum system. The vacuum and the atomic beam for the locking system are similar to the atomic oven we used for the main system. A small portion of the laser beam about 1-2 mW is upshifted about 200 MHz by a double-passed AO and sent into the locking system. The DC voltage for AO frequency shift is modulated by 10 KHz sine wave to provide a reference frequency for a Stanford Research System SR510 lock-in amplifier. The modulation depth is chosen less than 2 % of the amplitude of the carrier wave to avoid the amplitude modulation of the laser power. The amplitude modulation can be caused by the efficiency variation of the AO when the AO driving frequency changes.

The up-shifted probe beam passes through a $\lambda/4$ waveplate to produce a circular polarized light beam. The circular polarized light beam perpendicularly intersects the atomic beam in the locking vacuum chamber. The resonance fluorescence signal is collected by a PMT. The current signal from the PMT is converted into a voltage signal by a current-to-voltage converter and sent into the lock-in amplifier. The lock-in amplifier outputs a linear error signal, which is used as the error signal for a home-built electronic servo circuit. The circuit of the servo electronics is shown in Fig. 8.8. The servo circuit drives the laser reference cavity, which then locks the laser frequency to the required frequency corresponding to the maximum fluorescence signal.

Optical Beam Generation

The optics layout for beam generation and routing is shown in Fig. 8.9. We generate multiple frequency optical beams with different power from a single frequency beam output by one laser. This is accomplished by using polarized beam splitter cubes (PBS) and acousto-optic modulators (AO). By changing the polarization of the optical beam using a half waveplate (Half WP), the power in the vertical and horizontal polarization is distributed as needed. After passing through the polarized beam splitter, the beams with different power are separated in space according to their different polarizations. For each beam, we can use AOs to tune its frequency and intensity, or use quarter waveplates (Quater WP) to change its polarization. These kinds of methods are repeatedly used to generate all the locking beam, imaging beam, slowing beam, MOT beam and repumper

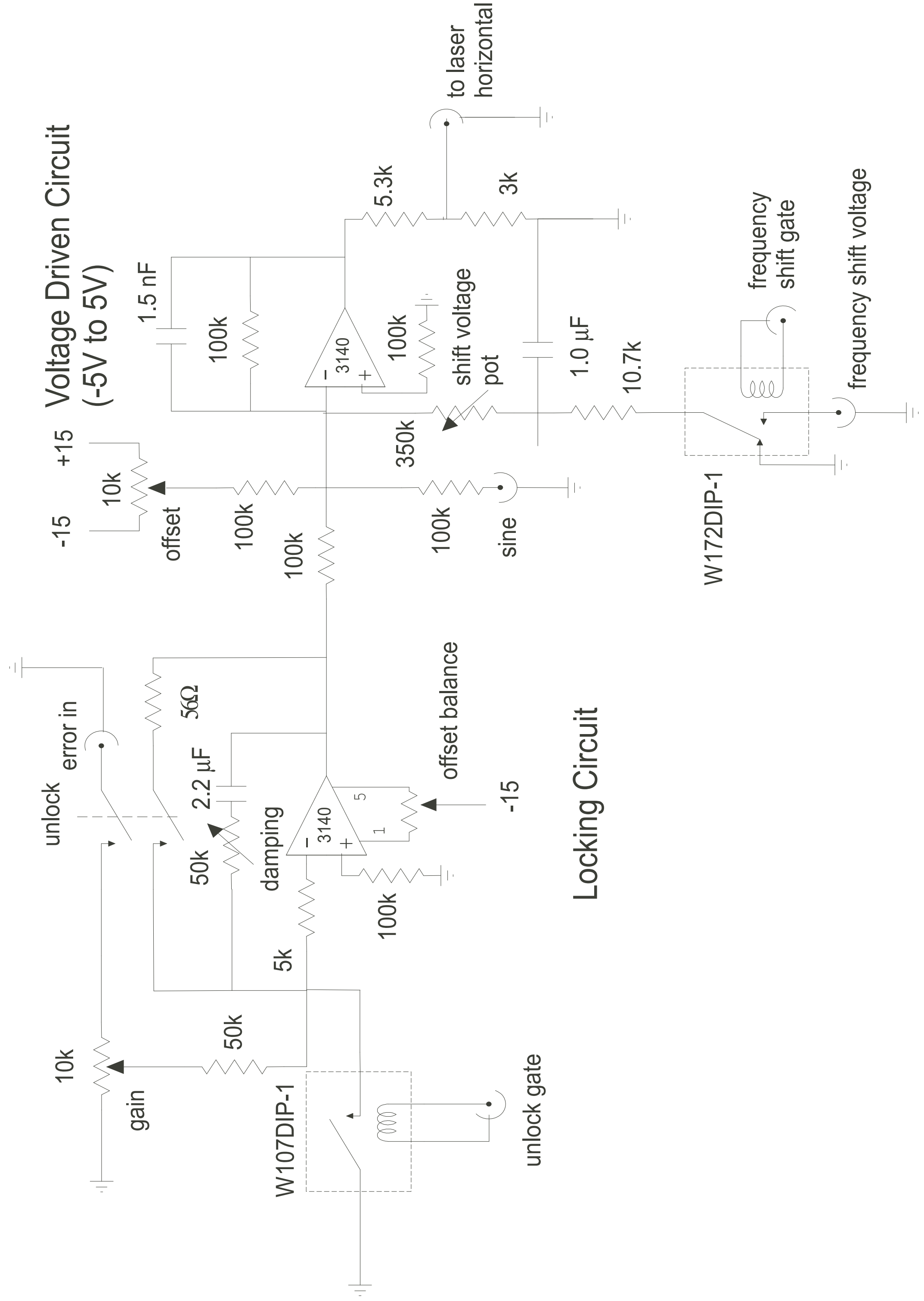

Figure 8.8: The circuit diagram for an electronic servo circuit used for laser frequency locking.

beam.

Typically the laser outputs a single frequency beam of about 600 mw. A thick glass plate is used as a beam splitter, which reflects about 4% power on both the front and rear surface. One reflected beam is used as the imaging beam and the other is used as the locking beam. The frequency of the locking beam is up-shifted about 200 MHz by a double-passed AO, and sent into the locking chamber. This reason to choose the laser locked 200 MHz below the resonance is that we want to directly use the high intensity beam output from the laser as the slowing beam without any frequency shift. The slowing beam is required to run roughly 200 MHz below the resonance.

After the first beam splitter, a half waveplate and a polarizing beam splitting cube directs about 120 mW laser power for the slowing beam. A telescope placed in the slowing beam path expands the beam diameter, which make a cone-shaped beam geometry. The focus of the slowing beam is put to the place near the exit of the oven, which provides radial confinement for the atoms by the optical dipole force and improves the loading rate of the MOT. A combination of a glan prism and a quarter waveplate ensures a nearly perfect circular polarization as required for the optical transition in the Zeeman slower.

Most of the laser power is transmitted through the PBS cube without being reflected to the slowering beam. The transmitted beam is used to generate the MOT beam and repumper beam. A telescope is used to collimate the beam, which reduces the diverging angle of the beam. The beam first double passes a AO called “MOT AO”, which up-shifts the laser frequency roughly 165 MHz for the optical transition corresponding to the F=3/2 ground state. Then a half waveplate and a polarizing beam splitting cube direct about 1/4 of the total power

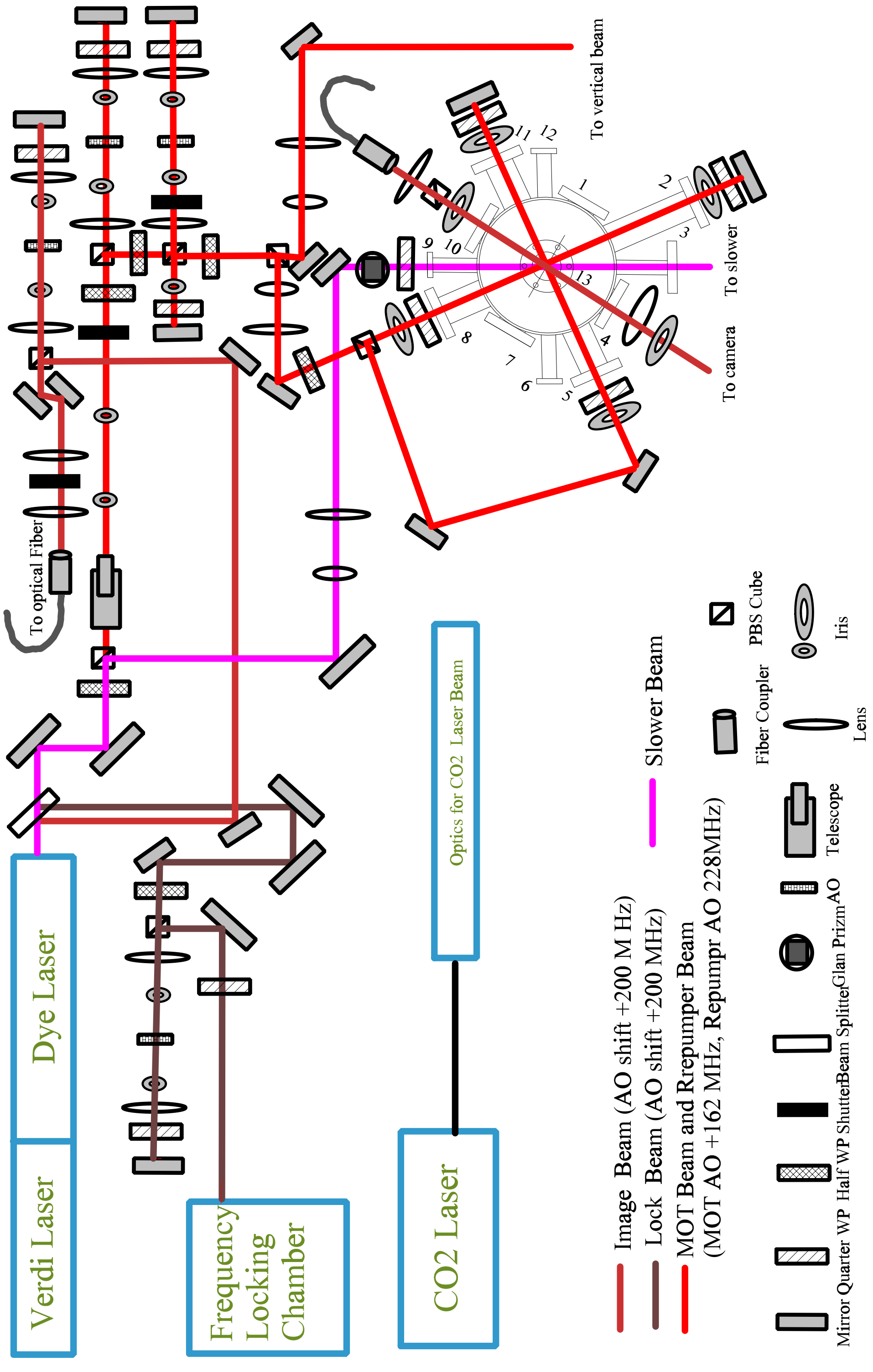

Figure 8.9: The layout of optics for generating the optical beams for a ^{6}Li MOT.

of the MOT beam into another AO, called “ repumper AO”, where the light is upshifted 228.2 MHz to produce the repumper beam for the optical transition corresponding to the F=1/2 ground state. The ratio of the power between the MOT beam and repumper beam is about 3 : 1 for the best loading performance. The MOT and repumper beams are then recombined and co-propagate toward the vacuum chamber. Before entering the vacuum chamber, the combined MOT and repumper beam is split into three separate beams: two for the horizontal beam of the MOT and the third one for the vertical beam of the MOT. The generation of these beams is done by two units of the combination of a half waveplate and a PBS cube. The first unit splits the horizontal beam and vertical beam with 1:1 ratio of the power. The second unit splits the two horizontal beam also with 1:1 ratio of the power.

In the end, the vertical beam has about 40 mW power and each horizontal beam has about 20 mW power. These three beams make up three mutually orthogonal beams for three-dimensional MOT, where the optics for each beam are nearly identical. Each beam is first expanded to 1.5 inch in diameter by a telescope, then passes through an quarter waveplate in front of the vacuum viewports to produce the required circular polarized light. After exiting the vacuum window, the beam passes through another quarter waveplate, then is retro-reflected by a mirror. The retro-reflected beam passes through the quater waveplate again, which ensures that the retro-reflected beam has required circular polarization for the MOT.

Double pass acousto-optic modulators are used extensively throughout our optical system to generate the beams with different frequencies. This scheme is discussed extensively in the previous dissertations [53, 59, 64], one of which is

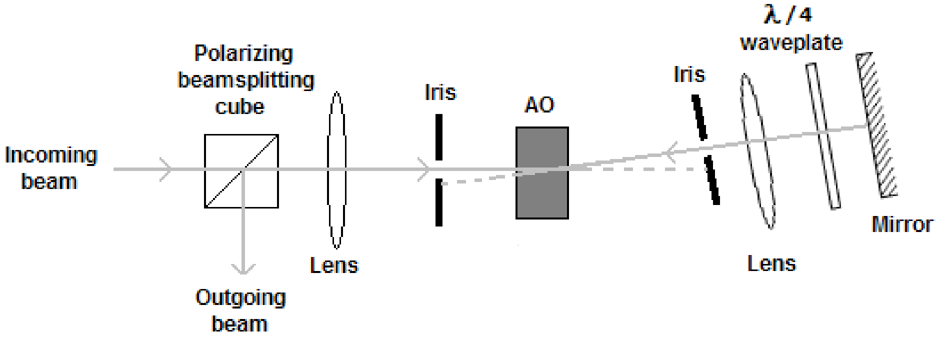

Figure 8.10: The optics for a double pass acousto-optic modulator. This figure is from [64]

shown in Fig. 8.10. A linearly polarized optical beam passes through a PBS cube, and then is focused into an AO crystal, which is at the focus of two confocal lenses. An iris placed behind the crystal blocks all refracted beams from the AO except of the first order beam. The first order beam travels through a quarter waveplate, then retro-reflected by a mirror. This retro-reflected beam has the same propagating path as the incident beam so that it experiences an equal frequency shifts from the AO. In the end, the retro-reflected beam hits the PBS cube again with the orthogonal polarization to the incident beam. This resulting outgoing beam is then reflected to another direction orthogonal to the incident face. The double-pass AO configuration enables twice frequency shift compared with a single-pass AO. It ensures that the direction of the outgoing beam remain constant when the AO frequency varies. Finally, better performance in the rejection of leakage light in the double pass AO helps us to reduce the resonance light heating in an optical trap.

8.3.3 Loading a MOT into an Optical Trap

For our experiment, the cold atoms in the MOT are the precursor for evaporation operated in a CO_2 laser optical dipole trap. So the maximum atom number in the MOT is not our ultimate goal. Instead we want to put as many atoms into the CO_2 laser trap as possible. To achieve this goal, we have three periods for the MOT instead of just a simple "MOT loading".

The first period of the MOT is "MOT loading". In this period, we load the as many atoms into the MOT as possible. For this purpose, the volume of the MOT can not to be too small. From Eq. (8.3), we know that the size of the MOT is proportional to the detuning of the MOT beam. Usually we set the detuning of the MOT beam about 6 linewidth below the resonance frequency. The second period is "MOT cooling". In this period, we compress the volume of the MOT so that trap depth of the MOT decreases according to Eq. (8.4). By doing that, only the coldest atoms close to the Doppler limit temperature stay in the MOT, and then are loaded into the optical trap. This stage is very sensitive to the frequency detuning, the power of the MOT and repumper beams, and the overlapping of the MOT and the optical trap. It is operated by a careful daily optimization of the fluorescence signal of the atoms loaded into the optical trap. Following the "MOT cooling", we conduct an "optical pumping", during which the repumper beams are extinguished while the MOT beams pump all the atoms into the $F = 1/2$ ground state. After those three periods, we usually load about 2 million atoms into the CO_2 laser trap.

Here I list the typical beam frequency, power, time and atoms number in each period in Table 8.2.

	Loading	Cooling	Pumping
Detuning	-30 MHz(MOT)	-5 MHz (MOT)	on resonance (MOT)
	-10 MHz(Repumper)	-5 MHz(Repumber)	Off (Repumber)
Intensity	Full	Decrease	Full
Duration	10 s	5 ms	200 μs
Atom Num	200×10^6	N.A.	2×10^6

Table 8.2: The parameters for the different periods of MOT

8.4 Magnets

To generate a strongly-interacting Fermi gas of ^{6}Li atoms, a uniform high magnetic field about 834 gauss is required for the broad Feshbach resonance. In our magnets, we integrated a MOT magnet coil and a high-field magnet coil into each of two sealed units, which are water-cooled to dissipated the heat. A pair of magnets is mounted around port 13 and port 14 of the main experimental chamber in Fig. 8.1. The MOT magnet and high field magnet units are designed and built by Bason Clancy as described in his thesis [39]. Here I will give a brief introduction to the operation of these magnets.

The MOT magnet coils are in an anti-Helmholtz configuration and are energized by an Agilent 6651A power supply using the constant current mode at approximately 14 A. This current produces a magnetic field gradient of 28 G/cm at the center of the trapping region.

The high field magnet coils are run in a Helmholtz configuration. The coil is powered by an Agilent 6691A power supply. It provides currents as high as 250 A,and produces uniform magnetic fields up to 1300 gauss. For magnetic fields less than 1100 gauss, the high field magnets coils can run continuously. At the 1200 gauss, the magnets can safely runs about 30 seconds without any overheating.

To avoid overheating and electrical shorts, interlocks are implemented to monitor the power consumption of the magnets as well as the flow of cooling water. An analog external voltage from 0 to +5 V is used to control the output current of the power supply. When we demand a magnetic field change by sending two different command voltages in sequence, the Agilent power supply has an internal delay, which makes the magnetic field exponentially increase or decrease from the original magnetic to the desired field. The full time for changing the magnetic field is about 0.5-0.7 second.

We also have three bias magnet coils to finely tune the zero point of the magnetic field produced by the MOT magnets. The three small coils are mounted around port 5, 8, 11 in Fig. 8.1. Each coils can provide a couple of gauss bias magnetic field. With these three bias coils, we can move the position of the MOT in horizontal plane, which helps us to overlap the center of the MOT and the center of the optical trap almost perfectly, which enhances the loading from the MOT to the FORT. Note that the center of optical trap is always aligned to overlap the center of the magnetic potential of high field magnets, and the center of the magnetic potential is almost fixed. So for loading the optical trap, we always move the MOT position to overlap the optical trap.

We use another method to move the MOT in the vertical direction. Originally the top MOT coils and the bottom MOT coils are in series and have the same amount of current. By add a 2 ohm range variable resistor in parallel with the bottom MOT coil, we make the current going though the top coil and bottom coil different. This enable us to move the MOT up and down by adjusting the variable resistor.

8.5 Ultrastable CO_2 Laser Trap

Magnetic traps can not be applied to trap ^{6}Li atoms at the lowest hyperfine states because they are high-magnetic-field seeking states. To study a strongly interacting Fermi gas constituted by these two hyperfine states, an optical dipole trap is required. In this chapter, first I will introduce the physics of CO_2 laser optical dipole traps. Then I will briefly describe loss and heating in optical dipole traps. After that I will describe how we build optics and electronics of a CO_2 laser trap, and discuss the storage time of our current trap.

8.5.1 Physics of a CO_2 Laser Optical Dipole Trap

When a neutral atom is in a static electric field, the energy level of atom splits because of interactions between the static dipole moment of the atoms and the external electric field. This is know as *Stark effect.* Similar interactions arise when an optical field is presented, where the oscillating electric field generates an induced dipole moment $\mathbf{d} = \alpha \mathbf{E}$, where α is the polarizability of the atoms. Interactions between the induced dipole moment and the optical field is known as *AC Stark effect*, which generates a potential for the atoms by

$$U = -\frac{1}{2}\overline{\mathbf{d} \cdot \mathbf{E}} = -\frac{1}{2}\alpha\overline{\mathbf{E}^2}. \tag{8.5}$$

This potential can be written in terms of the intensity of the optical field

$$U = -\frac{1}{4}\alpha\mathcal{E}^2 \quad = -\frac{2\pi}{c}\alpha I \text{ (CGS)} \quad = -\frac{1}{2\epsilon_0 c}\alpha I \text{ (MKS)}, \tag{8.6}$$

where the time averaging $\mathbf{E}^2$ is $\mathcal{E}^2/2$. $\mathcal{E}$ is the slowly-varying field amplitude of the optical field, and I is the optical field intensity.

To obtain the maximum optical intensity, we usually focus a laser beam to create a potential in the focal point. To make atoms attracted to the region with the highest intensity, α is required to be a positive value. The polarizability of the atoms in the ground state is given by [59]

$$\alpha = \frac{1}{\hbar} \sum_{|g\rangle,|e\rangle} \mu_{eg}^2 \left[\frac{1}{\omega_{eg} - \omega} + \frac{1}{\omega_{eg} + \omega} \right], \tag{8.7}$$

where μ_{eg} is the electric dipole moment transition matrix element between ground state $|g\rangle$ and excited state $|e\rangle$, and ω_{eg} is the associated transition frequency. From Eq. (8.7), we see that the laser frequency should be red tuned to make α positive.

Next, I will discuss the spacial profile of this attractive optical potential. The light intensity of a focused laser beam is nearly a Gaussian shape. In a cylindrical coordinate, it is given by [116]

$$I(r,z) = \frac{I_0}{1+(z/z_f)^2} \exp\left(-\frac{2\,r^2}{a_f^2} \right), \tag{8.8}$$

where λ is the wavelength of the laser beam. I_0 is the maximum beam intensity at the focal point $z = 0$. $z_f = \pi\, a_f^2/\lambda$ is the Rayleigh range, and a_f is the $1/e^2$ width of the intensity at the focal point. Accordingly, the optical potential also has the same Gaussian shape

$$\begin{aligned} U_{gauss}(r,z) &= -\frac{U_0}{1+(z/z_f)^2} \exp\left(-\frac{2r^2}{a_f^2} \right) && (8.9) \\ \text{with} \quad U_0 &= \frac{\alpha\, I_0}{2\,\epsilon_0\, c}. && (8.10) \end{aligned}$$

In most experiments of trapping cold atoms, cold atoms stay in the deepest portion of the optical trap by $r << a_f$. Under this condition the Gaussian shape optical potential can be well approximated as a harmonic potential. The Taylor expansion of Eq. (8.10) is

$$U(r,z) \simeq -U_0 + \frac{U_0}{z_f^2} z^2 + 2\frac{U_0}{a_f^2} r^2 + \dots \; . \tag{8.11}$$

By comparing the second and third terms with the harmonic oscillator potential for a particle with mass m, we obtain

$$\frac{U_0}{z_f^2}\, z^2 \equiv \frac{1}{2}\, m\omega_z^2 z^2, \quad 2\frac{U_0}{a_f^2}\, r^2 \equiv \frac{1}{2}\, m\omega_r^2 r^2. \tag{8.12}$$

The radial and axial harmonic frequencies are

$$\omega_z = \sqrt{\frac{2U_0}{m z_f^2}}, \quad \omega_r = \sqrt{\frac{4U_0}{m a_f^2}}. \tag{8.13}$$

I will explain why we choose CO_2 laser to create optical dipole traps for cooling and trapping ^{6}Li atoms. An *Optical dipole trap* provides space confinement for cold atoms, but it doesn't mean it can cool the atoms. Laser beams actually heat atoms by atom-photon scattering. To reduce the atom-photon scattering, people usually tune the wavelength of the laser beam far away from the resonance. This type of an optical dipole trap is known as a *Far Off-Resonance Trap* (FORT). Specially when the laser wavelength is tuned to the extremely far from the resonance, interactions between atoms and optical fields is quasi-electric. This kind of FORT is called *Quasi Electrostatic Trap* (QUEST). Our CO_2 laser trap is a QUEST, which has unique advantages for the application of all-optical cooling and trapping because of its extremely low optical heating rate.

The optical heating from the atoms-photon scattering is given by Larmor power, which describes the radiation power of the oscillating dipole $\mathbf{d}$ in a electromagnetical field by

$$P = \frac{2\overline{\ddot{\mathbf{d}}^2}}{3\,c^3} = \frac{1}{3c^3}\,\omega^4\,\alpha^2\,\mathcal{E}^2, \tag{8.14}$$

where α is the polarizability of atoms, ω is the frequency of photon, and $\mathcal{E}$ is the amplitude of the optical field. The atom-photon scattering rate R_{sc} is

$$R_{sc} = \frac{P}{\hbar\omega} = \frac{\sigma_s\,I_0}{\hbar\,c\,k}, \tag{8.15}$$

where $\sigma_s = 8\pi\,\alpha^2\,k^4/3$ is the atom-photon scattering crosssection.

When the resonance frequency ω_{eg} is much larger than the CO_2 laser frequency ω, Eq. (8.7) gives $\alpha = \alpha_s \equiv 2\mu_{eg}^2/\hbar\omega_{eg}$, which is the static polarizability of a two-level atom. In term of α_s, the depth and the atom-photon scattering rate of a CO_2 laser trap are given by

$$\begin{aligned} U_0 &= 2\pi\alpha_s I_0/c, && (8.16)\\ R_{sc} &= \frac{2\,\Gamma}{\hbar\,\omega_0}\left(\frac{\omega}{\omega_0}\right)^3 U_0, && (8.17) \end{aligned}$$

where $\Gamma = 4\mu_{eg}^2\omega_{eg}^3/3\hbar c^3$ is the spontaneous emission rate (resonance linewidth) for a two-level atom. Eq. (8.16) shows that the atom-photon scattering rate is reduced by a factor of $(\omega/\omega_{eg})^3$. By using an infrared beam with large intensity, we can get a reasonable trap depth and suppress the optical scattering rate to a negligible value.

In our lab, a 65 watt CO_2 laser laser beam is focused within a spot of the diameter of about 50 μ m. The trap potential is about 550 μ K. The wavelength of CO_2 laser is about 16 times larger than the wavelength of the resonance light of ^{6}Li atoms, which gives the scattering rate of about 4×10^{-4} Hz. This low scattering rate makes CO_2 laser traps very suitable for evaporative cooling and long time storage of cold atoms.

8.5.2 Loss and Heating in an Optical Trap

In the above section, we present an analysis of an CO_2 laser trap, and find that it is ideal for the purpose of all-optical cooling and trapping of cold atoms. However, there are still several loss and heating mechanisms arising in optical traps, which prevent a CO_2 laser trap from being an ideal conservative potential [117–119]. The first one is the heating due to the intensity and position noises of laser beams. Second one is the background gas heating in the vacuum. The last one is the optical heating from the resonant light. In principle resonant light should be completely prevented from entering into the vacuum chamber when evaporative cooling begins. But in the real setup, the leakage from the MOT beam path and the random reflection will cause a finite background resonant light in the vacuum.

Laser Beam Intensity Noise

The beam intensity noise is mainly from the intensity fluctuation of the laser itself as well as from that of an acousto-optical modulator used for controlling the CO_2 laser power. In this section I only give the theoretical analysis of the intensity noise. The real measurements of the beam noise are presented in the next section.

The fluctuation of the beam intensity can be treated as a perturbation on the harmonic potential, which results atomic transitions between quantum states of the harmonic trap. The heating rate from this transition is given by [119],

$$\langle \dot{E} \rangle = \frac{\omega_{tr}^2}{4} S_\epsilon[\omega_{tr}/\pi] \, \langle E \rangle, \tag{8.18}$$

where $\langle E \rangle$ is the average energy of the trapped atoms, and ω_{tr} is the angular frequency of the trap. The heating rate is sensitive to the noise spectrum near ω_{tr}/π because the intensity heating is actually a parametric process.

The $S_\epsilon[\omega]$ is defined as one-sided power spectrum of the fractional intensity noise $\epsilon(t)$ by

$$S_\epsilon[\omega] = \frac{2}{\pi} \int_0^\infty d\tau \, \cos \omega\tau \, \langle \epsilon(t)\epsilon(t+\tau) \rangle, \tag{8.19}$$

$$with \ \langle \epsilon(t) \, \epsilon(t+\tau) \rangle = \frac{1}{T} \int_0^T dt \, \epsilon(t) \, \epsilon(t+\tau), \tag{8.20}$$

where the factional fluctuation in the laser intensity $\epsilon(t) = (I(t) - I_0)/I_0$, and I_0 is the density without fluctuation.

Laser Beam Position Noise

The heating rate of the laser beam position noise is given by

$$\langle \dot{E} \rangle = \frac{\pi}{2} \, M \, \omega_{tr}^4 \, S_x[\omega_{tr}]. \tag{8.21}$$

Here $S_x[\omega]$ is the one-sided power spectrum of the position fluctuations in the trap center, which has the same definition formula with $S_\epsilon[\omega]$ in Eq. (8.20) by replacing the $\epsilon(t)$ with ϵ_x. $\epsilon_x = x(t) - x_0$ is the position fluctuation of the center of an optical trap.

The one sided power spectrum of the position fluctuation $S_x[\omega]$ can be decided from the intensity noise of a half-side-blocked beam by [59]

$$S_x[\omega] = \frac{\pi}{2}\, a^2\, \frac{S_\epsilon[\omega]}{4}, \tag{8.22}$$

where a is the $1/e^2$ intensity radius of a Gaussian beam, and the factor 1/4 arises from the fact that 1/2 beam is blocked when measuring the $S_\epsilon[\omega]$.

Background Gas Heating

The detailed analysis of the loss and heating of trapped atoms due to collisions background gases can be found in [117]. The loss rate is given by

$$\gamma_C = 1.05\, n_b\, u_b\, \sigma[u_b], \tag{8.23}$$

where the background gas density is n_b, the background gas $1/e$ width of thermal speed Maxwellian distribution is $u_b = \sqrt{2\, k_B\, T/m_b}$, m_b is the mass of the atom in the background gas, and $\sigma[u_b]$ is the total cross section of atom-atom collisions between the background gas and the trapped gas,

The heating rate is given by

$$\dot{Q} = 0.37\, \gamma_C[u_b]\, \frac{U_0^2}{\epsilon_d[u_b]}, \tag{8.24}$$

where the U_0 is the trap depth, and $\epsilon_d[u_b] = \frac{4\pi\hbar^2}{m_a \sigma[u_b]}$ is the diffraction energy change of a trapped atom with the mass of m_a.

Optical Resonant Light Heating

The resonant optical cross-section of the two-level atoms is given by

$$\sigma_0 = \frac{6\pi}{k^2}. \tag{8.25}$$

Inserting the above equation into Eq. (8.15), we get the optical resonant light scattering rate

$$R_{res} = \frac{6\pi\, I}{k^3\, \hbar\, c}. \tag{8.26}$$

For each scattering, the absorption and emission of photon induce the recoil energy heating by $2\epsilon_{rec} = \frac{\hbar k^2}{m}$. So the heating rate is given by

$$\dot{Q} = 2\epsilon_{rec}\, R_{res} = \frac{3\hbar\, \lambda\, I}{m\, c}. \tag{8.27}$$

For ^{6}Li atom the ϵ_{rec} is about 3.6 μK. When the resonance light intensity is about the $1\, nW/cm^2$, the optical resonance heating rate is about the $51 \mu K/s$. In the period of evaporative cooling, we ensure the total resonant light into the vacuum chamber less than $0.1 pW/cm^2$, which is the limit of our photodiode detector. The upper bound estimation of the resonance optical heating is $5 nK/s$, which is much smaller than the coldest gas temperature of about the $100 nK$ in our experiments.

8.5.3 Ultrastable CO$_2$ Laser

For the application of all-optical cooling and trapping, an ultrastable CO$_2$ laser with very low intensity and position noise is required. We choose a Coherent GEM Select 100 CO$_2$ laser, which has a maximum power of up to 120 W at the wavelength of 10.6μ m. The RF-charged CO_2 tube has all-metal seals for long life time. The RF source is from an external RF amplifier, which is powered by a stable Agilent 6573A DC power supply. When the laser operates on the continuous mode with full power, the required electrical power is 35 VDC and 55 A.

Our customized model has an external modulation input, which allows users to operate the laser in the pulse mode via an eternal TTL input after an initial 5 seconds start-up delay. The external modulation signal is provided by a pulse generator, which outputs TTL pulse trains with variable pulse duty factors. The minimum CO_2 laser output power in the pulsed mode is about 1 W, which is obtained by using 1 KHz TTL pulses with duty factors less than 0.05. This low power CO_2 laser beam is used for alignments of CO_2 laser beam optics. A home-made switch box is built to switch operations between the continuous mode and pulse mode. The CO_2 laser the RF power amplifier, and the AO for controlling the CO_2 laser beam are required to be water-cooled. The cooling system is introduced in the next section.

This CO_2 laser is a commercial product from Coherent for general applications. So we need to measure the intensity and position noise spectrum of this CO_2 laser to ensure that it satisfies our requirements. The measurement setup is shown in the CO_2 beam optics layout (see in Fig. 8.13). A 0.5 W refracted beam from AO is sent into a fast 10.6μm infrared photodetector(PD) from Boston Electronics. With a blade blocking the half area of the laser beam, the PD detects both the intensity and position noises of the laser beam. Without the blade, the whole beam enters into the PD, and only the intensity noise is detected. The output voltage signal is sent into an oscilloscope and the noise spectrum is di-

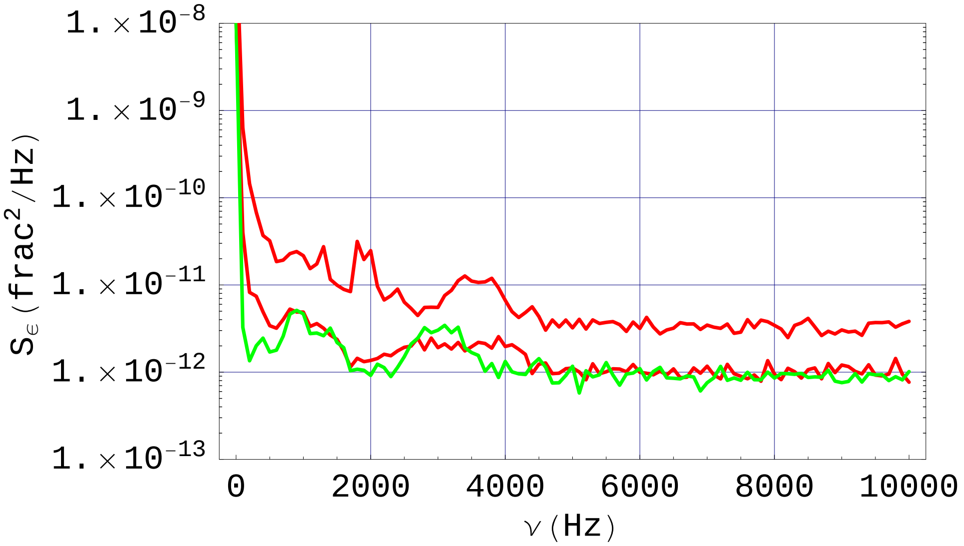

Figure 8.11: CO_2 laser intensity noise spectrum. The gray one is electronic noise without laser beam. The lower black one is the intensity noise without blade, and the upper black curve is the intensity noise with the blade

rectly obtained from fast fourier transform (FFT) operated by the oscilloscope. The laser intensity noise is shown in Fig. 8.11. The position noise is shown in Fig. 8.12

In the end, I list the specifications of our CO_2 laser in Table 8.3.

8.5.4 The Cooling System for CO_2 Laser

The Coherent GEM laser, the RF amplifier for the laser, and the IntraAction AO require water-cooling. A closed-loop cooling system is operated by a NesLab Merlin M75 chiller operates with a total 2.5 GPM coolant and the output pressure at 85 Psi. The coolant is made of distilled water and DowFrost with a volume ratio of 3:1. The cooling lines for the CO_2 laser and RF amplifier are in series having 2.2 GPM flow. The other 0.3 GPM flow is used for the AO, whose cooling

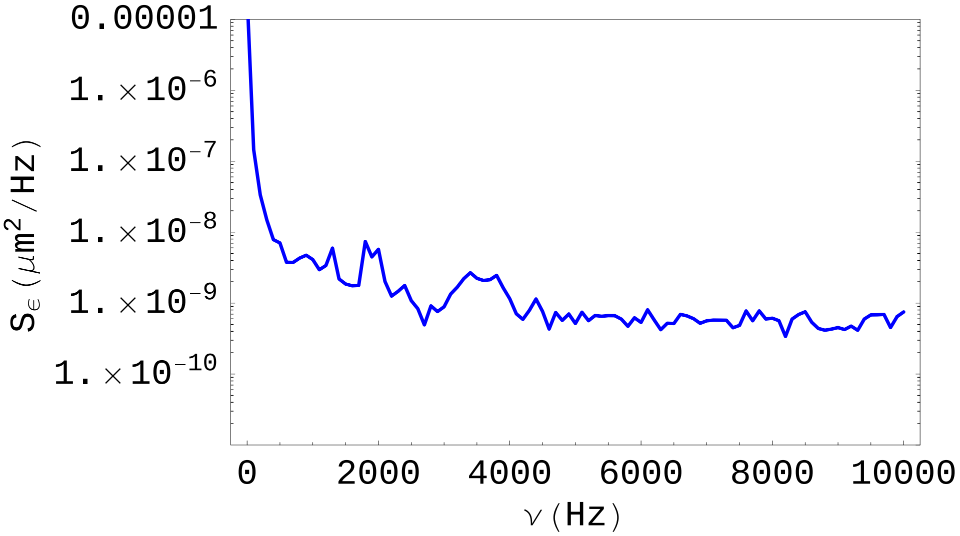

Figure 8.12: CO_2 laser position noise spectrum. The position noise is calculated according to Eq. (8.22), where $S_\epsilon[\omega]$ is obtained by subtracting the intensity noise without blade from the intensity noise with the blade.

Specification	GEM Select 100
Standard Output Power	100 W
Wavelength	$10.6\mu m$
Mode Quality	TEM_{00}
Polarization	Fixed Linear
$1/e^2$ Beam Diameter	$3.8 \pm 0.4mm$
Beam Divergence	$< 5mrad$
Long Time Power Stability	2%
Electrical	$35VDC < 55A$
Cooling	$20 \pm 5°C$
Intensity Noise	$1 \sim 2 \times 10^{-12}/Hz$
Position Noise	$10^{-10} \sim 10^{-9}\mu m^2/Hz$

Table 8.3: The specification of the CO_2 laser.

line is in parallel with that for the laser. The laser temperature is well controlled at 15.9°C with the fluctuation less than 0.1°C. The AO temperature is about 40°C when it operates with the full CO_2 laser power beam.

The piping and tubing parts for the cooling line are clean stainless components from the Swagelok. Several important components are used to control the coolant flow. One SS-1RF4 bonnet needle valve is used to control the total flow. Two PGI-50M-PG100-LAOX Gauge are used to monitor the flow pressure. A SS-44F4 ball valve is used to divide the initial flow into two parallel flows for the laser and the AO respectively. An Omega FTB2000 turbine flow rate sensor is inserted into the cooling system to detect the returning flow. The sensor outputs TTL pulses, whose frequency is proportional to the flow rate. An Omega DPF700 ratemeter reads the output TTL signals from the flow sensor, monitoring the flow rate in time and displaying it in a LED screen. When the flow rate drops below 2.0 GPM, the ratemeter generates interlock signals, which shut down the CO_2 laser automatically. When the flow rate comes back to the normal range, a manual reset is required to cancel interlock signals in the ratemeter.

8.5.5 Beam Generation and Optics for CO_2 Laser Trap

The optics layout to generate and control the CO_2 laser beam is shown in Fig. 8.13.

The CO_2 laser beam output is first reflected by two mirrors to pass a zigzag path. This setup increases the path length, which allows the beam to expand before entering the AO. A larger beam diameter reduces the thermal fluctuation in the interaction region of the AO crystal, and makes the beam power after the AO more stable.

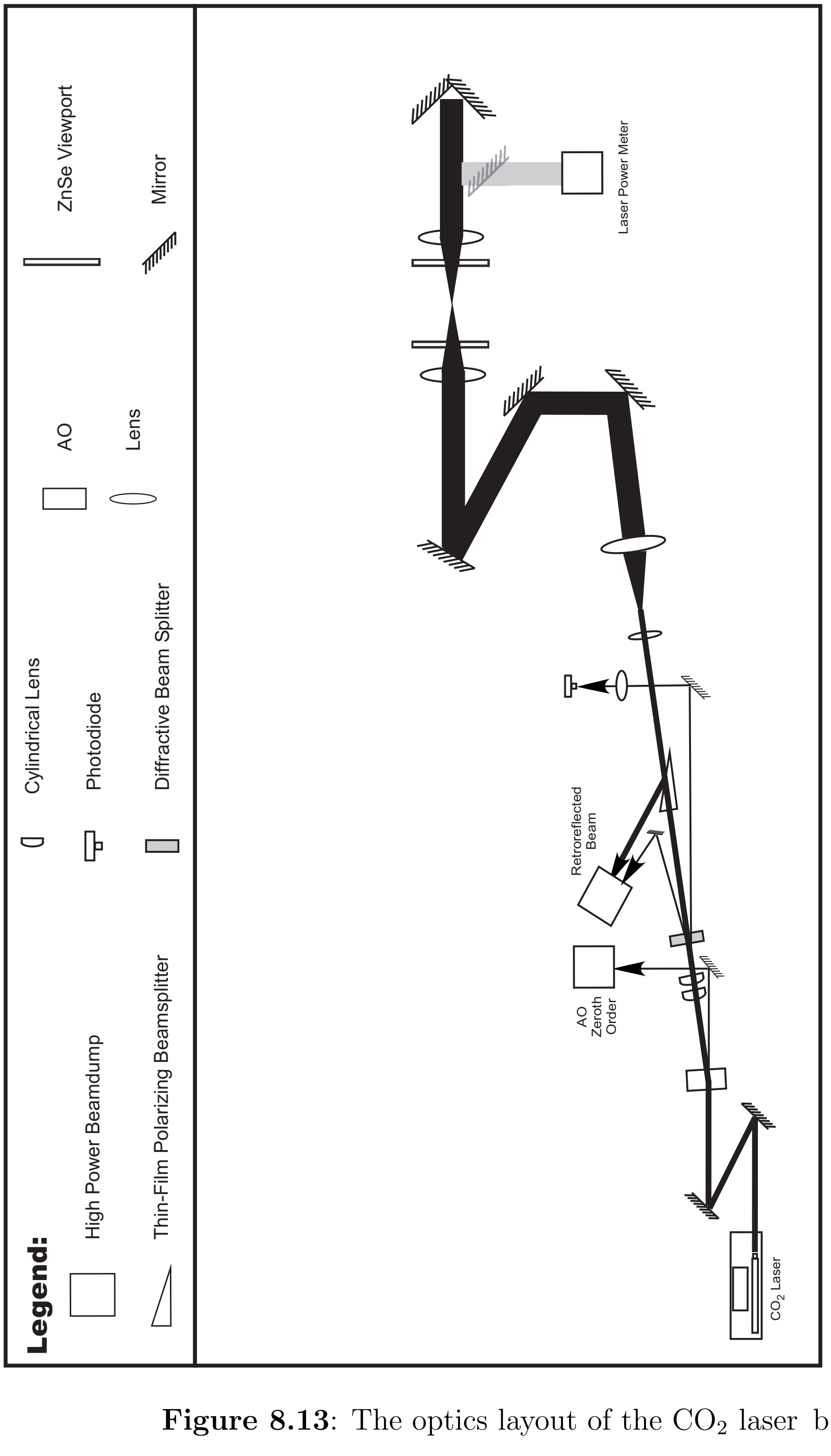

Figure 8.13: The optics layout of the CO$_2$ laser beam.

The first-order refracted beam from an IntraAction Corporation AGM-4010BG1 AO is used to generate the optical trap. This AO is driven by a modified IntraAction GE-4050 RF modulator. By changing the amplitude and frequency of the RF waves from the RF modulator, we control both the intensity and the direction of the first-order refracted beam. This method is used to lower the trap depth for evaporative cooling in Chapter 3, and also used to rotate the trap in Chapter 7. When the first-order beam power decreases, the zeroth-order beam contains significant power, which is reflected by a pick-up mirror into a 4-inch-diameter Kentek water-cooled beam dump for safety issue.

The AO is precisely adjusted at the Bragg angle to obtain the maximum power in the first-order beam. For the precise alignment, a pair of home-made co-axial cylinders is used to mount the AO. One of those is a solid cylinder with smaller diameter, which is inserted into a hollow cylinder with larger diameter. The AO is mounted on the solid cylinder, which can rotate in the horizontal direction and translate in the vertical direction inside the hollow cylinder. The relative position between the solid and hollow cylinder can be locked by three set screws. In the end, the hollow cylinder is fixed on a magnetic base.

As the CO_2 laser beam passes through the germanium crystal of the AO, the power deposited into the AO may cause the thermal lensing effect even we use water-cooling. The heat source is the region where the laser beam propagates, which is in the center of the crystal. However, the water-cooling is at the bottom of the crystal. This configuration builds a temperature gradient in the germanium, which results in a gradient of the index of refraction in the vertical direction. The variation of the index of refraction makes the germanium crystal act as a lens, which make the output beam from the AO have the different radii of curvature of the wavefront in the horizontal and vertical directions. After the beam propagates a certain distance, the cross-section of the beam will become elliptic. When this elliptic beam is focused, the horizontal and vertical focal points will separate. This effect will cause a non-harmonic potential in the axial direction and reduce the depth of optical trap. Such a loose confinement also reduces the loading efficiency of the optical trap. So this thermal lensing effect should be avoid in our experiments. In Fig. 8.13, a telescope of cylindrical lenses is placed after the AO to compensate the thermal lensing effect. The telescope is adjusted to ensure that the horizontal and vertical radii of curvatures of the wavefront are equal. Note that the equal horizontal and vertical radii of curvatures of the wavefront does not necessarily mean the beam shape is perfect round. Instead, we adjust the telescope by directly confirming that the axial confinement of the trap is tightest.

After the cylindrical lens, the beam passes through a holographic beam sampler, which splits an incoming beam and diffracts about 1% transmitted power into two first-order beam. One of them with about 0.5% power is reflected by a mirror and sent into the fast infrared photodiode, which is used to measure the laser noise (see in Section 8.5.2) as well as for precision measurements of the laser power to calibrate the trap lowering curve for evaporative cooling (see in Chapter 3).

A thin-film polarizer is placed in our CO_2 laser beam path to prevent the retroreflected CO_2 laser beam back into the CO_2 laser. In the loading period, we overlap the incoming beam and the retroreflected beam at the focal point to increase the optical trap potential. This method increases the loaded atom number by an order of magnitude. The retroreflected beam is reflected by a rooftop mirror, which flip the linear p-polarized incoming CO_2 laser beam by 90 degrees.

The thin film polarizer is designed as the Brewster's angle for the s-polarization, which exactly reflects the retroreflected beam into the beam dump. There are two major reasons for preventing the retroreflected beam into the laser: First, a high power retroreflected beam backing into the laser would induce possible damages in the optics insider the cavity. Second, even a small portion of the retroreflected power feeding back into the laser cavity would cause additional noises of the laser, which may fail our ultrastable optical trap.

After the thin-film polarizer, an approximate 10:1 ratio expanding telescope is used to expand the beam. By expanding the beam close to the full aperture of the viewports for the CO_2 laser beam, we can achieve the tight focus on the order of 50μm $1/e^2$ intensity radius, since the size of the focus is inversely proportional to the size of the incoming beam before the focusing lens [116].

After the telescope, three mirrors raise the beam from the optical table to the height of the CO_2 laser beam port of the vacuum chamber, and align the beam into the final focusing lens. The focusing lens is placed before a ZnSe viewport of the main vacuum chamber. All these three mirrors and the final focusing lens are placed on two-dimensional or three-dimensional translation stages for the precision alignment of the CO_2 laser trap position, which is required to overlap the center of the magnetic potential. The precision of such alignments requires the stages controlled by micrometers with 10 μm precision.

After exiting from the the vacuum chamber, the beam is recollimated by another focusing lens which is exactly same as the first focusing lens. These two focusing lens actually constitute a confocal cavity for overlaping the incoming beam and retroreflected beam at the focal point. The overlap of two focus requires a precision of $1\mu m$ compared with the radial trap diameter about $50\mu m$. So the recollimating lens is mounted on an ultra-high resolution xyz-stage with 1μm resolution. This xyz-stage is then mounted on a conventional translation stage to provide enough travel range.

A mechanic “chopper” is inserted between the second focusing lens and the rooftop mirror. The “chopper” is a deflecting copper mirror mounted to an electronic controlled translator moving in the vertical direction. When the chopper moves down, the beam is blocked and directed into a power meter. When the chopper moves up, the beam strikes the rooftop mirror and reflected with a 90 degree rotation of the linear polarization. In the period of MOT and loading CO_2 laser trap, the “chopper” stays up. It moves down only when and after the free evaporation. Note that the beam shape at the rooftop mirror is the Fourier-transformation to the beam shape at the focal point [116]. Hence, only the low-frequency spatial component of the beam at the rooftop mirror can have an effect on the shape of the optical trap. The perturbation of inserting a deflection mirror only has high-frequency spatial components, which does not disturb the optical trapping potential near the focal point.

The roof top mirror is made by putting two truncated silicon reflector into 90 degree angle. Each silicon reflector is truncated in one side and enhanced gold coated at $10.6\mu m$ shown in Fig. 8.14. The truncated side is about 2.5 inch long and has a sharp edge without any bevel.

The rooftop mirror is placed to a home-made mount by a three-point support provided by spherical bearing balls. The three-point support ensures the surface of each mirror in a nearly perfect plane. The mount has six freedom adjustment, where two translation adjustments in the horizontal plane, three angle adjustments for the space orientation of the rooftop mirror, and one angle adjustment

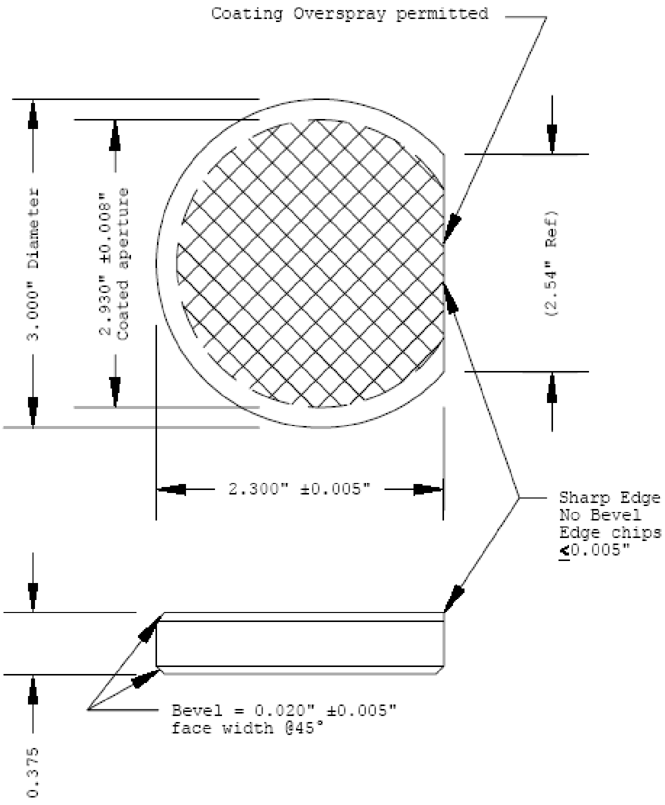

Figure 8.14: The truncated silicon reflector for making the rooftop mirror.

for the angle between the two reflection surface.

The specification of the CO_2 laser optics is listed below. Except for the specification, all these components are from II-VI Incorporated. Some abbreviations are used below: PG-Plano, CX-Convex, EG-Enhanced gold, EFL- Effective focal length, DIA-Diameter, THK-Thickness, CT-Center Thickness.

- Mirrors for zigzag path: Silcion Reflector 1.0 inch DIA, 0.12 inch THK, PG/EG.
- Mirrors for picking up the beam from the AO and the holographic beam splitter: Silcion Reflector 2.0 inch DIA, 0.12 inch THK, PG/EG.
- Cylindrical lens: ZnSe, 1.0 inch × 1.0 inch Dimension, 0.12 inch CT, 2.00 inch EFL.
- Thin film polarizer: ZnSe, coated at $10.6\mu m$ to reflect S-polarization and transmit P-polarization, 0.90 Clear Aperture.
- Focusing lens for the photodiode: ZnSe, PO/CX lens coated at $10.6\mu m$, 1.1 inch DIA, 3.75 inch EFL.
- Short focus lens for the beam expander: ZnSe, Aspheric lens coated at $10.6\mu m$, 2.5 inch DIA, 0.25 inch CT, 11.496 inch EFL.
- Large focus lens for the beam expander: ZnSe, Aspheric lens coated at $10.6\mu m$, 1.1 inch DIA, 0.12 inch CT, 1.255 inch EFL.
- Mirrors for the expanded beam: Silcion Reflector 3.85 inch DIA, 0.5 inch THK, PG/EG.

- Focusing lens for the optical trap: ZnSe, Aspheric lens coated at $10.6\mu m$, 2.5 inch DIA, 0.25 inch CT, 7.50 inch EFL.

8.5.6 Electronic Controlling System for CO_2 Laser Trap

The key method of producing a strongly interacting Fermi gas in our apparatus is forced evaporative cooling of atoms in a CO_2 laser trap. As discussed above, it is done by lowering the intensity of the CO_2 laser laser beam. The laser intensity lowering should be continuous and quite to avoid heating the atoms by the intensity and position fluctuation. This lowering process is realized by controlling the power of the first-order diffraction beam from the IntraAction Corporation AGM-4010BG1 AO. The laser power in the diffraction beam is proportional to the power of the RF source sent into the AO. The RF source is a 40 MHz sinusoidal wave provided by an IntraAction GE-4050 AO-driver. By varying the amplitude of the RF source, we control the power in the diffraction beam.

In the real application, the decrease of 40 MHz RF power causes the AO cool down. The temperature variation in the AO would cause the change of the index of refraction, which makes the propagation direction of the CO_2 laser beam shift. This effect finally moves the optical trap position and causes the lowering process very unstable. To overcome this problem, we input double frequency component RF waves into the AO: 40 MHz and 32 MHz. 40 MHz one is for the CO_2 laser trap, while 32 MHz one is used for the temperature compensation. The procedure is as the following: Before the optical trap lowering process, the 40 MHz RF component has the full power and the 32 MHz component has zero power. When the lowering process begins, the RF power of 40 MHz decreases and the power of 32 MHz increases so that the total power deposited into the

AO is nearly constant. Using this method, we can keep the temperature of the AO nearly unchanged during the lowering process, which maintain the position of the CO_2 laser trap nearly unshifted during the evaporative cooling process. The extra diffraction beam generated by the 32 MHz RF wave is sent into the beam dump by the same pick-up mirror we used for the zero-order 40 MHz beam (shown in Fig. 8.13).

To apply this method, we need to make modification to the commercial IntraAction GE-4050 AO-driver. The commercial product can only generate an internal single frequency RF power at 40 MHz. By bypassing the electronics of the oscillation generation circuit in the AO-drive, we directly input the external RF sources into the amplification circuit of the AO-drive.

Using the external RF source to drive the AO amplifier has five advantages: First it allows us to implement the temperature compensation we discussed above. Second it generates a modulation curve for the RF power by digital wavefunction generators, which enables us apply complex lowering curves in the forced evaporation. Third, the RF system can be used for parametric-resonance measurements of the trap frequencies only by replacing the lowering curve with a sinusoidal amplitude modulation. Fourth, the external RF source can generate very precise RF pules, which is used to suddenly turn the optical trap on and off. Fifth, it is easy to do frequency modulation for the external RF diving source, which provides a tool to change the orientation of the CO_2 laser beam, thus rotate the optical trap.

To achieve all the advantages, I built a radio frequency electronic system to control the refracted CO_2 laser beam from the AO. The block diagram of this radio frequency electronic system is shown in Fig. 8.15.

The 40 MHz and 32 MHz RF generators are Agilent E4423B and Marconi

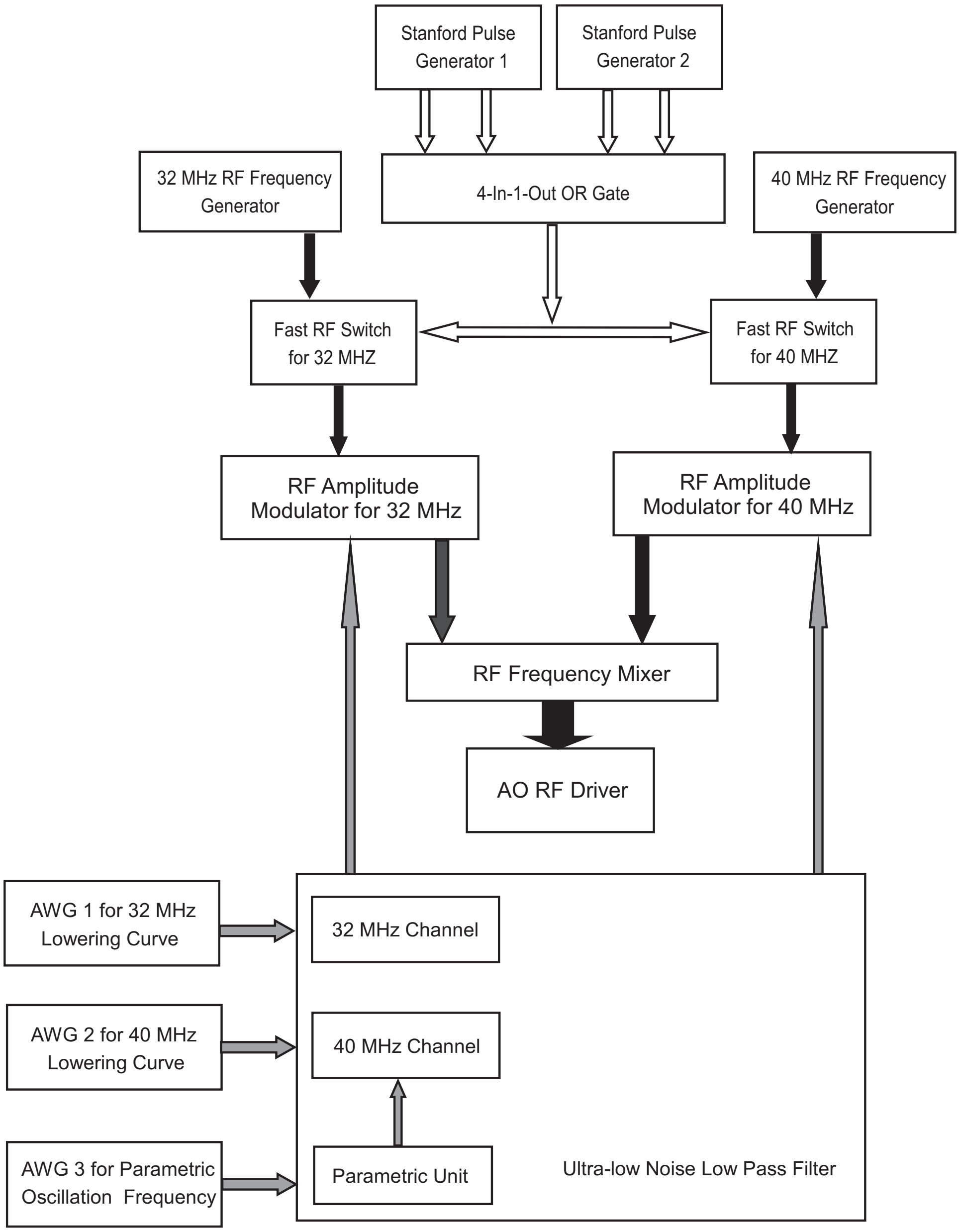

Figure 8.15: The block diagram of an electronic controlling system for the CO_2 laser beam.

Instrument 2024 respectively.

The fast RF switch is Mini Circuit ZYSWA-2-50DR. The on/off state of the switch is controlled by a TTL logic input, which is connected to the output of the OR gate.

The 4 input OR gate is a home-made electronics using the Fairchild Semiconductor 74AC32 IC. 74AC32 IC has four units of 2-input OR gate. By connecting two 2-input OR gates in parallel, then putting the third OR gate in series with the first two, we implement the function of 4-input OR gate. The output of the OR gate is always logic high as long as one of the input is the logic high. This logic gate enables us to turn the optical trap on and off multiple times in a sequence of pulses generated by Stanford pulse generators.

The RF amplitude modulator is Mini Circuit ZLW-1. In the initial application, ZLW-1 mixes two input RF frequencies and generates the output wave as the frequency difference between two input waves. By reversing the output port as one of the input port, we input a DC lowering curve and a RF carrier wave into this circuit. In the end, we obtain an amplitude modulated RF wave from the third port. After that, the 40 MHz and 32 MHz RF sources are combined by the power combiner circuit of Mini Circuit ZSC-2-1. Finally the combined RF power is sent into the RF drive of the AO.

Agilent 33250A arbitrary wave function generators are used to generate the lowering curve and parametric oscillation of the optical trap. The lowering curves generated by the arbitrary wavefunction generator are digital signals, which are constituted by a series of small voltage jumps of commanding digital voltages. Those small jumps add additional noises into the RF source for the AO, thus increase the final noises in the CO_2 laser beam. Ideally, a smooth analog curve has much smaller noises than the digital one. But the complex function that we need for the lowering curve is very difficult to be generated by analog circuits. Here we put a low-pass filter to "wash out" the high frequency noise in the digital signals. The circuit diagraph of the low pass filter is shown in Fig. 8.16. The circuit is mainly based on the Analog Devices ultralow noise operational amplifier AD797. In our experiment, only the frequencies above tens of Hz are harmful to our optical trap, so we put the cut-off frequency of the low pass filter circuit at about 20 Hz.

8.5.7 Storage Time of CO_2 Laser Trap

The storage time of the atoms in the CO_2 laser trap of our new apparatus is measured by the atom number versus the holding time of a single forward beam. The single exponential fit gives the $1/e$ time storage time of about 60 seconds, which is shorter than the best record of about 300 seconds that we obtained in the old system . Here I will explain the main reason for the reduction of the storage time of the CO_2 laser trap.

First, the measured laser intensity noise and position noise of our CO_2 laser beam are in the scale of $1 \times 10^{-12}/Hz$ and $5 \times 10^{-10} \mu m^2/Hz$ respectively. According to Eq. (8.18) and Eq. (8.21), the intensity noise heating time is 3000 seconds, and the position noise heating rate is about $100 nK/s$, which is unlikely to respond to the reduction of the lifetime of the CO_2 laser trap since the full depth of CO_2 laser trap is $500\,\mu$K, and the cloud temperature before the evaporative cooling is tens of microkelvins. So we can exclude the reasons due to the CO_2 laser beam noises.

Second, in Section 8.5.2 we find the upper bound resonant optical heating is

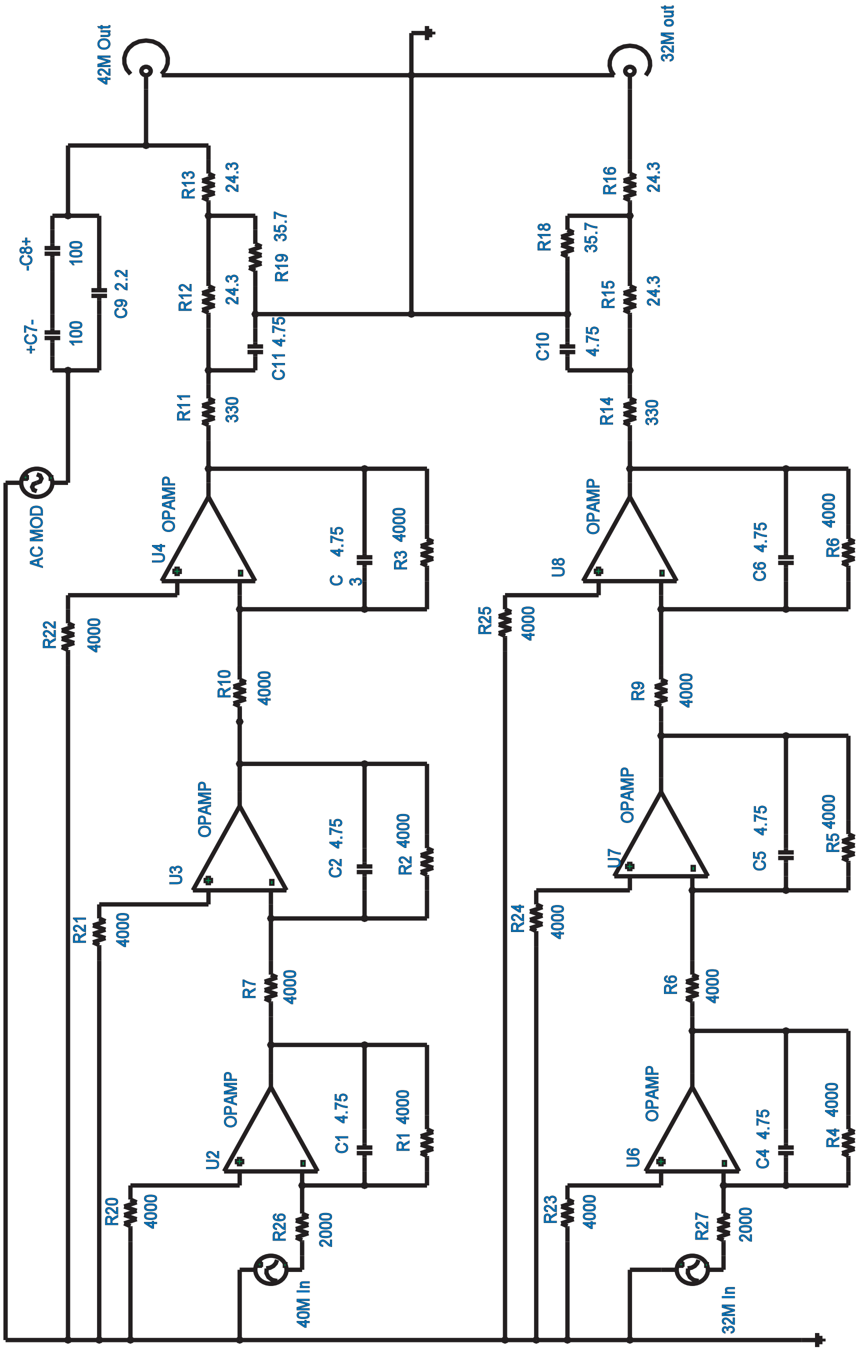

Figure 8.16: The circuit diagram of the ultralow noise low pass filter used for the digital lowering curve. For parametric oscillation experiment, we need to couple the modulating frequency close to the optical trap frequency into the RF source. A parametric feed through circuit is added on the top-left corner after the main low-pass circuit .

$5nK/s$, which is also unlikely to respond to the reduction of the lifetime of the CO_2 laser trap.

Based on the above analysis, the most possible reason for the reduction of the life time is the background gas collision. In our system, the measured vacuum in the main chamber is well below 3×10^{-11} Torr. According to Eq. (8.23) and the cross section data $\sigma[u_b]$ listed in [117], we find only ^{6}Li-^{6}Li collisions at $T = 300\,K$ has a cross section of about $9.2\,(nm)^2$, which is large enough to support a loss rate with time constant of about 100 seconds. Other collision mechanisms, such as ^{6}Li-He and ^{6}Li-H_2, have very small collision cross section, which is not consistent with the loss rate we observed.

Based on this conjecture, we compare the pumping rate of the main chamber in our new vacuum system with that in the old system. We find the 20 liter per second pumping rate in our new chamber is far less than the 400 liter pre second pumping rate of the main chamber in the old system. So it is very likely that the new system can not pump out the atomic beam of lithium very quickly, which cause the untrapped hot ^{6}Li atoms to stay in the vacuum chamber, and then collide with the trapped ^{6}Li atoms. It is an important lesson to apply a higher pumping rate in the main vacuum chamber to avoid such background gas collisions due to the atomic beam. This is extremely important for the case where the long storage time of ultracold atoms is needed.

8.6 High Vacuum Infrared Viewport

One of the major challenges of applying CO_2 laser beams for an optical dipole trap is availability of high-quality infrared viewports for ultrahigh vacuum application.

Crystalline zinc selenide (ZnSe) is transparent at wavelength of 10.6 μm. It is the most idea optical material as windows for high power CO_2 laser beams. However, ZnSe is very soft material, which can not bear a high clamping force. The standard hard sealing methods for BK7 glass, such as a knife edge cutting into copper, is not suitable for crystalline ZnSe. The standard soft sealing methods, such as using elastomer O rings and Vac-Seal resin, can not satisfy our requirement of ultrahigh vacuum of less than 10^{-10} torr because O rings and resin have serious outgassing and very low bakeout temperature. Currently the only applicable method of ZnSe viewports is to use the soft-metal seal technique.

Our previous CO_2 laser windows in the old apparatus are differentially pumping ZnSe viewports made by Insulator Seal, Inc. These windows are custom built, which are extremely expensive with the price about 10,000 USD per piece. Since CO_2 lasertrap is an ace-in-the-hole technique in our lab, it is much better for us not to be limited by the availability of the commercial products. So we decide to develop our own techniques for ultrahigh vacuum windows for CO_2 laser beam. Meanwhile, we found that a flux-free eutectic solder made by soft Pb-Ag-Sn alloy was used to make seals for ZnSe viewports by Adams's group in University of Durham [120]. In their viewports, a single seal achieves 10^{-10} torr pressure in vacuum system. This gives us a hope that by combining "soft-metal seal" and "differentially pumping" techniques, we may build an ultrahigh vacuum ZnSe viewport working in 10^{-11} torr vacuum.

In this section, I will explain the building and operation of ZnSe viewports step by step, which includes several processes: designing and machining vacuum parts; welding and cleaning vacuum parts; preparing tools and optical material; making the seal; constructing a small vacuum system for testing; assembling viewports and leak testing; translating viewports to the main vacuum chamber and daily maintenance.

8.6.1 ZnSe Viewport Design

A crystalline ZnSe optical window from II-VI Incorporated is used to make the vacuum viewport. The home-made viewport consists: the clamping flange (Top part), the blank flange (Bottom part), an inner seal ring and an outer seal ring, a differentially pumping area between the inner and outer seals.

The cross-sectional view of an assembled viewport is show in Fig. 8.17. The top-view with dimensions of the top and bottom part of flanges is shown in Fig. 8.18. The cross-sectional view with dimensions of the top and bottom part of flanges is shown in Fig. 8.19. The differential vacuum port of the viewport is connected to a small differentially pump chamber through a brained vacuum roughing hose. The blank flange has 1.6 inch diameter optical aperture. Eight silver plated 10-32 hex screws couple the clamping flange to the blank flange. The blank flange is weld to one end of a vacuum tube (1.5 inch diameter) called “half nipple” from MDC. The other end of the “half nipple” is a standard 2.5 inch Del-Seal Conflat flange, which is directly connected to the port in the main vacuum chamber.

8.6.2 Tools and Materials

To build an ultrahigh vacuum ZnSe viewport, the tool kits and required parts are listed below.

- The top and bottom flanges show in Fig. 8.18 and Fig. 8.19 are fabricated in

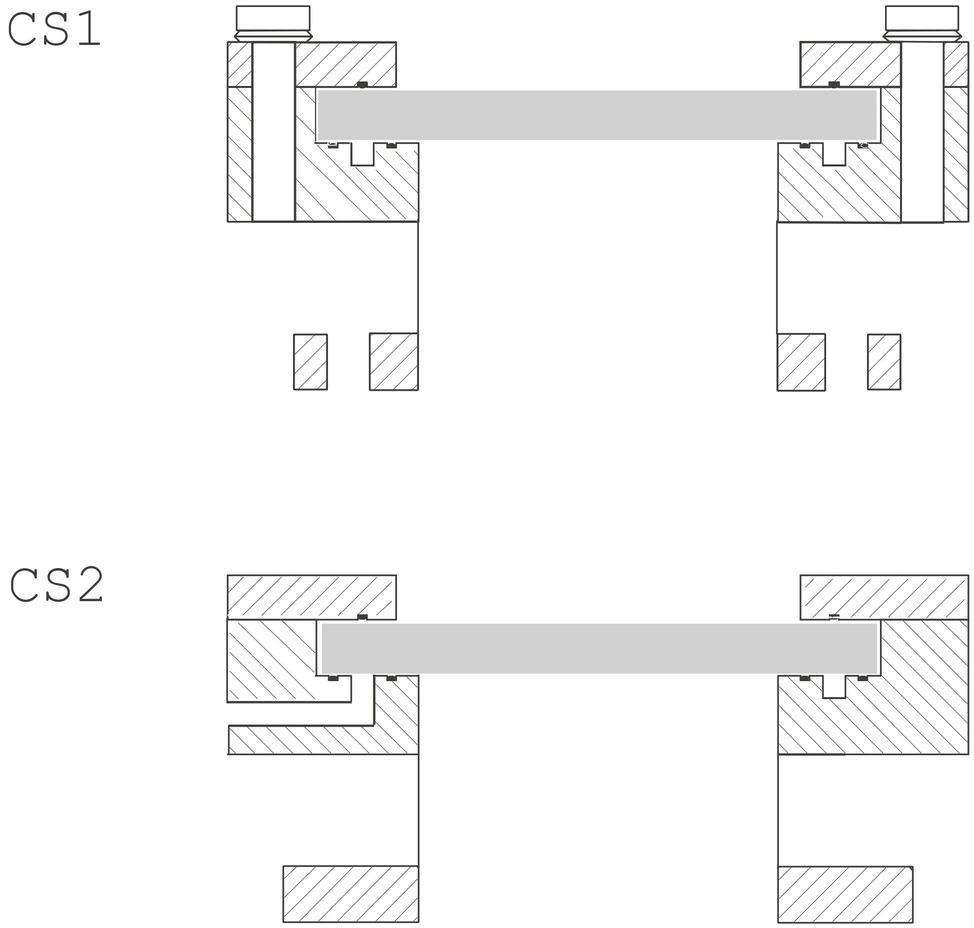

Figure 8.17: The structure diagram of an assembled ZnSe Viewport

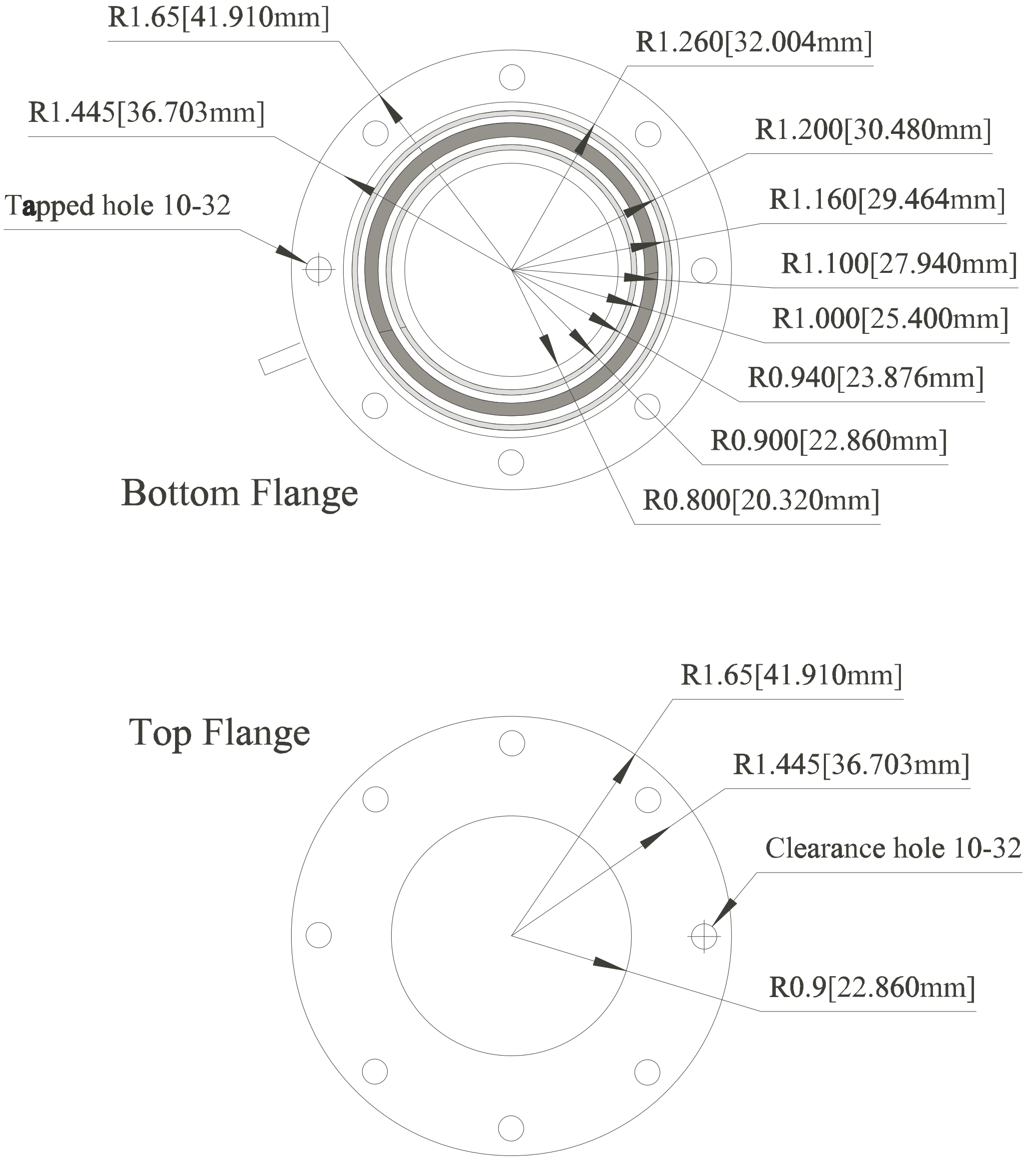

Figure 8.18: The top view of the clamping and blank flanges

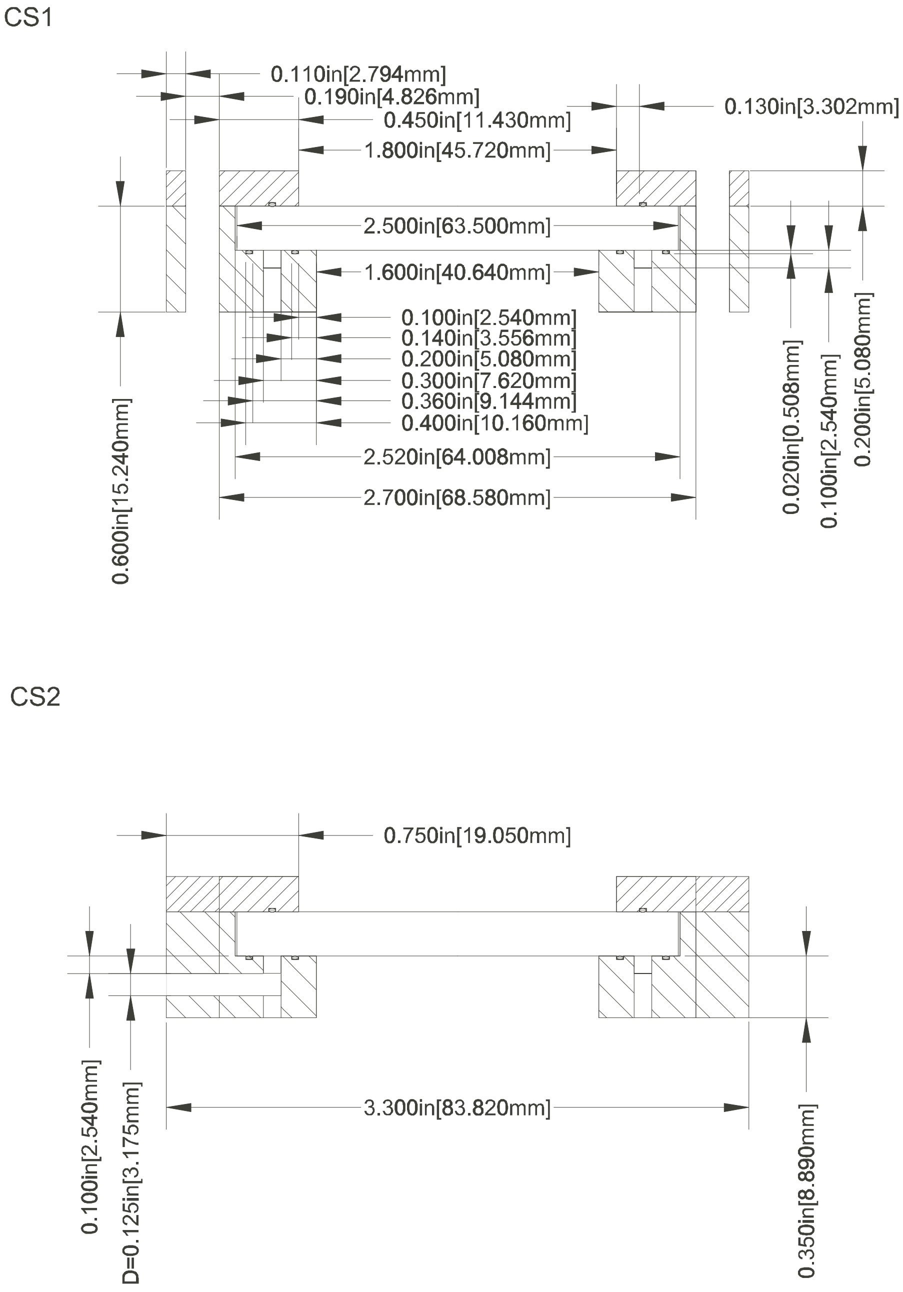

Figure 8.19: The cross-sectional view of the clamping and blank flanges

Duke Physics machining shop. The building material is 304 stainless steel. The required precision of machining is $\pm 10\,\mu$m.

- Vacuum parts for the differential pumping region, including: VCR Braided vacuum hose, Male VCR to Del-Seal Adaptor, 1/4 inch angle valve for ultrahigh vacuum, VCR metal gasket face seal fittings etc. Most of those parts are from MDC and Swagelok.
- Material for the seal is Indalloy 165 solder. This solder is an alloy with 97.5% Pb, 1.5% Ag, and 1% Sn, which has a melting point of 309°C and Young's modulus of about 18 GPa. It is a soft metal compared with copper of 117 GPa.
- Metcal 745 high temperature soldering tips for fabricating the rings of solder seals.
- II-VI ZnSe window. This crystalline ZnSe window is anti-reflection coated at $10.6 \mu m$ wavelength with reflectivity less than 0.20%. The window is plano in both surface with 2.5 inch diameter and 0.25 inch thickness. The surface figure is about 1 fringe $\sim$ 1/2 fringe at 0.63 microns.
- SCHOTT BK-7 glass window with the same dimension with the ZnSe window. It is used for compressing and testing the seals.
- Silver plated 10-32 hex screws. These screw are used to couple the clamping flange with the blank flange. Also 1/4-28 set screws, which are used to connect the window with the vacuum chamber.
- Key Bellevilles disk spring washers for each 10-32 hex screws. They are

used to compensate the toque loss induced by the thermal expansion during bakeout.

- Precision 1/4 inch drive dial torque wrench. They are used to apply the precise torque for the bolts when installing the viewport.
- Loctite 246 medium strength and high temperature threadlocking materials. They are used to lock 1/4-28 set screws into the tapped hole in the main vacuum chamber.

8.6.3 Welding and Cleaning

The first step of making window is to weld the home-made blank flange with the “half nipple” from MDC. The welding of the ultrahigh vacuum parts needs special technique to avoid the small leakage and outgassing. Duke FEL vacuum workshop helped us to complete this project. After welding, the vacuum parts of viewport are first cleaned by ultrasonic cleaner using methanal and distill water. After that, the acetone and methanal is used several times to clean the surface of each part.

8.6.4 Vacuum Chamber for Testing

A small vacuum chamber is built to test viewports. This small chamber is made by a 2.75 inch diameter crossing tube with 5 ports. The top port is located in the center of the crossing tube, and used for a ZnSe veiewport. The other four ports are located at the four ends of the crossing tube. One port is just simple closed by a blank flange. One port is used for a vacuum ion gauge. One port is connected to a 20 liter/sec ion pump. The last one is coupled to an angle valve. The other end of the angle valve is connected to one end of a “T” shape VCR adaptor. The other two ends of the “T” shape VCR adaptor have the following connections: One is connected to a Varian turbo pump, and the other is connected to the differential pumping hose of the viewport. When the angle valve is open, the turbo pump works as a roughing pump to prepare preliminary vacuum required by running the ion pump. After the ion pump begins to operate, the angle valve is closed and the turbo pump plays the role of differentially pumping. After the viewport is transferred to the main vacuum chamber, this small vacuum chamber is used as the differentially pumping region operated only by the ion pump.

8.6.5 Making the Seal Ring

Making solder seal rings is a meticulous work. By practice, I find that 0.05 inch diameter solder rings have the best performance in sealing for the seal gap of 0.04 inch width and 0.02 inch depth in our viewports. A high temperature soldering tip with very sharp needlepoint shape is needed to weld a solder wire into a ring. A good sealing requires critical quality of the welding of the ring. Based on my experience, only the ring with a very smooth joint, which has a shining surface without any protuberance, can be used to seal a vacuum to 1×10^{-9} torr. To make seal rings with good quality, repeating practice is necessary.

8.6.6 Installation of ZnSe Viewport

A typical process to install a ZnSe viewport is given below. Before sealing a ZnSe window, a BK-7 glass window is always placed into the viewport first to test the seal rings. All the torques to the clamping flange are required to add uniformly and slowly by tightening the eight 10-32 hex screws using a precise dial torque wrench. The maximum toque imbalance between screw to screw is prohibited up to 1 $in \cdot lb$ in the whole tightening process. The maximum torque applied to the screws for the ultimate vacuum pressure should be carefully controlled. I find, for BK-7 glass, a 20 $in \cdot lb$ torque added to each screw will break the window. For crystalline ZnSe, the failure of the window has not been observed by slowing adding up to 10 $in \cdot lb$ toque to each screw. I also find that in all the successful cases of sealing a ZnSe window, a vacuum pressure of about 1×10^{-9} torr is reached when the torque is added up to 8 $in \cdot lb$ to each screw.

If a vacuum sealing of about 1×10^{-9} torr is not seen after adding a torque of 10 $in \cdot lb$ toque to a ZnSe window, the process of adding torque should be STOPPED. I will treat 10 $in \cdot lb$ as the critical torque of crystalline ZnSe window. Above this torque, ZnSe crystal may BREAK! I find that the most possible reason for an unsuccessful sealing is the unqualified solder rings. The ZnSe window is about 2,000 USD per piece, so extremely carefulness should be paid to avoid breaking the crystal. Readers can use the following record of installing a ZnSe viewports as a reference.

1. The 0.05 inch diameter solder ring is placed into the seal gaps inside the flange. Two rings are put into the blanking flange, and one ring is put into the clamping flange. A BK-7 glass window is placed into the viewport for testing the seal rings.

2. The initially distance between top and bottom flange is measured as 0.077 inch. After pre-compressing with 5-7 $in \cdot lb$ torque, the measured gap is 0.067 inch.

3. A 13-14 $in \cdot lb$ torque is applied to get preliminary sealing with a BK-7 glass

window. The measured distance between top and bottom flange is 0.040 inch, which indicates the clearance distance between the window and the bottom flange is 0.020 inch. This distance is the effective thickness of the seal for sealing the vacuum.

4. After 12 hours relaxation of mechanic stress in the seal rings, a 11 $in \cdot lb$ torque is reapplied to the clamping screws. Then a Turbo pump is turned on to get 7.3×10^{-6} torr after 2-hours operation.
5. Bake the ion pump to 180°C for 24 hours. Then turn on the ion pump and close the angle valve. A vacuum of 5×10^{-10} torr pressure is achieved, which indicates the seals work normally.
6. Turn off the pump, and dissemble the viewport. Use a ZnSe window to replace the glass window. A 2.5 $in \cdot lb$ torque is applied to each screw to get preliminary seal.
7. Turn on Turbo pump again. A 7.0×10^{-5} torr vacuum is obtained. By slowing adding the torque several times in one day period, a 7 $in \cdot lb$ torque is finally applied to get 1×10^{-5} torr pressure. The measured gap between top and bottom parts is 0.040 inch.
8. Turn on ion pump and close the angle valve for the differentially pumping. A vacuum of 1.4×10^{-7} torr pressure is obtained after 20 minutes.
9. After baking the ion pump to 180°C for 24 hours. A vacuum of 2.5×10^{-10} torr is achieved.
10. Reapply 7 $in \cdot lb$ torque. The measured distance between top and bottom parts are 0.038 inch, which indicates the clearance distance between the

window and the bottom flange is 0.018 inch. The view port is operated the ultimate pressure between 2×10^{-10} torr to 8×10^{-10} torr, which is only limited by the small pumping rate in our testing chamber.

8.6.7 Translation and Maintenance

After a viewport reaches the 10^{-10} torr range in the testing chamber, the last step is to transfer the ZnSe viewport to our main vacuum chamber. Before the translation of ZnSe viewport, our main vacuum is baked to 350°C and archives an ultimate pressure less than 3×10^{-11} torr, which is below the detectable value of our ion vacuum gauge. We shut down the pump, and refill argon gas into the vacuum chamber, then translate our ZnSe window from the test chamber to the main vacuum chamber in a protection atmosphere of argon gas. When the installation is completed, we pump the main vacuum chamber again and get an ultimate pressure less than 3×10^{-11} torr again without baking the system again. The advantage of this translation method is that we avoid the risk of breaking the ZnSe window or failing the solder seals, which may happen during the high temperature baking.

A good maintenance of ZnSe viewports will reduce the risk of damaging this critical part in our apparatus. By blowing the compressed gas, we can clean the dusts accumulated on the surface of the window, which ensures the optical quality of the window. An ion vacuum gauge located in the differentially pump region is turned on to monitor the vacuum when intense CO_2 laser beams go through ZnSe viewports. An improper alignment of the CO_2 laser beam will make the beam hit the flange of the viewports thus heat the solder rings. For a couple of seconds heating with the full power CO_2 laser beam, the pressure in the differential pump region will double. A longer time heating from the CO_2 laser beam should be avoid, which may cause the failure of the seals. For three years, the pressure of differentially pumping region keeps as below $\leq 1 \times 10^{-7}$ torr read by the ion gauge.

By the end of 2007, our home-made ZnSe viewports had been operated for three years for the ultrahigh vacuum of 3×10^{-11} Torr and the differentially pumping region of about 5×10^{-8} Torr. This shows our home-made ultrahigh vacuum ZnSe viewport is a successful technique.

8.7 Imaging and Probing System

To extract physical information from cold atoms, the imaging and probing system is required. In our apparatus, there are mainly three devices to detect cold atoms: photomultiplier tube (PMT), CCD camera, and RF antenna. PMT is used to collect the fluorescence of cold atoms, which help us to estimate the atom number in the trap. CCD camera is our main tool to record the absorption images of the atoms. RF antenna has a dual role: It not only provides a RF spectroscopy measurement but also can be used as a tool to manipulate the spin states of the atoms.

8.7.1 PMT Probing System

In our system, the PMT and the CCD camera share the same port, so we use a folding mirror to pick-off the fluorescence and send it into the PMT, shown in Fig. 8.20.

If we assume the atoms are fully saturated by resonant light, the atoms number can be approximately estimated from the output voltage V from the PMT by

$$n = \frac{W_{MOT}}{W_{sat}} = \frac{4V}{\alpha R \Omega h \gamma_s \nu}, \tag{8.28}$$

where W_{MOT} is the fluorescence power emitted by the MOT, while W_{sat} is the saturation fluorescence power of a single atoms. α is the PMT amplifying coefficient beteen the current and photon power (Amps/watt). R is the output resistor of the PMT. Ω is the spacial angle of the lens for collecting the fluorescence. γ_s is the natural linewidth of the resonant light, and ν is the laser frequency.

8.7.2 Imaging Optics and CCD Camera

The generation of the imaging beams is shown in Fig. 8.9. In the imaging beam path, a double passed AO provides the up-shifted frequency to compensate for the frequency offset generated by the locking AO. For high field imaging, the frequency detuning is generated by unlocking the dye laser and shifting the laser frequency. The laser frequency shift is implemented by sending a commanding voltage into the external scan of the dye laser electronic control box. The imaging beam is coupled into an optical fiber, whose output is close to the imaging port (port 10 in the main vacuum chamber).

After exiting the fiber, the imaging beam first passes through a polarizing beam splitting cube to obtain a linear polarization orthogonal to the bias magnetic field. After the cube, the beam is collimated by a converging achromatic lens and enters into the vacuum chamber.

The optics for absorption imaging is shown inFig. 8.20. The light from the incident beam as well as the scatter light from the atoms are collected by a

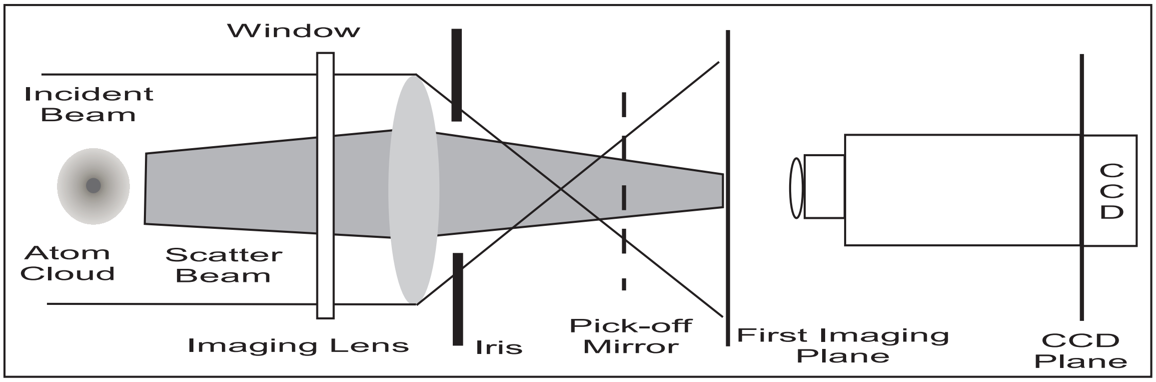

Figure 8.20: The imaging optics for the CCD camera.

high quality achromatic lens, which is designed to compensate for the aperture aberration due to the exit vacuum window. This lens makes a 1:1 image of the trapped atoms at the place before a microscopic objective. An iris is put between the image plane and the lens to block the unwanted incident beam beyond the region of trapped atoms, which helps to improve the contrast of the image. When we use the PMT to collect the fluorescence, this iris is full opened to get the maximum fluorescence signal.

Real images are took by the microscope objective, which is mounted on the front of a CCD camera, an Andor Technology DV434-BV. The image plane of the microscopic objective is adjusted to be in the plane of the CCD chip. The CCD chip provides a 1024 × 1024 array of pixels with each pixel size of 13 μm. The CCD camera has several acquisition modes. We usually use the fast kinetics mode. By enabling this mode, the CCD screen is divided into several stripes in vertical direction and takes several images continually in a very short time. For each image, there is only one strip exposed while other strips are blocked by a razor blade in the imaging plane of the imaging lens. After exposure, the photoelectron charges in the exposed strip are transferred to the unexposed stripes with a very

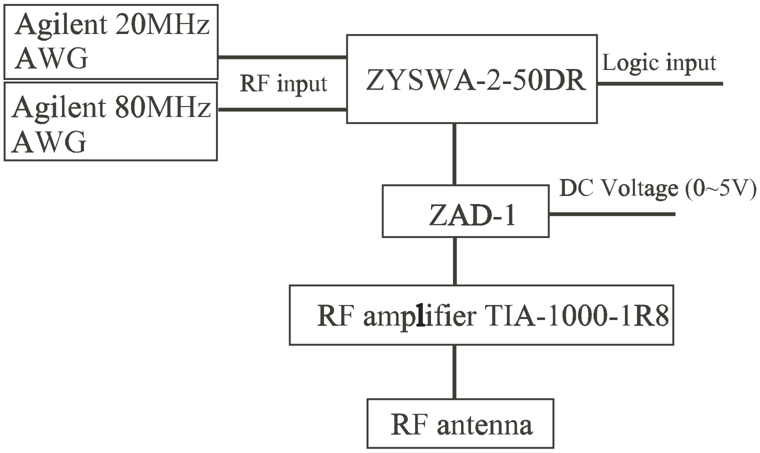

Figure 8.21: The schematic diagram of the control circuit for the RF-antenna.

fast rate up to $16\mu s$/row.

8.7.3 Radio-frequency Antenna

A RF-antenna is a powerful tool to manipulate the spins of the cold atoms. In the thermodynamics and rotation experiments presented in this dissertation, the RF antenna mainly works to make a balanced spin mixture in the two lowest hyperfine states. In our recent coherent spin mixture experiments [121], the RF-antenna works as a tool to measure the transition frequency between the hyperfine level.

The RF-antenna in our system is designed by James Joseph. The vacuum seal of the electrical feedthrough is made by Insulator Seal. The seal can stand a maximum of 3 A and 250 V DC, which enables us to provide enough RF power in a broad RF range from several MHz up to several GHz into the RF transmission line.

The schematic diagram of the control circuit for the RF-antenna is shown in Fig. 8.21. The RF signal source is provided by an Angilent 33220A 20MHz and/or an Angilent 33250A 80MHz arbitrary wavefunction generator. By using a Mini-

Circuits ZYSWA-2-50DR (a 2-in-1-out logic gate), one of the input RF signals is selected and directed to a Mini-Circuits ZAD-1 (a frequency mixture). The ZAD-1 multiplies the RF signal with a DC signal, which is used to turn on/off the RF. Finally the RF is amplified by a RF amplifier and coupled into the RF antenna. The RF amplifier is a Mini-Circuits TIA-1000-1R8 providing a 35 dB Gain for 0.5-1000 MHz RF signals with 4 W saturation power.

8.8 Computer and Electronic Control System

For cold atom experiments, all the optical, magnetic and electronic devices need to work in a precise time sequence, which requires a computer control system providing timing sequence for each component. There are two different precision requirements for the timing: First, for the MOT stage and the free and forced evaporation, a time precision of about 100 μs is necessary. Second, for imaging cold atoms and studying dynamical behavior of cold atoms, the required precision is about 1 μs.

To satisfy both requirements with minimum costs, we apply two timing systems: one is a computer-controlled 32-channel I/O system, the other is a network of interlinked Stanford Research pulse generators. The I/O system is responsible for the duty of 100 μs timing precision, and Stanford generators do the job for 1 μs timing precision. In addition, for the GPIB communication enabled equipments, we send GPIB commands to store some timing sequences in the memory of those equipments. To control some components that require analog signals, a multiplexer is used to convert digital timing signals to the analog ones.

All the timing sequences are managed by a Labview program. End-users use a text file called “timing file” to set the timing sequences for each experiments. The Labview program is developed by the previous students in our lab and also described in several thesis [64,122]. Here I put my emphasis on the hardware part of the computer control system, whose structure is quite different from that in our old apparatus.

8.8.1 Architecture of Timing System

The block diagram of the architecture of the timing system is shown in Fig. 8.22. The timing system is controlled by a Dell computer with 2.5 GHz Pentium-4 CPU and at least 1 GB RAM. Fast CPU and large RAM are important for operating the timing system because the timing sequences are stored in the RAM as the form of a very large matrix. The actual timing signals are a series of digital pules of 0V or 5V, which are generated by a National Instrument (NI) PCI-6534 high speed Digital I/O card. This card is connected to a NI SCB-68 shield connector box via a SH-68-68-D1 shield cable. From the connector box, 32 channel digital signals transmit via a rainbow cable and enter into a home-made schottky diode breakout panel. The schottky diode breakout panel connects to BNC cables, which send 32 channel digital signals to different components.

The 32 Channel digital signals are used for several different applications. As shown in Fig. 8.22, a portion of them are directly used as logic gates for some components, such as PMT gate, RF pulse gate, dye laser frequency unlock/shift gate, and camera shutter gate. Others are used as the TTL-logic inputs of the multiplexer, where the digital signals are used to choose the different input analog voltages for output. Those output voltages are mainly used as the control voltage in the AO modulators. The last portion of the digital signals are used as the

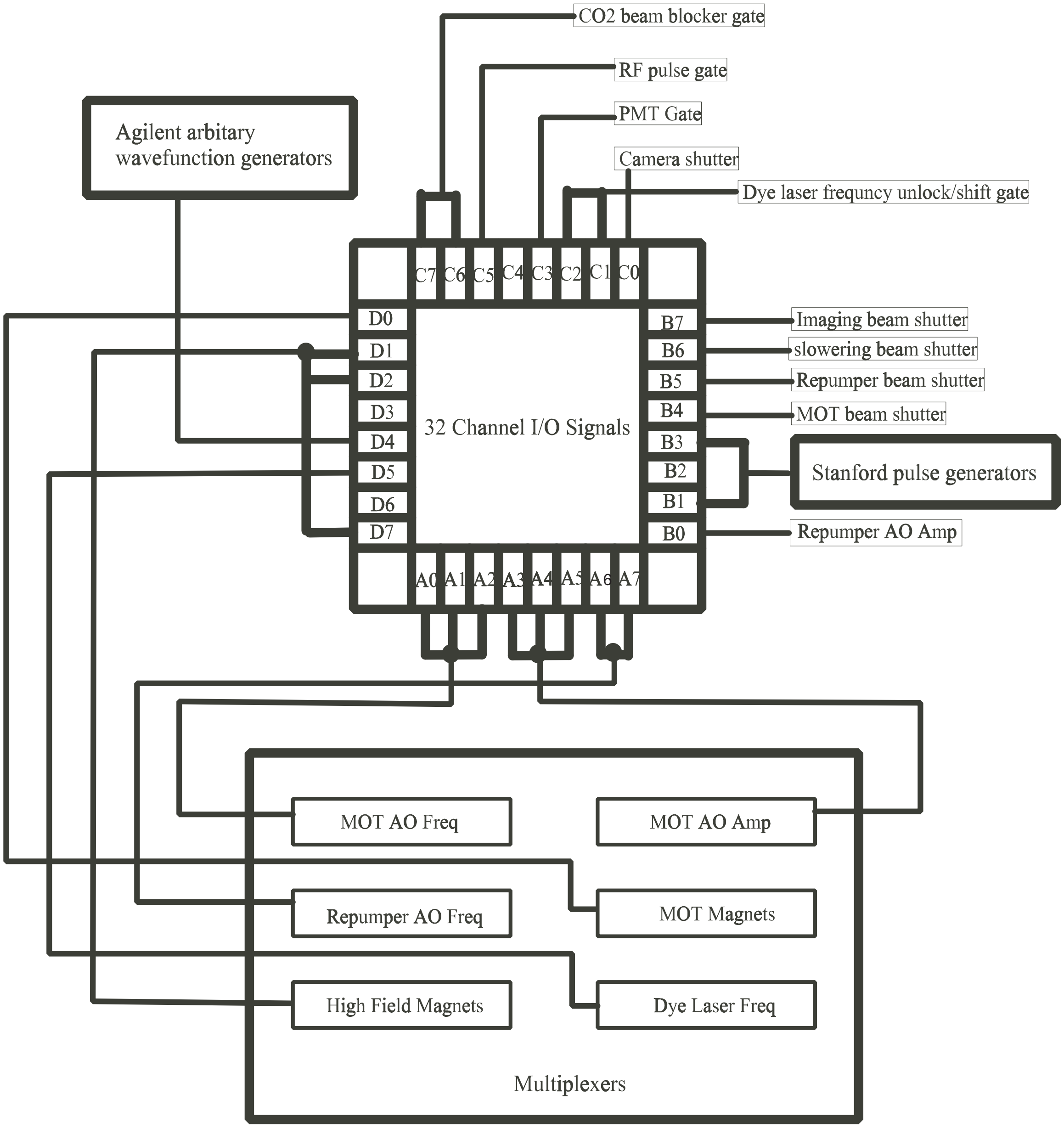

Figure 8.22: The block diagram of the architecture of the timing system.

trigger signals for Stanford pulse generator and arbitrary wavefunction generator.

8.8.2 Multiplexer

The home-made multiplexer is a large electronics box that consists of about 20 circuit boards. The most important circuits in the multiplexer are analog switches. We use three 8-channel switches, six 4-channel switches and four 2-channel switches in the multiplexer. Those switches use ADG408/409/419 IC from Analog Devices to implement the multiplexer function. As an example, for a 8-channel switch with three TTL-logic inputs, we apply different logic inputs form "000" to "111" to choose one of eight input voltages as the output. The multiplexer has a maximum of 56 analog voltages. Those voltages can be provided either by the external power supply or the internal power supply. The circuits of the internal power supply, including transforms, National Semiconductor LM350 current regulators, and KBL02 bridge rectifier, provides 15V DC up to 3A. For each internal voltage, a potentiometer is used to adjust the output voltage value. A voltage probe circuit samples the input voltages in each channel and display its value in a digital LCD.

8.8.3 Electronics for Imaging Pulse Generation

The block diagram of the electronics for image pulse generation is shown in Fig. 8.23. The imaging pulses are mainly generated by Stanford pulse generators.

One important issue in the imaging pulse system is that we set the imaging beam AO at the state of “on” for most of time during experiments to keep it warm. By doing that, we keep the AO temperature constant and maintain the imaging beam direction. Meanwhile, the shutter for the imaging beam is closed to block the beam into the vacuum chamber. When we are ready to take an image, the AO is turned "off" for a small amount of time before the shutter is opened. After the shutter is opened, the AO then is turned "on" for a precise time by a voltage pulse from a Stanford pulse generator and generates the optical imaging pulse. After this process, the shutter is closed, then the imaging beam is turn "on" again to keep the AO warm. This scenario needs two control voltage for the imaging beam AO. One is called "pulse voltage", and the other is called "warming voltage". As shown in Fig. 8.23, the "pulse voltage" is from the Stanford pulse generator, and "warming voltage" is from the multiplexer.

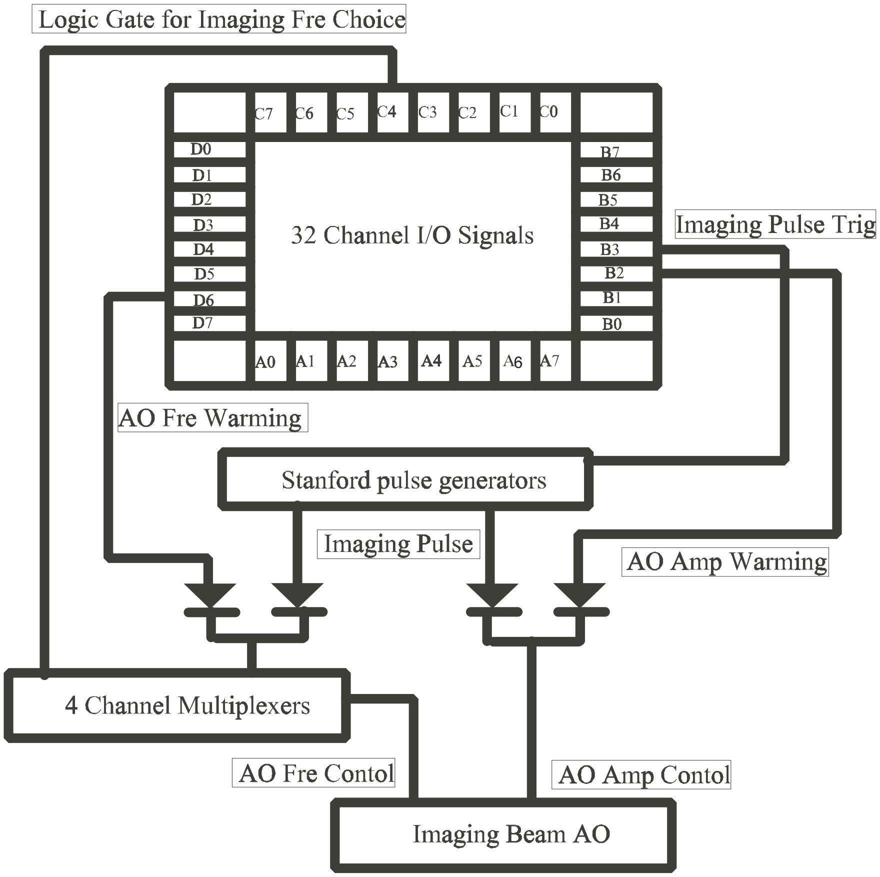

Figure 8.23: The block diagram of the electronics for imaging pulses generation.

Chapter 9

Conclusion

My dissertation provides experimental investigations of thermodynamics and low viscosity hydrodynamics of a strongly interacting Fermi gas of ultracold degenerate ^{6}Li atoms.

For the purpose of this research, a new all-optical cooling and trapping apparatus was built during the first stage of my Ph.D. work. The new apparatus adopts several upgraded techniques: an air-cooling short Zeeman slower, a compact ultrahigh vacuum chamber, and home-made infrared ultrahigh vacuum viewports etc. Using the new apparatus, we studied the unique evaporative cooling of a unitary Fermi gas in an optical trap. By applying the optimal optical trap lowering curve for the energy-dependent evaporative cross section, we obtain a runaway evaporation in the unitary limit, which generates a degenerate Fermi gas of about 2×10^5 atoms per spin state in a fraction of a second [63].

Our measurements of both the entropy and energy of a strongly interacting Fermi gas provide the first model-independent thermodynamic measurements in this system [49]. We observe a transition behavior in the entropy versus energy curve near $E_c/E_F = 0.83(0.02)$ and $S_c/k_B = 2.2(0.1)$, which is interpreted as a thermodynamic signature of a superfluid transition in a strongly interacting Fermi gas. Our measured energy-entropy data is treated as a benchmark by many theoretical groups to test the theoretical predictions, including pseudogap theory, NSR theory, and QMC simulations etc [6, 8, 77]. The precision of our measurement enables a careful examination of the validity of the above strong coupling theories, which have no small parameters for estimating the calculation errors in the strongly interacting regime. In this regime, the experimental measurement is the only reliable method to justify the goodness of many-body quantum theories. Recently an important achievement is to demonstrate universal thermodynamics in strongly interacting Fermi gases, which is done by comparing our experimental data with the energy-entropy calculation based on a many-body quantum theory [6].

Our studies of hydrodynamics of a strongly interacting Fermi gas reveals extremely low viscosity in this system. Both irrotational flow arising in a expanding, rotating Fermi gas [51] and the damping ratio of a breathing mode [95] indicate that the viscosity of strongly interacting Fermi gases is extraordinary low. Although zero viscosity behavior is easy to understand in the superfluid regime, in the normal regime the mechanism for such low viscosity is not clear yet. Recently a string theory method predicted that the ratio of viscosity to the entropy density has a lower bound of $\hbar/(4\pi k_B)$, which can be approached in a unitary strongly interacting system [3]. From our entropy data and viscosity estimates, we find that this ratio in strongly interacting Fermi gases enters into the quantum limited regime.

In the remaining sections of this chapter, I will provide a brief summary of the preceding chapters. I will also give my outlook for the possible improvements in the current apparatus as well as some experiments can be operated for exploring the physics of strongly interacting Fermi gasesin the future.

9.1 Summary

Chapter 1 begins with the motivation for studying strongly interacting Fermi gases. The significance of the work is also presented in that chapter as well as an outline of this dissertation.

Chapter 2 describes the hyperfine energy levels and Feshbach resonance in a strongly interacting Fermi gas of ^{6}Li atoms.

Chapter 3 describes the general experimental methods we use to generate and characterize a strongly interacting Fermi gas. I mainly present our studies on evaporation cooling of a unitary Fermi gas in an optical trap.

Chapter 4 presents our methods of measuring the energy of a strongly interacting Fermi gas. Following that, in Chapter 5, I explain how to measure the entropy of a strongly interacting Fermi gas.

Chapter 6 presents a model-independent measurement of both the energy and entropy in a strongly interacting Fermi gas as well as the analysis and parametrization of the energy-entropy data. Also I compare the data with the predictions of several strong coupling theories.

Chapter 7 presents my studies of expansion hydrodynamics a rotating strongly interacting Fermi gas that exhibits a very low viscosity. Following that, by modeling the damping of a breathing mode, I extract an estimate of the ratio of viscosity to entropy density in a strongly interacting Fermi gas.

Chapter 8 describes technical details on building an all-optical cooling and trapping apparatus for ^{6}Li atoms.

The present chapter provides a summary of the work discussed in this dissertation, and also give my personal perspective on the future of the research in our lab.

There are two appendices in this dissertation.

Appendix A presents the Mathematica codes for calculating a number of thermodynamic properties for a noninteracting trapped degenerate Fermi gas.

Appendix B includes the updated Igor procedure functions written by myself for the data analysis and imaging processing.

9.2 Upgrade of the Apparatus

In our current apparatus, a Coherent 899-21 dye laser pumped by a Verdi laser produces the optical beams for the MOT and the imaging beam. Although our lab has accumulated rich knowledge to operate and maintain dye lasers before, dye lasers still require much time and many efforts to keep it stable. In the last several years, progress in diode laser technology had made diode chips at a wavelength of ^{6}Li of about 671 nm commercially available.

Switching our laser system from dye lasers to diode lasers has several advantages: First, diode lasers are much easier to operate and maintain than dye lasers. Diode lasers can work as key-switch instruments. Second, diode lasers are easily home-made by buying a master diode laser chip and an amplifier chip. This enables us to build multiple diode lasers for different applications, i.e. a diode laser detuned several nanometers away from the transition line can be used to preload an optical trap. Third, the maintenance cost for the diode laser is much cheaper than the dye laser. Our lab already has some existing techniques to build electronics and optics for diode lasers, such as electronics for current regulation, circuits for temperature stability, and optical gratings for frequency selection. There are no fundamental difficulties to make a diode laser system for

^{6}Li atoms, as that has already been accomplished by other groups. The major technique needed to be developed in our lab is the amplification of diode laser power to several hundred mW by an laser amplifier chip.

Another major improvement that can be done is our camera system. Our current Andor camera uses a fast-kinetic mode to take multiple pictures continuously. The fastest rate to take two consecutive images is about 20 ms. For some applications, such as taking two images for atoms at the two different spin states in the same cloud, this rate is too slow. We recently bought a new camera form cooKe. The cooKe camera has two CCD arrays inside. One is for exposure while the other is for data storage. This property supports a very fast data transfer rate, which enables two consecutive pictures as fast as 5 μs. Installing this new camera will help us to implement several new experiments that require fast continuous imaging.

A third improvement can be a fast switching system for the magnets. Our high field magnets turn on and off very slowly with a time scale of a fraction of a second. Turning magnetic fields on and off or switching to other magnetic fields quickly is a crucial technique for some cold atom experiments, such as experiments on projection of Fermi condensates. So we may also develop such techniques in our lab. The core technique for fast magnetic field switching is to use insulated-gate bipolar transistors (IGBT), which are a power semiconductor device for fast switching the electric power in many appliances. We have constructed part of the needed electronics using IGBT, which can be finished by the new members in our lab.

Finally, the software for the controlling system can be updated to a new level. In our current software, a Labview program sends timing sequences and commands to the hardware of the control system while Andor software controls the camera and obtains the images. After that, an Igor program analyzes the images and data. By updating those programs, the updated Labview program can direct control the cooKe camera and obtain the images. Meanwhile, the Igor program can be implanted into the Labview program, which helps to enable real-time and on-site data processing.

9.3 Outlook for the Future Experiment

The field of cold Fermi gases still keeps rolling even though substantial new physics has already been found in the last several years. People now are more and more interested in using strongly interacting Fermi gases as a paradigm to study the universal physics that is related to other strongly interacting Fermi systems. Among of these studies, quantum viscosity is especially interesting and important. Studies of quantum viscosity can provide the first experimental test of a conjecture based on sting theory methods. Also, the comparison of the measured quantum viscosity in ultracold Fermi gases with that estimated from the high energy experiments of ultrahot quark-gluon plasmas will provide a unique perspective to study dynamics of these two systems, both of which represent extremes of temperature in nature.

Other directions in this field are to study some novel quantum phases, which includes spin polarized Fermi superfluids [31, 32], Bose-Fermi superfluid mixtures [123], and strongly interacting Fermi gases in reduced dimensions [124]. Thermodynamic studies of spin polarized Fermi gases is a missing piece in the current research, which can be done by the same method presented in this dissertation. Studies of strongly interacting Fermi gases in reduced dimensions will enable exploration of quantum-confined nonperturbative dynamics. Our CO_2 laser trap provides a convenient way to load cold atoms directly into a one-dimensional optical lattice, which can be generated by a standing wave of CO_2 beams. In our apparatus, the standing wave can be readily formed by reflecting the forwarding propagating CO_2 beam using a flat mirror instead of the rooftop mirror.

Looking back over the past several years in John's lab, I would like to say that the journey of exploring the world of ultracold atoms let me experience many challenges as well as having lots of fun. The most amazing thing for me is that through this journey I peek into one of the most compelling quantum systems in nature, then I am stunned by the beauty of physics.

Appendix A

Mathematica Program for Thermodynamic Properties of a Trapped Ideal Fermi Gas

A.1 Thermodynamic Properties for an Ideal Fermi Gas in a Harmonic Trap

PROGRAM DESCRIPTION: This Mathematica 5.0 program calculates the thermodynamical parameters of the trapped gas in a harmonic trap.

```
The Chemical Potential,Energy and Entropy for Noninteracting Fermi Gas
in a harmonic profile trap.
Note that all energies and temperatures are in EF units.


1. Physcis constant and the basic parameters related to the Li6

c = 3*10^8;,
hbar = 1.055*10^(-34);
e = 1.60219*10^(-19);
h = 2 Pi hbar;
m = 6.015*1.66*10^(-27); (*Li6 mass, kg*)
AtomN = 130000;
k = 1.3806505*10^(-23);
Omegaz = 2 Pi 42;     (*Measured trap angular frequency*)
```

```
Omegax = 2 Pi 1050;
Omegay = 2 Pi 1200;
```

2.Fermi temperature

```
EF = (6*AtomN)^(1/3)*hbar*(Omegay*Omegax*Omegaz)^(1/3);
(*Fermi Energy,J*)
TF = EF/k ;                          (* Fermi Temperature, K *)
kF = (2*m*EF)^(1/2)/hbar;            (* Fermi Wavevecter, 1/m *)
```

3. Chemical Potential vs T:

```
f1[x_, mu_, T_] : = x^2/(Exp[(x - mu)/T] + 1);
Integrate[f1[x, mu, T1], {x, 0, Infinity}];
g1[mu_, T_] = -2 T^3* PolyLog[3, -Exp[mu/T]];
j2[T_] := FindMinimum[(1 - 3*g1[z, T])^2, {z, {0.01, 1}}];
mu[T_] := {z /. Part[j2[T], 2]}[[1, 1]];
mulist = Table[{T, mu[T]}, {T, 0.01, 2.0, 0.01}];
```

4. Energy vs T:

```
f2[x_, mu_, T_] := x^3/(Exp[(x - mu)/T] + 1);
Integrate[f2[x, mu, T1], {x, 0, Infinity}];
g2[T_] := -6 T^4 PolyLog[4, -Exp[mu[T]/T]];
epsilon[T_] := 3*g2[T];
EoverEZero[T_] := epsilon[T]/(3/4);
```

5.Entropy vs T and Entropy vs Energy:

```
f[x_, mu1_, T_] := 1/(Exp[(x - mu1)/T] + 1);
s[x_, mu1_, T_] := f[x, mu1, T]*Log[f[x, mu1, T]] +
(1 - f[x, mu1, T])*Log[1 - f[x, mu1, T]];
g3[T_, mu1_] := NIntegrate[x^2*s[x, mu1, T], {x, 0, Infinity}];
SP[T_] := -3*g3[T, mu[T]];
SPlist = Table[{T, SP[T]}, {T, 0.03, 1.1, 0.01}];
epslist = Table[{epsilon[T], T}, {T, 0.01, 2.0, 0.01}];
Temp = Interpolation[epslist];
SvsE[En_] := SP[Temp[En]];
SvsElist = Table[{En, SvsE[En]}, {En, 0.76, 2.0, 0.01}];
```

A.2 Thermodynamic Properties for an Ideal Fermi Gas in a Gaussian Trap

PROGRAM DESCRIPTION: This Mathematica 5.0 program calculates the thermodynamical parameters of the trapped gas in a Gaussian trap.

```
The Chemical Potential,Energy and Entropy for Noninteracting Fermi
Gas in a Gaussian Profile Trap.
Note that all energies and temperatures are in EF units.


1.Make integration g which is the factor of density of state in
Gaussian trap divided by a harmonic one

c[y_] := (-Log[1 - y])^(3/2)*Sqrt[1 - y]/y^2*(16/Pi);
g[y_] := c[y]*NIntegrate[u^2*Sqrt[(1 - y)^(u^2 - 1) - 1], {u, 0, 1}];
gtable = Table[{y, g[y]}, {y, 0.001, 0.999, 0.001}];
ginterp = Interpolation[gtable];

2.Deciding Chemical Potential  from T/TF and U/EF.
(Let UF=U/EF is the well depth in units of the Fermi energy of
Harmonic Trap.T is the temperature and mu is the chemical potential.)

f1[x_,mu_,T_]:=1/(Exp[(x-mu)/T]+1);
g1Gaussian[mu_,T_,UF_]:=NIntegrate[ginterp[x/UF]*x^2*f1[x,mu,T],
{x,0.001,0.999*UF}];
j2Gaussian[T_,UF_]:=FindMinimum[(1-3*g1Gaussian[z,T,UF])^2,{z,-2,1}];
muGaussian[T_,UF_]:=Part[{z/.Part[j2Gaussian[T,UF],2]},1];
mulistGaussian=Table[{T,muGaussian[T,10]},{T,0.01,2.0,0.01}];
muGaussianinterp=Interpolation[mulistGaussian];

3.Deciding Energy from T/TF and U/EF.

EGaussian[mu_,T_,UF_]:=3*NIntegrate[ginterp[x/UF]*x^3*f1[x,mu,T],
{x,0.001,0.999*UF}]
EnergyGaussian[T_,UF_]:=EGaussian[muGaussian[T,UF],T,UF]
EnergyGaussian[0.001,100];              (* Note this should be 3/4 *)
GaussianEnergyTable=Table[{T,EnergyGaussian[T,10]},{T,0.01,2.0,0.01}]
```

```
(*Comparing with a harmonic trap result.*)

g1[mu_, T_] = -2 T^3*PolyLog[3, -Exp[mu/T]];
j2[T_] := FindMinimum[(1 - 3*g1[z, T])^2, {z, {0.01, 1}}]
mu[T_] := {z /. Part[j2[T], 2]}[[1, 1]]
g2[T_] := -6 T^4* PolyLog[4, -Exp[mu[T]/T]]
epsilon[T_] := 3*g2[T]
```

4.Deciding Entropy from T/TF and U/EF.

```
s[x_,mu1_,T_]:=f1[x,mu1,T]*Log[f1[x,mu1,T]]+(1-f1[x,mu1,T])
*Log[1-f1[x,mu1,T]]
g3[T_,mu1_,UF_]:=NIntegrate[x^2*ginterp[x/UF]*s[x,mu1,T],
{x,0.001,0.999*UF}]
SP[T_,UF_]:=-3*g3[T,muGaussian[T,UF],UF]
SPlistlong=Table[{T,SP[T,10]},{T,0.01,2.00,0.01}]
SPInterp=Interpolation[SPlistlong];

(*Comparing with low Tenperature approxiamtion.*)

SPanalyt[T_]:=Pi^2T;
SPanalytplot=Plot[SPanalyt[T],{T,0,1}];
```

5.Now using the A.3 to calculate the mean square size of the cloud in Gaussian trap and making Entropy-Size relation for a Gaussian Trap.
(we want E/EF units for z^2/zF^2, so multiply IZSQ by 3/4.
IZSQ is normalized to 1 for mean squre size of T=0).

```
ZSQlistlong[UF_]:=Table[{T,(3/4)*IZSQ[T, UF]},{T, 0.03, 2.03, 0.01}];
ZSQlistlong[10];
ZSQInterp = Interpolation[ZSQlistlong[10]];
SetDirectory["E:\Entropy-Size Calculation"];
(*The directory that the mean square size data saved*)
EntropyGaussian=Range[200];
Do[EntropyGaussian[[j]]=SPInterp[0.03+j*0.01];  ,{j,200}];
ZSQGaussian=Range[200];
Do[ZSQGaussian[[j]]=ZSQInterp[0.03+j*0.01];  ,{j,200}];
Export[EntropyGaussian.dat,EntropyGaussian,List];
Export[ZSQGaussian.dat,ZSQGaussian,List];
```

```
6.Now make Entropy-Energy relation for a Gaussian Trap

Entropy2NG=Range[200];
Do[Entropy2NG[[j]]=SP[j*0.01,10];  ,{j,200}];
Energy2NG=Range[200];
Do[Energy2NG[[j]]=EnergyGaussian[j*0.01,10];  ,{j,200}];
Export[Entropy2NG.dat,Entropy2NG,List];
Export[Energy2NG.dat,Energy2NG,List];
```

A.3 Mean Square Sizes for an Ideal Fermi Gas in a Gaussian Trap

PROGRAM DESCRIPTION: This Mathematica 5.0 program calculates the mean square cloud size of the trapped gas in a Gaussian trap.

```
Mean Square Width  versus  kT/EF and U/EF for Noninteracting Fermi
Gas in a Gaussian Trap.

1.Make interpolators for integration function f0 which relating to
chemical potential.

g0[u_, x_] := u^2*Sqrt[(1 - x)^(u^2) - (1 - x)];
f0[x_] := (16/Pi)*(-Log[1 - x])^(3/2)*NIntegrate[
g0[u, x], {u, 0, 1}, Compiled -> True]/x^2;
V0 = Table[{x, f0[x]}, {x, 0.0001, 0.9999, 0.0001}];
VT0 = Interpolation[V0];

2.Make interpolators for integration function f2 which relating to
mean square size.

g2[u_, x_] := u^4*Sqrt[(1 - x)^(u^2) - (1 - x)];
f2[x_] := (32/Pi)*(-Log[1 - x])^(5/2)*NIntegrate[
g2[u, x], {u, 0, 1}, Compiled -> True]/x^3;
V2 = Table[{x, f2[x]}, {x, 0.0001, 0.9999, 0.0001}];
VT2 = Interpolation[V2];

3.Deciding Chemical Potential  from T/TF and U/EF.
```

```
(Note that  UF=U/EF is the well depth in units of the HO Fermi
energy, T is the temperature and mu is the chemical potential)

f1[y_, mu_, T_] := 1/(Exp[(y - mu)/T] + 1);
f12[y_, mu_, T_, UF_] := y^2*f1[y, mu, T]*VT0[y/UF];
INUM[mu_, UF_, T_] := 3*NIntegrate[f12[y,
mu, T, UF], {y, 0.0001*UF, 0.9999*UF}, Compiled -> True];
j2[T_, UF_] := FindMinimum[(1 - INUM[z, UF, T])^2, {z, 0}];
mu[T_, UF_] := z /. Part[j2[T, UF], 2];

4.Deciding MeanSquareSize from T/TF , U/EF and mu.
(<z^2> in units of  sigzF^2/8, where sigzF is the Fermi radius.)

f22[y_, mu_, T_, UF_] := y^3*f1[y, mu, T]*VT2[y/UF];
IZSQ1[T_, UF_, mu1_] := 4*NIntegrate[f22[y, mu1, T,
 UF], {y, 0.0001*UF, 0.9999*UF}, Compiled -> True];
IZSQ[T_, UF_] := IZSQ1[T, UF, mu[T, UF]];
(* The mean square size as a funtion of temperature and trap depth)
```

A.4 The Ground State Properties for a Weakly Interacting Fermi Gas in a Gaussian Trap

PROGRAM DESCRIPTION: This Mathematica 5.0 program calculates the ground state thermodynamic parameters of the trapped gas in a Gaussian trap, which is weakly interacting and in the BEC-BCS crossover region. The calculation for the uniform gas follows the method in [78].

```
The Chemical Potential,Energy and Entropy for BEC-BCS Crossover
Fermi Gas of the ground state in a Gaussian profile trap.
Note that all energies and temperatures are in EF units

1.Physcis constant and the basic parameters related to the Li6

c = 3*10^8;,
hbar = 1.055*10^(-34);
e = 1.60219*10^(-19);
h = 2 Pi hbar;
```

```
m = 6.015*1.66*10^(-27); (*Li6 mass, kg*)
AtomN = 130000;
k = 1.3806505*10^(-23);
a0 = 5.29177*10^(-11);  (*Bohr radius, m*)

2.Chemical Potential from BCSMF, BECMF and ChengChinMF

kF = (6*Pi^2*n)^(1/3);
EF = (hbar*kF)^2/(2*m); (* Thomas-Fermi Energy, J*)

muBCS[IC_]:=(hbar^2/(2*m)*(6*Pi^2*n)^(2/3)+(4*Pi*hbar^2)
/(m*IC*kF)*n))/EF;
(*Atom Chemical Potential from BCS theory,
  IC in unit of 1/(kF*a) *)

muBCSStrinati[IC_]:= 1+4/(3*Pi*IC)+4/(15*Pi^2)*(11-2*Log[2])
/IC^2;
(*Atom Chemical Potential from Strinatis's theory *)

aM = 0.6*a; (*Molecules scattering length*)
nM = n/2;   (*Molecules density*)

muMolecule[IC_]:=(2*hbar^2)/m*aM/(a*kF*IC)*nM*
(1 + 32/(3*Pi^(1/2))*(nM*aM^3/(a*kF*IC)^3)^(1/2))/EF;
(*Molecule Chemical Potential for BEC gas*)

EBinding[IC_] := If[IC >= 0, hbar^2*kF^2*IC^2/(2*m*EF), 0];
(*Binding Energy per atom*)
muBEC[IC_] := muMolecule[IC]/2 - EBinding[IC];
(*chemical potential substact Binding Energy per atom*)

j1CCMF[IC_] := If[IC >= 0,
FindMinimum[
(1 + AiryAi[-2.338*z]/AiryAiPrime[-2.338*z]*IC*2.338^(1/2))^2,
{z, -4, 1}],
FindMinimum[
(1 + AiryAi[-2.338*z]/AiryAiPrime[-2.338*z]*IC*2.338^(1/2))^2,
{z, 1, -4}]];
muCCMF[IC_] := Part[{z /. Part[j1CCMF[IC], 2]}, 1];
(*Atom Chemical Potential from Chin's Mean Field theory *)
muCCMFAtomic[IC_] := muCCMF[IC] + EBinding[IC];
```

```
(*Atomic Chemical Potential substract molecule binding energy.*)
TmuCCMFAtomic = Table[{x, muCCMFAtomic[x]},
{x, -4.05, 4.05, 0.02}];
ImuCCMFAtomic = Interpolation[TmuCCMFAtomic];
```

3.The MeanSquareSize for Harmonic Trap using the chemical potential from Chin's mean field thoery.

3.1 Calulate the mean cloud size for kF*a=-0.75.

```
ICSweep = -1/0.75;
muScaled[Sdens_,IC_]:=(Sdens)^(2/3)*ImuCCMFAtomic[IC*Sdens^(-1/3)]
muScaled[1, ICSweep]
TmuScaled = Table[{x, muScaled[x, ICSweep]}, {x, 0.01, 1, 0.01}];
ImuScaled = Interpolation[TmuScaled];
TdnsScaled = Table[{muScaled[x, ICSweep], x}, {x, 0.01, 1, 0.01}];
IdensScaled = Interpolation[TdnsScaled];
g0[mu_, q_] := IdensScaled[q]*Sqrt[mu-q];
f0[mu_] := (16/Pi)*NIntegrate[g0[mu,q],{q,0,mu},Compiled->True];
j0 = FindMinimum[(1 - f0[mu])^2, {mu, 1}];
muGlobe = mu/.Part[j0, 2];
g1[mu_, q_] := IdensScaled[q]*(mu - q)^(3/2);
MSSHO[mu_]:=2*(16/Pi)*NIntegrate[g1[mu,q],{q,0,mu},Compiled->True];
MSSHO[muGlobe];
```

3.2 Calulate the mean cloud size for variable kF*a.

```
Do[
 ICSweep = i;
 TdnsScaled = Table[{muScaled[x, ICSweep], x}, {x,0.01,1,0.01}];
 IdensScaled = Interpolation[TdnsScaled];
 g0[mu_, q_] := IdensScaled[q]*Sqrt[mu - q];
 f0[mu_]:=(16/Pi)*NIntegrate[g0[mu, q],{q,0,mu},Compiled->True];
 j0 = FindMinimum[(1 - f0[mu])^2, {mu, 1}];
 muGlobe = mu /. Part[j0, 2];
 g1[mu_, q_] := IdensScaled[q]*(mu - q)^(3/2);
 MSSHO[mu_]:=2*(16/Pi)*NIntegrate[g1[mu,q],{q,0,mu},Compiled->True];
 If[MSSHO[muGlobe] >=0, MSSHOIC[i] = MSSHO[muGlobe], MSSHOIC[i] = 0];
 ICData[i] = i;
    , {i, -2.0, 1.0, 0.1}];
TMSSHOIC = Table[{ICData[i], MSSHOIC[i]}, {i, -2.0, 0.7, 0.1}]
```

```
IMSSHOIC = Interpolation[TMSSHOIC];
(*IMSSHOIC gives the mean square size for kF*a from -2.0 to 0.7.*)
```

4. The MeanSquareSize for Gaussian Trap using the chemical potential from Chin's mean field thoery.

4.1 Calulate the mean cloud size for kF*a=-0.75.

```
muScaled[Sdens_,IC_]:=(Sdens)^(2/3)*ImuCCMFAtomic[IC*Sdens^(-1/3)];
ICSweep = -1/0.75;
muScaled[1, ICSweep];
TmuScaled = Table[{x, muScaled[x, ICSweep]}, {x, 0.01, 1, 0.01}];
ImuScaled = Interpolation[TmuScaled];
TdnsScaled = Table[{muScaled[x, ICSweep], x}, {x, 0.01, 1, 0.01}];
IdensScaled = Interpolation[TdnsScaled];
g2[mu_,q_,U0_]:=IdensScaled[q]/(q-mu+U0)*(Log[U0/(q-mu+U0)])^(1/2);
f2[mu_,U0_]:=(16/Pi)*U0^(3/2)*NIntegrate[g2[mu,q,U0],{q,0,mu}
,Compiled -> True];
j2[U0_]:= FindMinimum[(1 - f2[mu, U0])^2, {mu, 1}];
muGaussian[U0_]:= mu /. Part[j2[U0], 2];
g3[mu_, q_, U0_]:= IdensScaled[q]/(q-mu+U0)*(Log[U0/(q-mu+U0)])^(3/2);
MSSGA[mu_,U0_]:= 2*(16/Pi)*U0^(5/2)*NIntegrate[
g3[mu, q, U0], {q, 0, mu}, Compiled -> True];
MSSGA[muGaussian[10], 10];
```

4.2 Calulate the mean cloud size for variable kF*a.

```
Do[
  ICSweep = i;
  UTrap = 10;
  TdnsScaled = Table[{muScaled[x, ICSweep], x}, {x, 0.01, 1, 0.01}];
  IdensScaled = Interpolation[TdnsScaled];
  g2[mu_,q_,U0_]:=IdensScaled[q]/(q-mu+U0)*(Log[U0/(q-mu+U0)])^(1/2);
  f2[mu_,U0_]:=(16/Pi)*U0^(3/2)*NIntegrate[g2[mu,q,U0],{q,0,mu},
  Compiled -> True];
  j2[U0_] := FindMinimum[(1 - f2[mu, U0])^2, {mu, 1}];
  muGaussian[U0_] := mu /. Part[j2[U0], 2];
  g3[mu_,q_,U0_]:=IdensScaled[q]/(q-mu+U0)*(Log[U0/(q-mu+U0)])^(3/2);
  MSSGA[mu_,U0_]:=2*(16/Pi)*U0^(5/2)*NIntegrate[
  g3[mu, q, U0], {q, 0, mu}, Compiled -> True];
  If[MSSGA[muGaussian[UTrap], UTrap] >= 0,
```

```
     MSSGAIC[i]= MSSGA[muGaussian[UTrap],UTrap], MSSGAIC[i] = 0];
  GAICData[i] = i;
    , {i, -2.0, 1.0, 0.1}];
TMSSGAIC = Table[{GAICData[i], MSSGAIC[i]}, {i, -2.0, 0.7, 0.1}]
IMSSGAIC = Interpolation[TMSSGAIC];
(* IMSSHOIC gives the mean square size for kF*a from -2.0 to 0.7. *)
```

Appendix B

Igor Program for Data Analysis and Image Processing

In our lab, the data analysis and image processing are done by the Igor program. For different tasks, we wrote the procedure files in Igor to implement the different functions. Previously, Stephen Granade and Joe Kinast wrote the core parts for calculation of column density of the absorption images and fitting the 1D profile of the cloud. The file was named as “ProcessingImage v1.0” in our lab. For the experiment presented in these dissertation, I added the data analysis for the entropy and 2D cloud profile fit for the rotating gas. The corresponding file was named “ProcessingImage v2.0”. Furthermore, for the experiment required the double spin imaging, I wrote a new section for this application, and named the new file as “ProcessingImage v3.0”, which had almost 300 pages. This procedure file can be obtained by inquiring of John Thomas by Email jet@phy.duke.edu.

Here I list the added functions since ”ProcessingImage v1.0”, and a brief introduction will be given if the annotation is not included in the procedure file.

```
#############################################################
        Basic Data File  Processing
#############################################################
```

```
StatisticalGraphAverage(WavetoAvg)
This function averages the data Y for the same X, and excludes
any individual point that is beyond 3 stand deviation of of
the average value.

FindXYPeak(xwave, ywave, ymin, avgedpoint)
This function find the local maximum whihc is larger than YMIN.

#############################################################
        Measure  Position  and  Width
#############################################################

BatchAverageRadia(saveAverage)
This function first produces the integrated radial density,then
averages the radial profiles that belong to the same data set.

BatchAverageAxial(saveAverage)

#############################################################
           CURVE FITTING ROUTINES
#############################################################

LinearPlusPower(w,x)
ShiftPower(w,x)
JointTwoPower(w,x)
ShiftJointTwoPower(w,x)
LowEneTwoPower(w,x)
OriginFixTwoPower(w,x)
OriginShiftTwoPower(w,x)
BiasOriginFixTwoPower(w,x)
OneDerConOriginFixTwoPower(w,x)
CriticalExpansionTwoPower(w,x)
Lorentz(w,h)
IncreasedSine(w,t)
BiasDampedSine(w,t)
DualDampedSine(w,t)
SimGauss2D(w,x,y)

#############################################################
            Entropy Measurement Section
#############################################################
```

```
MeanSquareSizeTFFits(TFWidthNum, ToverTFNum)
BatchMeanSquareSizeTFFits(TFWidth, ToverTF)
These two functions calculate the mean square size
form the finite temperature Thomas-Fermi fit of the 1D
cloud profile.

EntropyAverage( )
This function averages entropy data by binning in a
certain energy range.

AFSAverage( )
This function averages MeanSuareSize data by binning
in a certain energy range, and treats the standard
deviaton of single shot equally.

AFSAverage2( )
This function averages MeanSuareSize data by binning in a
certain energy range, and treats the standard deviaton of
single data point and the standard deviation of the binning
data set seperately.

ViscosityEntropyRatioCal(Alpha, AlphaStdDev,EoverEf,EoverEfStdDev)
This function gives the estimation of the viscosity and
entropy ratio.

ChemicalPotentialPlot( )
ChemicalPotentialCal_PL(S, SStdDev,E,EStdDev)
ChemicalPotentialCal_DualPL(S, SStdDev,E,EStdDev)
These three function give the chemical potential versus energy
according to the different parametrization.

TvsEPlot( )
TvsEHeatCapaPlot( )
These two function compares the temperature versus energy
according to the entropy and heat comapcity experiment
respectively.

#############################################################
              Rotation Mode Section
#############################################################
```

```
Center(nameoffile)
BatchCenter()
These two function use 1D Gaussian fit for the axial and radial
profile, then anlyze the center of 2D rotating cloud.

AngleCenter(nameoffile)
BatchAngleCenter( )
These two function use 1D Gaussian fit for the axial and radial
profile, then anlyze the angle and center of 2D rotating cloud.

AngleCenterWidth(nameoffile)
BatchAngleCenterWidth()
These two function use 1D Gaussian fit for the axial and radial
profile, then anlyze the angle, center and Gaussian width
of the principle axis of 2D rotating cloud.

INTAngleCenterWidth(nameoffile)
BatchINTAngleCenterWidth( )
These two functions use 1D Gaussian fit for the axial and raidal
profile, then integrate the 1D cloud profiles belong to the same
data set, and analyze the angle, center and Gaussian width
of the principle axis of 2D rotating cloud.

CenterOverlapCD(saveIntegration)
This function integrates the 2D column densities belonging to
the same data set by overlapping the centers of each cloud
profile together.

INT2DGaussian(nameoffile)
BatchINT2DGaussian( )
These two functions make 2D Gaussian fit for the integrated
column density generated by "CenterOverlapCD", then provide
the center, rotating angle and Gusssian width of the primary
axis of 2D rotating cloud.

TWODGaussian(nameoffile,displaygraph)
BatchTWODGaussian(displaygraph)
These two functions make 2D Gaussian fit for the origin data file,
then provide the center, rotating angle and Gusssian width of the
primary axis of 2D rotating cloud.
```

```
#############################################################
              Two Spins Imaging Section
#############################################################

SRSR2SSRR(nameoffile)
BatchSRSR2SSRR( )
These two function convert the 4-fast kinetic images from the
Andor camera with the time sequnce of
"signal-reference-signal-reference"
to "signal-signal-reference-reference’’.This helps us apply
the exsisted function for 4-images processing without rewritting
the whole set of new functions.

CalculateAbsorptionSSRR(nameoffile,crop)
This function caluclate the absorption images for the
’’SSRR’’ images.

ViewROISSRR(nameoffile)
This function shows the pseudo color images for the
’’SSRR’’ images.

CalculateColumnDensitySpin2(nameoffile,crop,bin)
This function calculate the coulumn density of spin2.

AtomNumberSSRR(nameoffile)
BatchAtomNumberSSRR()
These two functions calculate the atom numbers for the
’’SSRR’’ images.

BatchWidthSSRR(fittype,dimension,displaygraph)
This function calculates the number independent Thomas-Fermi
width of the cloud for the ’’SSRR’’ images.

BatchWidthSSRRCoherent(fittype,dimension,displaygraph)
This function calculates the number-independent Thomas-Fermi
width of the cloud in the coherent two-spin superposition.
Noted that the cloud in coherent superposition state has the
different from of the number-independent width withthe spin
mixture cloud.
```

BatchTemperatureSSRR(fittype,dimension,holdwidth,displaygraph)
This function obtains the Thomas-Fermi temperature of the cloud
for the ''SSRR'' images.

WaveABSDensity(wvname,displaygraph)
This function fits a gausssian to a 1-D profile and finds the
center to be used in the BatchProfileSubtract function.

DensitySubstract(Position1,Density1,Position2,Density2,displaygraph)
Batch1DDensityDifference(dimension,displaygraph)
These two functions show the difference of 1D density profile
between spin 1 and spin 2.

Batch2DAxialCentralDensityDif(displaygraph)
Batch2DRadialCentralDensity(displaygraph)
These two functions show the spin 1 and spin 2 difference of 1D
density profile integrated from the central 2D slice.

TwoSpinCenter(nameoffile, spin)
This function obtains the cloud center for the ''SSRR'' images.

BatchCDDifference(SaveDifference)
This function shows the difference of 2D column density of two spins.

CDSelfAverage(initialcd, savechoice)
This function self-averages the of 2D column density by applying the
symmetry of the principle axis.

BatchCDDifferenceSelfAverage(SaveDifference)
This function shows the difference of 2D column density generated by
"CDSelfAverage".

Bibliography

[1] B. Müller. Physics of the quark-gluon plasma. nucl-th/9211010, November 1992.

[2] M. Asakawa, S.A. Bass, and B. Muller. Anomalous viscosity of an expanding quark-gluon plasma. *Phys. Rev. Lett.*, 96:252301, 2006.

[3] P.K.Kovtun, D.T.Son, and A.O.Starinets. Viscosity in strongly interacting quantum field theories from black hole physics. *Phys. Rev. Lett.*, 94:111601, 2005.

[4] H. Heiselberg. Fermi systems with long scattering lengths. *Phys. Rev. A*, 63:043606, 2001.

[5] T.-L. Ho. Universal thermodynamics of degenerate quantum gases in the unitarity limit. *Phys. Rev. Lett.*, 92:090402, 2004.

[6] H. Hu, P. D. Drummond, and X.-J. Liu. Universal thermodynamics of strongly interacting fermi gases. *Nature Physics*, 3:469, 2007.

[7] B. A. Gelman, E. V. Shuryak, and I. Zahed. Cold strongly coupled atoms make a near-perfect liquid. arXiv:nucl-th/0410067, 2005.

[8] H. Hu, X.-J. Liu, and P. D. Drummond. Comparative study of strogn-coupling theories of a trapped fermi gas at unitarity. arXiv:cond-mat/0712.0037, 2007.

[9] A. Cho. Ultracold atoms spark a hot race. *Science*, 301:750, 2003.

[10] G. P. Collins. The next big chill. *Scientific American*, page 26, October 2003.

[11] P. Rodergers. The revolution that has not stopped. *Physics World*, page 8, June 2005.

[12] K. M. O'Hara, S. L. Hemmer, M. E. Gehm, S. R. Granade, and J. E. Thomas. Observation of a strongly interacting degenerate Fermi gas of atoms. *Science*, 298:2179, 2002.

[13] B. DeMarco and D. S. Jin. Onset of Fermi degeneracy in a trapped atomic gas. *Science*, 285:1703, 1999.

[14] A. G. Truscott, K. E. Strecker, W. I. McAlexander, G. B. Partridge, and R. G Hulet. Observation of Fermi pressure in a gas of trapped atoms. *Science*, 291:2570, 2001.

[15] K. Dieckmann, C. A. Stan, S. Gupta, Z. Hadzibabic, C. H. Schunck, and W. Ketterle. Decay of an ultracold fermionic lithium gas near a Feshbach resonance. *Phys. Rev. Lett.*, 89:203201, 2002.

[16] F. Schreck, L. Kaykovich, K. L. Corwin, G. Ferrari, T. Bourdel, J. Cubizolles, and C. Salomon. Quasipure Bose-Einstein condensate immersed in a Fermi sea. *Phys. Rev. Lett.*, 87:080403, 2001.

[17] S. R. Granade, M. E. Gehm, K. M. O'Hara, and J. E. Thomas. All-optical production of a degenerate Fermi gas. *Phys. Rev. Lett.*, 88(12):120405, 2002.

[18] S. Jochim, M. Bartenstein, G. Hendl, J. Hecker Denschlag, R. Grimm, A. Mosk, and M. Weidemüller. Magnetic field control of elastic scattering in a cold gas of fermionic lithium atoms. *Phys. Rev. Lett*, 89:273202, 2002.

[19] J. Kinast, A. Turlapov, and J. E. Thomas. Damping of a unitary Fermi gas. *Phys. Rev. Lett.*, 94:170404, 2005.

[20] J. Kinast, S. L. Hemmer, M.E. Gehm, A. Turlapov, and J. E. Thomas. Evidence for superfluidity in a resonantly interacting Fermi gas. *Phys. Rev. Lett.*, 92:150402, 2004.

[21] M. Bartenstein, A. Altmeyer, S. Riedl, S. Jochim, C. Chin, J. Hecker Denschlag, and R. Grimm. Collective excitations of a degenerate gas at the BEC-BCS crossover. *Phys. Rev. Lett.*, 92:203201, 2004.

[22] A. Altmeyer, S. Riedl, C. Kohstall, M. J. Wright, R. Geursen, M. Bartenstein, C. Chin, J. Hecker Denschlag, and R. Grimm. Precision measurements of collective oscillations in the bec-bcs crossover. *Phys. Rev. Lett.*, 98:040401, 2007.

[23] A. Altmeyer C. Kohstall E. R. Sanchez-Guajardo J. Hecker Denschlag R. Grimm M. J. Wright, S. Riedl. Finite-temperature collective dynamics of a fermi gas in the bec-bcs crossover. *Phys. Rev. Lett.*, 99:150403, 2007.

[24] M. W. Zwierlein, J. R. Abo-Shaeer, A. Schirotzek, C. H. Schunck, and W. Ketterle. Vortices and superfluidity in a strongly interacting Fermi gas. *Nature*, 435:1047, 2005.

[25] C. H. Schunck, M. W. Zwierlein, A. Schirotzek, and W. Ketterle. Superfluid expansion of a rotating fermi gas. *Phys. Rev. Lett.*, 98:050404, 2007.

[26] M. Greiner, C. A. Regal, and D. S. Jin. Emergence of a molecular Bose-Einstein condensate from a Fermi gas. *Nature*, 426:537, 2003.

[27] S. Jochim, M. Bartenstein, A. Altmeyer, G. Hendl, S. Riedl, C. Chin, J. Hecker Denschlag, and R. Grimm. Bose-Einstein condensation of molecules. *Science*, 302:2101, 2003.

[28] M. W. Zweirlein, C. A. Stan, C. H. Schunck, S. M. F. Raupach, S. Gupta, Z. Hadzibabic, and W. Ketterle. Observation of Bose-Einstein condensation of molecules. *Phys. Rev. Lett.*, 91:250401, 2003.

[29] M. W. Zwierlein, C. A. Stan, C. H. Schunck, S. M. F. Raupach, A. J. Kerman, and W. Ketterle. Condensation of pairs of fermionic atoms near a Feshbach resonance. *Phys. Rev. Lett.*, 92:120403, 2004.

[30] C. A. Regal, M. Greiner, and D. S. Jin. Observation of resonance condensation of fermionic atom pairs. *Phys. Rev. Lett.*, 92:040403, 2004.

[31] M. W. Zwierlein, A. Schirotzek, C. H. Schunck, and W. Ketterle. Fermionic superfluidity with imbalanced spin populations. *Science*, 10.1126/science.1122318, 2005.

[32] G. B. Partridge, W. Li, R. I Kamar, Y. Liao, and R. G. Hulet. Pairing and phase separation in a polarized Fermi gas. *Science*, 311:503, 2006.

[33] S. Jochim, M. Bartenstein, A. Altmeyer, G. Hendl, C. Chin, J. Hecker Denschlag, and R. Grimm. Pure gas of optically trapped molecules created from fermionic atoms. *Phys. Rev. Lett.*, 91:240402, 2003.

[34] C. A. Regal, C. Ticknor, J. L. Bohn, and D. S. Jin. Creation of ultracold molecules from a Fermi gas of atoms. *Nature*, 424:47, 2003.

[35] M. Tinkham. *Introduction to superconductivity.* McGraw-Hill, New York, 1966.

[36] L. Pitaevskii and S. Stringari. The quest for superfluidity in fermi gases. *Science*, 298(5601):2144–2146, 2002.

[37] M.J. Wright C. Kohstall J. Hecker Denschlag R. Grimm A. Altmeyer, S. Riedl. Dynamics of a strongly interacting fermi gas: the radial quadrupole mode. *Phys. Rev. A*, 76:033610, 2007.

[38] C. Chin, M. Bartenstein, A. Altmeyer, S. Riedl, S. Jochim, J. Hecker Denschlag, and R. Grimm. Observation of the pairing gap in a strongly interacting Fermi gas. *Science*, 305:1128, 2004.

[39] B.E. Clancy. *Hydrodynamics of A Roatating Strongly Interacting Fermi Gas*. PhD thesis, Duke University, 2008.

[40] Q. Chen, J. Stajic, S. Tan, and K. Levin. BCS-BEC crossover: From high temperature superconductors to ultracold superfluids. *Physics Reports*, 412:1, 2005.

[41] M. Holland, S. J. J. M. F. Kokkelmans, M. L. Chiofalo, and R. Walser. Resonance superfluidity in a quantum degenerate Fermi gas. *Phys. Rev. Lett.*, 87:120406, 2001.

[42] S. J. J. M. F. Kokkelmans, J. N. Milstein, M. L. Chiofalo, R. Walser, and M. J. Holland. Resonance superfluidity: renormalization of resonance scattering theory. *Phys. Rev. A*, 65:053617, 2002.

[43] J. Stajic, J. N. Milstein, Q. Chen, M. L. Chiofalo, M. J. Holland, and K. Levin. Nature of superfluidity in ultracold Fermi gases near Feshbach resonances. *Phys. Rev. A*, 69:063610, 2004.

[44] A. Perali, P. Pieri, L. Pisani, and G. C. Strinati. BCS-BEC crossover at finite temperature for superfluid trapped Fermi atoms. *Phys. Rev. Lett.*, 92:220404, 2004.

[45] Joseph Kinast, Andrey Turlapov, John E. Thomas, Qijin Chen, Jelena Stajic, and Kathryn Levin. Heat capacity of a strongly interacting Fermi gas. *Science*, 307:1296–1299, 2005.

[46] M. Greiner D.S. Jin Q.J. Chen, C.A. Regal and K. Levin. Understanding the superfluid phase diagram in trapped fermi gases. *Phys. Rev. A*, 73:041601(R), 2006.

[47] A. Schirotzek W. Ketterle M.W. Zwierlein, C.H. Schunck. Direct observation of the phase transition for fermions. *Nature*, 442:54, 2006.

[48] J. E. Thomas, J. Kinast, and A. Turlapov. Virial theorem and universality in a unitary Fermi gas. *Phys. Rev. Lett.*, 95:120402, 2005.

[49] L. Luo, B. Clancy, J. Joseph, J. Kinast, and J. E. Thomas. Measurement of the entropy and critical temperature of a strongly interacting fermi gas. *Phys. Rev. Lett.*, 98:080402, 2007.

[50] P. Massignan, G. M. Bruun, and H. Smith. Viscous relaxation and collective oscillations in a trapped fermi gas near the unitarity limit. *Phys. Rev. A*, 71:033607, 2005.

[51] B. Clancy, L. Luo, and J. E. Thomas. Observation of nearly perfect irrotational flow in normal and superfluid strongly interacting fermi gases. *Phys. Rev. Lett.*, 99:140401, 2007.

[52] E. Arimondo, M. Inguscio, and P. Violino. Experimental determinations of the hyperfine structure in the alkali atoms. *Rev. Mod. Phys.*, 49:31, 1977.

[53] M. E. Gehm. *Preparation of an Optically-trapped Degenerate Fermi gas of* ^{6}*Li: Finding the Route to Degeneracy.* PhD thesis, Duke University, 2003.

[54] D. J. Griffiths. *Introduction to Quantum Mechanics.* Prentice Hall, Upper Saddle River, NJ, 1995.

[55] R. Shankar. *Principles of Quantum Mechanics.* Plenum, New York, 2nd edition, 1994.

[56] J. J. Sakurai. *Modern Quantum Mechanics.* Addison-Wesley, New York, revised edition, 1994.

[57] C. Cohen-Tannoudji, B. Diu, and F. Laloë. *Quantum Mechanics*, volume One. John Wiley & Sons, New York, 1977.

[58] C. Cohen-Tannoudji, B. Diu, and F. Laloë. *Quantum Mechanics*, volume One. John Wiley & Sons, New York, 1977.

[59] K. M. O'Hara. *Optical Trapping and Evaporative Cooling of Fermionic Atoms.* PhD thesis, Duke University, 2000.

[60] M. Houbiers, H. T. C. Stoof, W. I. McAlexander, and R. G. Hulet. Elastic and inelastic collisions of ^{6}Li atoms in magnetic and optical traps. *Phys. Rev. A*, 57:R1497, 1998.

[61] K. M. O'Hara, S. L. Hemmer, S. R. Granade, M. E. Gehm, J. E. Thomas, V. Venturi, E. Tiesinga, and C. J. Williams. Measurement of the zero crossing in a Feshbach resonance of fermionic ^{6}Li. *Phys. Rev. A*, 66:041401(R), 2002.

[62] M. Bartenstein, A. Altmeyer, S. Riedl, R. Geursen, S. Jochim, C. Chin, J. H. Denschlag, R. Grimm, A. Simoni, E. Tiesinga, C.J. Williams, and P.S. Julienne. Precise determination of ^{6}Li cold collision parameters by radio-frequency spectroscopy on weakly bound molecules. *Phys. Rev. Lett.*, 94:103201, 2005.

[63] L. Luo, B. Clancy, J. Joseph, J. Kinast, and and J. E. Thomas A.Turlapov. Evaporative cooling of unitary fermi gas mixtures in optical traps. *New Journal of Physics*, 8:213, 2006.

[64] J. M. Kinast. *Thermodynamics and Superfluidity of A Strongly Interacting Fermi Gas*. PhD thesis, Duke University, 2006.

[65] K. E. Strecker, G. B. Partridge, and R. G. Hulet. Conversion of an atomic Fermi gas to a long-lived molecular Bose gas. *Phys. Rev. Lett.*, 91:080406, 2003.

[66] K. M. O'Hara, M. E. Gehm, S. R. Granade, and J. E. Thomas. Scaling laws for evaporative cooling in time-dependent optical traps. *Phys. Rev. A*, 64:051403(R), 2001.

[67] M.W.Reynolds O.J.Luiten and J.T.M. Walraven. Kinetic theory of the evaporative cooling of a trapped gas. *Phys. Rev. A*, 53:381, 1996.

[68] W. Ketterle and N. J. Van Druten. Evaporative cooling of trapped atoms. *Adv. At. Mol. Opt. Phys.*, 37:181, 1996.

[69] G.Zerza L.Windholz, M.Musso and H.Jäger. Precise Stark-effect investigations of the lithium D1 and D2 lines. *Phys. Rev. A*, 46:5812, 1992.

[70] J. Zhang, E. G. M. van Kempen, T. Bourdel, L. Khaykovich, J. Cubizolles, F. Chevy, M. Teichmann, L. Tarruell, S. J. J. M. F. Kokkelmans, and C. Salomon. P-wave Feshbach resonances of ultracold ^{6}Li. *Phys. Rev. A*, 70:030702(R), 2004.

[71] C. H. Schunck, M. W. Zwierlein, C. A. Stan, S. M. F. Raupach, W. Ketterle, A. Simoni, E. Tiesinga, C. J. Williams, and P. S. Julienne. Feshbach resonances in fermionic ^{6}Li. *Phys. Rev. A*, 71:045601, 2005.

[72] G. A. Baker Jr. Neutron matter model. *Phys. Rev. C*, 60:054311, 1999.

[73] D. A. Butts and D. S. Rokhsar. Trapped Fermi gases. *Phys. Rev. A*, 55:4346, 1997.

[74] K. Huang and C. N. Yang. Quantum mechanical many-body problem with hard-sphere interaction. *Phys. Rev.*, 105:767, 1957.

[75] R. K. Pathria. *Statistical Mechanics*. Butterworth-Heinemann, Boston, 2nd edition, 1996.

[76] Q. Chen, pseudogap theory of a trapped Fermi gas, private communication.

[77] A. Bulgac, J. E. Drut, and P. Magierski. Thermodynamics of a trapped unitary fermi gas. *Phys. Rev. Lett.*, 99:120401, 2007.

[78] C. Chin. Simple mean-field model for condensates in the BEC-BCS crossover regime. *Phys. Rev. A*, 72:041601(R), 2005.

[79] M. E. Gehm, S. L. Hemmer, S. R. Granade, K. M. O'Hara, and J. E. Thomas. Mechanical stability of a strongly interacting Fermi gas of atoms. *Phys. Rev. A*, 68:011401(R), 2003.

[80] H.B.Callen. *Thermodynamics*. Wiley, New York, 1960.

[81] J. Carlson, S.-Y. Chang, V. R. Pandharipande, and K. E. Schmidt. Superfluid Fermi gases with large scattering length. *Phys. Rev. Lett.*, 91:050401, 2003.

[82] A. Perali, P. Pieri, and G.C. Strinati. Quantitative comparison between theoretical predictions and experimental results for the BCS-BEC crossover. *Phys. Rev. Lett.*, 93:100404, 2004.

[83] G. E. Astrakharchik, J. Boronat, J. Casulleras, and S. Giorgini. Equation of state of a Fermi gas in the BEC-BCS crossover: A quantum Monte-Carlo study. *Phys. Rev. Lett*, 93:200404, 2004.

[84] H. Hu, X.-J. Liu, and P. D. Drummond. Equation of state of a superfluid fermi gas in ther bcs-bec crossover. *Europhys. Lett.*, 74:574, 2006.

[85] S. Y. Chang, V. R. Pandharipande, J. Carlson, and K. E. Schmidt. Quantum Monte-Carlo studies of superfluid Fermi gases. *Phys. Rev. A*, 70:043602, 2004.

[86] J. Joseph, B. Clancy, L. Luo, J. Kinast, A. Turlapov, and J. E. Thomas. Measurement of sound velocity in a fermi gas near a feshbach resonance. *Phys. Rev. Lett.*, 98:170401, 2007.

[87] Q. Chen, J. Stajic, and K. Levin. Thermodynamics of interacting fermions in atomic traps. *Phys. Rev. Lett.*, 95:260405, 2005.

[88] A. Bulgac, J. E. Drut, and P. Magierski. Spin 1/2 fermions in the unitary regime: A superfluid of a new type. *Phys. Rev. Lett.*, 96:090404, 2006.

[89] R. Haussmann, W. Rantner, S. Cerrito, and W. Zwerger. Thermodynamics of the BCS-BEC crossover. *Phys. Rev. A*, 75:023610, 2007.

[90] J. Kinnunen, M. Rodríguez, and P. Törmä. Pairing gap and in-gap excitations in trapped fermionic superfluids. *Science*, 305:1131, 2004.

[91] Etienne Guyon, Jean-P. Hulin, Luc.Petit, and Mitescu D.Catalin. *Physical Hydrofyanmics*. Oxford University Press, 2001.

[92] D.T.Son. Vanishing bulk viscosities and conformal invariance of the unitary fermi gas. *Phys. Rev. Lett.*, 98:020604, 2007.

[93] P. F. Kolb and U. Heinz. *Quark Gluon Plasma 3*, page 634. World Scientific, 2003.

[94] E. Shuryak. Why does the quark-gluon plasma at RHIC behave as a nearly ideal fluid? *Prog. Part. Nucl. Phys.*, 53:273, 2004.

[95] A. Turlapov, J. Kinast, B. Clancy, Le Luo, J. Joseph, and J. E. Thomas. Is a gas of strongly interacting atomic fermions a nearly perfect fluid? *Journal of Low Temp. Phys.*, 150:567, 2008.

[96] T. Bourdel, L. Khaykovich, J. Cubizolles, J. Zhang, F. Chevy, M. Teichmann, L. Tarruell, S. J. J. M. F. Kokkelmans, and C. Salomon. Experimental study of the BEC-BCS crossover region in Lithium 6. *Phys. Rev. Lett.*, 93:050401, 2004.

[97] C. A. Regal and D. S. Jin. Measurement of positive and negative scattering lengths in a Fermi gas of atoms. *Phys. Rev. Lett.*, 90:230404, 2003.

[98] Mark Edwards, Charles W. Clark, P. Pedri, L. Pitaevskii, and S. Stringari. Consequence of superfluidity on the expansion of a rotating bose-einstein condensate. *Phys. Rev. Lett.*, 88:070405, 2002.

[99] G. Hechenblaikner, E. Hodby, S. A. Hopkins, O. M. Maragó, and C. J. Foot. Direct observation of irrotational flow and evidence of superfluidity in a rotating Bose-Einstein condensate. *Phys. Rev. Lett.*, 88:070406, 2002.

[100] M. Modugno, G. Modugno, G. Roati, C. Fort, and M. Inguscio. Scissors mode of an expanding bose-einstein condensate. *Phys. Rev. A*, 67:023608, 2003.

[101] D. Guéry-Odelin and S. Stringari. Scissors mode and superfluidity of a trapped bose-einstein condensed gas. *Phys. Rev. Lett.*, 83:4452, 1999.

[102] C. Menotti, P. Pedri, and S. Stringari. Expansion of an interacting Fermi gas. *Phys. Rev. Lett.*, 89:250402, 2002.

[103] A.Recati, F.Zambelli, and S. Stringari. Overcritical rotation of a trapped bose-einestein condensate. *Phys. Rev. Lett.*, 86:377, 2001.

[104] M. Cozzini and S. Stringari. Fermi gases in slowly rotating traps: Superfluid versus collisional hydrodynamics. *Phys. Rev. Lett.*, 91:070401, 2003.

[105] F.Zambelli and S. Stringari. Moment of intria and quadrupole response function of a trapped superfluid. *Phys. Rev. A*, 63:033602, 2001.

[106] O.M.Maragó, G.Hechenblaikner, E.Hodby, S.A.Hopkins, and C.J.Foot. the moement of inertia and the scissors mode of a bose condensed gas. *J. Phys.: Condens. Matter*, 14:343, 2002.

[107] G. M. Bruun and H. Smith. Shear viscosity and damping for a fermi gas in the unitary limit. *Phys. Rev. A*, 75:043612, 2007.

[108] J. Kinast, A. Turlapov, and J. E. Thomas. Breakdown of hydrodynamics in the radial breathing mode of a strongly interacting Fermi gas. *Phys. Rev. A*, 70:051401(R), 2004.

[109] Kerson Huang. *Statistical Mechanics*. John Wiley & Sons, New York, 2nd edition, 1987.

[110] L. D. Landau and E. M. Lifshitz. *Fluid Mechanics*. Pergamon Press, New York, 1975.

[111] D. Guéry-Odelin, F. Zambelli, J. Dalibard, and S. Stringari. Collective oscillations of a classical gas confined in harmonic traps. *Phys. Rev. A*, 60:4851, 1999.

[112] S.Bass, Estimation of the ratio of viscosity and entropy density in QGP, private communication.

[113] W. D. Phillips. Laser cooling and trapping of neutral atoms. *Rev. Mod. Phys.*, 70:721, 1998.

[114] M. Harris. Design and construction of an improved zeeman slower. Master's thesis, Duke University, 2003.

[115] I. Kaldre. A compact, air-cooled zeeman slower as a cold atom source. Master's thesis, Duke University, 2006.

[116] A. Yariv. *Quantum Electronics.* John Wiley and Sons, New York, 2nd edition, 1975.

[117] S. Bali, K. M. O'Hara, M. E. Gehm, S. R. Granade, and J. E. Thomas. Quantum-diffractive background gas collisions in atom-trap heating and loss. *Phys. Rev. A*, 60:R29, 1999.

[118] M. E. Gehm, K. M. O'Hara, T. A. Savard, and J. E. Thomas. Dynamics of noise-induced heating in atom traps. *Phys. Rev. A*, 58:3914, 1998.

[119] T. A. Savard, K. M. O'Hara, and J. E. Thomas. Laser-noise-induced heating in far-off resonance optical traps. *Phys. Rev. A*, 56:R1095, 1997.

[120] S.G.Cox, P.F.Griffin, C.S.Adams, D.DeMille, and E.Riis. Reusable ultrahigh vacumm viewport bakeable to 240°c. *Rev.Sci.Instrum.*, 74:6, 2003.

[121] Our Group, Spin segregation in a two-component Fermi gas.

[122] S. R. Granade. *All-optical Production of a Degenerate Gas of* ^{6}*Li: Characterization of Degeneracy.* PhD thesis, Duke University, 2002.

[123] C. A. Regal, M. Greiner, and D. S. Jin. Lifetime of molecule-atom mixtures near a Feshbach resonance in ^{40}K. *Phys. Rev. Lett.*, 92:083201, 2004.

[124] J.K. Chin, D.E. Miller, Y. Liu, C. Stan, W. Setiawan, C. Sanner, K. Xu, and W. Ketterle. Evidence for superfluidity of ultracold fermions in an optical lattice. *Nature*, 443:961, 2006.

Biography

Le Luo was born on February 20, 1977 in Wuhan, China. He grew up in Wuhan and Guangzhou, and graduated from Zhixin High School in 1995. He obtained the B.S. in Physics with honors in June, 1999 from Sun Yat-sen University. During his undergraduate time, he was awarded the Jianhao Scholarship, China's top award for the best-performing university students, by All-China Students' Federation. In the fall of 1999, he joined in Institute of Modern Optics at Peking University. During that time, he was awarded the Wang Da-yan Prize in Optics by Chinese Optical Society for his contribution on studies of interactions of intense ultrafast laser pulses with optical materials. He got the M.S. in Optics in 2002. In the February of 2002, he married Xiaofang Huang, who he had met while attending Sun Yat-sen University. Then he enrolled in the graduate school at Duke University in the same year. He joined John Thomas's research group for atom cooling and trapping in June 2003. During his time at Duke, he received the Fritz London Fellowship for his researches on investigating thermodynamics and fluidity of degenerate, strongly interacting Fermi gases. He also received the Chinese Government Award for Outstanding Self-Financed Students Abroad. In May 2005, he was awarded the A.M. in Physics, with the Ph.D. in Physics following in May 2008. After that he was selected as the Joint Quantum Institute(JQI) Postdoctoral Fellow.

Publications

Since 2003:Strongly Interacting Ultracold Fermionic Atoms

A. Turlapov, J. Kinast, B. Clancy, Le Luo, J. Joseph, and J. E. Thomas" Is a gas of strongly interacting atomic fermions a nearly perfect fluid?", *Journal of Low Temperature Physics*, **150**, 567 (2008).

B. Clancy, L. Luo, and J. E. Thomas, "Observation of nearly perfect irrotational flow in normal and superfluid strongly interacting Fermi gases", *Physical Review Letters*, **99**, 140401 (2007).

L. Luo, B. Clancy, J. Joseph, J. Kinast, and J. E. Thomas, "Measurement of the entropy and critical temperature of a strongly interacting Fermi gas", *Physical Review Letters*, **98**, 080402 (2007).

J. Joseph, B. Clancy, L. Luo, J. Kinast, A. Turlapov, and J. E. Thomas, "Sound propagation in a Fermi gas near a Feshbach resonance" , *Physical Review Letters*, **98**, 170401 (2007).

L. Luo, B. Clancy, J. Joseph, J. Kinast, A. Turlapov, and J. E. Thomas, "Evaporative cooling of unitary Fermi gas mixtures in optical traps", *New Journal of Physics*, **8**, 213 (2006).

J. E. Thomas, J. Joseph, B. Clancy, L. Luo, J. Kinast, and A. Turlapov, "Optical trapping and fundamental studies of atomic Fermi gases", *Proc. SPIE*, **6326**, 632602 (2006).

Before 2003:Interactions of Intense Ultrafast Laser Pulses with Optical Materials

Hengchang Guo, H. Jiang, Le Luo, C. Wu, Hongcang Guo, X. Wang, H. Yang, Q. Gong, F. Wu, T. Wang, M.Shi, "Two-photon polymerization of gratings by interference of a femtosecond laser pulse", *Chemical Physics Letters*, **374**, 381 (2003).

Z.X.Wu, H.B.Jiang, Le Luo, H.C.Guo, H.Yang, Q.Gong, "Multiple focus and long filament of focused femtosecond pusle propagation in fused silica", *Optics Letters*, **27**, 448 (2002).

Le Luo, D.Wang, C.Li, H.Jiang, H.Yang, Q.Gong, "Formation of diversiform microstructures in wide band gap materials by tight focusing femtosecond laser pulses", *Journal of Optics A*, **4**, 105 (2002).

Le Luo, C.Li, D.Wang, H.Yang, H.Jiang, Q.Gong, "Pulse-parameter dependence of the configuration characteristics of a micro-structure in fused SiO2 induced by femtosecond laser pulses", *Apply Physics A*, **74**, 497 (2002).

Le Luo, C.Li, S.Wang, W.Huang, C.Wu, H.Yang, H.Jiang, Q.Gong, “Optical microstructures fabricated by femtosecond laser two-photon polymerization”, *Journal of Optics A*, **3**, 489 (2001).

C.Li, Le Luo, S.Wang, W.Huang, Q.Gong, “Two-photon microstructure-polymerization initiated by a coumarin derivative/iodonium saltsystem”, *Chemical Physics Letters*, **340**, 444 (2001).

Gong Qihuang, Luo Le, Yang Hong, Wang Dangling, Jiang Hongbing, “The mechanism and application of microfabrication by ultrafast laser beam”, *Bulletin of National Natural Science Foundation of China*, **15, November**, 7 (2001) (in Chinese).

C.Li, D.Wang, Le Luo, H.Yang, Z.J.Xia, Q.Gong, “Feasibility of femtosecond laser writing multi-layered bit planes in fused silica for three-dimensional optical data storage”, *Chinese Physics Letters*, **18**, 541 (2001).

D.Wang, C.Li, Le Luo, H.Yang, Q.Gong, “Sub-diffraction-limited voids in bulk quartz induced by femtosecond laser pulses”, *Chinese Physics Letters*, 18, 65 (2001).

Li Chengde, Wang Dangling, Luo Le, Yang Hong and Gong Qihuang, “Femtosecond laser applications in three-dimensional micro-systems”, *Physics*, **29**, 719 (2000) (in Chinese).

Contributed Presentations

Le Luo, B.Clancy, J.Joseph, and J.E. Thomas, “Strongly interacting fermions: exploring universal thermodynamics and perfect fluidity”, Seminar in Join Quantum Institute, NIST and University of Maryland, February, 2008.

Le Luo, B.Clancy, J.Joseph, and J.E. Thomas, “Strongly interacting fermions: perfect fluidity in both the coldest and the hottest matter in nature”, Seminar in Rowland Institute at Harvard University, February, 2008.

A.Turlapov, J.Kinast, B.Clancy, Le Luo, J.Joseph, and J.E. Thomas, “Is a gas of strongly interacting atomic fermions a nearly perfect fluid?”, QFS2007, Kazan, Russia, August 2007.

J.E.Thomas, B.Clancy, Le Luo, J.Joseph A.Turlapov, J.Kinast, “Thermodynamic measurements in a strongly interacting Fermi gas”, DAMOP 2007, Calgary, Canada, June 2007.

B.Clancy, Le Luo, J.Kinast, J.Joseph, A.Turlapov, J.E.Thomas, ”Sound in a strongly interacting Fermi gas”, APS March Meeting 2006, Baltimore, Maryland, March 2006.